Fundamentals of Thermocapillary Sculpting of Liquid Nanofilms and Applications to Thin Film Micro-Optics

Thesis by
Kevin Robert Fiedler

In Partial Fulfillment of the Requirements for the
degree of
Doctor of Philosophy

CALIFORNIA INSTITUTE OF TECHNOLOGY
Pasadena, California

2017
Defended May 5, 2017

Kevin Robert Fiedler
ORCID: 0000-0002-9656-7663

For Sam

"It's the song of a promising heart, of the souls that the ocean unite."

-Roy Khan

ACKNOWLEDGEMENTS

I would like to thank Dr. Troian for the opportunity to work in the Laboratory of Interstitial and Small Scale Transport (LIS^2T) for six years. I have learned a great deal about fluid dynamics, heat transfer, and optics, but more importantly you have fostered a sense of independence in scientific inquiry. You let me shape and sculpt my projects while providing wisdom, support, and guidance along the way. I truly appreciate your care and concern for the present and future plans of both Sam and I. You have also grown the group into a vibrant place with good people whom I have had the privilege to work with. To Euan McLeod, thank you for teaching me about the lab when I first arrived and how to run your experiment. To my office mates Gerry della Rocca, Zack Nicolaou, Teddy Albertson, Chengzhe Zhou, and Nick White, thank you for being my travel buddies, answering all my COMSOL questions, and your scientific insights. To my undergraduate students, Lisa Lee, Charlie Tschirhart, Tatiana Roy, Daniel Lim, Cassidy Yang, Nancy Wu, and Yanbing Zhu, thank you for your excitement while working in lab with me and letting me hone my lab safety officer speeches on you. To Dr. Thompson, thank you for installing every piece of software that I requested and keeping the computers running smoothly.

I am extremely grateful to NASA because the final four years of my graduate work were supported by a 2013 NASA Space Technology Research Fellowship (NSTRF). The NSTRF team has been a joy to work with and has provided me an outstanding opportunity to work at the Jet Propulsion Laboratory (JPL). While at JPL, I have collaborated with the Quantum Science and Technology group which is guided by Nan Yu. It has been a privilege to work with everyone at JPL and it has been an undeniably positive aspect of my time during graduate school. In particular, I am thankful to Nan for helping shape my intuition about waveguides, resonators, and optics in general. Thank you to Thanh Le for teaching me how to couple light into waveguides and answering my practical questions in lab. Additional thanks go to the rest of the members of the Quantum Science and Technology group, especially Ivan Grudinin, Tabitha Joiner, Janice Magnuson, Vincent Huet, and Shouhua Huang.

During my time at Caltech, I have used several pieces of equipment from outside the group that were crucial for the success of my projects. In particular, I would like to thank Dr. Yunbin Guan and the Caltech Microanalysis Center for use of the Zygo NewView 600 scanning white light interferometer. I would also like to thank Dr. Rustem Ismagilov for use of his cleanroom and the Zemetrics Zegage scanning

white light interferometer. In addition, I want to thank Ali Ghaffari for use of the equipment in the Micro/Nano Fabrication Laboratory in Watson. Finally, thank you to the Molecular Materials Research Center of the Beckman Institute for the use of their profilometer, atomic force microscope, and ellipsometer.

I would also like to thank my thesis committee composed of Dr. Sandra Troian, Dr. Kenneth Libbrecht, Dr. David Politzer, and Dr. Nan Yu. I greatly appreciate your commitment of both time and effort to be part of my committee. I am also thankful for the wisdom and guidance you have provided over the course of my graduate career. You have helped and advised me during my candidacy examination and have continued through to my final dissertation and defense.

The preparation for my graduate career started long before I set foot on Caltech's campus and there are so many people who have helped and mentored me along my academic journey. I specifically want to thank my undergraduate advisor, Dr. Uriel Nauenberg. Uriel, thank you for opening your lab to undergraduates and teaching me about the Standard Model and the International Linear Collider. Additional thanks goes to my other undergraduate mentors, Dr. Jerry Qi, Dr. Kris Westbrook, Dr. David Rusch, Dr. Joan Gabriele, and Dr. Harvey Segur. I appreciate your efforts in teaching a young physicist about academic research. I am eternally grateful to the Boettcher Foundation for giving me the means to perform my undergraduate studies. Thank you to all my teachers from kindergarten through high school who fostered creativity and curiosity. I also want to thank Coach Boley, Coach Vande Hoef, Coach Scott, Coach Tingley, and Coach Dunn for teaching me the value of punctuality and how to tie a tie.

My time at Caltech would have been woefully incomplete without the cornucopia of friends I have encountered throughout my time in graduate school. I have been incredibly fortunate to have met Christy Jenstad who makes everything at Caltech run smoothly. I also shared the camaraderie of a lunch table who provided stories and a daily dose of vitamin D, so thank you to Fadl Saadi, John Lloyd, Erik Verlage, Ivan Papusha, Mark Harfouche, Dongwan Kim, Renee McVay, Yufeng Huang, Cris Flowers, Chengyun Hua, Sunita Darbe, and Oliver Shafaat. Outside of normal working hours I spent a large amount of time playing intramural basketball and pickup with Anandh Swaminathan, David Chen, Murat Kologlu, Sacha di Poi, Lorenzo Moncelsi, Sahin Lale, Ron Appel, and Dennis Ko. Thanks for keeping me in shape and letting me win from time to time. Thank you to my trivia buddies, Max Jones, Ioana Craiciu, Andrew McClung, Hannah Goodwin, and Sean O'Blenis, all

of whom carried the team to victory on many occasions. Thank you to all my St. Rita friends, Susan Blakeslee, Running Bear Bunch, Jo and Paul Hanson, Joe Feeney, Florian and Riza Schwandner, Jim Blackford, Jonathan Blakeslee, and Lisa Bowman, for providing stimulating discussion and excellent snacks. Thank you to all my friends from afar, Max Ederer, Steve Bloom, Chris Messick, Jess Townsend, John Chen, Kelsey and Matanya Horowitz, and Nate Mutkus. Even though I don't see you as much as I should, you still put up with me. A special thanks goes to Chris Marotta and Lisa Mauger, who were not only excellent friends, but also provided me delicious meals while I was writing my thesis.

My family has always supported my academic endeavors and I want to express my sincere thanks to them for their continued support. Scott, thank you for keeping me honest, enlightening me about the world of finance, and perpetually finding me new book series to read. Dad, thank you for expanding my intellectual horizons, whether that was by playing "Saved by the Brain" in the car, teaching me during Math Olympiads, quizzing me on powers of two, or crushing me in backgammon. Mom, thank you for your tireless effort and dedication. I truly could not have done it without you and you made a difference in my life in countless ways.

Last, but certainly not least, I want to thank my wife, Sam. You light up my life and give me cause to smile each time I think of you. You have been an invaluable keystone of my graduate education and I could not have done it without you. Thank you for all you do, and I look forward to our future adventures both in life and science. I love you more than words can express and so this thesis is dedicated to you.

ABSTRACT

This doctoral thesis describes experimental work conducted as part of ongoing efforts to identify and understand the source of linear instability in ultrathin liquid films subject to large variations in surface temperature along the air/liquid interface. Previous theoretical efforts by various groups have identified three possible physical mechanisms for instability, including an induced surface charge model, an acoustic phonon model, and a thermocapillary model. The observed instability manifests as the spontaneous formation of arrays of nano/microscale liquid protrusions arising from an initially flat nanofilm, whose organization is characterized by a distinct in-plane wavelength and associated out-of-plane growth rate. Although long range order is somewhat difficult to achieve due to thin film defects incurred during preparation, the instability tends toward hexagonal symmetry within periodic domains achieved for a geometry in which the nanofilm is held in close proximity to a cooled, proximate, parallel, and featureless substrate.

In this work, data obtained from a previous experimental setup is analyzed and it is shown how key improvements in image processing and analysis, coupled with more accurate finite element simulations of thermal profiles, lead to more accurate identification of the fastest growing unstable mode at early times. This fastest growing mode is governed by linear instability and exponential growth. This work was followed by re-examination of real time interference fringes using differential colorimetry to quantify the actual rate of growth of the fastest growing peaks within the protrusion arrays. These initial studies and lingering questions led to the introduction of a new and improved experimental setup, which was redesigned to yield larger and more reproducible data sets. Corresponding improvements to the image analysis process allowed for the measurement of both the wavelength and growth rate of the fastest growing mode simultaneously. These combined efforts establish that the dominant source of instability is attributable to large thermocapillary stresses. For the geometry in which the nanofilm surface is held in close proximity to a cooled and parallel substrate, the instability leads to a runaway process, characterized by exponential growth, in which the film is attracted to the cooled target until contact is achieved.

The second part of this thesis describes fabrication and characterization of microlens arrays and linear waveguide structures using a similar experimental setup. However, instead of relying on the native instability observed, formation and growth of liquid

shapes and protrusions is triggered by pre-patterning the cooled substrate with a desired mask for replication. These preformed cooled patterns, held in close proximity to an initially flat liquid nanofilm, induce a strong non-linear response via consequent patterned thermocapillary stresses imposed along the air/liquid interface. Once the desired film shapes are achieved, the transverse thermal gradient is removed and the micro-optical components are affixed in place naturally by the resultant rapid solidification. The use of polymer nanofilms with low glass transition temperatures, such as polystyrene, facilitated rapid solidification, while providing good optical response. Surface characterization of the resulting micro-optical components was accomplished by scanning white light interferometry, which evidences formation of ultrasmooth surfaces ideal for optical applications. Finally, linear waveguides were created by this thermocapillary sculpting technique and their optical performance characterized. In conclusion, these measurements highlight the true source of instability in this geometry, and the fabrication demonstrations pave the way for harnessing this knowledge for the design and creation of novel micro-optical devices.

PUBLISHED CONTENT AND CONTRIBUTIONS

[1]K. R. Fiedler, and S. M. Troian, "Early time instability in nanofilms exposed to a large transverse thermal gradient: improved image and thermal analysis", J. Appl. Phys. **120**, 205303 (2016),

KRF assisted with the design of the project, remeasured characteristic instability wavelengths, improved the numerical simulations, prepared draft plots and figures, and participated in the writing of the manuscript.

[2]K. R. Fiedler, E. McLeod, and S. M. Troian, "Differential colorimetry measurements of instability growth in nanonfilms exposed to a large transverse thermal gradient", To be submitted to J. Appl. Phys. (May 2017),

KRF recomputed the interference fringe spectra of nanofilms to establish local film thickness, measured the peak heights as a function of time and associated growth rates, compared results to theoretical predictions of the thermocapillary model, prepared draft plots and figures, and participated in the writing of the manuscript.

[3]K. R. Fiedler, and S. M. Troian, "Optical observations of a long-wavelength thin film instability driven by thermocapillary forces", To be submitted to Phys. Rev. E. (2017),

KRF assisted with the design of the project, built the experimental setup, measured the wavelength of the fastest growing mode, performed the numerical simulations, prepared draft plots and figures, and participated in the writing of the manuscript.

[4]S. W. D. Lim, K. R. Fiedler, C. Zhou, and S. M. Troian, "Converging and diverging microlens arrays by spatiotemporal control of thermocapillary forces", To be submitted to Appl. Phys. Lett. (2017),

KRF assisted with the design of the project, measurements obtained, discussions of the results, and preparation of the manuscript.

[5]K. R. Fiedler, S. W. D. Lim, Y. Zhu, and S. M. Troian, "Fabrication of microdevices through thermocapillary sculpting of molten polymer nanofilms", In preparation (2017),

KRF assisted with the design of the project, built the fabrication setup, assisted with device characterization, prepared draft plots and figures, and participated in the writing

of the manuscript.

[6]K. R. Fiedler, Y. Zhu, T. Le, N. Yu, and S. M. Troian, "Characterization of linear optical waveguides formed by thermocapillary sculpting of nanoscale polymer melt films", In preparation (2017),

KRF assisted with the design of the project, fabricated and characterized the waveguides, performed the numerical simulations of waveguide properties, prepared draft plots and figures, and participated in the writing of the manuscript.

TABLE OF CONTENTS

LIST OF ILLUSTRATIONS

LIST OF TABLES

NOMENCLATURE

This is a compilation of the abbreviations and symbols which are used in this work. Generally, dimensional variables are lower case letters while dimensionless variables are the corresponding upper case letters. In the case of operators, the nomdimensional analogs typically have a tilde over them. Within the body of this document, certain variables will be subscripted by i. This subscript will typically represent different layers in the system, primarily either "film" or "air".

$[\cdot]$	Denotes a difference across the air/nanofilm interface
α	RGB channel index
α_4	First aspheric coefficient
β	Nondimensional growth rate
ΔT^{curr}	Temperature drops computed using the expanded domain in Ch. 3
ΔT^{orig}	Temperature drops computed in Ref. [1]
$\delta\phi$	Perturbed electric potential
ΔT_{out}	Difference between the heater and chiller setpoints
ΔT_{sin}	Temperature drop across the sinusoidally perturbed bilayer
$\delta\vec{D}$	Perturbed electric displacement field
$\delta\vec{E}$	Perturbed electric field
$\delta h_{k'}$	Fourier coefficients describing the current interface height
Δl	Fabry-Pérot etalon change in length
Δt	Time step between peak observation images
δ	Normalized mask pin height
ΔT	Temperature difference between the bounding plates
$\delta_j(\lambda_{opt})$	Optical phase
$\dot{Q}_{ITO}$	Volumetric heat flux density within the ITO heater
ϵ	Long wavelength expansion parameter
Γ	Dimensionless surface tension
γ	Surface tension of the fluid/air interface
Γ_c	Characteristic scale of the surface tension
γ_T	Thermocapillary coefficient
$\hat{n}$	Unit normal vector at the nanofilm/air interface
$\hat{t}$	Tangential unit vector
$\hbar$	Reduced Planck's constant
κ	Thermal conductivity ratio

λ_{opt}	Wavelength of optical illumination
λ_o	Lateral spacing of instability protrusions
$\mathbf{E}$	Rate of strain tensor
$\mathbf{M}_{j,j+1}$	Optical transmission matrix from layer j to layer $j+1$
$\mathbf{M}_j$	Optical transmission matrix through layer j
$\mathbf{T}$	Stress tensor
$\mathbf{T}^{\text{em}}$	Maxwell stress tensor
$\mathcal{F}(k,t)$	Peak fitting function
$\mathcal{G}(k)$	Gaussian fitting function
$\mathcal{L}(k)$	Lorentzian fitting function
T	Temperature
T_+	Temperature measured by the thermocouple on the chiller
T_-	Temperature measured by the thermocouple underneath the heater
T_{C}	Temperature of the cooled top plate
T_{H}	Temperature of the heated bottom plate
$\mathrm{T}_{\mathrm{Int}}$	Temperature at the interface of the molten nanofilm
T_g	Glass transition temperature
μ	Dynamic viscosity of the fluid
∇_s	Surface gradient
$\nabla_{\parallel}$	Horizontal components of the gradient
ν	Mode order
ω	Frequency of an oscillator
$\overline{Ca}$	Modified capillary number
$\overline{Ma}$	Modified Marangoni number
$\overline{Q}$	Acoustic quality factor
ϕ	Electric potential
ϕ^o	Base state electric potential
Φ_c	Characteristic scale of the electric potential
Φ_c'	Alternative electric potential scale in the EHD model
Φ_o	Applied potential difference
Π	MicroAngelo mask pitch
ρ	Density of the fluid
σ	Surface charge density at the fluid/air interface
σ_{free}	Free charge density at an interface
τ	Dimensionless time
$\mathrm{v}_{\text{exp}}(x,y,t,\alpha)$	Experimental fringe color values

$\mathrm{v}_{\mathrm{theor}}(h, \alpha)$	Fringe color values
Θ	Nondimensional temperature
θ	Angle between principal axes and the raw data axes
$\tilde{\mathrm{v}}_{\mathrm{theor}}(h, \alpha)$	Normalized fringe color values
ε	Relative permittivity
ε_o	Permittivity of free space
$\vec{D}$	Electric displacement field
$\vec{E}$	Electric field
$\vec{E}^o$	Base state electric field
$\vec{f}_{\mathrm{body}}$	Body forces acting on the bulk of the fluid
$\vec{K}$	Nondimensional wavevector of the instability
$\vec{k}$	Wavevector of the instability
$\vec{q}$	Heat flux density
$\vec{u} = (u, v, w)$	Velocity field within the nanofilm
$\vec{u}_{\parallel} = (u, v)$	Horizontal components of the velocity
$\widetilde{\delta h}$	Nondimensional perturbation used in linear stability analysis
$\widetilde{\nabla_s}$	Dimensionless surface gradient
$\widetilde{\nabla_{\parallel}}$	Dimensionless lateral gradient
$\widetilde{\phi_i}$	Nondimensional electric potential
$\vec{E}_i$	Nondimensional electric field
A	Amplitude of peak fitting function
a	Width of an infinite square well
A_{lens}	Individual MLA lens area
A_{wg}	Waveguide amplitude
b_o	Growth rate of peak fitting function
C^{AP}	Fitting constant for the material constants in the AP model
C^{TC}	Fitting constant for the material constants in the TC model
c_p	Specific heat capacity
D	Dimensionless gap separation
d_1	MicroAngelo mask pin or block height
d_2	MicroAngelo mask depression height
D_{lens}	Characteristic MLA lens diameter
d_o	Separation between bounding plates
D_p	MicroAngelo mask pin or depression diameter
D_{wg}	Gaussian decay of waveguide envelope
E_ν	Energy of mode ν

f_1	Larger microlens focal length
f_2	Smaller microlens focal length
F_{array}	Fresnel number of the microlens array
F_{lens}	Fresnel number of an individual microlens
f_p	Mask pin protrusion function
G	Functional form of the mask topography
$g(x, y, t, h)$	Peak height cost function
H	Dimensionless film thickness
$h(x, y, t)$	Interface position between molten nanofilm and air
$h_{\text{meas}}(x, y, t)$	Measured peak height as a function of time
h_{paste}	Thermal paste thickness
$h_{\text{pk}}(t)$	Peak height during film growth
h_o	Initial film thickness
I	Measured intensity signal
$I(\lambda_{\text{opt}})$	Intensity spectrum of the halogen light source
I_R	Reflected intensity from a Fabry-Pérot etalon
k	Thermal conductivity
k_+	Right half maximum point of peak fitting function
k_-	Left half maximum point of peak fitting function
k_{max}	Upper bound for the peak fitting function
k_{min}	Lower bound for the peak fitting function
k_o	Maximum point of peak fitting function
l	Fabry-Pérot etalon length
m	Mass of a particle in an infinite square well
n	Index of refraction
P	Dimensionless pressure
p	Pressure within the fluid
P_{ac}	Nondimensional acoustic pressure used in the AP model
p_{ac}	Acoustic pressure used in the AP model
P_{el}	Nondimensional electric pressure used in the SC model
p_{el}	Electric pressure used in the SC model
P_c	Characteristic scale of the pressure in the fluid
Pr	Prandtl number
$R(\lambda_{\text{opt}}, h)$	Reflectance from a multilayer stack
R_1	Microlens radii of curvature along the larger principal axis
R_2	Microlens radii of curvature along the smaller principal axis

r_{paste}	Thermal paste radius
$r_{j,j+1}$	Fresnel amplitude reflection coefficient
Re	Reynolds number
$rn(x, y)$	Random number generator in COMSOL
$S\left(\vec{k}, t\right)$	Power spectral density
$S_\alpha(\lambda_{\text{opt}})$	Spectral responsivity of the camera
t_{final}	Last time which was analyzed in the wavelength analysis
t_{meas}	Time of initial wavelength measurement
t_f	Final time of the peak observation
t_{ref}	Time stamp of the image which was used as the reference image
$t_{j,j+1}$	Fresnel amplitude transmission coefficient
U, V, W	Dimensionless fluid velocities
u_c	Characteristic lateral scale of the flow velocity
u_p	Speed of sound in the molten nanofilm
$W(k)$	Background plus peak fitting function
w_c	Characteristic vertical scale of the flow velocity
w_{wg}	Waveguide width
x', y'	Microlens principal axes
X, Y, Z	Dimensionless position variables
$x_{\text{pk}}, y_{\text{pk}}$	Peak location as a function of time
x_f, y_f	Location of peak at final time
x_o, y_o	Coordinates of the microlens vertex in raw data coordinates
z_j	Thickness of layer j
z_{max}	Height of individual microlens
AP	Abbreviation for the acoustic phonon model
AR	Asphericity ratio
EHD	Abbreviation for the electrohydrodynamic model
HeNe	Helium neon
IPA	Isopropyl alcohol
ITO	Indium tin oxide
JPL	Jet Propulsion Laboratory
LIS^{2}T	Laboratory of Interstitial and Small Scale Transport
NSTRF	NASA Space Technology Research Fellowship
PBS	Polarizing beam splitter
PDMS	Polydimethylsiloxane
PID	Proportional integral derivative

PMMA	Poly(methyl methacrylate)
PS	Polystyrene
RGB	Red green blue
RMS	Root mean square
RTD	Resistance temperature detector
SC	Abbreviation for the surface charge model
SHWS	Shack-Hartmann wavefront sensor
SSR	Sum of squared residuals
TC	Abbreviation for the thermocapillary model
TE	Transverse electric electromagnetic wave polarization
TM	Transverse magnetic electromagnetic wave polarization

Chapter 1

INTRODUCTION

Almost twenty years ago, the spontaneous formation of pillars from a molten nanofilm in a confined geometry subject to a transverse thermal gradient was observed by Chou and Zhuang [2, 3]. In their experiment, solid polymeric nanofilms were spun coat on a silicon wafer with an initial film thickness, h_o, of approximately one hundred nanometers. Subsequently, another silicon wafer was overlaid on this coated wafer. To ensure an air gap between the top surface of the nanofilm and the overlaid wafer, the wafer was patterned with spacers which determined the total plate separation distance, d_o, and this distance was typically on the order of several hundred nanometers to a micron. A schematic of their experimental setup is shown in Fig. 1.1. Upon heating, the temperature of the system was raised significantly above the glass transition temperature so that the film was in a molten state. After deformation times ranging from 5 to 80 minutes, the molten film was allowed to solidify and hexagonal arrays of pillars with lateral spacing on the order of microns were observed after the bounding plate was removed. These pillars had spanned the air gap during deformation and contacted the top plate, creating pillars with flat tops and fairly vertical sidewalls. At the time, there was no explanation for this phenomenon. It has since generated controversy over the dominant physical mechanism that causes the molten nanofilm to be unstable in this system. Several possibilities have been put forth and will be discussed in turn.

Figure 1.1: Basic nanofilm instability geometry

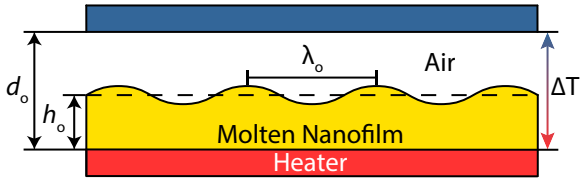

Schematic of the nanofilm geometry. The molten nanofilm is bounded from below by a heated substrate and from above by an air layer. The air layer is bounded from above by a plate where the total plate separation, d_o, is typically on the order of a micron, while the initial film thickness, h_o, is on the order of hundreds of nanometers. The temperature drop from bottom to top plates is typically on the order of 10 °C. The lateral spacing of the protrusions, λ_o, is on the order of microns to tens of microns.

1.1 Previous Instability Investigations: Surface Charge (SC) Model

The first model proposed to explain the instability of this film was put forward by Chou and Zhuang [2, 3]. Their model treats the molten nanofilm from the perspective of fluid dynamics wherein it is linearly unstable to perturbations. They hypothesized that charges at the nanofilm's free interface induce image charges in the heating and cooling plates. The combined effect of these charges creates an electric field which exerts a destabilizing electrostatic stress on the interface to overcome the stabilizing force of surface tension. Due to its dependence on interfacial charge density, this model will be referred to as the surface charge (SC) model. Interestingly, they noted that in addition to electrical effects, thermal effects might be playing a role because if the molten nanofilm was not bounded from above by the overlaid wafer, then the pillars were not observed after solidification of the film. However, they did not intentionally impose a thermal gradient across the system with active cooling of the top plate. Additionally, they estimated that the critical numbers for cellular convection driven by thermal effects such as Rayleigh-Bénard and Bénard-Marangoni convection were far too small for instability to occur. Regardless, the spatial period of the observed hexagonal arrays showed an unexplained dependence on the temperature of the system.

1.2 Previous Instability Investigations: Acoustic Phonon (AP) Model

Nearly simultaneously with the work of Chou and Zhuang, Schäffer and co-workers investigated an instability in a similar geometry [4–6]. As before, they spun coat polymeric nanofilms onto silicon substrates and placed them in a confined geometry through the use of spacers. The key difference from the experiments of Chou and Zhuang is that in the experiments of Schäffer *et al.* the top plate was actively cooled. The cooler top plate was held at a temperature above the glass transition temperature of the polymer and the temperature difference between the bounding plates was on the order of 10 °C. The setup was subjected to this externally imposed transverse thermal gradient overnight and then the nanofilm was solidified. Once again, hexagonal arrays of pillars with flat tops were observed upon removal of the top plate. To rule out any electrostatic effects, both of the bounding plates were electrically grounded. As Chou and Zhuang did, Schäffer *et al.* calculated the Rayleigh-Bénard and Bénard-Marangoni numbers in nanofilm experiments and found that they were many orders of magnitude smaller than the critical ones required for instability. To explain the observed results, they suggested that the instability might be due to an acoustic phonon mechanism leading to periodic modulation of the acoustic pressure

within the film. In this model, acoustic phonon reflections create a net acoustic pressure which destabilizes the interface and causes protrusions to grow. Specifically, they conjectured that phonons with low frequency would be coherently reflected off the nanofilm/air interface while high frequency phonons would be unaffected by the interface and conduct most of the heat flux through the system. These low frequency phonon reflections would then contribute a significant destabilizing radiation pressure which overpowers surface tension to create protrusions. This model will be referred to as the acoustic phonon (AP) model.

Following a derivation of a complete hydrodynamic theory describing the instability in terms of the radiation pressure, they used linear stability analysis to derive a result for the characteristic spacing of the film's fastest growing mode, λ_o, as a function of the initial film thickness, h_o, total plate separation, d_o, and temperature drop, ΔT. They then performed a set of experiments to probe the functional dependence of λ_o on d_o by introducing a tilt between the bottom and top plates to measure a range of d_o for a single run at a given h_o value. They repeated this procedure for several values of h_o. By fitting one of the parameters in their theory, they were able to find agreement between the experimental data and the theoretical prediction for λ_o over a limited range of d_o. Due to their decision to vary d_o through substrate tilt, they were only able to measure values of d_o that varied by a factor of three in a given experimental run and only achieved a range of a factor of six over all the experimental runs. Furthermore, the induced substrate tilt induced an extra lateral gradient which was not included in their model. More problematic for their comparisons to the wavelength predicted by linear stability theory, the values that they reported for λ_o were all measured far outside of the linear regime because the deformations were allowed to contact the top plate and solidify. Prolonged contact with the top plate can drastically changed the pattern morphology through coarsening or van der Waals interactions which were not considered in the AP model. Furthermore, several measurements were made in regions where growth of structures was nucleated by defects which would also invalidate the comparison of the experimental data to linear stability theory.

Following in this vein, Peng *et al.* demonstrated formation of hexagonal arrays from heated polymeric nanofilms in confined geometries [7], similar to what had been previously reported by Schäffer *et al.*. They then took the hexagonal patterns and transferred them to a stamp made of polydimethylsiloxane (PDMS) which could then be used for future microfabrication steps. Even though there was strong ordering in

these systems, Peng *et al.* did not measure the spacing of their arrays as a function of h_o, d_o, or ΔT, nor did they compare to any proposed model.

1.3 Previous Instability Investigations: Thermocapillary (TC) Model

Several years later, Dietzel and Troian began to investigate these issues and re-evaluated the assumptions of the SC and AP models [8–10]. In particular, they noted that phonon mean free paths on the order of ten to one hundred nanometers required for coherent reflection from the film interface in the AP model have only been measured in solid polymer systems at temperatures far below the glass transition temperature. They conclude that it is unlikely that molten amorphous films would be able to support the long attenuation lengths due to the increased mobility of the polymeric system above the glass transition temperature. They also reexamined the assertion by both Chou *et al.* [2] and Schäffer *et al.* [6] that the critical numbers which typically govern Bénard-Marangoni convection would be too small in nanofilm experiments for instability. Their theoretical and computational work [8–10] has indicated that the instability represents a new limit of the long wavelength Bénard-Marangoni instability, distinguished by extremely large thermocapillary forces and negligible hydrostatic forces, which is not governed by the traditional critical numbers. The underlying concept for this model is that protrusions will be slightly cooler than valleys and they will have a correspondingly higher surface tension. This gradient in surface tension between peaks and valleys creates a destabilizing shear stress along the interface which causes lateral flow and, through incompressibility, out of plane protrusion growth. This model will be referred to as the thermocapillary (TC) model. Based on the TC model, they also derived a prediction for the characteristic spacing of the film's fastest growing mode, λ_o, as a function of the initial film thickness, h_o, total plate separation, d_o, and temperature drop, ΔT, and compared it to the experimental data of Schäffer *et al.* [4–6] and concluded that the TC model was consistent with the experimental data to that point, and could potentially play a critical, if not dominant, role in the film evolution.

Shortly thereafter, McLeod *et al.* performed a series of experimental wavelength measurements to further investigate the underlying instability mechanism [1]. These experiments focused on improving the experimental measurement techniques to more accurately compare the measured wavelengths to the predictions of linear stability theory from the SC, AP, and TC models. In particular, they performed *in situ* optical measurements of the instability during the deformation process to

measure λ_o when the deformations were small compared to the initial film thickness and well before the protrusions contacted the top plate. Furthermore, none of the previous experiments had measured or calculated the temperature drop across the nanofilm/air bilayer. Due to the minute size of the gap, it is impossible to directly measure the temperature in the gap using a thermocouple. Instead, the difference between heater and chiller setpoints was taken to be equal to the temperature drop across the bilayer. McLeod *et al.* improved upon this procedure by performing finite element simulations of the experimental setup based on thermocouple measurements to compute the temperature difference across the bilayer. They also performed many more experimental runs than Schäffer *et al.* [4–6] and swept a much larger range of d_o, h_o, and ΔT. With this experimental setup, they found that the experimental data for the measured wavelength was most consistent with the TC model, but that close numerical agreement required the thermal conductivity of the polymer nanofilm to be fit. The required value for the vertical, out-of-plane polymer thermal conductivity was found to be five times larger than the bulk value. It was originally postulated that polymer chain alignment could account for the increase in thermal conductivity, but this hypothesis is problematic for two reasons. First, in cases where polymer alignment has been observed [11], the polymer used was well above the entanglement molecular weight where long chains can interact. Conversely, the polymer used in the work of McLeod *et al.* was well below the entanglement limit so a potential alignment mechanism is not clear. Second, the increase in thermal conductivity of spin coated polymeric thin films has been observed in the lateral direction, not the vertical one [12]. As such, even with the improved experimental setup, there remained discrepancies between the experimental measurements and the theoretical predictions.

1.4 Pattern Replication through Controlled Film Deformation

Concurrently with the fundamental science investigations into the underlying instability mechanism presented above, there has been research into controlling and localizing feature deformation as a potential manufacturing technique. To do this, the locally flat top plate from Fig. 1.1 was patterned with another set of features which stretch toward the nanofilm in addition to the spacers. A schematic of this geometry is shown in Fig. 1.2. In all three models, the presence of a patterned mask on the top plate will localize deformation and allow for control of the film because the mask changes the local gap width.

The first demonstration of pattern replication in these types of geometries was by

Figure 1.2: Basic nanofilm deformation geometry with a patterned top plate

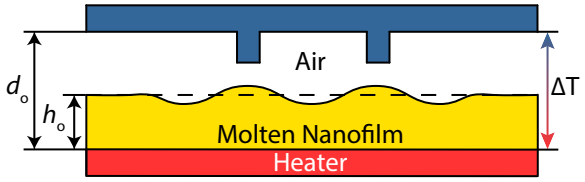

Schematic of the nanofilm geometry where the feature deformation is localized by patterns on the top plate. The ranges for the experimental parameters are the same as for Fig. 1.1.

Chou and co-workers where they patterned the top plate with a triangle, a square and the text "PRINCETON" [2, 13]. In each case, they observed pillar arrays in the shape of the patterned mask and virtually no deformation in the regions outside the mask. In a related study, Chou *et al.* observed that the film would completely cover the applied mask if it was closer in proximity to the initial film height [14]. In this case, the pillar arrays merged into a continuous feature which replicated the mask. Similarly, Schäffer *et al.* demonstrated pattern replication of hexagonal arrays, square arrays, and lines with feature sizes as small as 500 nm [4, 15]. In all of the cases just discussed, the features were allowed to grow until they contacted the mask. This meant that all the features had flat tops due to their interaction with the mask. Instead of allowing the film to grow unchecked, McLeod and Troian stopped the film deformation before it interacted with the mask to produce a square array of curved lenses [16]. This experimental work corresponds more closely with the schematic in Fig. 1.2 than the previous studies which would have touched the mask protrusions. The ability to localize nanofilm deformations using patterned masks opens up a new avenue for the fabrication of unique structures with ultrasmooth surfaces. This system profiles as a novel lithographic technique, but more work needs to be done to understand the advantages and limitations.

1.5 Thesis Outline

In the spirit of the previous studies mentioned above, this thesis seeks to investigate and understand the residual discrepancies between the experimental instability data and the theoretical predictions. It also seeks to deform nanofilms into structures through the use of patterned masks on the top plate and then characterize their properties. As such, the remainder of this thesis is organized as follows. In Ch. 2, the equations describing the distinct sources of instability proposed to explain the spontaneous nanofilm deformation are reviewed. For each of the three previously proposed linear instability models (SC, AP, and TC), predictions for the fastest

growing mode and its corresponding wavelength and growth rate are compared. The next three chapters focus on the experimental and numerical work which investigated the dominant physical mechanism driving this thin film instability. Specifically, in Ch. 3 improved analysis techniques for image analysis and thermal simulation are detailed to improve the comparison of measured wavelengths to the AP and TC models. In Ch. 4 the growth of protrusions are measured as a function of time using colorimetric information derived from thin film interference fringes. The resulting growth rates are compared to the predictions of the TC model. Next, an improved experimental setup is detailed and the instability measurements which were made with it are described in Ch. 5. The results of these experiments strongly indicate that the dominant instability mechanism is caused by interfacial thermocapillary stresses. After this, the next two chapters focus on the fabrication of two kinds of micro-optical components using thermocapillary forces. First, microlens arrays were fabricated and characterized. The results of this study are presented in Ch. 6. Beyond microlens arrays, linear optical waveguides were also fabricated and characterized and this work is described in Ch. 7. Finally, Ch. 8 describes conclusions from the thesis and suggests experimental improvements for future studies.

Chapter 2

REVIEW AND COMPARISON OF THREE THIN FILM INSTABILITY MODELS

As mentioned above in Ch. 1, nanofilms on a heated substrate are found experimentally to be unstable. To better understand this phenomenon, several groups have approached this process theoretically by modeling it as a fluid instability. All of the proposed mechanisms for this phenomenon revolve around thin film hydrodynamic instability theory. They differ in the specific driving force which destabilizes the film against the force of surface tension but possess several unifying features. In this chapter we review the three proposed mechanisms and synthesize the previous work into one derivation which has consistent notation and serves to highlight the origin and influence of the various driving forces. We also present the derived expressions which the later experimental results are compared with in Ch. 3, Ch. 4, and Ch. 5.

The remainder of this chapter is organized as follows. In Sec. 2.1, a thin film height evolution equation is derived for the position of the nanofilm/air interface, $h(x, y, t)$, starting from the basic equations of fluid mechanics. Subsequently in Sec. 2.2 these equations are nondimensionalized and simplified using the long wavelength approximation. Then in Sec. 2.3 linear stability analysis is applied for each of the three proposed models. The results of the linear stability analysis give tangible predictions for the wavelength and growth rate of the fastest growing mode.

2.1 Fluid Dynamics Governing Equations

To specify the system completely, we define the domain, the governing equations, and the boundary conditions for the system. As mentioned in Ch. 1, the system of interest is a free surface molten nanofilm bounded by an air layer. Note that this derivation is only concerned with the fluid dynamics of the liquid nanofilm and not the air layer. Due to the large difference between the density and viscosity of the liquid nanofilm and the density and viscosity of the air layer only the dynamics of the fluid layer are explicitly considered.

2.1.1 Nanofilm Instability Geometry

The domain which we will consider is a thin liquid film which has an initial height h_o. This can also be interchangeably referred to as the film thickness. The film is

Figure 2.1: Schematic of the instability geometry

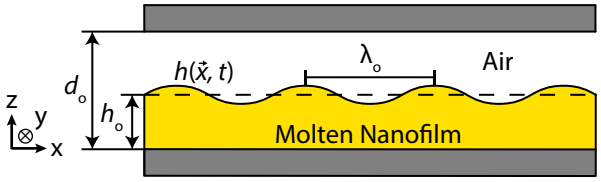

The molten nanofilm is bounded from below by a heated substrate and from above by a plate which is cooled. The total plate separation is denoted by d_o, while the initial film thickness is denoted by h_o. The temperature drop from hot to cold plates is denoted by $\Delta T = T_H - T_C$ and the lateral spacing of the protrusions is denoted by λ_o.

supported from below by a rigid, impermeable, heated substrate. The upper surface of the film is a free interface and a distance d_o from the bottom of the film there exists a cooled, upper plate which constrains the system in the vertical direction.

2.1.2 Mass and Momentum Continuity Equations

There are two differential equations which we will use to describe this system. The first differential equation is the mass continuity equation. We will assume incompressible flow and the resulting equation is

$$\nabla \cdot \vec{u} = 0. \tag{2.1}$$

In this equation $\vec{u} = (u, v, w)$ is the velocity of the molten nanofilm as a function of space and time. The other differential equation which governs the fluid dynamics in the molten layer is the Navier-Stokes equation where we have assumed that the fluid is Newtonian. This equation physically represents the conservation of momentum and has the form

$$\rho \frac{D\vec{u}}{Dt} = -\boldsymbol{\nabla} p + \mu \boldsymbol{\nabla}^2 \vec{u} + \vec{f}_{\text{body}}, \tag{2.2}$$

where ρ is the density of the fluid, p is the pressure, μ is the shear viscosity and $\vec{f}_{\text{body}}$ is the effect of body forces on the fluid. The most common body force which acts on fluids is gravity. Previous theoretical work [8–10] has estimated that gravity is negligible in nanofilm experiments due to the minuscule height scales. As such, f_{body} will be set to zero for the remainder of this work. The notation for the time derivative on the left hand side of the equation is the convective, or material, derivative and is defined by

$$\frac{D}{Dt} \equiv \frac{\partial}{\partial t} + \vec{u} \cdot \boldsymbol{\nabla}. \tag{2.3}$$

This describes how a quantity changes in time as well as local changes due to variations along the local velocity field.

2.1.3 Fluid Velocity and Pressure Boundary Conditions

With the governing equations specified, we now outline the boundary conditions required for solution of $\vec{u}$ and p. At the bottom of the liquid layer ($z = 0$ in Fig. 2.1) there is a no-slip and impenetrability condition with the solid wall

$$\vec{u}(z = 0) = 0. \tag{2.4}$$

At the free interface there is both a kinematic boundary condition and an interfacial stress balance. The kinematic boundary condition relates the vertical component of the fluid velocity to the change of the film height at the interface

$$w(z = h) = \frac{\partial h}{\partial t} + \vec{u}_{\parallel} \cdot \boldsymbol{\nabla}_{\parallel} h. \tag{2.5}$$

The subscript $\parallel$ denotes that only the $\hat{x}$ and $\hat{y}$ components of the subscripted quantity should be included in the expressions. Consequently, the horizontal velocity is defined by

$$\vec{u}_{\parallel} \equiv u\hat{x} + v\hat{y}. \tag{2.6}$$

Similarly, the horizontal gradient, $\boldsymbol{\nabla}_{\parallel}$, is composed of the derivatives solely in the $\hat{x}$ and $\hat{y}$ directions. In other words,

$$\boldsymbol{\nabla}_{\parallel} = \hat{x}\frac{\partial}{\partial x} + \hat{y}\frac{\partial}{\partial y}. \tag{2.7}$$

Beyond the kinematic boundary condition, we must balance the normal and tangential stresses at the interface which can be encapsulated in the following equation which applies at $z = h(x, y, t)$

$$(\mathbf{T}_{\text{air}} - \mathbf{T}_{\text{film}}) \cdot \hat{n} + p_{\text{ac}}\hat{n} + p_{\text{el}}\hat{n} + \boldsymbol{\nabla}_s\gamma - \gamma\hat{n}\,(\boldsymbol{\nabla}_s \cdot \hat{n}) = 0. \tag{2.8}$$

In this equation the stress tensors, $\mathbf{T}$, are subscripted by their respective layers and will be described in detail below. The unit normal vector, $\hat{n}$, is perpendicular to the nanofilm surface everywhere and points from the film to the air. The terms p_{ac} and p_{el} are pressures arising from acoustic or electrical sources, respectively, and will be defined in the relevant sections below since they correspond to specific proposed models. These have been explicitly removed from the fluid pressure p in the stress

tensor so that limiting cases can be considered for each model. Additionally, γ is the surface tension at the air/film interface and $\boldsymbol{\nabla}_s$ is the surface gradient which is defined by

$$\boldsymbol{\nabla}_s \equiv \boldsymbol{\nabla} - \hat{n}(\hat{n} \cdot \boldsymbol{\nabla}). \tag{2.9}$$

This means that the surface gradient operator only exists in the plane of the interface, by definition, since the normal components have been removed. Furthermore, note that $\boldsymbol{\nabla}_s = \boldsymbol{\nabla}_{\|}$ only where the interface is flat and $\hat{n} = \hat{z}$.

2.2 Scaling the Governing Equations and Applying the Lubrication Approximation

The system of interest has been defined and now the governing equations are scaled to simplify the analysis. In particular, we know that both the overall system dimensions and the characteristic lateral length scale of the instability growth, λ_o, are much larger than the initial film thickness, h_o. As such, we define a small quantity

$$\epsilon \equiv \frac{h_o}{\lambda_o}, \tag{2.10}$$

and after scaling the equations we only keep terms to first order in ϵ since $\epsilon^2 \ll 1$. This approximation has several names including the lubrication or long wavelength approximation [17–19]. All the horizontal lengths are scaled by λ_o and all the vertical lengths scaled by h_o. Time is scaled using the horizontal length and a characteristic lateral speed, u_c, which can be chosen arbitrarily. Therefore,

$$X = \frac{x}{\lambda_o}; Y = \frac{y}{\lambda_o}, \tag{2.11}$$

$$Z = \frac{z}{h_o}; H = \frac{h}{h_o}; D = \frac{d}{h_o}, \tag{2.12}$$

$$U = \frac{u}{u_c}; V = \frac{v}{u_c}; W = \frac{w}{w_c}, \tag{2.13}$$

$$\tau = \frac{t u_c}{\lambda_o}; P = \frac{p}{P_c}; \Gamma = \frac{\gamma}{\Gamma_c}, \tag{2.14}$$

$$\widetilde{\boldsymbol{\nabla}_s} = \lambda_o \boldsymbol{\nabla}_s; \widetilde{\boldsymbol{\nabla}_{\|}} = \lambda_o \boldsymbol{\nabla}_{\|}. \tag{2.15}$$

The scalings for the pressure, P_c, and surface tension, Γ_c, will be determined below during the simplification of the Navier-Stokes equations. The quantity w_c is a characteristic velocity scale for flow in the vertical direction. Due to the disparate length scales, it would not be correct to scale all the fluid velocities by the same quantity. Now we return to the governing equations and scale them using the

quantities above which will illuminate several relationships between these quantities and allow us to simplify the equations significantly.

The first equation we will scale is the continuity equation to get a relationship between u_c and w_c. Scaling Eq. (2.1) results in

$$\frac{\partial U}{\partial X} + \frac{\partial V}{\partial Y} + \frac{w_c}{\epsilon u_c}\frac{\partial W}{\partial Z} = 0.$$

To ensure that all the terms in the continuity equation are of the same order the vertical velocity scale is set by $w_c = \epsilon u_c$. Consequently, the scaled continuity equation is

$$\frac{\partial U}{\partial X} + \frac{\partial V}{\partial Y} + \frac{\partial W}{\partial Z} = 0. \tag{2.16}$$

Using these velocity scalings, the Navier-Stokes equations are simplified. For simplicity, the equations are resolved into components during the scaling process. These are

$$\begin{aligned}
\hat{x} &: \epsilon Re\frac{DU}{D\tau} = -\frac{\epsilon h_o P_c}{\mu u_c}\frac{\partial P}{\partial X} + \epsilon^2\frac{\partial^2 U}{\partial X^2} + \epsilon^2\frac{\partial^2 U}{\partial Y^2} + \frac{\partial^2 U}{\partial Z^2},\\
\hat{y} &: \epsilon Re\frac{DV}{D\tau} = -\frac{\epsilon h_o P_c}{\mu u_c}\frac{\partial P}{\partial Y} + \epsilon^2\frac{\partial^2 V}{\partial X^2} + \epsilon^2\frac{\partial^2 V}{\partial Y^2} + \frac{\partial^2 V}{\partial Z^2},\\
\hat{z} &: \epsilon^3 Re\frac{DW}{D\tau} = -\frac{\epsilon h_o P_c}{\mu u_c}\frac{\partial P}{\partial Z} + \epsilon^2\left(\epsilon^2\frac{\partial^2 W}{\partial X^2} + \epsilon^2\frac{\partial^2 W}{\partial Y^2} + \frac{\partial^2 W}{\partial Z^2}\right).
\end{aligned}$$

In these equations, the Reynolds number, Re, has been defined as

$$Re = \frac{\rho u_c h_o}{\mu}. \tag{2.17}$$

The Reynolds number represents the ratio of inertial forces to viscous forces within the fluid [19]. Based on the similarity of the terms in front of the pressure in each of the three components, there is a clear scaling for the pressure

$$P_c = \frac{\mu u_c}{\epsilon h_o}. \tag{2.18}$$

With this definition for the nondimensionalization of the pressure, the long wavelength approximation is now implemented which requires that (1) $\epsilon^2 \ll 1$ and (2) $\epsilon Re \ll 1$. This approximation takes advantage of the disparity between vertical and lateral length scales to greatly reduce the complexity of the analysis. Neglecting terms of second order in ϵ or higher, the scaled Navier-Stokes equations are

$$\| : \frac{\partial^2 \vec{U}_\|}{\partial Z^2} = \widetilde{\nabla}_\| P, \tag{2.19}$$

$$\hat{z} : \frac{\partial P}{\partial Z} = 0. \tag{2.20}$$

Moving on to the boundary conditions, the no-slip and impenetrability condition from Eq. (2.4) scales in a straightforward manner

$$\vec{U}(Z = 0) = 0. \tag{2.21}$$

Similarly, the kinematic boundary condition from Eq. (2.5) becomes

$$W(Z = H) = \frac{\partial H}{\partial \tau} + \vec{U}_{\parallel}(Z = H) \cdot \boldsymbol{\nabla}_{\parallel} H. \tag{2.22}$$

Scaling the interfacial stress balance in Eq. (2.8) within the long wavelength approximation is more complicated and intermediate results will first be derived and then compiled into the final expression. Specifically the normal vector, $\hat{n}$, the surface gradient, $\boldsymbol{\nabla}_s$, the surface divergence of the normal vector, $\boldsymbol{\nabla}_s \cdot \hat{n}$, and the stress tensor, $\mathbf{T}_i$, are scaled.

2.2.1 Scaling the Normal Vector to a Surface

The surface of the film described by $h(x, y)$ can be expressed in three dimensions as a locus of points where a function F is equal to zero.

$$F(x, y, z) = z - h(x, y) = 0.$$

The unit normal to the surface is found by taking the gradient of F and normalizing it

$$\hat{n} = \frac{\boldsymbol{\nabla} F}{|\boldsymbol{\nabla} F|} = \left(\left(\frac{\partial h}{\partial x} \right)^2 + \left(\frac{\partial h}{\partial y} \right)^2 + 1 \right)^{-1/2} \left(-\frac{\partial h}{\partial x} \hat{x} - \frac{\partial h}{\partial y} \hat{y} + \hat{z} \right). \tag{2.23}$$

Each of these quantities scales as defined above, so the terms in the preceding square root will be of order ϵ^2 and will be neglected in this analysis. Consequently, the scaled unit normal in nondimensional units becomes

$$\hat{n} = -\epsilon \widetilde{\boldsymbol{\nabla}}_{\parallel} H + \hat{Z}. \tag{2.24}$$

2.2.2 Scaling the Surface Gradient Operator

We can now take the scaled normal vector in Eq. (2.24) and use it to compute the scaled surface gradient, $\widetilde{\boldsymbol{\nabla}_s}$. Recalling the definition of the surface gradient in Eq. (2.9), this expression scales to

$$\widetilde{\boldsymbol{\nabla}_s} = \widetilde{\boldsymbol{\nabla}} - \hat{n} \left(\hat{n} \cdot \widetilde{\boldsymbol{\nabla}} \right).$$

After substitution of the normal vector from Eq. (2.23) into the definition of the surface gradient in Eq. (2.9), scaling the resulting expression, and simplifying, the scaled surface gradient becomes

$$\widetilde{\boldsymbol{\nabla}}_s = \widetilde{\boldsymbol{\nabla}}_\parallel + \left(\widetilde{\boldsymbol{\nabla}}_\parallel H\right)\frac{\partial}{\partial Z} + \hat{Z}\epsilon\left(\widetilde{\boldsymbol{\nabla}}_\parallel H\right)\left(\widetilde{\boldsymbol{\nabla}}_\parallel + \left(\widetilde{\boldsymbol{\nabla}}_\parallel H\right)\frac{\partial}{\partial Z}\right). \tag{2.25}$$

Note that in this equation the derivatives grouped with H within parentheses only act on H, not on the argument of the surface gradient operator itself.

2.2.3 Scaling the Surface Divergence of the Normal Vector

The last term in the stress balance from Eq. (2.8) represents the effect of surface tension and depends on the surface divergence of the normal vector. Since these two quantities have been scaled in Eq. (2.9) and Eq. (2.24), they are combined to find

$$\widetilde{\boldsymbol{\nabla}}_s \cdot \hat{n} = -\epsilon\widetilde{\boldsymbol{\nabla}}_\parallel^2 H. \tag{2.26}$$

When computing this expression, we note that none of the quantities in the normal vector shown in Eq. (2.24) depend on Z.

2.2.4 Scaling the Stress Tensor

The stress tensors in the film and air layers are crucial pieces of the interfacial stress balance in Eq. (2.8). Within each layer i, the stress tensor takes the form

$$\mathbf{T}_i = -p_i\mathbf{I} + 2\mu_i\mathbf{E}_i. \tag{2.27}$$

Here p_i is the fluid pressure and $\mathbf{E}_i$ is the rate of strain tensor. Since the viscosity of air is many orders of magnitude smaller than the viscosity of the molten nanofilm, the product $2\mu_{\text{air}}\mathbf{E}_{\text{air}}$ will be neglected as a small contribution. The subscripts on μ_{film} and E_{film} will be dropped since there can be no confusion. The rate of strain tensor is defined by

$$\mathbf{E} \equiv \frac{1}{2}\left(\boldsymbol{\nabla}\vec{u} + \left(\boldsymbol{\nabla}\vec{u}\right)^{\text{tr}}\right) = \frac{1}{2}\begin{bmatrix} 2\dfrac{\partial u}{\partial x} & \dfrac{\partial u}{\partial y}+\dfrac{\partial v}{\partial x} & \dfrac{\partial u}{\partial z}+\dfrac{\partial w}{\partial x} \\ \dfrac{\partial v}{\partial x}+\dfrac{\partial u}{\partial y} & 2\dfrac{\partial v}{\partial y} & \dfrac{\partial v}{\partial z}+\dfrac{\partial w}{\partial y} \\ \dfrac{\partial w}{\partial x}+\dfrac{\partial u}{\partial z} & \dfrac{\partial w}{\partial y}+\dfrac{\partial v}{\partial z} & 2\dfrac{\partial w}{\partial z} \end{bmatrix}. \tag{2.28}$$

In the stress balance of Eq. (2.8), the quantity which enters the equation is the stress tensor difference dotted with the normal vector, $\hat{n}$. From the definition of the stress

tensor in Eq. (2.27) one obvious scaling for the stress tensor is the characteristic pressure, P_c. Therefore,

$$\frac{1}{P_c}\left(\mathbf{T}_{\text{air}} - \mathbf{T}_{\text{film}}\right)\cdot\hat{n} = \frac{p_{\text{air}} - p_{\text{film}}}{P_c}\hat{n} - \frac{2\mu}{P_c}\mathbf{E}\cdot\hat{n}.$$

Note that $p_{\text{air}} - p_{\text{film}} = p$. Additionally, converting the rate of strain tensor to nondimensional units, dotting by the normal vector on the right, and dropping terms of order ϵ^2 yields

$$\frac{2\mu}{P_c}\mathbf{E}\cdot\hat{n} = \epsilon\begin{bmatrix} 2\epsilon\dfrac{\partial U}{\partial X} & \epsilon\dfrac{\partial U}{\partial Y} + \epsilon\dfrac{\partial V}{\partial X} & \dfrac{\partial U}{\partial Z} \\ \epsilon\dfrac{\partial V}{\partial X} + \epsilon\dfrac{\partial U}{\partial Y} & 2\epsilon\dfrac{\partial V}{\partial Y} & \dfrac{\partial V}{\partial Z} \\ \dfrac{\partial U}{\partial Z} & \dfrac{\partial V}{\partial Z} & 2\epsilon\dfrac{\partial W}{\partial Z} \end{bmatrix}\begin{bmatrix} -\epsilon\dfrac{\partial H}{\partial X} \\ -\epsilon\dfrac{\partial H}{\partial Y} \\ 1 \end{bmatrix} = \epsilon\frac{\partial \vec{U}_{\parallel}}{\partial Z}.$$

Inserting these results above yields

$$\frac{1}{P_c}\left(\mathbf{T}_{\text{air}} - \mathbf{T}_{\text{film}}\right)\cdot\hat{n} = P\hat{n} - \epsilon\frac{\partial \vec{U}_{\parallel}}{\partial Z}. \tag{2.29}$$

All the intermediary results in Eqs. (2.24), (2.25), (2.26), and (2.29) are inserted back into the full stress balance in Eq. (2.8) to find

$$P\hat{n} - \epsilon\frac{\partial \vec{U}_{\parallel}}{\partial Z} + P_{\text{ac}}\hat{n} + P_{\text{el}}\hat{n} + \frac{\Gamma_c}{\lambda_o P_c}\widetilde{\boldsymbol{\nabla}}_s\Gamma + \frac{\epsilon\Gamma_c}{\lambda_o P_c}\Gamma\left(\widetilde{\boldsymbol{\nabla}}_{\parallel}^2 H\right)\hat{n} = 0.$$

Note that this equation contains both normal and tangential components. This equation now suggests a natural scaling for Γ_c so that all the tangential components (the second and the fifth terms above) will be of order ϵ and all the vertical components will be of order unity

$$\Gamma_c = \epsilon\lambda_o P_c = \frac{\mu u_c}{\epsilon}. \tag{2.30}$$

The nondimensionalized surface tension has the form reminiscent of the traditional capillary number, Ca, [19] except scaled by a factor of ϵ^{-3}. As such, the modified capillary number is defined as

$$\overline{Ca} = \frac{1}{\epsilon^2\Gamma} = \frac{\mu u_c}{\gamma\epsilon^3} = \frac{Ca}{\epsilon^3}. \tag{2.31}$$

The capillary number represents the ratio of viscous forces to forces due to surface tension. Similar to the way that we split the vectorial Navier-Stokes equations into

vertical and horizontal components in Eqs. (2.19) and (2.20), the interfacial stress balance is decomposed into components

$$\| : \frac{\partial \vec{U}_{\|}}{\partial Z} = -\widetilde{\boldsymbol{\nabla}}_s \Gamma, \tag{2.32}$$

$$\hat{z} : P = -\frac{1}{\overline{Ca}} \left(\widetilde{\boldsymbol{\nabla}}_{\|}^2 H \right) - P_{\mathrm{ac}} - P_{\mathrm{el}}. \tag{2.33}$$

2.2.5 Summary of Scaled Equations

The governing equations and the boundary conditions have all been scaled to transform them into nondimensional equations which were then simplified using the lubrication approximation. For convenience, here are all the scaled equations which will be referenced when deriving the thin film height evolution equation

$$\frac{\partial U}{\partial X} + \frac{\partial V}{\partial Y} + \frac{\partial W}{\partial Z} = 0, \tag{2.34}$$

$$\frac{\partial^2 \vec{U}_{\|}}{\partial Z^2} = \widetilde{\boldsymbol{\nabla}}_{\|} P, \tag{2.35}$$

$$\frac{\partial P}{\partial Z} = 0, \tag{2.36}$$

$$\vec{U}(Z = 0) = 0, \tag{2.37}$$

$$W(Z = H) = \frac{\partial H}{\partial \tau} + \vec{U}_{\|} \cdot \boldsymbol{\nabla}_{\|} H, \tag{2.38}$$

$$\frac{\partial \vec{U}_{\|}(Z = H)}{\partial Z} = -\widetilde{\boldsymbol{\nabla}}_s \Gamma, \tag{2.39}$$

$$P(Z = H) = -\frac{1}{\overline{Ca}} \left(\widetilde{\boldsymbol{\nabla}}_{\|}^2 H \right) - P_{\mathrm{ac}}(Z = H) - P_{\mathrm{el}}(Z = H). \tag{2.40}$$

2.2.6 Thin Film Height Evolution Equation

To proceed from these equations to a single differential equation for the interface evolution, the general approach will be to use the kinematic boundary condition to introduce a temporal derivative of $H(X, Y, \tau)$ and then rewrite everything in terms of $H(X, Y, \tau)$. Note that the interface height is both a function of time and position. For notational convenience, we will drop this explicit functional dependence in the following equations. To do this, consider a slightly rewritten form of the continuity equation in Eq. (2.34) (or equivalently Eq. (2.16))

$$\widetilde{\boldsymbol{\nabla}}_{\|} \cdot \vec{U}_{\|} + \frac{\partial W}{\partial Z} = 0.$$

Integrating this equation with respect to Z from $Z = 0$ to $Z = H$ results in

$$W(Z = H) - W(Z = 0) + \int_0^H \widetilde{\boldsymbol{\nabla}}_{\parallel} \cdot \vec{U}_{\parallel} dZ = 0.$$

The first term is the kinematic boundary condition from Eq. (2.38) (or equivalently Eq. (2.22)) and the second is the impenetrability condition from Eq. (2.37) (or equivalently Eq. (2.21)). After substitution this equation becomes

$$\frac{\partial H}{\partial \tau} + \vec{U}_{\parallel}(Z = H) \cdot \widetilde{\boldsymbol{\nabla}}_{\parallel} H + \int_0^H \widetilde{\boldsymbol{\nabla}}_{\parallel} \cdot \vec{U}_{\parallel} dZ = \frac{\partial H}{\partial \tau} + \widetilde{\boldsymbol{\nabla}}_{\parallel} \cdot \int_0^H \vec{U}_{\parallel} dZ = 0. \quad (2.41)$$

In the second equality the Leibnitz rule for differentiation has been used to bring the derivative outside the integral [19]. All that remains now is to solve for $\vec{U}_{\parallel}$ and then integrate the result to find the height evolution equation. To accomplish this, the remaining equations are used. From the vertical component of the scaled Navier-Stokes equations in Eq. (2.36) (or equivalently Eq. (2.20)), it is clear that the pressure, P, is independent of the vertical coordinate. As such, the lateral components of the scaled Navier-Stokes equations in Eq. (2.35) (or equivalently Eq. (2.19)) are integrated twice to solve for

$$\vec{U}_{\parallel} = \frac{Z^2}{2} \widetilde{\boldsymbol{\nabla}}_{\parallel} P + A_{\parallel} Z + B_{\parallel}. \quad (2.42)$$

In this equation, $A_{\parallel}$ and $B_{\parallel}$ are two component vectors which are the integration constants for each component equation. Based on the no-slip condition from Eq. (2.37) (or equivalently, Eq. (2.21)) it follows that $B_{\parallel} = 0$. The other integration constant can be determined by using the horizontal components of the interfacial stress balance in Eq. (2.39) (or equivalently Eq. (2.32)). Since this poses a condition on the derivative of the horizontal velocity at $Z = H$, the velocity which satisfies this equation is clearly

$$\vec{U}_{\parallel} = \left(\frac{Z^2}{2} - HZ \right) \widetilde{\boldsymbol{\nabla}}_{\parallel} P - Z \widetilde{\boldsymbol{\nabla}}_s \Gamma.$$

The horizontal gradient of the pressure can be computed from the vertical component of the interfacial stress balance in Eq. (2.40) (or equivalently Eq. (2.33)). If we insert this expression for the gradient of the pressure into the preceding equation we find that

$$\vec{U}_{\parallel} = \left(\frac{Z^2}{2} - HZ \right) \left(\frac{-1}{Ca} \left(\widetilde{\boldsymbol{\nabla}}_{\parallel}^3 H \right) - \widetilde{\boldsymbol{\nabla}}_{\parallel} P_{\mathrm{ac}}(Z = H) - \widetilde{\boldsymbol{\nabla}}_{\parallel} P_{\mathrm{el}}(Z = H) \right) - Z \widetilde{\boldsymbol{\nabla}}_s \Gamma.$$

As mentioned previously, the specific forms of P_{ac}, P_{el}, and $\widetilde{\boldsymbol{\nabla}_s}\Gamma$ depend on the chosen model and will be discussed further below. Regardless, none of these values depend on Z and the evaluation at $Z = H$ will be suppressed from now on. Consequently, this equation for the horizontal velocity can be integrated from $Z = 0$ to $Z = H$ to find

$$\int_0^H \vec{U}_{\parallel} dZ = \frac{H^3}{3}\left(\frac{1}{\widetilde{Ca}}\left(\widetilde{\boldsymbol{\nabla}_{\parallel}^3}H\right) + \widetilde{\boldsymbol{\nabla}_{\parallel}}P_{\text{ac}} + \widetilde{\boldsymbol{\nabla}_{\parallel}}P_{\text{el}}\right) - \frac{H^2}{2}\widetilde{\boldsymbol{\nabla}_s}\Gamma. \tag{2.43}$$

Inserting Eq. (2.43) back into Eq. (2.41) yields the height evolution equation

$$\frac{\partial H}{\partial \tau} + \widetilde{\boldsymbol{\nabla}_{\parallel}} \cdot \left[\frac{H^3}{3}\left(\frac{1}{\widetilde{Ca}}\left(\widetilde{\boldsymbol{\nabla}_{\parallel}^3}H\right) + \widetilde{\boldsymbol{\nabla}_{\parallel}}P_{\text{ac}} + \widetilde{\boldsymbol{\nabla}_{\parallel}}P_{\text{el}}\right) - \frac{H^2}{2}\widetilde{\boldsymbol{\nabla}_s}\Gamma\right] = 0. \tag{2.44}$$

2.3 Linear Stability Analysis

While the exact forms for P_{ac}, P_{el}, and $\widetilde{\boldsymbol{\nabla}_s}\Gamma$ have not been specified yet, it will be shown below they all depend exclusively on H. As such, through the chain rule the derivatives will act on H and therefore any constant H will satisfy this differential equation. To investigate the stability of this family of solutions, the initially flat interface (denoted by $H = 1$) is perturbed by a function of the form

$$H = 1 + \widetilde{\delta h} e^{\beta(K)\tau} e^{i\vec{K}_{\parallel}\cdot\vec{X}_{\parallel}}. \tag{2.45}$$

The quantity $\widetilde{\delta h}$ is the magnitude of the perturbation and is assumed to be small so that we neglect terms of second order in this quantity. The real exponential contains the nondimensional growth rate, β, and the imaginary exponential contains explicit dependence on the horizontal wavevector, $\vec{K}_{\parallel}$, which contains only $\hat{x}$ and $\hat{y}$ components. The magnitude of the wavevector is related to the real space wavelength, λ, by

$$K = |\vec{K}_{\parallel}| = \frac{2\pi\lambda_o}{\lambda}. \tag{2.46}$$

The nondimensional growth rate, β, is related to the dimensional growth rate, b, through

$$\beta(K) = \frac{b(k)\lambda_o}{u_c}. \tag{2.47}$$

To proceed any further with the linearization, the forms of each model will be specified separately in turn.

Figure 2.2: Instability geometry in SC model

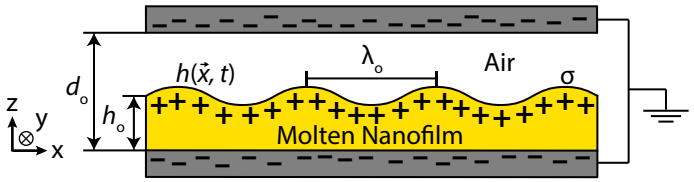

The distinguishing feature of the SC model is the presence of a surface charge density, σ, along the interface which induces an electric field that leads to the destabilizing electric pressure.

2.3.1 SC Model: Electrostatic Pressure

Within the SC model the driving force is posited to be electrostatic in origin. In the work of Chou and Zhuang [2, 3], there was assumed to be a surface charge density along the interface which would induce image charges in the upper and lower bounding plates which were grounded, as illustrated in Fig. 2.2. The presence of the electric charges creates an electric field which they hypothesized was responsible for the deformation of the interface. Because the AP model had not yet been published by Schäffer *et al.*, the net pressure from acoustic phonon reflections is zero and so $P_{\text{ac}} = 0$. Furthermore, they did not consider the surface tension to vary with any external field which implies that $\widetilde{\boldsymbol{\nabla}_s \Gamma} = 0$. All that remains is to define the electric pressure, P_{el}, created by the interfacial charge density and complete the linear stability analysis.

The electrostatic pressure arises from the difference between the Maxwell stress tensors, $\mathbf{T}_i^{\text{em}}$, in the air and nanofilm layers. Explicitly, the magnitude of the pressure in the normal direction is

$$P_{\text{el}} = \frac{1}{P_c} \hat{n} \cdot \left(\mathbf{T}_{\text{air}}^{\text{em}} - \mathbf{T}_{\text{film}}^{\text{em}} \right) \cdot \hat{n}. \tag{2.48}$$

The Maxwell stress tensor in matter without any magnetic fields has the form [20]

$$\mathbf{T}^{\text{em}} = \vec{E}\vec{D} - \frac{1}{2}\mathbf{I}\left(\vec{E} \cdot \vec{D}\right), \tag{2.49}$$

where $\vec{E}$ is the electric field and $\vec{D} = \varepsilon_o \varepsilon \vec{E}$ is the electric displacement field. ε_o is the the permittivity of free space. Note that ε is the relative permittivity of the medium, and is distinct from ϵ which is the long-wavelength expansion parameter. In air we assume that the relative permittivity is equal to unity, so that $\varepsilon_{\text{air}} = 1$. To proceed further, the electric fields in both the air and film layers are solved using Laplace's equation and then the Maxwell stress tensors are computed. These are

then inserted into the electrostatic pressure term, P_{el}. Once P_{el} has been computed, linear stability analysis is applied to the resulting thin film height evolution equation to find the wavevector and growth rate of the fastest growing mode.

Electrostatic Governing Equations

Within the derivation of Chou and Zhuang, it was assumed that there are no significant magnetic fields present in the system. This reduces the problem of solving for the electric field within the system to a simple electrostatics problem. Furthermore, it was assumed that there was no volumetric charge density present within either the air or film layers and that the only charge is present at the interface between the two layers. The interfacial charge density is constant during deformation and denoted by σ. These assumptions imply that the governing differential equation is Laplace's equation

$$\boldsymbol{\nabla}^2 \phi_i = 0. \tag{2.50}$$

In this expression ϕ_i is the potential in the ith layer. Since there is no externally applied voltage in this system, both the upper and lower bounding plates are assumed to be grounded so that

$$\phi_{\text{film}}(z = 0) = 0, \tag{2.51}$$

$$\phi_{\text{air}}(z = d) = 0. \tag{2.52}$$

Along the interface, the usual electrostatic boundary conditions are applied [20]

$$\hat{n} \cdot \left(\vec{D}_{\text{air}} - \vec{D}_{\text{film}} \right) = \varepsilon_o \hat{n} \cdot \left(\vec{E}_{\text{air}} - \varepsilon_{\text{film}} \vec{E}_{\text{film}} \right) = \sigma, \tag{2.53}$$

$$\hat{n} \times \left(\vec{E}_{\text{air}} - \vec{E}_{\text{film}} \right) = 0. \tag{2.54}$$

Finally, the relationship between the electric field and the electric potential is

$$\vec{E}_i = -\boldsymbol{\nabla} \phi_i. \tag{2.55}$$

Scaled Electrostatic Equations

To scale the electrostatic equations, the same scalings which were defined in Sec. 2.2 are used but there are two more for the electric potential and the electric field.

$$\widetilde{\phi_i} = \frac{\phi_i}{\Phi_c}; \widetilde{\vec{E}}_i = \frac{\vec{E}_i h_o}{\Phi_c}. \tag{2.56}$$

The quantity Φ_c is a characteristic potential which will be determined in the course of scaling the equations, similar to how P_c and Γ_c were determined above. The relationship between the nondimensional electric potential and electric field transforms from Eq. (2.55) to

$$\widetilde{\vec{E}}_i = -\epsilon\widetilde{\boldsymbol{\nabla}}_{\parallel}\widetilde{\phi}_i - \frac{\partial\widetilde{\phi}_i}{\partial Z}. \tag{2.57}$$

Once we nondimensionalize Laplace's equation from Eq. (2.50) we find that to second order

$$\frac{\partial\widetilde{\phi}_i}{\partial Z^2} = 0. \tag{2.58}$$

The exterior Dirichlet boundary conditions simply become

$$\widetilde{\phi}_{\text{film}}(Z = 0) = 0, \tag{2.59}$$

$$\widetilde{\phi}_{\text{air}}(Z = D) = 0. \tag{2.60}$$

The tangential electrostatic boundary condition of Eq. (2.54) is equivalent to the requirement that the potential be continuous across the interface. Therefore,

$$\widetilde{\phi}_{\text{film}}(Z = H) = \widetilde{\phi}_{\text{air}}(Z = H). \tag{2.61}$$

The final electrostatic boundary equation is the one shown in Eq. (2.53) for the normal components of the electric displacement field at the interface. Using the scaled normal vector which was derived above in Eq. (2.24), this yields

$$\frac{\Phi_c\varepsilon_o}{h_o}\left(-\epsilon\widetilde{\boldsymbol{\nabla}}_{\parallel}H + \hat{Z}\right)\cdot\left(-\epsilon\widetilde{\boldsymbol{\nabla}}_{\parallel}\widetilde{\phi}_{\text{air}} - \varepsilon_o\frac{\partial\widetilde{\phi}_{\text{air}}}{\partial Z}\hat{Z} + \epsilon\varepsilon_{\text{film}}\widetilde{\boldsymbol{\nabla}}_{\parallel}\widetilde{\phi}_{\text{film}} + \varepsilon_{\text{film}}\frac{\partial\widetilde{\phi}_{\text{film}}}{\partial Z}\hat{Z}\right) = \sigma.$$

From this it is clear that all the tangential terms in this equation are order ϵ^2 and can be neglected. Furthermore, the characteristic electric potential scale arises from the charge density at the interface and should be

$$\Phi_c = \frac{\sigma h_o}{\varepsilon_o}. \tag{2.62}$$

This boundary condition then simplifies to

$$\varepsilon_{\text{film}}\frac{\partial\widetilde{\phi}_{\text{film}}(Z = H)}{\partial Z} - \frac{\partial\widetilde{\phi}_{\text{air}}(Z = H)}{\partial Z} = 1. \tag{2.63}$$

Electric Field Solution

The scaled Laplace equation from Eq. (2.58) was integrated twice with respect to Z, yielding electric potentials in each layer that are linear.

$$\widetilde{\phi}_{\text{film}} = A^{\text{SC}}_{\text{film}} Z + B^{\text{SC}}_{\text{film}},$$
$$\widetilde{\phi}_{\text{air}} = A^{\text{SC}}_{\text{air}} Z + B^{\text{SC}}_{\text{air}}.$$

In this equation $A^{\text{SC}}_{\text{film}}$, $B^{\text{SC}}_{\text{film}}$, $A^{\text{SC}}_{\text{air}}$, and $B^{\text{SC}}_{\text{air}}$ are integration constants. The Dirichlet boundary conditions on the bounding plates from Eqs. (2.59) and (2.60) imply that $B^{\text{SC}}_{\text{film}} = 0$ and $B^{\text{SC}}_{\text{air}} = -DA^{\text{SC}}_{\text{air}}$

$$\widetilde{\phi}_{\text{film}} = A^{\text{SC}}_{\text{film}} Z,$$
$$\widetilde{\phi}_{\text{air}} = A^{\text{SC}}_{\text{air}} (Z - D).$$

The electric potential must be continuous across $Z = H$ according to the boundary condition in Eq. (2.61), so that $A^{\text{SC}}_{\text{film}}$ can be expressed in terms of $A^{\text{SC}}_{\text{air}}$

$$A^{\text{SC}}_{\text{film}} = A^{\text{SC}}_{\text{air}} \frac{(H - D)}{H}.$$

This implies that the electric potentials should have the form

$$\widetilde{\phi}_{\text{film}} = A^{\text{SC}}_{\text{air}} \frac{Z(H - D)}{H},$$
$$\widetilde{\phi}_{\text{air}} = A^{\text{SC}}_{\text{air}} (Z - D).$$

The only remaining boundary condition is Eq. (2.63) and this implies that the one remaining integration constant is

$$A^{\text{SC}}_{\text{air}} = \frac{H}{(\varepsilon_{\text{film}} - 1) H - \varepsilon_{\text{film}} D}.$$

Returning to the electric potentials, they have the form

$$\widetilde{\phi}_{\text{film}} = \frac{Z(H - D)}{(\varepsilon_{\text{film}} - 1) H - \varepsilon_{\text{film}} D}, \tag{2.64}$$
$$\widetilde{\phi}_{\text{air}} = \frac{H(Z - D)}{(\varepsilon_{\text{film}} - 1) H - \varepsilon_{\text{film}} D}. \tag{2.65}$$

Based on the relation in Eq. (2.57) between the electric potential and the electric field, the nondimensional electric fields at the interface are

$$\widetilde{\vec{E}}_{\text{film}} = \epsilon \left(\frac{DH\widetilde{\boldsymbol{\nabla}}_{\parallel} H}{\left[\varepsilon_{\text{film}} D - (\varepsilon_{\text{film}} - 1)\, H\right]^2} \right) - \frac{(D-H)}{\varepsilon_{\text{film}} D - (\varepsilon_{\text{film}} - 1)\, H} \hat{Z}, \tag{2.66}$$

$$\widetilde{\vec{E}}_{\text{air}} = \epsilon \left(\frac{\varepsilon_{\text{film}} D(H-D)\widetilde{\boldsymbol{\nabla}}_{\parallel} H}{\left[\varepsilon_{\text{film}} D - (\varepsilon_{\text{film}} - 1)\, H\right]^2} \right) - \frac{H}{\varepsilon_{\text{film}} D - (\varepsilon_{\text{film}} - 1)\, H} \hat{Z}. \tag{2.67}$$

The most important thing to note about these electric fields is that the vertical components do not have an ϵ, while the horizontal components are first order in ϵ. This means that when these electric fields are inserted into the Maxwell stress tensor, all terms which contain products with two tangential components, such as $E_x E_y$, $E_x E_x$, and $E_y E_y$, are order ϵ^2 and can be neglected. Computing the expression for the normal component of the stress tensor dotted into the normal vector yields

$$\hat{n} \cdot \mathbf{T}^{\text{em}} \cdot \hat{n} = \varepsilon_o \varepsilon \begin{bmatrix} -\epsilon \dfrac{\partial H}{\partial X} & -\epsilon \dfrac{\partial H}{\partial Y} & 1 \end{bmatrix} \begin{bmatrix} -\dfrac{1}{2}E_z^2 & 0 & E_x E_z \\ 0 & -\dfrac{1}{2}E_z^2 & E_y E_z \\ E_x E_z & E_y E_z & \dfrac{1}{2}E_z^2 \end{bmatrix} \begin{bmatrix} -\epsilon \dfrac{\partial H}{\partial X} \\ -\epsilon \dfrac{\partial H}{\partial Y} \\ 1 \end{bmatrix} = \frac{\varepsilon_o \varepsilon}{2} E_z^2.$$

Recalling the form of the electric pressure from Eq. (2.48), the electric pressure is

$$P_{\text{el}} = \frac{\varepsilon_o}{2P_c} \left(E_{\text{air},z}^2 - \varepsilon_{\text{film}} E_{\text{film},z}^2 \right).$$

In terms of the electric fields which are expressed in Eqs. (2.66) and (2.67), this pressure becomes

$$P_{\text{el}} = \frac{\sigma^2}{2\varepsilon_o P_c} \left(\frac{(1-\varepsilon_{\text{film}})H^2 + 2\varepsilon_{\text{film}} DH - \varepsilon_{\text{film}} D^2}{\left[\varepsilon_{\text{film}} D - (\varepsilon_{\text{film}} - 1)\, H\right]^2} \right). \tag{2.68}$$

Linear Stability Predictions

Returning to the height evolution equation in Eq. (2.44), the gradient of the electrostatic pressure was computed and substituted yielding the following expression

$$\frac{\partial H}{\partial \tau} + \widetilde{\boldsymbol{\nabla}}_{\parallel} \cdot \left[\frac{H^3}{3\overline{Ca}} \left(\widetilde{\boldsymbol{\nabla}}_{\parallel}^3 H \right) + \frac{H^3 \sigma^2}{3\varepsilon_o P_c} \left(\frac{\varepsilon_{\text{film}} D^2}{\left[\varepsilon_{\text{film}} D - (\varepsilon_{\text{film}} - 1)\, H\right]^3} \right) \widetilde{\boldsymbol{\nabla}}_{\parallel} H \right] = 0. \tag{2.69}$$

Insertion of the linear stability perturbation function from Eq. (2.45) and cancellation of the common exponentials yields a nondimensional dispersion relation where terms of order $\widetilde{\delta h}^2$ have been dropped

$$\beta^{\mathrm{SC}}(K) + \frac{K^4}{3\overline{Ca}} - \frac{\sigma^2}{3\varepsilon_o P_c}\left(\frac{\varepsilon_{\mathrm{film}} D^2}{\left[\varepsilon_{\mathrm{film}} D - (\varepsilon_{\mathrm{film}} - 1)\right]^3}\right) K^2 = 0. \tag{2.70}$$

This specific dispersion relation has a representative form that will be borne out in the other proposed models. The dispersion relations for each model are of the general form

$$\beta(K) = A_2 K^2 - A_4 K^4, \tag{2.71}$$

where A_2 and A_4 are constants whose exact form depends on the model. As such, the location and magnitude of the maximum growth rate can be found from this general form. The mode with the maximum growth rate is assumed to be the one observed experimentally so the wavevector at which this maximum occurs should then correspond to the characteristic wavelength of the real space pattern which is observed. The form of the dispersion relation in Eq. (2.71) can be solved analytically for the wavevector corresponding to the maximum growth rate. This maximum wavevector is denoted by K_o

$$K_o = \sqrt{\frac{A_2}{2A_4}}. \tag{2.72}$$

The maximum value of the growth rate is then

$$\beta_o \equiv \beta(K_o) = \frac{A_2^2}{4A_4}. \tag{2.73}$$

For the SC model, A_2 and A_4 are

$$A_2^{\mathrm{SC}} = \frac{\sigma^2}{3\varepsilon_o P_c}\left(\frac{\varepsilon_{\mathrm{film}} D^2}{\left[\varepsilon_{\mathrm{film}} D - (\varepsilon_{\mathrm{film}} - 1)\right]^3}\right), \tag{2.74}$$

$$A_4^{\mathrm{SC}} = \frac{1}{3\overline{Ca}}. \tag{2.75}$$

Consequently, K_o and β_o for the SC model are

$$K_o^{\mathrm{SC}} = \sqrt{\frac{\sigma^2 h_o D^2}{2\varepsilon_o \varepsilon_{\mathrm{film}}^2 \gamma \epsilon^2}}\left(D + \frac{1}{\varepsilon_{\mathrm{film}}} - 1\right)^{-3/2}, \tag{2.76}$$

$$\beta_o^{\mathrm{SC}} = \frac{\lambda_o h_o}{3\mu u_c \gamma}\left(\frac{\sigma^2 D^2}{2\varepsilon_o \varepsilon_{\mathrm{film}}^2}\right)^2\left(D + \frac{1}{\varepsilon_{\mathrm{film}}} - 1\right)^{-6}. \tag{2.77}$$

Figure 2.3: Instability geometry in AP model

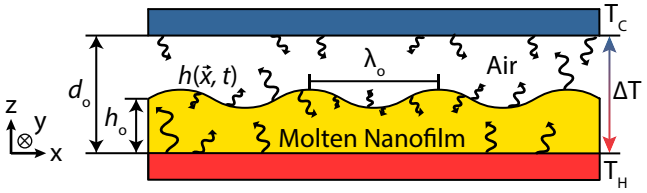

The distinguishing feature of the AP model is the coherent propagation of acoustic phonons through the bilayers, which create a destabilizing radiation pressure.

These are the same quantities as those derived by Zhuang [3], just expressed in nondimensional terms. The dimensional quantities will be presented in Sec. 2.3.4 with the results from the other two models.

2.3.2 AP Model: Acoustic Phonon Radiation Pressure

As opposed to the SC model which relies on electric fields, the driving instability mechanism in both the AP and TC models is a thermal one. The AP model was derived by Schäffer and co-workers [4–6] and they assumed that phonon reflections from all the interfaces in the system would sum to create a net pressure, P_{ac}, which acted as a destabilizing force on the interface. They did not consider the surface tension to vary with any external field which implies that $\widetilde{\nabla}_s\Gamma = 0$, as in the SC model. They did not expect any charge density to be present in the system and did not apply an external voltage, so they did not include any electric effects and therefore $P_{\text{el}} = 0$. To derive an expression for P_{ac}, the temperature in the system was computed from which the thermal flux through the system was calculated. The heat flux was then substituted into the acoustic phonon radiation pressure.

Within the AP model, Schäffer and co-workers assumed that the magnitude of the acoustic phonon pressure was

$$p_{\text{AP}} = -\frac{2\overline{Q}}{u_p}|\vec{q}|, \tag{2.78}$$

where $\vec{q}$ is the heat flux density, u_p is the speed of sound in the molten nanofilm, and $\overline{Q}$ is the acoustic quality factor. A microscopic derivation of $\overline{Q}$ was published [4, 6], but in their subsequent analysis it has been treated as a fitting parameter during analysis of experimental data. To proceed further with their derivation, the governing thermal equations are defined, scaled, and then solved to find the temperature in the system. From the temperature in the system the heat flux through the bilayers is calculated and then substituted into the acoustic phonon radiation

pressure. The acoustic phonon radiation pressure is then substituted into the height evolution equation, and linear stability analysis is performed to find the maximum growth rate and its corresponding wavevector for the AP model.

Thermal Governing Equations

There are two differential equations which govern the temperature in the system. The first is Fourier's law of thermal conduction:

$$\vec{q} = -k\boldsymbol{\nabla}\mathrm{T}. \tag{2.79}$$

In this expression, k is thermal conductivity and T is the temperature. The second is the equation describing the conservation of heat

$$\rho c_p \frac{D\mathrm{T}}{Dt} = -\boldsymbol{\nabla}\cdot\vec{q}. \tag{2.80}$$

The quantity c_p is the specific heat capacity. These two equations were combined using a simple substitution and the assumption that the thermal conductivities of each layer in the system are constant and isotropic. This assumption allows the resulting equation to be written as the usual heat equation

$$\rho c_p \frac{D\mathrm{T}}{Dt} = k\boldsymbol{\nabla}^2\mathrm{T}. \tag{2.81}$$

For boundary conditions, the bottom surface of the nanofilm was assumed to be isothermal at a temperature $\mathrm{T_H}$ while the top surface of the air layer was assumed to be isothermal at a temperature $\mathrm{T_C}$ with $\mathrm{T_H} > \mathrm{T_C}$. Finally, both temperature and heat flux density must be continuous at the interface. In total, these requirements are summarized in the following set of equations

$$\mathrm{T}_{\mathrm{film}}(z=0) = \mathrm{T_H}, \tag{2.82}$$

$$\mathrm{T}_{\mathrm{air}}(z=d) = \mathrm{T_C}, \tag{2.83}$$

$$\mathrm{T}_{\mathrm{film}}(z=h) = \mathrm{T}_{\mathrm{air}}(z=h), \tag{2.84}$$

$$-k_{\mathrm{film}}\boldsymbol{\nabla}\mathrm{T}_{\mathrm{film}}(z=h) = -k_{\mathrm{air}}\boldsymbol{\nabla}\mathrm{T}_{\mathrm{air}}(z=h). \tag{2.85}$$

Scaled Thermal Equations

To scale these equations only one new scaling is needed in addition to the ones contained in Sec. 2.2. This scaling is for the temperature

$$\Theta \equiv \frac{\mathrm{T} - \mathrm{T_C}}{\mathrm{T_H} - \mathrm{T_C}} = \frac{\mathrm{T} - \mathrm{T_C}}{\Delta \mathrm{T}}, \tag{2.86}$$

where Θ is the nondimensional temperature and $\Delta \mathrm{T} \equiv \mathrm{T_H} - \mathrm{T_C}$ is the temperature drop between the bounding plates. The utility of this scaling will become apparent when the isothermal boundary conditions are scaled. First, the heat equation in Eq. (2.81) becomes

$$\epsilon Pr Re \frac{D\Theta}{D\tau} = \epsilon^2 \left(\frac{\partial^2 \Theta}{\partial X^2} + \frac{\partial^2 \Theta}{\partial Y^2} \right) + \frac{\partial^2 \Theta}{\partial Z^2}.$$

In this expression an additional dimensionless number has been defined in addition to the Reynolds number, Re, which was defined in Eq. (2.17). This new number is the Prandtl number, Pr, and has the form

$$Pr = \frac{c_p \mu}{k}. \tag{2.87}$$

The Prandtl number reflects the ratio of the viscous diffusion of momentum to the thermal diffusivity. On the size scales relevant to experiment, the product $\epsilon Pr Re$ is small [8–10], so the temporal dependence of the left half of Eq. (2.87) will be neglected in addition to the terms of order ϵ^2. It becomes

$$\frac{\partial^2 \Theta}{\partial Z^2} = 0. \tag{2.88}$$

The boundary conditions have the following scalings

$$\Theta_{\mathrm{film}}(Z = 0) = 1, \tag{2.89}$$

$$\Theta_{\mathrm{air}}(Z = D) = 0, \tag{2.90}$$

$$\Theta_{\mathrm{film}}(Z = H) = \Theta_{\mathrm{air}}(Z = H), \tag{2.91}$$

$$\widetilde{\boldsymbol{\nabla}} \Theta_{\mathrm{film}}(Z = H) = \kappa \widetilde{\boldsymbol{\nabla}} \Theta_{\mathrm{air}}(Z = H). \tag{2.92}$$

In the last equation the quantity $\kappa \equiv k_{\mathrm{air}}/k_{\mathrm{film}}$ has been defined as the thermal conductivity ratio.

Temperature Field Solution

The scaled heat equation was integrated directly in both the film and air layers to yield

$$\Theta_{\text{film}} = A^{\text{AP}}_{\text{film}} Z + B^{\text{AP}}_{\text{film}},$$
$$\Theta_{\text{air}} = A^{\text{AP}}_{\text{air}} Z + B^{\text{AP}}_{\text{air}}.$$

As in the SC model section, $A^{\text{AP}}_{\text{film}}$, $B^{\text{AP}}_{\text{film}}$, $A^{\text{AP}}_{\text{air}}$, and $B^{\text{AP}}_{\text{air}}$ are integration constants. The two Dirichlet boundary conditions in Eqs. (2.89) and (2.90) imply that $B^{\text{AP}}_{\text{film}} = 1$ and $B^{\text{AP}}_{\text{air}} = -DA^{\text{AP}}_{\text{air}}$ such that

$$\Theta_{\text{film}} = A^{\text{AP}}_{\text{film}} Z + 1,$$
$$\Theta_{\text{air}} = A^{\text{AP}}_{\text{air}} (Z - D).$$

From Eq. (2.91) the continuity of temperature requires that

$$A^{\text{AP}}_{\text{air}} = \frac{A^{\text{AP}}_{\text{film}} H + 1}{H - D}.$$

Then the temperatures in each layer must be of the form

$$\Theta_{\text{film}} = A^{\text{AP}}_{\text{film}} Z + 1,$$
$$\Theta_{\text{air}} = \left(A^{\text{AP}}_{\text{film}} H + 1 \right) \frac{Z - D}{H - D}.$$

The final boundary condition is the continuity of thermal flux in Eq. (2.92). This determines the last constant to be

$$A^{\text{AP}}_{\text{film}} = \frac{-\kappa}{D + (\kappa - 1) H}.$$

Consequently, the nondimensional temperature in each layer is

$$\Theta_{\text{film}} = \frac{D - H + \kappa (H - Z)}{D + (\kappa - 1) H}, \tag{2.93}$$
$$\Theta_{\text{air}} = \frac{D - Z}{D + (\kappa - 1) H}. \tag{2.94}$$

Based on these expressions, the magnitude of the thermal flux density will be in the $\hat{Z}$ direction to first order in ϵ. This implies that the nondimensional acoustic phonon pressure at the interface is

$$P_{\text{AP}} = -\frac{2\overline{Q} k_{\text{air}} \Delta \text{T}}{u_p P_c h_o} \frac{\partial \Theta_{\text{air}}}{\partial Z} = \frac{2\overline{Q} k_{\text{air}} \Delta \text{T}}{u_p P_c h_o} \left(\frac{1}{D + (\kappa - 1) H} \right). \tag{2.95}$$

Linear Stability Predictions

Returning to the height evolution equation in Eq. (2.44), the horizontal gradient of the acoustic phonon pressure was computed and substituted to yield the following height evolution equation for the AP mode

$$\frac{\partial H}{\partial \tau} + \widetilde{\boldsymbol{\nabla}_{\parallel}} \cdot \left[\frac{H^3}{3\overline{Ca}} \left(\widetilde{\boldsymbol{\nabla}_{\parallel}^3} H \right) + \frac{2\overline{Q} k_{\text{air}} \Delta \text{T} H^3}{3 u_p P_c h_o} \left(\frac{1-\kappa}{\left[D + (\kappa - 1) H \right]^2} \right) \widetilde{\boldsymbol{\nabla}_{\parallel}} H \right] = 0. \quad (2.96)$$

Once again the perturbation function from Eq. (2.45) was inserted into the height evolution equation to find the dispersion relation for the AP model

$$\beta^{\text{AP}}(K) + \frac{K^4}{3\overline{Ca}} - \frac{2\overline{Q} k_{\text{air}} \Delta \text{T}}{3 u_p P_c h_o} \left(\frac{1-\kappa}{\left[D + \kappa - 1 \right]^2} \right) K^2 = 0. \quad (2.97)$$

The general forms for K_o and β_o that were derived in Eq. (2.72) and Eq. (2.73) yield the wavevector and growth after association of the constants

$$A_2^{\text{AP}} = \frac{2\overline{Q} k_{\text{air}} \Delta \text{T}}{3 u_p P_c h_o} \left(\frac{1-\kappa}{\left[D + \kappa - 1 \right]^2} \right), \quad (2.98)$$

$$A_4^{\text{AP}} = \frac{1}{3\overline{Ca}}. \quad (2.99)$$

The nondimensional values of K_o^{AP} and β_o^{AP} are

$$K_o^{\text{AP}} = \sqrt{\frac{\overline{Q} k_{\text{air}} (1-\kappa) \Delta \text{T}}{\gamma u_p \epsilon^2}} \left(D + \kappa - 1 \right)^{-1}, \quad (2.100)$$

$$\beta_o^{\text{AP}} = \frac{L}{3\gamma \mu u_c h_o} \left(\frac{\overline{Q} k_{\text{air}} (1-\kappa) \Delta \text{T}}{u_p} \right)^2 \left(D + \kappa - 1 \right)^{-4}. \quad (2.101)$$

Once again, these are the same quantities as those derived by Schäffer and co-workers [4–6], just expressed in nondimensional terms. The dimensional quantities will be presented in Sec. 2.3.4 with the results from the other two models.

2.3.3 TC Model: Thermocapillary Shear

The TC model is similar to the AP model in that the driving force for the instability is thermal, but it has a different origin for the destabilizing force. The AP model defines a destabilizing pressure acting normal to the interface while in the TC model the force is a shear tangential to the interface. This tangential shear arises from differences in surface tension which occur due to the temperature variations along

Figure 2.4: Instability geometry in TC model

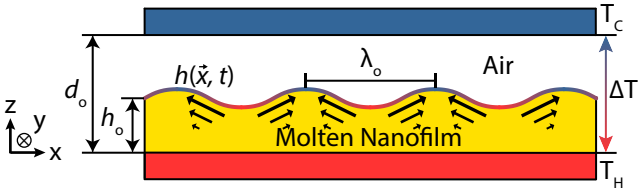

The distinguishing feature of the TC model is variation of surface tension with temperature that drives a destabilizing thermocapillary shear.

the interface. Within this model, originally posited by Dietzel and Troian [8–10], the dominant force arises from the $\widetilde{\boldsymbol{\nabla}}_s\Gamma$ term while the pressure terms from the other two models, P_{ac} and P_{el}, are both equal to zero. The derivation of this model is relatively shorter than those of the SC and AP models because the temperature field throughout the system has already been computed in Sec. 2.3.2 and the scaled results from Eq. (2.93) and Eq. (2.94) port over directly.

When computing the $\widetilde{\boldsymbol{\nabla}}_s\Gamma$ term, Dietzel and Troian assumed that the surface tension only depends on temperature and that the surface tension depends linearly on temperature. This implies that the surface gradient of the surface tension is

$$\widetilde{\boldsymbol{\nabla}}_s\Gamma = \frac{\Delta \mathrm{T}}{\Gamma_c}\frac{\partial \gamma}{\partial \mathrm{T}}\widetilde{\boldsymbol{\nabla}}_s\Theta = -\frac{\epsilon\gamma_T\Delta \mathrm{T}}{\mu u_c}\widetilde{\boldsymbol{\nabla}}_s\Theta. \tag{2.102}$$

In this expression the thermocapillary coefficient, γ_T, was defined as

$$\gamma_{\mathrm{T}} = -\left|\frac{\partial \gamma}{\partial \mathrm{T}}\right|. \tag{2.103}$$

The minus sign has been explicitly brought out to the front of this equation since for single component fluids, this quantity must always be negative. The quantity in front of the gradient is a scaled Marangoni number [19], which represents the ratio of surface tension forces to viscous forces. It was defined by

$$\overline{Ma} \equiv \frac{\epsilon\gamma_{\mathrm{T}}\Delta \mathrm{T}}{\mu u_c} = \epsilon Ma. \tag{2.104}$$

From here, the temperature at the interface was substituted from either Eq. (2.93) or Eq. (2.94). From the continuity of temperature at the interface they must have the same value at $Z = H$. Then we take the surface gradient to find

$$\widetilde{\boldsymbol{\nabla}}_s\Gamma = -\frac{\kappa D\overline{Ma}}{\left[D + (\kappa - 1)H\right]^2}\left(\widetilde{\boldsymbol{\nabla}}_{\parallel}H + \epsilon\left(\widetilde{\boldsymbol{\nabla}}_{\parallel}H\right)^2\hat{Z}\right). \tag{2.105}$$

The $\hat{Z}$ components in this expression are second order in ϵ when $\widetilde{\boldsymbol{\nabla}}_s\Gamma$ is substituted into the scaled interfacial stress balance from Eq. (2.30). Consequently, they do not appear below.

Linear Stability Predictions

Substitution of the surface gradient of the surface tension from Eq. (2.105) into the height evolution equation from Eq. (2.44) yields

$$\frac{\partial H}{\partial \tau} + \widetilde{\boldsymbol{\nabla}}_{\parallel} \cdot \left[\frac{H^3}{3\overline{Ca}} \left(\widetilde{\boldsymbol{\nabla}}_{\parallel}^3 H \right) + \frac{H^2 \kappa D \overline{Ma}}{2\left[D + (\kappa - 1) H\right]^2} \widetilde{\boldsymbol{\nabla}}_{\parallel} H \right] = 0. \tag{2.106}$$

In this case the dispersion relation is

$$\beta^{\mathrm{TC}}(K) + \frac{K^4}{3\overline{Ca}} - \frac{\kappa D \overline{Ma}}{2\left[D + \kappa - 1\right]^2} K^2 = 0. \tag{2.107}$$

For the TC model the dispersion relation constants are

$$A_2^{\mathrm{TC}} = \frac{\kappa D \overline{Ma}}{2\left[D + \kappa - 1\right]^2}, \tag{2.108}$$

$$A_4^{\mathrm{TC}} = \frac{1}{3\overline{Ca}}. \tag{2.109}$$

This then implies that the values of K_o^{TC} and β_o^{TC} are

$$K_o^{\mathrm{TC}} = \sqrt{\frac{3\kappa\gamma_{\mathrm{T}}\Delta\mathrm{T}}{4\gamma\epsilon^2}} \left(\sqrt{D} + \frac{\kappa - 1}{\sqrt{D}} \right)^{-1}, \tag{2.110}$$

$$\beta_o^{\mathrm{TC}} = \frac{3L}{\gamma\mu u_c h_o} \left(\frac{\kappa\gamma_T\Delta\mathrm{T}}{4} \right)^2 \left(\sqrt{D} + \frac{\kappa - 1}{\sqrt{D}} \right)^{-4}. \tag{2.111}$$

As in the previous two cases, these are the same quantities as those derived by Dietzel and Troian [8–10], expressed in nondimensional terms. The dimensional quantities will be presented in Sec. 2.3.4 with the results from the other two models.

2.3.4 Summary of Dimensional Linear Stability Predictions

After completion of the derivations for each model and computation of the predictions for K_o and β_o for each model, these quantities are converted to their dimensional analogs: the dimensional growth rates, b, and the dimensional wavelengths, λ_o. This

Table 2.1: Dimensional wavelengths and growth rates for each proposed model

Wavelength	**Growth Rate**
$\frac{\lambda_o^{\mathrm{SC}}}{2\pi h_o} = \sqrt{\frac{2\varepsilon_o\varepsilon_p^2\gamma}{\sigma^2 h_o D^2}}\left(D + \frac{1}{\varepsilon_p} - 1\right)^{3/2}$	$b_o^{\mathrm{SC}} = \frac{\sigma^4 h_o D^4}{12\mu\gamma\varepsilon_o^2\varepsilon_p^4 h_o^3}\left(D + \frac{1}{\varepsilon_p} - 1\right)^{-6}$
$\frac{\lambda_o^{\mathrm{AP}}}{2\pi h_o} = \sqrt{\frac{\gamma u_p}{Q(1-\kappa)k_a\Delta\mathrm{T}}}\,(D + \kappa - 1)$	$b_o^{\mathrm{AP}} = \frac{[Q(1-\kappa)k_a\Delta\mathrm{T}]^2}{3\mu\gamma u_p^2 h_o}\,(D + \kappa - 1)^{-4}$
$\frac{\lambda_o^{\mathrm{TC}}}{2\pi h_o} = \sqrt{\frac{4\gamma}{3\kappa\gamma_{\mathrm{T}}\Delta\mathrm{T}}}\left(\sqrt{D} + \frac{(\kappa-1)}{\sqrt{D}}\right)$	$b_o^{\mathrm{TC}} = \frac{3\,(\kappa\gamma_{\mathrm{T}}\Delta\mathrm{T})^2}{16\mu\gamma h_o}\left(\sqrt{D} + \frac{(\kappa-1)}{\sqrt{D}}\right)^{-4}$

will remove any ambiguity in the choice of characteristic scales from Sec. 2.2 and allow different functional dependencies to be elucidated more easily. Using Eq. (2.46) and Eq. (2.47), the dimensional quantities are

$$\lambda = \frac{2\pi L}{K}, \tag{2.112}$$

$$b = \frac{\beta u_c}{L}. \tag{2.113}$$

This can be done readily for each model and the resulting expressions are summarized in Table 2.1. These expressions will be used extensively throughout Ch. 3, Ch. 4, and Ch. 5.

Chapter 3

INSTABILITY MECHANISM IDENTIFICATION: IMPROVED IMAGE AND THERMAL ANALYSIS

3.1 Background

With the analytic expressions for the wavelength and growth rate derived in Ch. 2 and summarized in Table 2.1, we can work to differentiate between the different instability mechanisms. It is often possible to identify the mechanism leading to instability by measuring the characteristic wavelength at early times and comparing the value to λ_o computed from linear stability theory. The length separating adjacent convection cells in macroscopic systems is often measured directly or estimated by Fourier analysis of images obtained by shadowgraphy, particle seeding, or particle image velocimetry. Unfortunately, for the reasons described below, such techniques are not feasible in liquid films whose initial thicknesses measure only a few hundred nanometers nor can the temperature drops across such thin films be directly measured. These challenges have posed difficulties in identifying the competitive forces leading to the spontaneous development of array protrusions in nanofilms, as discussed next.

In previous work, McLeod *et al.* obtained good functional fits between the experiment and the TC model prediction for λ_o but close quantitative agreement seemed to require input values of the liquid thermal conductivity many times larger than reported in the literature [1]. We have since revisited their analysis to ascertain whether this problem can be resolved by making improvements to the image analysis in order to extract λ_o at much earlier times and improvements to the thermal simulations used to assess ΔT. In this chapter, we still focus on the dominant Fourier peak from time resolved microscopy images of surface deformations observed in reflection mode to extract the values of λ_o. However, we have implemented more robust image analysis routines to help isolate this main peak at much earlier times during instability. Such early time measurements better conform to the main assumption of linear stability analysis, namely that interface fluctuations remain very small in comparison to the initial film thickness.

Accurate estimates of ΔT are also required for quantitative comparison to theoretical models. Unfortunately, the bilayer thickness d_o is typically of the order of 1 μm

in experiment, a gap too small to allow direct measurement by thermocouple or infrared techniques. Estimates of ΔT are therefore obtained from thermal simulations based on a more complete and more accurate finite element model which more closely mimics the experimental system consisting of thermal conduction through a multilayer structure at steady state conditions. In this chapter, we therefore also show how improved simulations result in revised values of ΔT which on average are half as large as those previously reported [1].

In what follows, we describe the improved image analysis for isolating the fastest growing mode and a more accurate thermal model for assessing the temperature drop across the confined air/nanofilm bilayer. Feature extraction at much earlier times, coupled with more realistic thermal simulations, leads to better overall functional and quantitative agreement with the thermocapillary model. Despite these improvements, there persists a quantitative discrepancy with theory which we attribute to a number of experimental challenges.

We first briefly review the predictions for λ_o arising from three different physical models, namely the induced surface charge (SC), acoustic phonon (AP) and thermocapillary (TC) models which were derived in Ch. 2 and presented in Table 2.1. Listed in Tables 3.1, 3.2, and 3.3 are the analytic expressions for λ_o normalized by the initial film thickness h_o, along with key system dimensions and material constants from experiments reported in the literature. As evident, the SC instability is independent of the temperature drop ΔT, which disagrees with experimental measurements [1, 5]. In the remainder of this chapter, we therefore exclude this model from consideration and only explore differences between the AP and TC models.

Experiments to date have used either polystyrene (PS) or poly(methylmethacrylate) (PMMA) films spun coat onto a silicon wafer to produce a flat and uniform film then melted in situ. The main advantage to using polymer films is that the their low glass transition temperatures [24] facilitate rapid melting and solidification. Estimates of the shear rates incurred in experiment yield very small Deborah numbers, indicating that non-Newtonian effects play no role at early times and that the liquid film can be modeled as a simple Newtonian fluid. All three models therefore assume that the film viscosity is independent of shear rate. However, the viscosity of polymers depends strongly on temperature. While this dependence ultimately slows the late time growth of protrusions as they approach the opposing cold substrate, it is not expected to affect early time growth when surface deformations are of the order of tens of nanometers or less. All three models therefore assume that the relevant film

Table 3.1: Material constants for the SC model

$$\frac{\lambda_o^{\mathrm{SC}}}{2\pi h_o} = \sqrt{\frac{2\varepsilon_o \varepsilon_p^2 \gamma h_o}{\sigma^2 d_o^2}} \left(\frac{d_o}{h_o} + \frac{1}{\varepsilon_p} - 1 \right)^{3/2}$$

h_o	Initial film thickness	50 - 103 nm
d_o	Substrate separation distance	180 - 640 nm
λ_o	Fastest growing wavelength	2 - 8 μm
ε_o	Vacuum permittivity	8.85×10^{-12} F/m
ε_p	PMMA permittivity	3.5
γ	PMMA surface tension	30 mN/m
σ	Interfacial charge density	10^{-3} mC/m^2

Normalized wavelength for the fastest growing mode in the induced surface charge (SC) model. Listed are the relevant system dimensions and material constants for low molecular weight poly(methylmethacrylate) (PMMA 2 kg/mol) films heated to 130 °C used in experiment. [2, 3]

viscosity for the linear stability analysis is constant and equal to the temperature of the supporting substrate.

The expression for λ_o in the acoustic phonon model (AP) in Table 3.2 relies on the constant $\overline{Q}$, the so-called acoustic quality factor, which arises from phonon transmission and reflection from the three interfaces comprising the bilayer system, namely the silicon/polymer, the air/polymer and air/silicon surfaces. Positive values of $\overline{Q}$ lead to film destabilization and protrusion growth. In all experiments conducted so far, the value of $\overline{Q}$ has been treated as a fitting parameter. The remaining material constants, namely the liquid film surface tension, γ, and thermal conductivity of the air and liquid film, have been obtained from literature values. In the AP model then, the normalized wavelength of the fastest growing mode increases linearly with the normalized substrate separation distance $D \equiv d_o/h_o$.

The expression for λ_o in the thermocapillary (TC) model in Table 3.3 also relies on the liquid film surface tension, γ, the magnitude of the surface tension coefficient, $|\partial\gamma/\partial \mathrm{T}|$, and the air and liquid thermal conductivity, all values also obtained from the literature. In contrast to the AP model, however, the normalized wavelength of the fastest growing mode increases with the normalized substrate separation distance D according to $\sqrt{D} + (\kappa - 1)/\sqrt{D}$. While the original experiments [4–6,

Table 3.2: Material constants for the AP model

$$\frac{\lambda_o^{\mathrm{AP}}}{2\pi h_o} = \sqrt{\frac{\gamma u_p}{\overline{Q}(1-\kappa)k_a \Delta \mathrm{T}}}\left(\frac{d_o}{h_o} + \kappa - 1\right)$$

h_o	Initial film thickness	80 - 130 nm
d_o	Substrate separation distance	100 - 600 nm
λ_o	Fastest growing wavelength	1 - 10 μm
ΔT	Temperature differential	10 - 55 °C
γ	PS surface tension	30 mN/m
u_p	Speed of sound in PS	1850 m/s [21]
$\overline{Q}$	Acoustic phonon coefficient	6
k_a	Air thermal conductivity	34 mW/m-°C [21]
k_p	PS thermal conductivity	160 mW/m-°C
κ	Thermal conductivity ratio k_a/k_p	0.213

Normalized wavelength for the fastest growing mode in the acoustic phonon (AP) model. Listed are the relevant system dimensions and material constants for high molecular weight polystyrene (PS 108 kg/mol) films used in experiment [4–6, 15].

15] were designed to probe values of $D \lesssim 5$, the experiments reported in Ref. [1] and reanalyzed in this chapter allowed access to a larger range $D \lesssim 25$. This feature, coupled with the ability to view the film instability *in-situ*, has allowed more accurate measurements of λ_o for several reasons, including rejection of runs suffering from non-parallel substrates or defective films containing pinholes, embedded particles, or surface contaminants.

Prior work [10] outlined the challenges inherent in making direct comparison between theory and experiment. The biggest problem of all is that the majority of experiments prior to 2011 reporting measurements of λ_o had little to do with the actual instability in that the formations were allowed to grow, make contact with the opposing substrate, and solidify in place before the cold substrate was removed and measurements of λ_o taken. Measurements obtained in this way not only violate the assumptions of linear stability theory but also include influences and effects not incorporated into the theoretical analysis. For example, contact of a warm protrusion with the opposing cold substrate tends to induce coalescence of adjacent protrusions

Table 3.3: Material constants for the TC model

$$\frac{\lambda_o^{\mathrm{TC}}}{2\pi h_o} = \sqrt{\frac{4\gamma}{3\kappa|\partial\gamma/\partial \mathrm{T}|\Delta \mathrm{T}}}\left(\sqrt{\frac{d_o}{h_o}} + (\kappa - 1)\sqrt{\frac{h_o}{d_o}}\right)$$

h_o	Initial film thickness	95 - 390 nm
d_o	Substrate separation distance	605 - 2360 nm
λ_o	Fastest growing wavelength	27 - 68 μm
ΔT	Temperature difference	16 - 44 °C
γ	Surface tension (100 °C)	33 mN/m [22]
k_a	Air thermal conductivity (80 °C)	30 mW/m-°C [23]
k_p	PS thermal conductivity (100 °C)	128 mW/m-°C [22]
κ	Thermal conductivity ratio k_a/k_p	0.234
$\lvert\partial\gamma/\partial \mathrm{T}\rvert$	Surface tension coefficient	78 μN/m-°C [22]

Normalized wavelength for the fastest growing mode in the thermocapillary model. Listed are the relevant system dimensions and material constants for low molecular weight polystyrene (PS 1.3 kg/mol) films used in experiment [1, 8–10].

followed by flow migration along the underside of the cold substrate, both of which strongly affect the final measured values of λ_o. Film shrinkage during solidification can also play a role. For accurate comparison to model predictions for λ_o, the amplitude of features which emerge from an initial flat air/liquid interface must be infinitesimally small. In this chapter, we focus exclusively on estimates of the instability wavelength measured at the earliest possible time given the experimental setup and other limitations described.

The remainder of this chapter is divided as follows. In Sec. 3.2, we briefly review some details of the experimental apparatus used in Ref. [1], from which the raw images analyzed in this chapter were obtained. In Sec. 3.3, we outline significant improvements to the image analysis and processing routines which lead to more accurate measurements of λ_o at much earlier times than reported in Ref. [1]. In Sec. 3.4, we detail a new finite element model used to extract more accurate estimates of ΔT which better mimics the experimental system. These two improvements lead to better overall agreement with the thermocapillary model. We conclude by examining some persistent deficiencies in Sec. 3.6 which are traceable to uncertainties in

measurement of key parameters needed to make contact with theory.

3.2 Brief Description of Experimental Setup

We review some key aspects of the experimental setup shown in Fig. 3.1. More extensive discussion, including sample preparation procedures, can be found in Ref. [1]. The resistive heating element used to enforce the temperature differential ΔT across the bilayer film consisted of an indium tin oxide (ITO) coated glass slide. The current passed through the ITO layer for increasing the overall thermal flux was regulated via proportional integral derivative (PID) feedback control. Heat loss beneath the glass slide was minimized by a thin layer of fiberglass insulation. The thermal sink used to draw heat vertically and away from the air/liquid bilayer consisted of a thin copper sheet (Cu) in contact with a chiller loop perforated with a small cylindrical viewing port. Strong suction was applied to the region beneath the glass coverslip (i.e. vacuum region) to enforce good contact between the sapphire disk and cold Cu sheet. The heat sink enforced through the chiller loop and the thinness of the interstitial material layers guaranteed that the dominant heat flux traversing the layered stack was due to conduction and not convection or radiation. (In Sec. 3.4, we provide estimates of the thermal flux due to thermal conduction, convection and radiation and conclude that conduction is dominant.)

In most of the experimental runs listed in Table 3.7, the underside of the sapphire window was patterned with a transparent cylindrical disk of SU-8. This cooled disk helped trigger and localize the instability to the region directly below the disk where the nominal temperature gradient, $\Delta T/d_o$, was largest. The thickness of the air layer above the nanofilm was enforced by four SU-8 spacers patterned onto the sapphire disk. In each run, two thermocouples were used to measure T_+ (beneath the exterior edge of the silicon wafer) and T_- (top surface of the Cu layer just beyond the glass coverslip). Time stamped color images of reflections from the liquid surface were captured by a CCD camera at 10X magnification. Tables 3.6 and 3.7 list all relevant dimensions, operating conditions, material constants, and numerical estimates of ΔT for all runs analyzed.

In the experiments which provided the raw images reanalyzed in this chapter [1], a polymer coated silicon wafer was inserted into the assembly prior to a run and the opposing hot and cold substrates were leveled and made parallel by adjusting external screws until interference fringes observed were all but eliminated. Data collection began once power was delivered to the indium tin oxide (ITO) slide, which set the

Figure 3.1: Diagram of the experimental setup

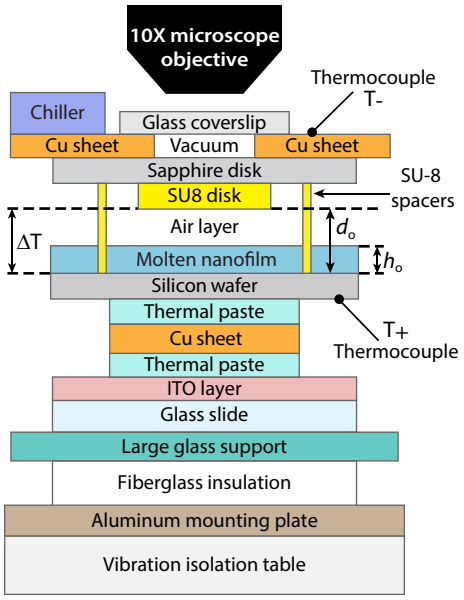

Diagram of the experimental setup [1] illustrating the many layers affecting heat transfer throughout the system (not drawn to scale). Dimensions and thermal conductivities of each layer are listed in Table 3.6. Designated temperature readings, T_+ and T_-, were registered using small thermocouples and used to calibrate boundary temperatures in the finite element simulations described in Sec. 3.4.

origin of time for each run. Thereafter, images were captured at regular intervals, typically between 20 seconds and 2 minutes, depending on the flow speed generated and the rapidity with which protrusions grew. To ensure that the temperature drop ΔT had reached steady state conditions before any measurements of λ_o were initiated, the rise time to reach T_+ was monitored. Depending on the power applied, the rise time ranged from 1.5 to 5 minutes, only after which were measurements of λ_o recorded.

3.3 Estimates of the fastest growing wavelength from improved image analysis

Accurate measurement of the instability wavelength at early times requires feature extraction from rather noisy images which appear featureless to the naked eye. Here we describe the various steps used to facilitate identification of emergent structure formation.

3.3.1 Image analysis protocol

The color image sequences for each experimental run were first separated into three color channels (RGB) - the channel exhibiting the highest contrast was selected for analysis. Typically, the blue channel offered highest contrast (see Table 3.7).

Image subtraction was then carried out to reduce image noise, which was especially problematic at early times, or to eliminate obvious artifacts such as stationary dust particles on any of the optical components. For each image sequence, a reference image captured at time t_{ref} was selected and subtracted from all subsequent images. This reference image was always obtained after the thermocouple registering the value T_+ had reached the desired set point and the color of the nanofilm had stabilized. (The ITO coated slide typically required several minutes to achieve steady state after the power was applied.) The mean intensity of each image was then computed and that value subtracted from each image to yield a mean intensity of zero. This step eliminated the zero wave number Fourier component which sometimes occluded the peak of interest associated with the instability.

3.3.2 Extraction of λ_{o} from power spectra

The 2D discrete Fourier transform for each image in a run sequence was then computed using a 2D fast Fourier transform routine [25]. The data was radially averaged by first segmenting the image into concentric rings of width $\Delta k = 2\pi/L_i$, where L_i denotes the smaller of the raw image dimensions given in Table 3.7, and then averaging the Fourier transform within each ring. The corresponding power spectrum, i.e. modulus squared of the Fourier transform, was then re-scaled in amplitude so that the maximum peak value of the final image in chronological order was equal to one. This step ensured that the Jacobian values generated during the nonlinear regression were well-conditioned - otherwise, large Fourier amplitude coefficients tended to overwhelm and distort the peak fitting parameters. The resulting scaled data was then fit to the curve $G[k(t)]$ given by Eq. (3.1), which represents the sum of a Lorentzian peak with an exponentially decaying background, according to which

$$G[(k(t)] = f_o(t)\,\frac{a^2(t)}{a^2(t) + [k(t) - k_o(t)]^2} + f_1(t)e^{-b(t)k(t)} + f_2(t), \qquad (3.1)$$

where $k(t) = |\vec{k}(t)|$ and t denotes time. The fitting parameters describe a Lorentzian peak amplitude $f_o(t)$ with half-width at half-maximum $a(t)$ centered about the wave number $k_o(t) = |\vec{k_o}(t)|$ summed with an exponential curve of amplitude $f_1(t)$ and decay constant $b(t)$ (associated with the background intensity). The value $f_2(t)$ was used to set the vertical offset. The contribution from the decaying exponential is typical of spectral leakage which occurs when periodic extension of the observation window imposed on the fundamental image does not match the periodicity (or lack thereof) of the structure in the fundamental image [26]. Good fits were obtained by

analyzing images in reverse chronological order since the peak value $k_o(t)$, the most sensitive parameter in the nonlinear fitting process, was usually easily identifiable. Additionally, iteration on the fitting parameters proceeded more quickly by using the spectral curve fitting parameters at time t_{n+1} as initial estimates for the fitting parameters at the earlier time t_n.

The initial parameter values for the fitting routine generally fell into two categories - either the Lorentzian peak dominated the exponentially decaying background or else the exponential background was comparable or even larger than the Lorentzian peak amplitude. Correspondingly, the initial seed for the amplitude of the Lorentzian, f_o, was set to be much larger than f_1, i.e. 1.0 versus 0.1. Else, the initial seed values were reversed, i.e. $f_o = 0.2$ and $f_1 = 5.0$. The initial guesses for the peak half-width at half-maximum, $a(t)$ and decay value $b(t)$, were usually chosen to be 0.03 and 10, respectively - these values showed only weak dependence on the initial choices for f_o and f_1. The final parameter values for the nonlinear fitting routine for the image sequences shown in Fig. 3.2(d) and Fig. 3.3(d) can be found in Table 3.4 and Table 3.5.

On occasion, the automated fitting routine ran into problems of numerical overflow or division by zero, mostly for images obtained at very early times, well before any features were discernible by the naked eye. In such cases, the routine was re-initiated using a new set of parameter values for which the amplitude of the Lorentzian peak and the exponential background were set equal to the maximum of the spectral curve. The nonlinear fitting routine then converged on a successful fit even in the absence of a Lorentzian-like peak. Consequently, a set of selection criteria were established to define a valid peak fit. If a peak could not be reliably extracted no matter the initial parameter values, then that data point was discarded and the next image analyzed. Finally, the values of $k_o(t) = 2\pi/\lambda(t)$ were plotted in time and the earliest valid fit identified as λ_o. These improvements over the original analysis [1] led to more accurate and reproducible fits. More significantly, these enhancements produced measurement of the fastest growing wavelength at much earlier times than previously reported (see Fig. 3.5(b) for a direct comparison). In the absence of any defects or other spurious features, only a single peak appeared in the power spectra at early times, which greatly simplified analysis. For most but not all runs, the location of that peak remained relatively fixed in time, yielding a fairly constant value of k_o. In some cases, we did observe a slight decrease in k_o in time, as discussed next. In other cases, late time analysis was complicated by the appearance of interference

Table 3.4: Fit parameters of Eq. (3.1) for the curves shown in Fig. 3.2(d)

Time (min)	$f_o \times 10^2$	$a \times 10^2 (1/\mu\text{m})$	$k_o (1/\mu\text{m})$	$f_1 \times 10^2$	$b(\mu\text{m})$	$f_2 \times 10^4$
16	0.121	11.2	0.169	0.115	47.8	3.08
36	0.767	7.21	0.164	2.78	40.7	4.12
56	3.26	4.80	0.169	1.24	13.2	3.69
76	11.3	3.34	0.171	3.51	9.27	0.235
96	29.5	2.93	0.169	8.13	10.4	-7.08
116	66.4	2.55	0.168	18.5	12.0	-14.7
130	101	2.37	0.167	31.2	13.9	-12.2

Table 3.5: Fit parameters of Eq. (3.1) for the curves shown in Fig. 3.3(d)

Time (min)	$f_o \times 10^2$	$a \times 10^2 (1/\mu\text{m})$	$k_o (1/\mu\text{m})$	$f_1 \times 10^2$	$b(\mu\text{m})$	$f_2 \times 10^4$
22	0.0386	8.21	0.151	—	—	12.2
46	0.949	3.01	0.131	0.939	36.0	1.90
70	4.45	1.99	0.126	2.70	25.3	2.47
94	13.8	1.67	0.124	6.85	21.6	2.42
118	34.3	1.57	0.122	19.8	29.6	0.784
142	65.9	1.55	0.121	44.7	37.6	-3.26
170	112	1.59	0.119	108	56.4	-10.4

fringes arising from taller protrusions, either from instability growth or coalescence of neighboring fluid mounds. These images were discarded since they could not be analyzed by the procedure described.

3.3.3 Application of image processing routines to sample runs

Shown in Fig. 3.2 for experiment #56 are the results of the image processing routine used to extract the value of λ_o. Experimental information relevant to that particular run can be found in Table 3.7. Fig. 3.2(a) depicts three grey scale images from the blue channel for times t = 16 min, 56 min, and 96 min which illustrate structure formation at early, intermediate, and late times. Fig. 3.2(b) shows these images after subtraction and zeroing of the mean intensity value. (The images shown in

Fig. 3.2(b) have been rescaled in amplitude with MATLAB routine `imadjust` [25] to maximize contrast for visualization purposes only.) These first two steps helped maximize contrast of embedded structure formation, none evident to the naked eye. Fig. 3.2(c) shows the corresponding 2D Fourier transforms. Plotted in Fig. 3.2(d) are the radially averaged power spectral curves - the fit parameters can be found Table 3.4. The two earliest curves exhibit a very broad peak indicative of film isotropy as evident in the left panel of Fig. 3.2(b). From $t = 56$ min onwards, a sharp peak begins to develop. Inspection of images at $t = 56$ min and 96 min indicates emergent hexagonal order which produced six darker spots decorating the main ring in the middle and right panels of Figs. 3.2(b). Numerical simulations for the late time behavior of the thermocapillary model [10] have shown that the onset of the *nonlinear regime* is characterized by such hexagonal order. Plotted in Fig. 3.2(e) are the extracted values for $k_o(t)$ spanning the linear to nonlinear regime. The earliest value extracted, here $t = 16$ min, was identified with the instability wavelength, $\lambda_o = 2\pi/k_o$. The majority of experiments tended to generate fairly constant values of $\lambda_o(t)$ even beyond the linear regime, as illustrated by the curve in Fig. 3.2(e).

Occasionally the initial value $k_o(t)$ was observed to decrease in time before leveling off to a constant value. Shown in Fig. 3.3 is a representative example from experiment #69. Inspection of the 2D Fourier transform in Fig. 3.3(c) reveals late time structure formation more closely resembling square and not hexagonal ordering. Numerical simulations for the late time behavior of the thermocapillary model [10] have shown that non-parallel substrates, which introduce an additional unintended lateral thermal gradient, can generate nanopillar arrays exhibiting four-fold and not six-fold symmetry. This effect might help explain the observed decrease in $k_o(t)$ in Fig. 3.3(e). Nonetheless, the value used to compare with theoretical models was chosen to be the wavenumber at earliest time for which a Lorentzian peak could be identified, in this case the value of $k_o(t = 22$ min).

3.3.4 Complications incurred by film defects

Embedded or exposed defects in liquid nanofilms compromise film uniformity by causing local film thickening. While such defects are always a nuisance, they cause special problems in experiments with nanofilms due to the more rapid growth of thicker regions exposed to a large thermal gradient. Such growth, however, arises from a nucleation and growth process and not linear instability. While contaminant particles that appear on the surface of optical components or the sapphire window could be easily removed from view by image subtraction, defects integral to the

Figure 3.2: Illustration of the image analysis process

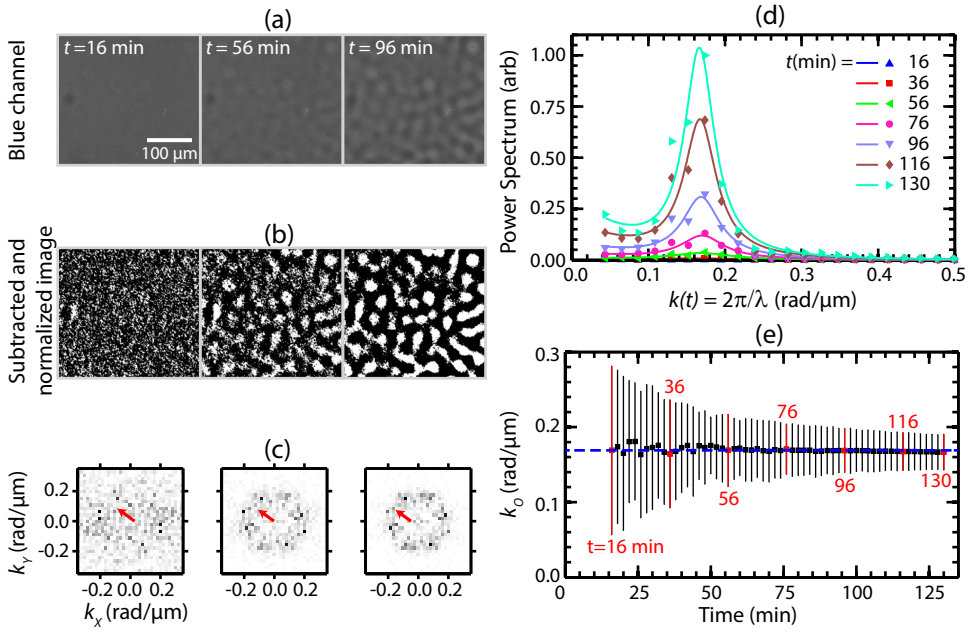

Representative images of structure formation in an initially flat and uniform PS nanofilm for experiment #56 in Table 3.7. (a) Grey scale images from the blue channel for times t = 16 min, 56 min, and 96 min. (b) Corresponding gray scale images after subtraction of reference image $t_{\rm ref}$ = 4 min and zeroing of mean intensity value. (c) Corresponding normalized power spectra. Red arrow denotes the wave number $\vec{k}_o(t)$. (d) Data and fit curves for the radially averaged power spectra during instability and growth. (e) Peak wave number $k_o(t)$ - dashed line represents initial value. Vertical bars represent the peak full width at half maximum, namely 2 $a(t)$. The wave number at t = 16 min equals k_o = 0.169 μm^{-1}, corresponding to a fastest growing wavelength λ_o = 37.2 μm.

thin liquid film could not so easily be removed since their presence tended to induce periodic film undulations nearby. In general, such defective films were either excluded from analysis or else the analysis was restricted to smaller defect-free regions far from the offending site. The latter, of course, tended to increase noise since the sample image size for analysis was smaller still.

The two most common defects observed in spun coat PS films are illustrated in Fig. 3.4(e). Embedded defects tended to produce isolated thickened regions encapsulating contaminants. Exposed defects produced ring-like elevations. Both caused film undulations in regions adjacent to the defect especially once the liquid was drawn toward the cold substrate. Shown in Fig. 3.4(a) are two gray scale images extracted from the green color channel for experiment #62 at time t = 10 min. Fig. 3.4(b) shows the corresponding images after subtraction by the reference image at $t_{\rm ref}$ = 3 min and zeroing of the mean intensity value. The image on the left shows structure formation as a result of the instability while the image on

Figure 3.3: Illustration of the image analysis process showing temporal dependence of the measured wavevector

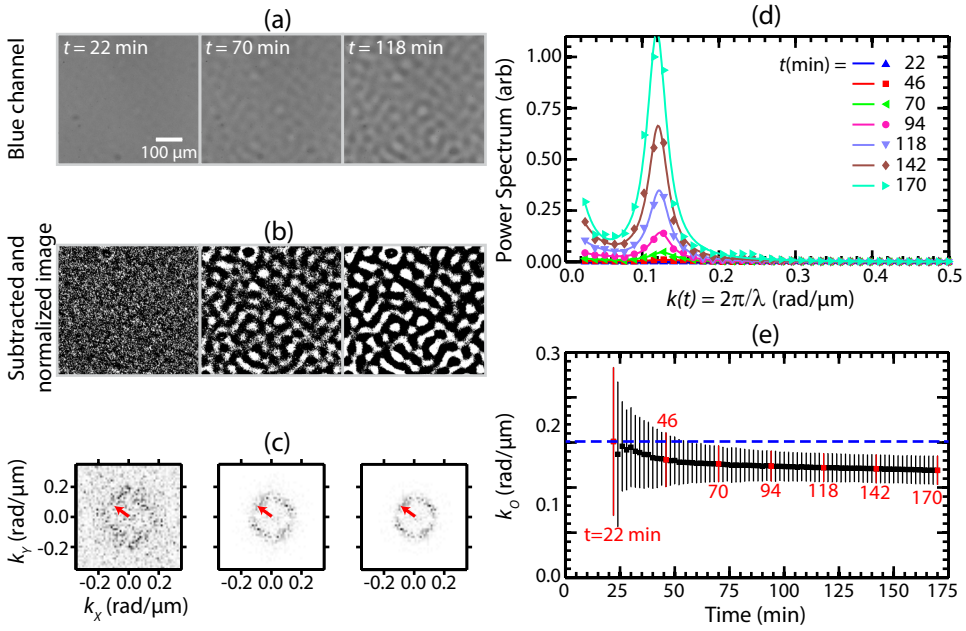

Representative images of structure formation in an initially flat and uniform PS nanofilm for experiment #69 in Table 3.7. (a) Grey scale images from the blue channel for times t = 22 min, 70 min, and 118 min. (b) Corresponding gray scale images after subtraction of reference image $t_{\rm ref}$ = 14 min and zeroing of mean intensity value. (c) Corresponding normalized power spectra. Red arrow denotes the wave number $\vec{k}_o(t)$. (d) Data and fit curves for the radially averaged power spectra during instability and growth. (e) Peak wave number $k_o(t)$ - dashed line represents initial value. Vertical bars represent the peak full width at half maximum, namely 2 $a(t)$. The wave number at t = 22 min equals k_o = 0.151 $(\mu{\rm m})^{-1}$, corresponding to a fastest growing wavelength λ_o = 41.6 μm.

the right shows the evolution of the instability modified by the presence of a large dewetted hole caused by an exposed particulate. A comparison of the two radially averaged and normalized Fourier transforms are shown in Fig. 3.4(c). Since the areas analyzed were small (see Table 3.7), defects had a pronounced effect on the characteristic wavelength λ_o extracted from the Lorentzian peak. The background intensity amplitude due that defect was large, which therefore led to much larger Fourier components and therefore more background noise. This effect remained a problem even when the image size was larger.

In the particular run shown, the wave number for the defect free region at t = 10 min was measured to be k_o = 0.164 $(\mu{\rm m})^{-1}$ for a value λ_o = 38.4 μm, while that for the exposed defect region was measured to be k_o = 0.216 $(\mu{\rm m})^{-1}$ for a value λ_o = 29.1 μm. Closer inspection revealed that exposed and embedded defects induced local ordering and growth in adjacent regions of the film, both of

Figure 3.4: Impact of defects during image analysis and wavelength measurement

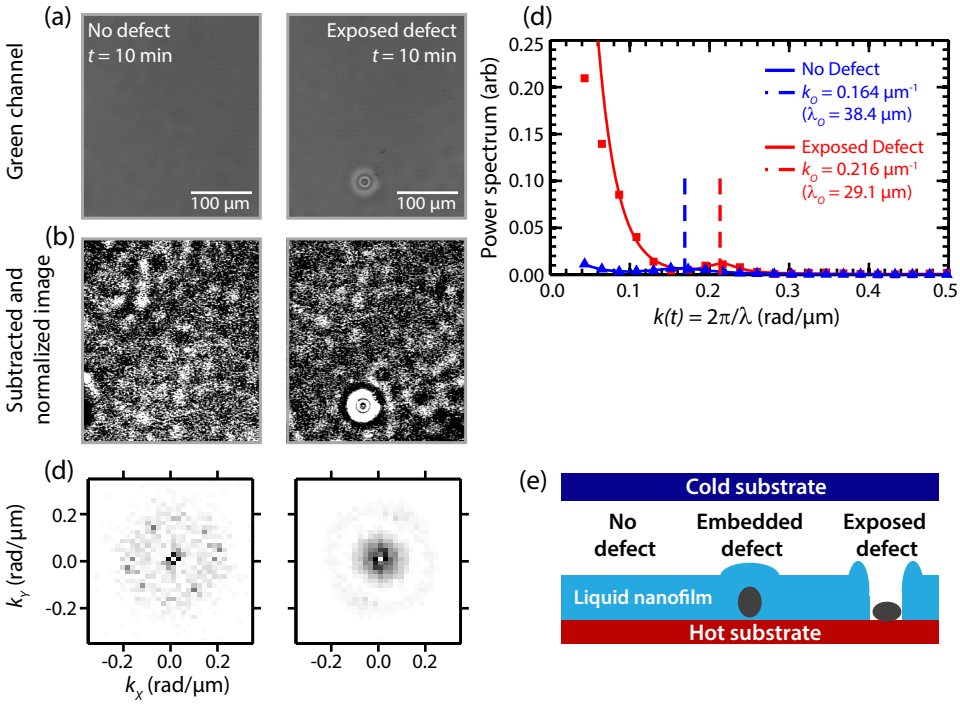

(a) Grey scale images from the green channel of experiment #62 in Table 3.7 showing both a defect-free region and a dewetted region caused by an exposed contaminant particle. (b) Corresponding gray scale images after subtraction of reference image $t_{\text{ref}} = 3$ min and zeroing of mean intensity value. (c) Corresponding 2D power spectra showing influence of dewetted hole. (d) Corresponding radially averaged and normalized power spectra. Estimates of k_o ($t = 10$ min) and λ_o ($t = 10$ min) obtained from fit to Eq. (3.1). The dewetted hole led to a smaller estimate of λ_o. (e) Sketch illustrating defect-free, embedded defect and exposed defect regions of a liquid nanofilm.

which interfered with measurement of the native instability wavelength. As a result, sequences or portion of sequences containing defects were eliminated from analysis.

3.3.5 Results of λ_o from enhanced image analysis

Shown in Fig. 3.5(a) is a direct comparison of λ_o values obtained from the current and the original study [1]. Fig. 3.5(b) shows a direct comparison of the times at which those values were extracted. The analysis procedure enhanced feature extraction, which in turn allowed identification of λ_o at earlier times. Shown in Fig. 3.5(c) is a comparison of the original and current data sets for the normalized quantity $\lambda_o(\Delta T)^{1/2}/h_o$ versus the normalized separation distance $D = d_o/h_o$ against the predictions of the AP (dashed line) and TC (solid curve) models, whose expressions are given in Tables 3.2 and 3.3 and Eqs. (3.2) and (3.3). Here, the coefficients C_{AP} and C_{TC} were treated as fit parameters. In that figure, the input values for ΔT are those estimates computed from the *original* thermal simulations [1], which are

labeled ΔT^{orig} in Table 3.7. (In Sec. 3.4, we describe improvements to the thermal simulations leading to revised current values for ΔT^{curr}.)

$$\lambda_o^{AP} \times \sqrt{\Delta T}/h_o = C^{AP}\,(D + \kappa - 1), \tag{3.2}$$

and

$$\lambda_o^{TC} \times \sqrt{\Delta T}/h_o = C^{TC}\left(\sqrt{D} + \frac{(\kappa - 1)}{\sqrt{D}}\right). \tag{3.3}$$

These fit constants were compared to the values derived from the theoretical models, namely

$$C^{AP} = 2\pi\sqrt{\gamma u_p/\overline{Q}(1-\kappa)k_a}, \tag{3.4}$$

and

$$C^{TC} = 2\pi\sqrt{4\gamma/3\kappa|\partial\gamma\partial T|}. \tag{3.5}$$

For consistency in testing the experimental data against the AP and TC model predictions, the input values of the material constants are those listed in Table 3.3. The speed of sound in PS was chosen [27] to be 1300 m/s. For the AP model, the experimental fit constant was computed to be $C_{AP} = 145\ (^\circ C)^{1/2}$ while the value computed from Eq. (3.4) was $C^{AP} = 111\ (^\circ C)^{1/2}$. Likewise, the experimental fit constant for the TC model was computed to be $C^{TC} = 576\ (^\circ C)^{1/2}$ while that computed from Eq. (3.5) was $C^{TC} = 308\ (^\circ C)^{1/2}$. Although the experimental and theoretical values for the fit constant are much closer in the AP model, the overall functional fit to the current data set is better approximated by the variation in D predicted by the TC model.

Unfortunately, the runs and images which manifested larger defect-free regions are clustered about smaller values of D ranging from about 2 to 8. Those runs correspond to cases in which the instability evolved beneath the cooled SU-8 disk, as depicted in Fig. 3.1. The experiments for which $D > 10$ contained no disk such that the instability was free to evolve anywhere beneath the larger cold sapphire window. While the linear and curved lines representing the AP and TC models better separate as D increases, experimental difficulties set in once $D > 10$. For example, the larger the value of D, the more difficult it was to level the substrates to ensure parallelism, which in turn led to more uncertainty in the value of d_o and therefore D. That said, the residual values plotted in Fig. 3.5(d) confirm closer agreement with

Figure 3.5: Comparison of the current wavelength measurements to the wavelengths measured by McLeod *et al.*

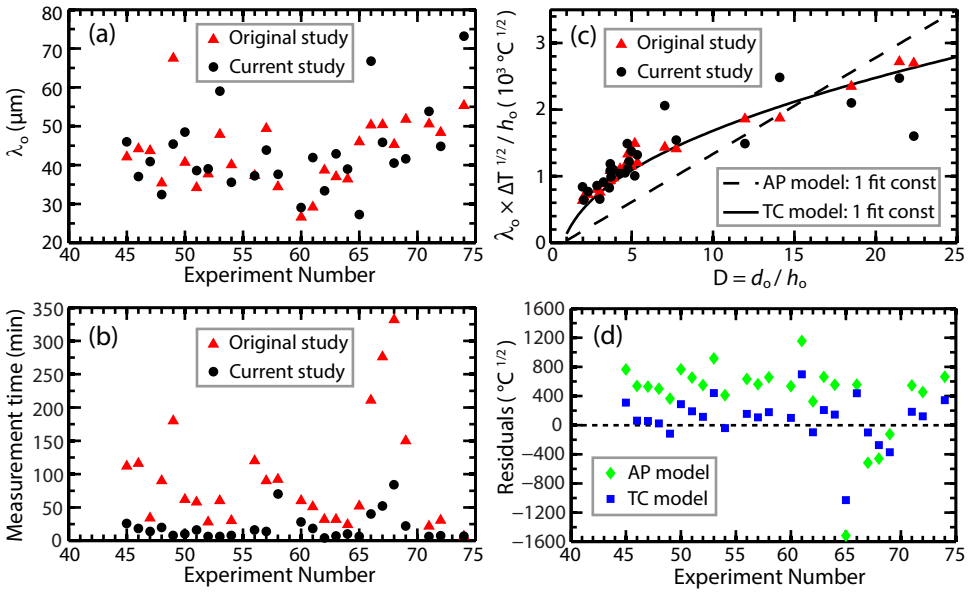

Comparison between the original [1] and current data sets for λ_o. (a) Extracted values of λ_o for the 26 experiments listed in Table 3.7. (b) Measurement times for reported values of λ_o. (c) Extracted values of the scaled quantity $\lambda_o \times \sqrt{\Delta T}/h_o$ versus normalized separation distance $D = d_o/h_o$. The solid and dashed lines represent least squares fits to the AP and TC models as described in the text. The fit constants are $C^{AP} = 145\ (°C)^{1/2}$ and $C^{TC} = 576\ (°C)^{1/2}$. (d) Residual values for the fits shown in (c). The sum of squared residuals was computed to be $SSR_{AP} = 1.15 \times 10^7$ °C and $SSR_{TC} = 2.73 \times 10^6$ °C.

the TC model. To quantify the quality of fit, we used the sum of squared residuals (SSR), here equal to $SSR_{AP} = 1.15 \times 10^7$ °C versus $SSR_{TC} = 2.73 \times 10^6$ °C.

3.4 Estimates of ΔT from Improved Finite Element Model

The temperature difference ΔT between the hot and cold substrates which confine the air/polymer bilayer is a key input parameter for estimating the wavelengths in Table 3.2 and Table 3.3. In all experiments to date reported in the literature, the separation distance d_o was far too small to accommodate even the smallest of thermocouples, so no direct measurement of ΔT could be made. Descriptions of previous experiments [2–6, 15] suggest that the values of ΔT were *incorrectly* assumed to be the difference in temperature between the set points of the hot and cold stages contacting the two substrates. Such estimates, however, tend to overestimate ΔT. The presence of thin interstitial material layers induced additional thermal resistance and the many edges which act like thermal fins also induce thermal losses which are not insignificant.

In the original study [1], finite element simulations [28] were therefore used to obtain

Figure 3.6: Computational geometry and boundary conditions for the finite element simulations of the temperature within the experimental setup

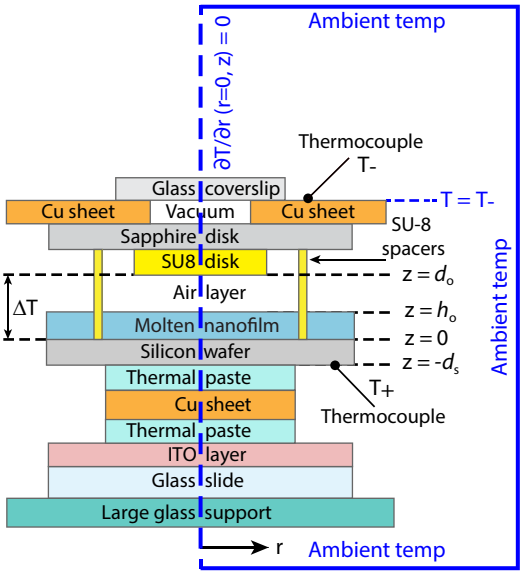

Axisymmetric geometry for finite element model used to assess steady state temperature distribution within the domain specified by the exterior (blue) boundary (not drawn to scale). Symmetry condition about the vertical axis: $\partial \mathrm{T}/\partial r(r = 0, z) = 0$. Isothermal boundary condition $\mathrm{T} = \mathrm{T}_-$ applied to the top surface of the cold Cu sheet beyond the edge of the glass coverslip. The heat per unit volume generated within the ITO layer was modeled by a constant heat generation term, $\dot{\mathrm{Q}}_{\mathrm{ITO}}$, whose value was adjusted until the resulting temperature T_+ matched the thermocouple measurement. Far field isothermal boundary conditions, $\mathrm{T}_{\mathrm{amb}} = 23$ °C, applied where shown. Table 3.6 lists the dimensions of all domains; Table 3.7 lists the values of T_+, T_-, and $\Delta\mathrm{T}^{\mathrm{curr}}$ for each computational run.

estimates of $\Delta\mathrm{T}$ for each experimental run, namely $\Delta\mathrm{T} = \mathrm{T}(r = 0, z = 0) - \mathrm{T}(r = 0, z = d_o)$. The experimental system was modeled by a simplified (axisymmetric) geometry consisting only of those material layers in Fig. 3.6 situated between the two thermocouples shown. Isothermal boundary conditions were imposed along the top of the air layer, $\mathrm{T}(r, z = d_o) = \mathrm{T}_-$, and the bottom of the molten PS nanofilm, $\mathrm{T}(r, z = 0) = \mathrm{T}_+$. The remaining external boundaries of the computational domain were made to coincide with the external edges of each material layer and assumed to be insulating boundaries, thereby subject to vanishing Neumann conditions. The numerical results were calibrated against experiment by ensuring that the temperature recorded by thermocouples placed at two designated locations outside the bilayer region, namely T_+ and T_- in Fig. 3.6, matched the numerical estimates. The original estimates for $\Delta\mathrm{T}$ obtained in this way are designated $\Delta\mathrm{T}^{\mathrm{orig}}$ in Table 3.7.

Table 3.6: Listing of domain sizes and thermal conductivities for the simulation domain shown in Fig. 3.1 and Fig. 3.6

Feature	**Thickness** (mm)	**Outer Radius** (mm)	**Thermal conductivity** (W/m-°C)
Glass coverslip	0.150	14.1	1.10 (23 °C) [29]
Upper (cold) Cu sheet (with 0.5 mm hole)	1.56	50.0	391 (20 °C) [30]
Evacuated air layer (i.e. vacuum)	1.56	0.500	0.0257-0.0454 (20-300 °C) [28]
Cylindrical sapphire window	0.400	3.75	31.0 (42-45 °C) [31]
SU-8 disk	1.38×10^{-3}	0.500	0.300 [32]
	1.48×10^{-3}	0.500	0.300 [32]
SU-8 spacers (modeled as ring) (width 4.24 μm)	d_o + SU-8 disk thickness	1.504	0.300 [32]
Air gap	$d_o - h_o$ (Table 3.7)	14.1	0.0257-0.0454 (20-300 °C) [28]
PS nanofilm	h_o (Table 3.7)	14.1	0.130 (100 °C) [22]
Silicon wafer	0.675	14.1	115 (77 °C) [33]
Thermal paste (Omegatherm 201)	0.100	8.75	2.31 [34]
Lower (hot) Cu sheet	1.50	8.75	391 (20 °C) [30]
ITO layer	1.50×10^{-4} [35]	13.0	5.00 [36]
Glass slide	0.700	13.0	1.10 (23 °C) [29]
Glass support	2.00	50.0	1.10 (23 °C) [29]

Dimensions and thermal conductivity values for the material layers shown in Figs. 3.1 and 3.6. The thermal conductivity of sapphire was chosen to be 31.0 W/m-°C since the orientation axis was unknown (32.7 W/m-°C at 45 °C for orientation parallel to c-axis; 30.2 W/m-°C at 42 °C for orientation perpendicular to c-axis). The thermal conductivity of ITO typically varies between 4.00 W/m-°C and 5.86 W/m-°C based on oxygen content, also unknown. A representative value 5.00 W/m-°C was therefore used.

In this current revised study, the computational domain was enlarged to include all those material layers shown in Fig. 3.6 (dimensions listed in Table 3.6) including the surrounding air. Far-field isothermal boundary conditions were set to an ambient temperature of 23 °C. The (axisymmetric) computational domain measured 100 mm in radius and 600 mm along the vertical axis. The maximum radial size of the interior material layers was set by the outer radius of the top (cold) Cu sheet and the large (bottom) glass support, both equal to 50 mm. An internal volumetric heat source, $\dot{Q}_{ITO}$, distributed within the volume of the ITO layer, was included in the model to mimic Joule heating from that layer. The isothermal boundary condition applied to the top surface of the top (cold) Cu sheet beyond the edge of the glass coverslip, namely $T = T_{-}$, acted as the thermal sink to draw heat away from the ITO layer. Conduction was estimated to be the dominant mode of heat transfer throughout the entire system (see discussion below). The equation governing the temperature distribution at steady state operation was therefore given by

$$\nabla \cdot (k_i \nabla T) + \dot{Q}_{ITO} = 0\,, \tag{3.6}$$

where k_i represents the thermal conductivity of the various elements listed in Table 3.6 and $\dot{Q}_{ITO} = 0$ everywhere except within the ITO layer. All k_i values were assumed to be constant and independent of temperature except for the value of air for which tabulated values as a function of temperature were readily available.

Finite element simulations [28] were conducted using a direct linear solver and Lagrange quadratic elements. Given the large range in material layer thicknesses (ranging from nm to cm), rectangular meshes containing a minimum of five elements were used to span the vertical dimensions of the thinnest domains - these included the ITO, PS and SU-8 layers. The air layer and SU-8 disk were meshed by free and extremely fine triangular meshes, respectively. All remaining layers were meshed with extremely coarse free triangular meshes modified to have a minimum element size of 0.01 micron, a maximum element growth rate of 1.75, and a resolution of narrow regions of 3. All other meshing parameters were set to extremely coarse defaults. The approximate number of elements was 460,000 with slightly more than 10^6 degrees of freedom.

The actual electrical power per unit volume generated by passage of current to the ITO layer was not measured in experiment. Instead, the quantity $\dot{Q}_{ITO}$ in Eq. (3.6) was adjusted for each run until it yielded a match with the temperature T_{+} ($r = 13.1$ mm, $z = -d_s$) measured by a thermocouple. The total input power

Figure 3.7: Finite element simulation of the temperature in the experimental setup

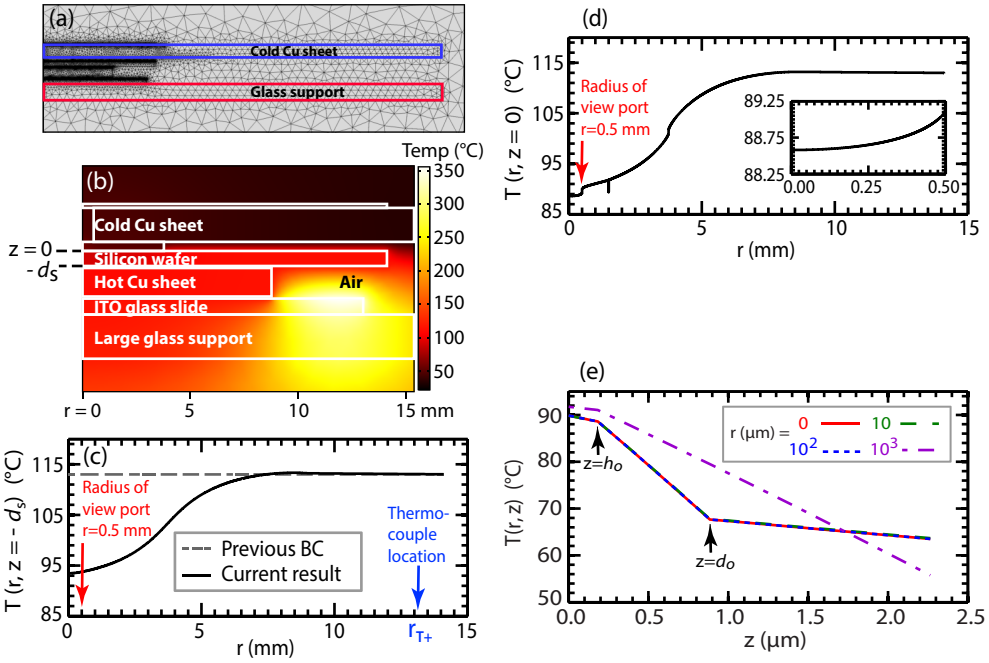

(a) Sample finite element mesh for domains in Fig. 3.6. (b) Steady state thermal distribution for experiment #56 (drawn to scale). (c) Solid line = $T(r, z = -d_s)$ (underside of Si wafer) showing current result. Dashed line = isothermal boundary condition $T(r, z = -d_s) = T_+$ used in previous simulations [1]. (d) Solid line = $T(r, z = 0)$ (along PS/Si interface). Jump at $r = 0.5$ mm due to edge of perforated hole (view port) in top (cold) Cu sheet shown in Fig. 3.6. Dip at $r = 1.5$ mm due to SU-8 spacer. Jump at $r = 3.75$ mm due to sapphire disk edge. Inset: Magnified view of $T(0 \le r \le 0.5 \text{ mm}, z = 0)$ (region within view port). (e) $T(r, z)$ for $r = 0,\ 10,\ 10^2$, and 10^3 μm.

determined in this way generated values between 14.5 W and 31.9 W, well below the 120 W maximum output of the power supply. The resulting values for $\dot{Q}_{ITO}$ are listed in Table 3.7 along with the corresponding solutions for $\Delta T^{curr} = T(r = 0, z = 0) - T(r = 0, z = d_o)$. For experiments #65 - 69 in Table 3.7 where there was no SU-8 disk, the location $z = d_o$ refers to the bottom surface of the cold sapphire disk.

Fig. 3.7 shows representative results for the steady state temperature distributions. The parameter values used here are for experiment #56 - see Table 3.7 and Table 3.6. Fig. 3.7(a) illustrates the large variation in mesh sizes needed for the various material layers. The densest meshes overlay the thinnest layers. Fig. 3.7(b) shows a color map of the temperature distribution matching the two boundary values, $T_+ = 113.0$ °C and $T_- = 35.3$ °C. The region of highest temperature shown in white is due to the ultra low thermal conductivity of the adjacent air, which acts as a thermal insulator. The solid line in Fig. 3.7(c) depicts the revised temperature

profile along the underside of the silicon wafer, $T(r, z = -d_s)$. By contrast, the dashed line represents the isothermal boundary condition enforced in the original study [1], namely $T(r, z = -d_s) = T_+$. While the isothermal assumption works well at large radial distances $r > 8$ mm, it fails significantly closer to the central axis $r = 0$. The revised simulations confirm that the Si wafer is significantly cooler than originally believed, consistent with the fact that the overhead SU-8 disk (or sapphire disk when the SU-8 is not present) cools the Si and PS layers beneath it. Shown in Fig. 3.7(d) are results of the temperature profile along the Si/PS interface, $T(r, z = 0)$. The inset is a magnified view of the temperature change within the radius defined by the view port (i.e. circular perforation) in the top (cold) Cu sheet, namely $T(0 \leq r \leq 0.5 \text{ mm}, z = 0)$. The maximum difference is less than 0.5 °C. Shown in Fig. 3.7(e) is also the temperature variation along the vertical direction for various radial distances $r = 0,\ 10,\ 10^2,$ and 10^3 μm. Superimposed on the data are the locations of the air/PS interface at $z = h_o$ and the bottom of the (cold) SU-8 disk at $z = d_o$. The data for radii $r \leq 100$ μm collapse onto a common curve indicating that the value of $\Delta T = T(r = 0, z = 0) - T(r = 0, z = d_o)$ is insensitive to the radial distance from the central axis $r = 0$ for $r < 100$ μm.

The linear stability calculations for the AP and TC models predicate a fluid base state exposed to a large transverse thermal gradient but no lateral gradient. For the results shown in Fig. 3.7(d), the estimated maximum radial thermal gradient was 1.6×10^3 °C/m, based on a maximum temperature increase of 0.8 °C over a radial distance of 0.5 mm. The estimated maximum vertical thermal gradient was 2.5×10^7 °C/m based on a maximum vertical difference of 22.1 °C at $r = 0$ over a vertical gap spacing of $d_o = 885$ nm. Consequently, the lateral thermal gradient was roughly four orders of magnitude smaller than the vertical gradient and therefore negligible. These estimates were typical of all runs conducted and confirmed the assumptions inherent in the AP and TC models.

Estimates were also used to confirm that thermal conduction was the dominant mechanism of heat transfer in the experimental system modeled. The Rayleigh number for the domain comprising the thin air layer just above the liquid nanofilm was estimated to be four orders of magnitude smaller than the critical number required for convective instability. Likewise, an estimate for the domain along the vertical edge of the hot Cu sheet above the ITO layer yielded a Rayleigh number roughly three orders of magnitude smaller than required for convection. Separate estimates confirmed that the thermal flux due to radiative losses was at least an

order of magnitude smaller than convective losses. As a result, the heat generated by the ITO layer was assumed to distribute throughout the system solely by thermal conduction.

The numerical model described provided more accurate estimates of the input parameter ΔT required for assessing the fastest growing wavelength predicted by the AP and TC models. Fig. 3.8(a) shows a direct comparison of ΔT obtained from the original and revised simulations. The current study generated lower average values for ΔT, i.e. $\Delta T_{avg}^{orig} = 26.9$ °C versus $\Delta T_{avg}^{curr} = 16.1$ °C. Fig. 3.8(b) shows the comparison between theory and experiment for the AP and TC model predictions based on Eqs. (3.2) and (3.3) using a single fit constant for each. Here, λ_o denotes values reported in the original study [1] while ΔT denotes current values based on the revised simulations. The original values of λ_o were input here in order to discern separately the influence of revisions to λ_o and ΔT. The fit constants were found to be $C^{AP} = 123$ °$C^{1/2}$ and $C^{TC} = 471$ °$C^{1/2}$. These numerical values exceed the theoretical values from Eqs. (3.4) and (3.5) by 10% and 53%, respectively. Fig. 3.8(c) depicts the corresponding residual values. Computation of the sum of squared residuals, namely $SSR_{AP} = 4.11 \times 10^6$ °C and $SSR_{TC} = 2.43 \times 10^5$ °C, nonetheless supports a better functional fit to the TC model albeit the fit constant is roughly 50% larger than the theoretical estimate.

3.5 Combined effect of improved estimates for λ_o and ΔT

In Secs. 3.3 and 3.4, we *separately* examined the influence of improvements to λ_o and ΔT. Here, we report the final combined results of these two improvements. Fig. 3.9(a) shows a direct comparison of the rescaled quantity $\lambda_o \times \sqrt{\Delta T}/h_o$ versus normalized separation distance D between the original and current data sets. The solid and dashed lines represent least squares fits to the data based either on one or no fit constant according to Eqs. (3.2) and (3.5). The best fit constants were estimated to be $C_{AP} = 112$ °$C^{1/2}$ and $C_{TC} = 447$ °$C^{1/2}$, exceeding the theoretical estimates computed from Eqs. (3.4) and (3.5) by 1% and 45%, respectively. The fact that the fitted and predicted coefficient values for C_{AP} are essentially equal, however, does not indicate closer agreement with the AP model since the functional dependence of the data on D is not well captured by that model.

To highlight this point, we show in Fig. 3.9(b) the corresponding residual values, i.e. the deviation between the data and fitted curve (TC) or line (AP). Clearly, the residual values for the TC model are closely distributed about zero, which indicates

Figure 3.8: Comparison of the temperature drops computed with the current thermal simulations to the temperature drops computed by McLeod *et al.*

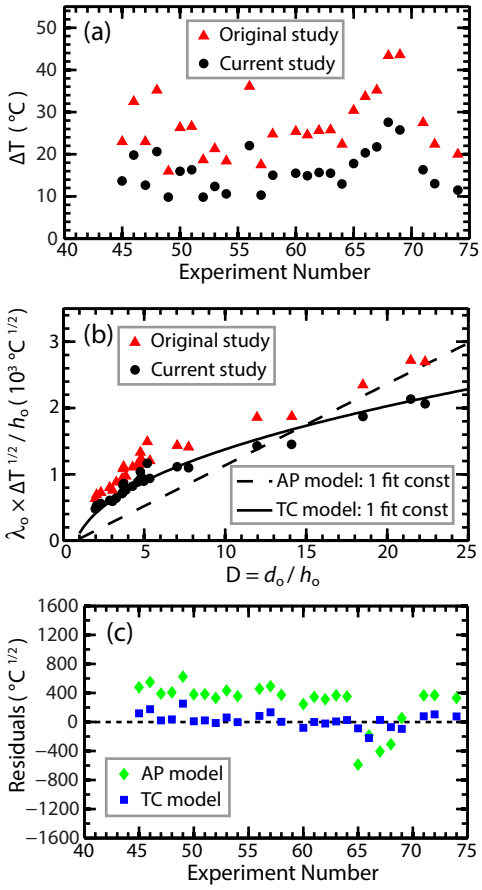

(a) Comparison of the temperature differences, $\Delta T = T(r = 0, z = 0) - T(r = 0, z = d_o)$, computed from the original [1] (triangles) and current numerical model (circles) for the experiments listed in Table 3.7. The complete set of experimental and simulation parameters can be found there and in Table 3.6. (b) Comparison of the original to current results for the scaled quantity $\lambda_o \times \sqrt{\Delta T}/h_o$ versus the normalized separation distance $D = d_o/h_o$. Here, λ_o refers to the original values reported previously [1] - ΔT denotes the values computed in the current study [plotted in (a)]. The dashed line is a least squares fit to the AP model with a single fit constant $C^{AP} = 123\ °C^{1/2}$; the solid line is a least squares fit to the TC model with a single fit constant $C^{TC} = 470\ °C^{1/2}$. (c) Residual values for the fits shown in (b). The sum of squared residuals was computed to be $SSR_{AP} = 4.12 \times 10^6\ °C$ and $SSR_{TC} = 2.42 \times 10^5\ °C$.

a better fit to the functional dependence on D. The sum of squared residuals, namely $\mathrm{SSR_{AP}} = 6.84 \times 10^6$ °C versus $\mathrm{SSR_{TC}} = 1.63 \times 10^6$ °C, confirms that the TC model more closely replicates the functional behavior with D measured experimentally.

A comparison (not shown) of the best fit TC curve in Fig. 3.9(a) with the corresponding curve in Fig. 4(a) of Ref. [1] reveals that the improved image analysis routines of this current study, however, do yield increased scatter in the data. This is because the extraction of λ_o at much earlier times relies on noisier data sets in which emergent features are yet so pronounced. This is evident from the sample images and wavenumber values shown in Fig. 3.2(b) and (e) and Fig. 3.3(b) and (e). The significant difference in extraction times for λ_o between the current and original studies are listed in Table 3.7 i.e. $t_{\mathrm{meas}}^{\mathrm{curr}}$ versus $t_{\mathrm{meas}}^{\mathrm{orig}}$. Despite the increased scatter, however, the fit constant for the improved data sets is closer to the theoretical estimate of $\mathrm{C_{TC}} = 308$ °C$^{1/2}$ – that is, the best fit (not shown) to the data (triangles) from the original study yielded $\mathrm{C_{TC}} = 607$ °C$^{1/2}$, while the best fit to the improved data (solid dots) shown in Fig. 3.9(a) yields $\mathrm{C_{TC}} = 447$ °C$^{1/2}$.

3.6 Discussion of experimental challenges

The combined results of the current study shown in Fig. 3.9 indicate closer agreement with the functional form predicted by the TC model. Unfortunately, the data is clustered mostly about smaller values of $D \leq 8$. The analytic expressions in Eqs. (3.2) to (3.5) clearly show that the models more strongly differentiate for larger values of D. We redesigned the experimental system in order to access larger substrate separation distances more easily and with higher reproducibility and this will be detailed in Ch. 5.

Both the AP and TC models predicate certain conditions which must be satisfied by experiment. These include a liquid nanofilm of constant viscosity, parallelism of the substrates confining the air/liquid bilayer, an initial flat and uniform liquid film, a substrate separation distance characterized by the slender ratio $(d_o/\lambda_o)^2 \ll 1$, heat transfer dominated by thermal conduction, and infinitesimally small fluctuation amplitudes to satisfy the condition of *linear* instability. As an aside, if the latter condition is satisfied, then so too is the assumption of constant viscosity since the interface is infinitesimally close to its original position and therefore the film viscosity is about the same as that of the original film.

To minimize misalignment from bow and warp of the silicon and sapphire layers and to enhance parallelism of the confining substrates, the interference fringes arising

Figure 3.9: Comparison of the analyzed experimental data with improved image and thermal analysis to the AP and TC model predictions

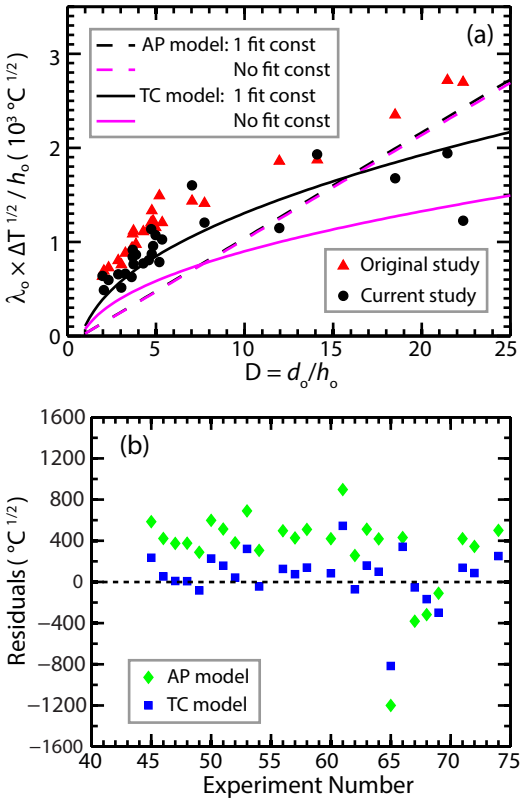

(a) Comparison of the original and current data sets for the scaled quantity $\lambda_o \times \sqrt{\Delta T}/h_o$ versus normalized separation distance D. Here, λ_o and ΔT denote the improved values reported in this chapter. The fit constant for the AP model is $C^{AP} = 112$ °C$^{1/2}$; the value estimated directly from Eq. (3.4) is 111 °C$^{1/2}$. The fit constant for the TC model is $C^{TC} = 447$ °C$^{1/2}$; the value estimated directly from Eq. (3.5) is 308 °C$^{1/2}$. (b) Residual values for the one fit constant curves shown in (a). The sum of squared residuals is $SSR_{AP} = 6.84 \times 10^6$ °C and $SSR_{TC} = 1.63 \times 10^6$ °C.

from non-parallel substrates were monitored and leveling screws adjusted accordingly. Film uniformity and flatness were maximized by conducting ellipsometric measurements of film thickness shortly after the polymer films were spun coat onto the silicon substrates. For each experiment listed in Table 3.7, we also confirmed that the slender gap approximation was well satisfied by ratios estimated to be less than 10^{-4}. As reported in Sec. 3.4, we also checked that the thermal flux due to conduction far outweighed thermal flux losses due to natural convection or radiation. Finally, as described earlier in this chapter, the substantial improvements to the image analysis allowed extraction of λ_o at much earlier times than originally reported. All in all, these checks ensured that the assumptions inherent in the theoretical models were fairly well satisfied in experiment.

Direct comparison of experiment to theory was nonetheless challenging. In particular, the influence of dust particles and other film imperfections is particularly deleterious in liquid nanofilms. For example, contaminant particles were sometimes trapped unintentionally beneath the SU-8 spacers used to preset the values of D. This problem led to underestimates in the value of D, as well as non-parallelism. Despite the rigidity of SU-8 after baking, there was concern too that the spacers might have undergone some compression during loading and leveling followed by expansion during heating, leading to uncertainty in the exact values of D.

An additional but small uncertainty in the numerical estimates of ΔT was also incurred since the *exact* location of the thermocouple denoted by T_+ in Fig. 3.6 was not known precisely. Furthermore, the actual silicon wafer substrates were square and not cylindrical, as modeled in the simulations. Finally, the layer of thermal paste between the silicon wafer and hot copper sheet used to enforce good thermal contact had to be applied anew for each experimental run. The thickness of this paste was not necessarily equal from run to run and the volume dispensed was not measured so the thickness of that layer was somewhat uncertain.

Small additional uncertainties were also likely incurred in having to rely on literature values for material constants, as listed in Tables 3.2 and 3.3. While the values of the surface tension, γ, and the temperature coefficient, γ_T, from Ref. [22] were interpolated with respect to temperature and linearly extrapolated with respect to molecular weight to better match the actual liquid films used experimentally, other film constants like the thermal conductivity, k_p, and the speed of sound, u_p, contained no information about the polymer molecular weight but were used as reported. There remains of course some uncertainly as well with regard to the fact that the literature values reported in Tables 3.2 and 3.3 refer to measurements made on bulk samples, which may not always properly reflect the values pertinent to nanofilms where large surface to volume ratios can influence material constants.

3.7 Summary

In this chapter, we have reanalyzed the experiments reported in McLeod *et al.*[1] in order to obtain improved estimates for λ_o, the wavelength of the fastest growing mode, and ΔT, the temperature drop across the air/nanofilm bilayer. Accurate values of these two key parameters are necessary for making contact with theoretical predictions in order to identify the mechanism leading to instability in flat nanofilms subject to a large applied transverse thermal gradient. The AP model ascribes periodic film

deformation due to buildup of acoustic phonon pressure within the nanofilm caused by the reflection of long wavelength phonons from interfaces within the confined bilayer. The TC model ascribes periodic film deformation to thermocapillary forces acting along the air/nanofilm interface which draw alternating portions of the liquid film toward the cooler substrate.

As detailed in this chapter, the improved image analysis for λ_o allowed extraction of emergent features at much earlier times of the instability than previously reported. In addition, the revised thermal simulations described, which better mimic the actual experimental system, led to smaller estimated values of ΔT. Refinement of these two parameter values leads to closer overall agreement with the predictions of the TC model rather than the AP model. In particular, the experimental data more closely follow the functional dependence on the normalized substrate separation distance $D = d_o/h_o$ described by the thermocapillary mechanism. However, the best fit to both models still requires one fit constant. While the value of that constant for the AP model is very close to its theoretical value, the same is not true for the TC model for which the fit constant is approximately 50% larger than the theoretical value. We have discussed several possible causes for this discrepancy.

Table 3.7: Listing of all analyzed experiments with their parameters and analysis results

Exp. No.	d_o (nm)	h_o (nm)	SU-8 disk thickness (μm)	T_+ (°C)	T_- (°C)	Analysis channel	Image size $H \times W$ (μm $\times$ μm)	λ_o^{orig} (μm)	t_{meas}^{orig} (min)	ΔT^{orig} (°C)	λ_o^{curr} (μm)	t_{meas}^{curr} (min)	ΔT^{curr} (°C)	t_{ref} (min)	$\dot{Q}_{ITO} \times 10^{11}$ (W/m^3)
45	685	186	1.48	113.5	53.4	Blue	297× 296	42.1	112.0	23.0	46.0	26.0	13.7	16.0	3.45
46	900	189	1.38	114.6	44.6	Blue	312× 270	44.2	116.0	32.5	37.0	18.0	19.8	4.0	3.89
47	810	189	1.38	114.3	64.8	Blue	270× 234	43.7	34.0	23.0	40.9	14.0	12.7	12.0	2.85
48	840	183	1.38	112.9	37.0	Blue	234× 246	35.4	90.0	35.2	32.5	20.0	20.6	14.0	4.24
49	940	181	1.38	114.6	80.2	Blue	354× 269	67.5	180.0	16.0	45.4	8.0	9.8	4.0	1.95
50	900	181	1.38	113.7	57.1	Blue	246× 190	40.7	62.0	26.3	48.5	10.0	16.0	2.0	3.17
51	700	181	1.48	113.4	43.9	Blue	310× 165	34.2	58.0	26.6	38.6	16.0	16.4	2.0	3.95
52	605	185	1.48	114.4	65.4	Blue	196× 206	37.7	28.0	18.7	39.1	6.0	9.8	4.0	2.89
53	865	183	1.38	114.4	68.5	Blue	401× 253	47.9	60.0	21.3	59.1	6.0	12.4	4.0	2.62
54	670	185	1.48	114.3	66.1	Blue	243× 270	40.1	30.0	18.4	35.6	8.0	10.6	6.0	2.80
56	885	183	1.38	113.0	35.3	Blue	318× 290	37.3	120.0	36.1	37.2	16.0	22.1	4.0	4.30
57	690	185	1.48	114.5	68.7	Blue	341× 296	49.4	90.0	17.5	43.9	14.0	10.3	6.0	2.66
58	760	142	1.48	113.9	55.6	Green	243× 144	34.4	92.0	24.8	37.6	70.0	15.0	10.0	3.27
60	735	95	1.48	114.0	54.5	Blue	179× 191	26.6	60.0	25.4	29.1	28.0	15.5	5.0	3.33
61	710	101	1.48	113.9	54.9	Green	270× 296	29.2	51.0	24.6	42.0	18.0	14.9	9.0	3.32
62	785	258	1.48	113.9	49.1	Green	291× 333	38.7	32.0	25.6	33.4	4.0	15.7	3.0	3.67
63	740	201	1.48	114.1	49.8	Blue	158× 163	37.0	32.0	25.8	42.9	7.0	15.5	6.0	3.64
64	615	215	1.48	114.2	49.2	Blue	261× 325	36.4	24.0	22.4	39.0	10.0	13.0	6.0	3.79
65	2100	94	0	114.8	71.8	Blue	396× 305	46.0	52.0	30.4	27.3	6.0	17.8	0.0	2.48
66	2200	156	0	114.7	66.7	Blue	185× 174	50.3	211.0	33.7	66.8	40.0	20.3	2.0	2.73
67	2360	110	0	114.6	66.1	Blue	369× 246	50.4	276.0	35.2	45.9	52.0	21.7	40.0	2.66
68	2350	127	0	114.4	53.0	Blue	239× 225	45.3	332.0	43.4	40.5	84.0	27.6	4.0	3.34
69	2200	184	0	114.2	53.3	Blue	539× 492	51.8	150.0	43.6	41.6	22.0	25.8	14.0	3.44
71	850	366	1.48	115.2	46.2	Blue	252× 239	50.6	21.7	27.5	53.8	6.5	16.4	5.0	3.92
72	680	331	1.48	115.3	47.2	Blue	189× 203	48.4	30.7	22.4	44.8	7.3	13.1	4.3	3.98
74	770	390	1.48	114.3	58.2	Blue	188× 195	55.3	6.7	20.0	73.2	6.7	11.5	5.0	3.28

Listing of all experiments analyzed along with relevant parameter values for the experimental setup sketched in Fig. 3.1. Symbol definitions: d_o denotes the separation distance between the proximal hot and cold substrates; h_o is the initial thickness of the PS nanofilm; SU-8 disk thickness refers to the overall separation distance between the hot silicon wafer and the cold sapphire window minus d_o; T_+ and T_- denote the measured thermocouple readings at the locations shown in Fig. 3.1; Analysis channel refers to the image color channel with the highest contrast (R, G or B); Image size refers to the image area dimensions; λ_o^{orig}, t_{meas}^{orig}, and ΔT^{orig}, as well as λ_o^{curr}, t_{meas}^{curr}, and ΔT^{curr}, denote the original [1] or current values of the fastest growing wavelength measured (meas) at the time indicated, along with the computed values of ΔT from numerical simulations. The time of the reference image used for image subtraction is denoted by t_{ref}. The power per unit volume for the source term in Eq. (3.6) is represented by $\dot{Q}_{ITO}$.

Chapter 4

INSTABILITY MECHANISM IDENTIFICATION: COLORIMETRIC HEIGHT RECONSTRUCTION

4.1 Background

In the previous chapter, the experimental data from Ref. [1] was reanalyzed to better measure the characteristic wavelength of the system. In this chapter, the same data set was used to reconstruct the height of the protrusions as a function of time. There has been previous work on a different instability driven by electric fields which examined the early time dynamics of peak growth using illumination from a laser to measure peak growth rates [37]. To date, there has been no similar study for the instability driven by large transverse thermal gradients. In this chapter, the peak elevations of the film surface are quantitatively measured *in situ* as a function of time through observation of film color, which varies due to thin-film interference effects and can remove some of the ambiguities introduced by single wavelength illumination [38]. From the peak elevations as a function of time, the growth rates of the instability peaks are measured and compared to the predictions of the TC model which was described in Ch. 2. The results presented here are consistent with general linear stability theory, and specifically support a thermocapillary mechanism for the instability. The experimental method and theoretical analysis may also be used to examine the formative dynamics of other thin-film instabilities.

4.2 Brief Summary of Experimental Details

The experimental setup and procedures have been described in greater detail in previous studies [1] and in Ch. 3, so this will only be a brief summary of the experimental details. A diagram of the experimental setup is shown in Fig. 4.1. The initially flat polystyrene (PS) nanofilm with thickness h_o was spun coat onto a silicon wafer and placed onto a heater. The upper half of the setup was composed of a glass coverslip, a copper sheet with a hole drilled in it which supported the chiller, and a sapphire window. The sapphire window was held to the copper sheet with a vacuum and the entire top half of the setup was clamped onto the bottom half. A set of SU-8 spacers on the sapphire window prevented contact and defined the total gap spacing, d_o, to the bottom of the SU-8 mesa. Three different mesa thicknesses were used: 1380 nm, 1480 nm, and 0 nm (no mesa).

Figure 4.1: Diagram of the experimental setup used for optical observation

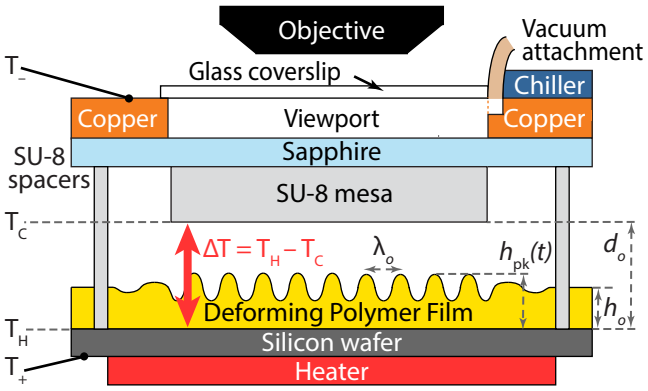

Experimental setup (not to scale). An instability in a polymer nanofilm was induced by a strong transverse thermal gradient and was observed *in situ* through a microscope objective.

Temperatures in the setup were monitored using thermocouples attached to the bottom of the silicon substrate (T_+) and to the top of the upper copper plate near the view port (T_-). Direct measurement of T_H and T_C (see Fig. 4.1) was not possible within the micron-scale gap due to its small dimension. Knowledge of the temperature drop $\Delta T = T_H - T_C$ is however critical for comparison to theoretical models, and therefore finite element simulations were used to compute the temperature profile of the whole setup, as described in detail in Ch. 3. The characteristic wavelength of the instability, λ_o, for these experiments has also been measured in Ch. 3 and was extracted from the peak of the power spectrum.

4.3 Growth Rate Predictions from Linear Stability Analysis

Previous theoretical analyses [8, 10] have shown that a long-wavelength thermocapillary instability can be generated in a nanofilm with a free interface which is subject to a large thermal gradient applied normal to the initially flat free interface. Within linear stability analysis, the instability is predicted to quickly become dominated by a maximally unstable mode of fixed wavelength in the initial linear regime. In this linear regime, the film's free interface can then be described by

$$h(x, y, t) = h_o + \delta h \; e^{bt} \; e^{i\vec{k}\cdot\vec{x}}, \tag{4.1}$$

where δh is the initial amplitude of surface fluctuations. The wavenumber and growth rate of the maximally unstable, or fastest growing, mode were found by computing the maximum of the dispersion relation, $b(k)$, which was found by inserting Eq. (4.1) into the nonlinear differential equation describing the interface evolution [10]. The details of this derivation can be found in Ch. 2 and the dimen-

sional form of the dispersion relation is

$$b(k) = \frac{k^2}{\mu(\mathrm{T})}\left[\frac{\kappa D h_o \gamma_\mathrm{T} \Delta\mathrm{T}}{2(D+\kappa-1)^2} - \frac{\gamma h_o^3}{3}k^2\right]. \tag{4.2}$$

Based on this equation, the maximum growth rate, $b_o(k_o)$, and the corresponding maximally unstable wavevector, k_o, are

$$b_o = \frac{3\kappa^2\gamma_\mathrm{T}^2\Delta\mathrm{T}^2}{16\mu(\mathrm{T})h_o\gamma}\frac{D^2}{(D+\kappa-1)^4}, \tag{4.3}$$

$$k_o = \frac{2\pi}{\lambda_o} = \frac{1}{h_o}\sqrt{\frac{3\kappa\gamma_\mathrm{T}\Delta\mathrm{T}}{4\gamma}}\frac{\sqrt{D}}{D+\kappa-1}. \tag{4.4}$$

In these expressions, λ_o is the real space wavelength, h_o is the initial film thickness, κ is the ratio of the polymer and air thermal conductivities, γ_T is the thermocapillary coefficient, $\Delta\mathrm{T}$ is the temperature drop across the polymer/air bilayer, γ is the surface tension of the molten nanofilm, $D = d_o/h_o$ is the gap ratio, and $\mu(\mathrm{T})$ is the viscosity of the molten nanofilm at the temperature T. A summary of the definitions and ranges of values for these quantities can be found in Table 4.1. Additionally, a full listing of the experimental parameters for each run can be found in Table 4.3.

The spatial portion of Eq. (4.1) has been previously investigated using experimental measurements of λ_o as a function of $\Delta\mathrm{T}$ and D which were then compared to Eq. (4.4) [1, 39]. The temporal evolution of the film has not been studied in detail for this system. In this work, the temporal portion of Eq. (4.1)) was investigated by computing b_o and comparing its functional dependence on D to Eq. (4.3)). Twenty experimental runs were analyzed, and for each experimental run, the elevations of 10 peaks were tracked at intervals ranging from 10 – 120 s using white light interference colors which will be described in detail below. The temporal evolution provides a more stringent test of the linear stability predictions than spatial measurements, due to the greater powers in the experimental parameters in Eq. (4.3) as compared to Eq. (4.4). However, we also note that Eq. (4.3) and λ_o are intimately related through the normalization

$$\beta_\Lambda \equiv b_o\frac{h_o\mu(\mathrm{T})}{\gamma_o} = \frac{(2\pi)^4}{3}\Lambda^{-4}, \tag{4.5}$$

where β_Λ is a nondimensional growth rate and $\Lambda \equiv \lambda_o/h_o$ is a nondimensional wavelength. This relationship is highly general for thin film systems which have a dispersion relation of the form

$$b(k) = k^2\left(A_1 - A_2k^2\right), \tag{4.6}$$

Table 4.1: Experimental parameter ranges for the experiments where the growth rate was measured

Description	**Symbol**	**Value(s)**
Thermal conductivity ratio	κ	0.242 [22, 23]]
PS surface tension (100 °C)	γ	33 mN/m [22]
Thermocapillary coefficient	γ_T	78 μN/(m–°C) [22]
Initial film thickness	h_o	95 – 390 nm
Plate separation	d_o	605 – 2200 nm
Gap ratio	D	1.97 – 14.1
Measured wavelength	λ_o	29.1 – 73.2 μm [39]
PS-substrate interface temperature	T_H	89.8 – 101 °C [39]
Air-superstrate interface temperature	T_C	67.8 – 88.7 °C [39]
Temperature difference	ΔT	9.83 – 25.8 °C [39]
Viscosity (T_H)	$\mu(T_H)$	30.9 – 94.4 Pa s [24]
Viscosity (T_C)	$\mu(T_C)$	104.8 – 3930 Pa s [24]
Measured growth rate	b_o	(0.345 – 158)$\times 10^{-4}$ s^{-1}

where A_1 and A_2 are constants determined by the specific instability. Eq. (4.5) is independent of the specific instability mechanism. Thus, we first probe the general linear stability framework by comparing the data to Eq. (4.5) before comparing it to the thermocapillary model specifically.

The remainder of this chapter is organized in the following sections. First, we discuss the details of the film height and growth rate measurement process in Section 4.4. Then we compare the resulting growth rate measurements to general linear stability theory and the predictions of the thermocapillary model specifically in Section 4.5. Finally, we discuss these results and address areas which will be improved in future work.

4.4 Film Height and Growth Rate Measurements using Color Interferometry

In this section we describe the method used to determine the peak heights during structure formation as a function of time. Since film deformations at early times were on the scale of nanometers, care is required both to calibrate and to track evolving peak heights by white light interferometry. The general approach in this technique is to use the thin film interference equations to compute the portion of

the incident light which is reflected as a function of wavelength. This reflection spectrum is then converted to red (R), green (G), and blue (B) color values using the camera response function for each channel. These RGB triplets form a set of curves against which the experimentally measured RGB pixel can be compared. Peak locations are well-defined at late times, so the center of the peak was easily identifiable and selected for reconstruction. Then, using the fact that the film height is monotonically increasing as a function of time at the location of a peak, we worked backwards in time to find the height of the current image based on the height of the next image in time which had already been analyzed. This procedure continued until the start of the experiment and yielded the peak height as a function of time from which the growth rate was extracted using a linear fit on a semilog plot. This is similar to the technique used to measure the characteristic wavelength in Ref. [39] and was described in Ch. 3.

Peak heights as a function of time were ascertained by comparison to a color chart produced for thin-film white light interference based on transmission and reflection from the distinct material layers in the experimental setup. In this system refractive index data as a function of optical wavelength for six distinct materials was used: glass, air, sapphire, SU-8, polystyrene, and silicon. To describe the variation of the refractive index of each material as a function of wavelength, Cauchy's equation was used [40]. It describes the variation of refractive index as a function of wavelength fairly well in the visible portion of the electromagnetic spectrum for materials with normal dispersion and has the form

$$n(\lambda_{\text{opt}}) = B + \frac{C}{\lambda_{\text{opt}}^2} + \frac{D}{\lambda_{\text{opt}}^4}. \tag{4.7}$$

In this equation, λ_{opt} is the wavelength of the optical illumination. For each material, the three constants in Eq. (4.7) can be found in Table 4.2. The refractive index of sapphire was chosen as the ordinary axis since the orientation of the window was not known and there is only one orientation where the extraordinary axis would be aligned correctly. Note that the silicon layer is the only material with significant absorption in the optical portion of the electromagnetic spectrum and so there is an additional set of Cauchy coefficients which describe the imaginary part of the refractive index as a function of wavelength. For each material, the Cauchy coefficients in Table 4.2 were substituted into Eq. (4.7) and $n(\lambda_{\text{opt}})$ was computed for 0.4 μm $\leq \lambda_{\text{opt}} \leq$ 0.8 μm in increments of 1 nm. Any refractive index values not already present in the list were linearly interpolated between the two closest values.

Table 4.2: Cauchy coefficients for the materials in the experimental setup

Material	B	$C \times 10^2(\mu m^2)$	$D \times 10^4(\mu m^4)$
Polystyrene [41]	1.563	0.929	1.20
SU-8 [32]	1.566	0.796	1.40
Sapphire [42]	1.750	0.654	-1.31
Corning 1737 [29]	1.505	0.455	-0.218
Silicon (real) [43]	3.819	-17.2	727
Silicon (imag.) [43]	0.106	-8.14	167

The reflectance of the experimental setup was calculated using a matrix formulation detailed in Ref. [44]. Within this formalism, both the transmission across an interface and the propagation through a homogeneous layer are represented by 2×2 matrices, which are then multiplied together for each layer in the stack to yield a single matrix. The reflectance can then be extracted easily from the elements of the total transfer matrix.

Assuming normal incidence of illumination from above through the microscope objective, the illumination beam undergoes reflection and transmission through a stack of $N-1$ internal interfaces separating N uniform planar interfaces comprising linear, isotropic, and homogeneous media. The index $j = 1$ denotes the first layer, which in this study is the glass coverslip. The index $j = N$ is the last layer, which in this study is silicon. The system is assumed to be bounded by two semi-infinite air layers corresponding to $j = 0$ and $j = N + 1$. The Fresnel amplitude reflection and transmission coefficients corresponding to the interface separating layers j and $j + 1$ are given by [45]

$$r_{j,j+1} = \frac{n_j - n_{j+1}}{n_j + n_{j+1}}, \tag{4.8}$$

$$t_{j,j+1} = \frac{2n_j}{n_j + n_{j+1}}. \tag{4.9}$$

The matrix describing transmission across an interface from layer j to layer $j + 1$ is given by [44]

$$\mathbf{M}_{j,j+1} = \frac{1}{t_{j,j+1}} \begin{bmatrix} 1 & r_{j,j+1} \\ r_{j,j+1} & 1 \end{bmatrix}. \tag{4.10}$$

Similarly, the matrix describing propagation through a layer j is given by [44]

$$\mathbf{M}_j = \begin{bmatrix} e^{-i\delta_j} & 0 \\ 0 & e^{-i\delta_j} \end{bmatrix}. \tag{4.11}$$

In this expression the phase accumulated by passing through a layer is denoted by δ_j and has the form

$$\delta_j(\lambda_{\text{opt}}) = \frac{2\pi n_j}{\lambda_{\text{opt}}} z_j, \tag{4.12}$$

where λ_{opt} denotes the optical wavelength and z_j is the thickness of layer j. To construct the total transfer matrix through the multilayer stack, we simply multiply the matrices together to yield

$$\mathbf{M} = \mathbf{M}_{0,1}\mathbf{M}_1\mathbf{M}_{1,2}\mathbf{M}_2 \ldots \mathbf{M}_N\mathbf{M}_{N,N+1} = \begin{bmatrix} M_{1,1} & M_{1,2} \\ M_{2,1} & M_{2,2} \end{bmatrix}. \tag{4.13}$$

Recall that the entire stack is assumed to be bounded on both sides by semi-infinite air layers so that layer $j = 0$ and $j = N + 1$ are simply air with a refractive index of 1. It can be shown [44] that the total reflectance of the multilayer stack is then

$$R(\lambda_{\text{opt}}, h) = \frac{|M_{2,1}|^2}{|M_{1,1}|^2}. \tag{4.14}$$

Due to the dependence of δ_j and n_j on the optical wavelength, λ_{opt}, the reflectance also is wavelength dependent. Furthermore, the reflectance depends on the thickness of the polymer nanofilm, h, implicitly through δ_j and we have explicitly highlighted this dependence in Eq. (4.14).

Fringe color values can therefore be computed as a function of h by estimating the convolution integral for each color channel α, where $\alpha = 1 \rightarrow$ red, $\alpha = 2 \rightarrow$ green, and $\alpha = 3 \rightarrow$ blue

$$\mathrm{v}_{\text{theor}}(h, \alpha) = \int I(\lambda_{\text{opt}})\, R(\lambda_{\text{opt}}, h)\, S_\alpha(\lambda_{\text{opt}})\, d\lambda_{\text{opt}}. \tag{4.15}$$

Here, $I(\lambda_{\text{opt}})$ represents the spectrum of the halogen light source (Osram HLX 64625, 12 V, 100 W max) as measured with a spectrometer (USB4000-VIS-NIR,

Figure 4.2: Theoretical interference fringe color for films with different thicknesses

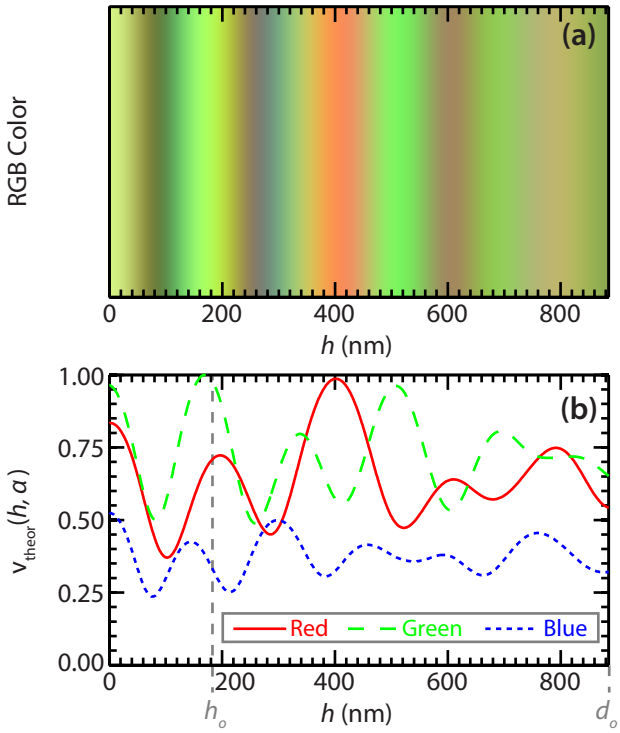

Sample plots of theoretical interference fringe color $\mathrm{v}_{\mathrm{theor}}(h, \alpha)$ as a function of PS film thickness, h, as predicted by Eq. (4.15) for experiment number #56. (a) Interference spectrum as a function of film thickness expressed as RGB triplets. (b) Interference spectrum as a function of film thickness expressed numerically.

Ocean Optics) at the exit of the microscope objective. $S_\alpha(\lambda_{\mathrm{opt}})$ denotes the spectral responsivity of the camera (DVC 1312C) for a given channel α as provided by the manufacturer. An example of computed values for $\mathrm{v}_{\mathrm{theor}}(h, \alpha)$ versus the film thickness h is shown in Fig. 4.2 for d_{o} = 885 nm and SU-8 mesa thickness = 1380 nm in experimental run #56. Note that these curves have been normalized so that the maximum value among all the channels is equal to 1 and that the numbering convention is consistent with Refs. [39] and Ch. 3.

The curves shown in Fig. 4.2 represent what we would expect to see with the camera in the experimental setup. However, they fail to account for the experimental brightness and white balance settings. The experimental brightness determines the amplitude of the curves from Fig. 4.2 based on the exposure time of the camera. The camera will also adjust the relative weight of each channel to achieve white balance under a given set of illumination conditions. To compensate for these effects, each theoretical curve was independently normalized by a linear scaling which spanned the minimum and maximum values of the experimentally measured values. This

transformation from $\mathrm{v}_{\mathrm{theor}}(h,\alpha)$ to $\tilde{\mathrm{v}}_{\mathrm{theor}}(h,\alpha)$, which helped account for differences introduced by experimental brightness and white balance conditions, was performed according to Eq. (4.16)

$$\begin{aligned} \min_{h\in[h_o,h_f]} \tilde{\mathrm{v}}_{\mathrm{theor}}(h,\alpha) &= \min_{t\in[0,t_f]} \mathrm{v}_{\mathrm{exp}}(x_f,y_f,t,\alpha), \\ \max_{h\in[h_o,h_f]} \tilde{\mathrm{v}}_{\mathrm{theor}}(h,\alpha) &= \max_{t\in[0,t_f]} \mathrm{v}_{\mathrm{exp}}(x_f,y_f,t,\alpha). \end{aligned} \tag{4.16}$$

In these equations x_f and y_f are the location of the peak at the time of the final image, t_f. The final height h_f is the estimated height of the peak at t_f. In most cases this equals d_o because the peak touched the SU-8 mesa. In some cases, particularly when there was no mesa, the peaks did not touch the upper plate and so the final height was not equal to d_o. In these cases h_f was estimated by matching the experimental peak color to the theoretical interference colors by hand.

Measurements of the peak amplitudes during film growth, $h_{\mathrm{pk}}(t)$, were then estimated as follows. A cost function was defined in order to minimize differences between the experimental RGB values as a function of time and the theoretical color variations expected as a function of the local film thickness according to

$$g(x,y,t,h) = \sum_{\alpha=1}^{3} \left[\left(\mathrm{v}_{\mathrm{exp}}(x,y,t,\alpha) - \tilde{\mathrm{v}}_{\mathrm{theor}}(h,\alpha) \right) \right]^2 . \tag{4.17}$$

Because the color of the film oscillates in h, finding the global minimum of this cost function does not accurately provide the film thickness at an arbitrary time due to noise and uncertainties in the thicknesses of the layers in the system. We worked backwards frame-by-frame, starting with the estimated height of the final frame where the peak was easily identified. We then restricted the range of h within which we searched for a minimum of g to a 70 nm window in height below the most recently computed height since the peak heights increase monotonically. Additionally, we allowed the location of the peak $(x_{\mathrm{pk}}(t),\ y_{\mathrm{pk}}(t))$ to shift by one pixel in the x-direction or one pixel in the y-direction between frames, and hence computed the film elevation for the five pixels within a 1-pixel radius neighborhood of the peak from the previously analyzed frame. This allows for a small amount of lateral movement in the peak location during each time step, Δt. The measured height $h_{\mathrm{meas}}(x,y,t)$ of each pixel within this neighborhood at time t was given by the value of h that minimizes $g(x,y,t,h)$ subject to the constraint, $h \in \left[h_{\mathrm{pk}}(t+\Delta t) - 70\ \mathrm{nm},\ \ h_{\mathrm{pk}}(t+\Delta t) \right]$. $h_{\mathrm{pk}}(t)$

and $(x_{\rm pk}(t),\ y_{\rm pk}(t))$ are then given by the value and location of the largest $h_{\rm meas}(x, y, t)$ within the neighborhood at time t.

A typical sequence of peak growth images is displayed in Fig. 4.3, showing only three of the ten peaks tracked in this sample. Each of the three analyzed peaks is highlighted by a circle in Fig. 4.3(b), (c), and (d). Once a peak was selected, the RGB pixel values of the peak center at (x_f, y_f) were extracted as a function of time and these values are plotted in Fig. 4.4(b) for the uppermost peak in Fig. 4.3. From the maximum and minimum values for each channel, the theoretical interference spectrum curves from Fig. 4.2 were scaled to produce the $\tilde{\rm v}_{\rm theor}(h, \alpha)$ curves for this experiment which are shown in Fig. 4.4(c). Note that as compared to the unscaled $\rm v_{theor}(h, \alpha)$ in Fig. 4.2, these colors match the experimental images much more accurately. Then, each vertical time slice in Fig. 4.4(b) was used to define an RGB triplet which was compared against the curve in Fig. 4.4(c), restricted to be within 70 nm of the most recently reconstructed height, and the cost function was minimized to yield the reconstructed height. Generally, these fits are fairly robust, particularly at height values less than $1.5h_o$. However, when the $\tilde{\rm v}_{\rm theor}(h, \alpha)$ curves are flat the reconstructed height can jump with small discontinuities. This is evident in Fig. 4.4(c) near h = 500 nm and h = 750 nm where two channels have extrema simultaneously. After this step, the reconstructed heights are plotted as a function of time in Fig. 4.4(d). At very early times (0 – 100 min in Fig. 4.4), fluctuations in film elevation are too small (< 20 nm) to be reliably measured *in situ*. After this point a linear growth regime consistent with the form of Eq. (4.1) is observed, and the growth rate $b_{\rm max}$ is recorded from the linear fit to the semilogarithmic data. For each experiment, the data was fit to the heights which satisfied 20 nm $\leq h_{\rm pk} - h_o \leq h_o/2$. The lower bound was chosen due to limitations in our measurement technique where the height data became very noisy. The upper bound was chosen to avoid the regime where nonlinear factors become dominant, such as contact with the top plate (e.g., the middle peak in Fig. 4.3) or local film depletion. This work only investigates the linear portion of the growth to compare to the predictions of linear stability analysis. A full listing of all the measured growth rate values can be found in Table 4.4.

4.5 Comparison of Observed Growth Rate to Linear Stability Analysis Predictions

With the measured growth rates, b_o, we investigated the predictions of general linear stability theory and then the specific predictions of the thermocapillary model. We first used the measured growth rates to validate general linear stability theory by

Figure 4.3: Images of peak growth as a function of time

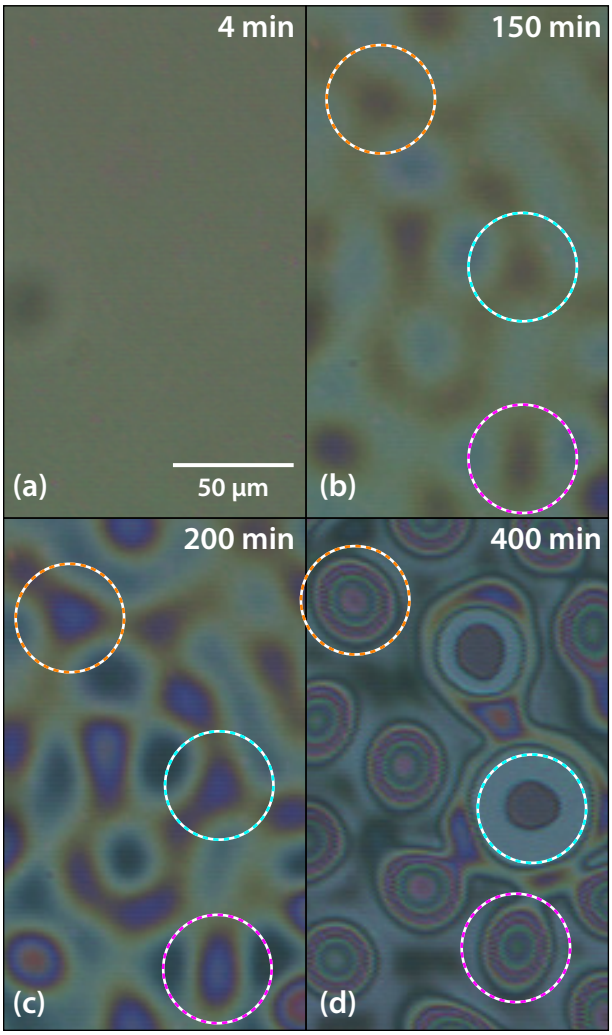

Brightfield micrographs showing thin-film interference colors in the destabilizing film under 10x magnification for experiment number #56. (a) At very early times, the film is flat and no peaks are visible. (b) Peaks begin to grow and can be identified as regions of darker color in this image. Three of the analyzed peaks are circled. (c) Peaks continue to grow and become more distinct. (d) At late times, the peaks are quite tall and show interference fringes (top and bottom) or have contacted the SU-8 mesa (middle).

Figure 4.4: Analysis of peak growth as a function of time and example of growth rate measurement

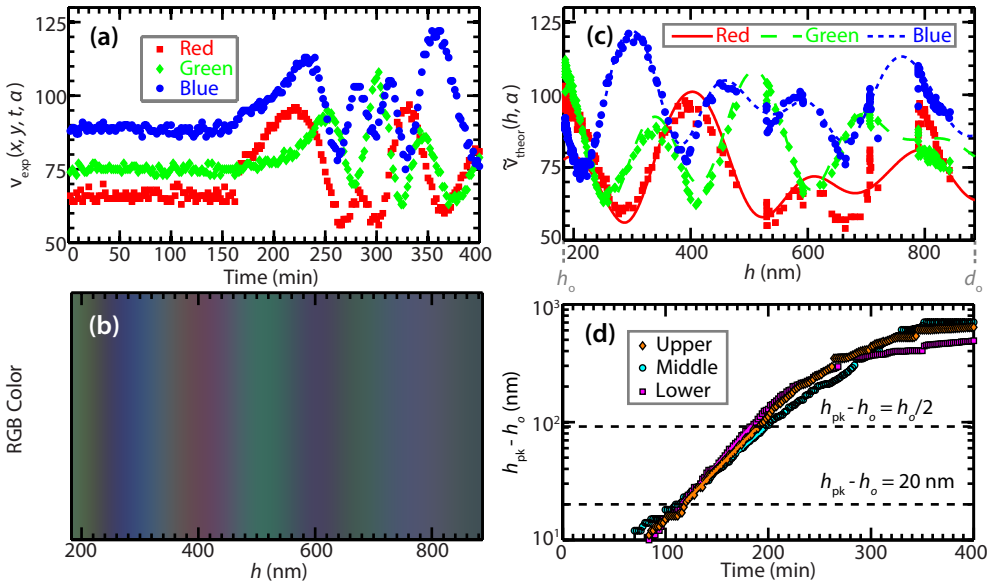

Typical growth rate measurements. (a) Experimental RGB pixel values, $v_{exp}(x, y, t, \alpha)$, as a function of time for the uppermost encircled peak from (a). (b) Scaled interference spectrum as a function of film thickness. (c) Scaled interference spectrum data for this experimental run which will be used to compute the cost function, $g(x, y, t, h)$. The matched v_{exp} points for the upper peak are also plotted to show the matching. (d) Peak elevations deduced from the interference colors matched from (c) for each of the three circled peaks in Fig. 4.3. Lines are fitted to the growth regime 20 nm $\leq h_{pk} - h_o \leq h_o/2$ in order to determine b_o.

examining their relationship to the characteristic wavelength λ_o which was shown in Eq. (4.5). The details of the λ_o measurements for these experiments have been described previously in Ref. [39] and Ch. 3.

When comparing to linear stability theory, the temperature at which to evaluate the viscosity is not entirely clear. In the theoretical analysis of Dietzel and Troian [8, 10] the viscosity was assumed to be constant and equal to the value of the viscosity at the temperature of the PS-substrate interface (T_H in Table 4.1) to complete the nondimensionalization of the Navier-Stokes equations. However, the viscosity of PS varies significantly with temperature and due to the large thermal gradient applied across the system there was a range of potential viscosities. The viscosity values for the PS have been linearly interpolated in temperature from a series of measurements made by Urakawa *et al.* [24] over a temperature range of 62 °C to 216 °C. They used PS from the same manufacturer (Scientific Polymer Products) with a slightly higher molecular weight (M_w = 1.9 kg/mol vs. M_w = 1.3 kg/mol in this study), but their results for the glass transition temperature agree with our experimental

Figure 4.5: Nondimensional growth rate plotted as a function of nondimensional wavelength

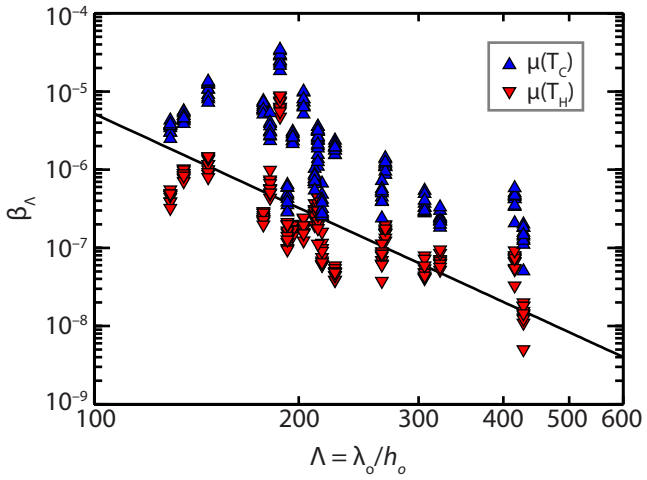

Black line: prediction given by Eq. (4.5). Red triangles: Nondimensional growth rates computed from $b_o h_o \mu(\mathrm{T_H})/\gamma$. Blue triangles: Nondimensional growth rates computed from $b_o h_o \mu(\mathrm{T_C})/\gamma$.

observations where T_g is approximately 60 °C. Comparing the viscosity of PS at the temperature of the PS-substrate interface ($\mathrm{T_H}$) and the air-superstrate interface ($\mathrm{T_C}$) shows a difference of up to two orders of magnitude (see $\mu(\mathrm{T_H})$ and $\mu(\mathrm{T_C})$ in Table 4.1). The experimental viscosity should be larger than $\mu(\mathrm{T_H})$ and smaller than $\mu(\mathrm{T_C})$ because viscosity is a monotonically decreasing function of temperature. Since it should lie between these two bounding values we can probe the consistency of Eq. (4.5) by using them as lower and upper bounds when nondimensionalizing b_o.

As seen in Fig. 4.5, the points (red triangles) where the growth rate measurements, b_o, were normalized by $\mu(\mathrm{T_H})$ almost all lie beneath the solid black line which corresponds to Eq. (4.5). Similarly, the points (blue triangles) which normalized the growth rate by $\mu(\mathrm{T_C})$ almost all lie above the solid black line. This bracketing shows the consistency of our data with the general expression given above. For the remainder of this paper, we will use the viscosity computed from the temperature at the initially flat PS-air interface ($\mathrm{T_{Int}}$).

To test the predictions of the thermocapillary theory specifically, the dependence of the growth rate on the gap ratio $D \equiv d_o/h_o$ was examined. Our previous thermocapillary wavelength analysis on this experimental data in Ch. 3 had determined that this experimental data is best described by a constant $C_{\mathrm{TC}} = 2\pi\sqrt{(4\gamma)/(3\kappa\gamma_T)}) = 447\ (^\circ\mathrm{C})^{1/2}$ which encapsulates all the material parameters of the system [39]. The

Figure 4.6: Nondimensional growth rates plotted as functions of normalized gap ratio

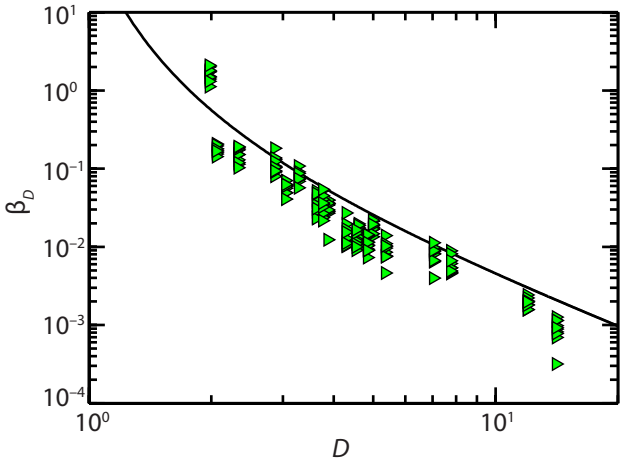

The solid black curve is given by Eq. (4.18) and the data points are the measured growth rates normalized to isolate the functional dependence on D.

use of this constant compensates for the fact that some of the values listed in Table 4.1 had to be extrapolated in molecular weight or were not provided with any molecular weight data. Since it was derived from a fit of experimental wavelength measurements to this same data set it is a more reliable quantity to make comparisons with. To ensure consistency between the wavelength analysis [39] and the current growth rate analysis, this value was held fixed. The functional dependency of b_o on D can be isolated by new scalings of the growth rate using the constant C_{TC} with Eq. (4.3)

$$\beta_D \equiv b_o \frac{\mu(\mathrm{T_{Int}}) h_o (2\pi)^4}{\gamma_o (\Delta \mathrm{T})^2 (C_{\mathrm{TC}})^4} = \frac{D^2}{3\,(D+\kappa-1)^4}. \tag{4.18}$$

The dependence of β_D on D is plotted in Fig. 4.6. As in Fig. 4.5, the measured growth rate is slightly smaller than expected with the data below the solid black curve. Recall from Ch. 2 that the TC model was derived under the assumption of constant viscosity, whereas in experiment the viscosity changes as the film deforms. Nevertheless, the agreement is remarkably good. This data lends further support to the thermocapillary theory, although it should be noted that this data barely spans a decade in D so more data is necessary to confirm these results.

4.6 Discussion of Results

To this point, the experimental data suggests that the thermocapillary mechanism is the dominant cause of this instability. However, there are several areas where these experiments could be improved. First, it was determined after the completion of these experiments that the sapphire windows that were used had a random crystallographic orientation. Sapphire is birefringent which means that the refractive index depends on the orientation of the crystal. If the c-axis of the sapphire is not parallel to the optical axis, then the value for the refractive index used above will not accurately capture the phase delay in the sapphire in the calculation of the interference colors. This in turn could affect the reconstructed height values. We expect this effect to be small, but this issue has been rectified in the redesigned experimental setup which is presented in Ch. 5. Additionally, we wanted to probe the functional dependence of b_o on ΔT as well as D but these experiments did not span a suitably large range of ΔT, only 10 – 26 °C, to permit a meaningful comparison to the theoretical predictions.

4.7 Summary

In this chapter we analyzed the early time growth dynamics of a molten nanofilm exposed to a destabilizing transverse thermal gradient. By using differential colorimetry to match the color of a deforming nanofilm to a height value we reconstructed the height of the peaks as a function of time. From this, the growth rate was measured during the linear regime. We have found that linear stability theory describes the growth rate of peaks in the unstable film by investigating the dependence of the nondimensional growth rate on the nondimensional wavelength. Furthermore, we found that the thermocapillary mechanism is consistent with the measured linear growth rates of the instability as a function of gap ratio, D. These results lend further credence to the thermocapillary mechanism and show avenues for experimental improvements in future nanofilm experiments.

Table 4.3: Growth rate analysis parameters and derived values

Exp. No.	d_o (nm)	h_o (nm)	D	SU-8 disk thickness (μm)	λ_o (μm)	T_H (°C)	T_{Int} (°C)	T_C (°C)	ΔT (°C)	$\eta(T_H)$ (Pa s)	$\eta(T_{Int})$ (Pa s)	$\eta(T_C)$ (Pa s)	Min b_o $\times 10^{-4}$ (1/s)	Max b_o $\times 10^{-4}$ (1/s)	Avg. b_o $\times 10^{-4}$ (1/s)
46	900	189	4.76	1.38	37.0	93.6	92.4	73.8	19.8	60.6	70.4	925	4.11	5.89	5.03
47	810	189	4.29	1.38	40.9	99.0	98.1	86.3	12.7	36.1	38.5	152	2.94	7.79	4.18
48	840	183	4.59	1.38	32.5	89.9	88.6	69.3	20.6	93.9	105	2440	3.84	5.68	4.78
50	900	181	4.97	1.38	48.5	96.8	95.8	80.8	16.0	45.2	49.6	323	4.99	8.13	6.57
51	700	181	3.87	1.48	38.6	91.8	90.5	75.4	16.4	76.5	87.9	755	2.70	8.74	7.01
52	605	185	3.27	1.48	39.1	98.5	97.6	88.7	9.83	37.2	41.2	105	9.45	17.9	13.1
53	830	183	4.54	1.38	59.1	100	99.7	88.1	12.4	33.0	34.6	116	2.87	5.23	3.79
54	670	185	3.62	1.48	35.6	99.0	98.1	88.4	10.6	36.2	38.7	109	4.73	10.7	7.53
56	885	183	4.84	1.38	37.2	89.8	88.6	67.8	22.1	94.4	106	3930	2.39	4.68	3.50
58	760	142	5.35	1.48	37.6	96.1	95.3	81.1	15.0	48.3	52.1	310	1.83	5.51	3.60
60	735	95.0	7.74	1.48	29.1	95.9	95.4	80.4	15.5	49.3	51.8	337	2.91	5.65	3.79
61	710	101	7.03	1.48	42.0	95.8	95.2	80.9	14.9	50.0	52.8	319	2.16	6.10	4.41
62	785	258	3.04	1.48	33.4	93.9	92.2	78.2	15.7	59.3	72.2	461	7.03	12.1	9.83
63	754	201	3.75	1.48	42.9	94.1	92.9	78.7	15.5	58.0	66.3	413	5.09	12.8	8.65
64	615	215	2.86	1.48	39.0	93.1	91.6	80.1	13.0	64.6	78.1	351	10.4	23.8	15.1
66	2200	156	14.1	0	66.8	101	101	81.0	20.3	30.9	31.7	314	0.345	1.38	0.974
69	2200	184	12.0	0	41.6	97.2	96.6	71.4	25.8	43.2	45.9	1740	1.62	2.49	1.99
71	850	366	2.32	1.48	53.8	93.7	91.3	77.4	16.4	59.9	81.3	549	12.1	22.5	17.7
72	680	331	2.05	1.48	44.8	93.0	90.6	79.9	13.1	65.6	87.6	359	10.9	15.9	13.5
74	770	390	1.97	1.48	73.2	96.2	94.0	84.7	11.5	47.9	58.9	187	84.5	158	122

Listing of all experiments analyzed along with relevant parameter values: d_o is the separation distance between the hot and cold plates; h_o is the initial thickness of the PS nanofilm; D is the normalized separation distance; SU-8 disk thickness denotes the overall separation distance between the hot silicon wafer and the cold sapphire window minus d_o; λ_o is the measured instability wavelengths from Ref. [39]; T_H and T_C are the temperatures at the hot and cold plates, respectively; ΔT is the difference between T_H and T_C and all temperature values were taken from the simulations in Ref. [39]; $\mu(T_H)$ and $\mu(T_C)$ are the viscosity values computed at the temperatures of the hot and cold substrates, respectively; the last three columns show the minimum, maximum, and mean values of the measured growth rate, b_o.

Table 4.4: Measured growth rates for each experimental run reported in units of 10^{-4} 1/s

46	47	48	50	51	52	53	54	56	58	60	61	62	63	64	66	69	71	72	74
5.89	5.63	4.22	6.54	5.94	17.9	3.46	4.91	3.46	5.51	5.65	5.02	10.3	8.14	14.0	1.38	2.49	20.5	13.0	106
5.18	2.94	5.39	6.26	2.70	13.3	3.56	7.77	4.57	3.03	2.91	2.16	9.68	9.50	10.4	0.756	2.29	17.9	15.9	114
4.43	3.33	5.04	7.85	6.21	11.4	3.76	8.24	2.39	4.36	3.00	3.51	8.49	12.4	13.5	0.888	1.87	15.3	15.0	131
5.53	4.84	5.68	6.23	7.95	12.2	2.87	7.08	3.06	3.38	5.17	4.45	8.45	5.56	23.8	1.24	2.09	17.8	12.3	131
5.65	2.99	4.50	8.13	8.69	15.1	3.94	10.7	3.76	3.00	3.45	4.38	12.1	6.31	17.2	1.07	1.62	13.4	13.9	84.5
5.03	3.69	4.53	4.99	7.84	13.2	3.75	5.86	3.39	4.05	3.03	4.74	10.5	7.59	17.9	0.962	1.63	14.1	15.5	151
4.48	7.79	4.79	6.29	7.56	12.2	4.73	9.75	4.68	3.82	3.88	5.28	10.8	10.6	16.1	0.848	2.03	21.0	11.8	112
4.11	2.99	5.46	6.89	6.52	14.4	3.45	9.96	2.96	1.83	3.42	3.63	10.2	12.8	11.9	1.25	1.85	21.9	13.7	136
5.03	4.43	4.39	5.45	8.74	12.3	5.23	4.73	3.73	2.96	3.14	4.86	7.03	5.09	13.6	0.345	2.03	12.1	10.9	158
4.97	3.19	3.84	7.17	7.94	9.45	3.15	6.35	2.95	4.07	4.23	6.10	10.8	8.55	12.2	1.00	2.03	22.5	12.9	99.0

Listing of all experimental runs with the ten measured growth rates. The top row of the table contains the experiment number, consistent with Table 4.3. The next ten rows are the measured growth rates.

Chapter 5

INSTABILITY MECHANISM IDENTIFICATION: REDESIGNED EXPERIMENTAL SETUP

5.1 Background

The present chapter aims to build upon the work of McLeod *et al.* [1] and the previous two chapters to further investigate the dominant driving mechanism experimentally. While the comparisons between the experimental data and the theoretical predictions presented in the previous chapters showed improvements with the reanalysis, there were further areas for improvement which will be addressed here. In particular, larger ranges of $D = d_o/h_o$ and ΔT were investigated with a completely redesigned experimental apparatus. Building upon previous work, a strong focus was placed on early time wavelength measurements and accurate thermal control and measurement to provide the cleanest comparison between experimental data and the predictions of linear stability theory from each proposed model to date. Additionally, we will measure the growth rate and the characteristic wavelength simultaneously with a new analysis procedure to provide the most comprehensive comparison between theory and experiment performed to date.

Nanofilm instability experiments have historically proven to be challenging for a number of reasons. Primarily, these difficulties stem from the minute size scales involved. Defects as innocuous as a piece of dust must be stringently avoided because they can be an order of magnitude larger than the nanofilm's thickness and will destroy the parallelism of the heating and cooling plates. They also serve as nucleation sites for nonlinear growth that can swamp the incipient instability growth. Beyond magnifying the importance of defects, the limited vertical scale means that experimental measurements of the wavelength are based on nanometer scale deflections of the interface which can be technically challenging to identify. This poses strict requirements on the optical measuring techniques to have this level of sensitivity. Next, the temperature drop across the nanofilm/air bilayer cannot be measured directly because the presence of a thermocouple or other direct temperature measurement device would disturb the parallelism and temperature profile in the setup. Consequently, the value of ΔT must be inferred through temperature simulations of the setup. Finally, achieving vertical parallelism to

within 100 nm over a lateral distance of centimeters is a difficult process that is further complicated by the fact that the system undergoes rapid heating which can lead to differential thermal expansion between components. Experimental components were chosen for their high thermal conductivities, not for their thermal expansion coefficients, so differential expansion can be a problem when trying to achieve parallelism over large distances. Due to the small scales involved, minute differences in the coefficients of thermal expansion can cause large changes in the observed interference fringes. The experimental setup and procedures described in the following sections were specifically designed to address these challenges and improve upon the experimental designs of previous studies.

The initial studies of Chou *et al.* [2, 3] and Schäffer *et al.* [4–6, 15] suffered from three major experimental limitations. Most importantly, their systems could not be observed during the deformation process. As such, they were limited to making measurements of the feature wavelength after the protrusions had touched the top plate and solidified. This restriction poses a severe obstacle when comparing to the characteristic wavelength derived from linear stability because linear stability analysis is a perturbative technique in the amplitude of the film height disturbance. Once the protrusions touch the top plate there is no guarantee that the resulting wavelength will be the same as the one predicted by linear stability. Second, these groups were limited in their temperature control and measurement. In the case of Chou *et al.*, the temperature was assumed to be equal to that of the heating plate and no ΔT values were reported because the system was assumed to be isothermal and the driving force was hypothesized to be temperature independent. In the case of Schäffer *et al.*, they took ΔT to be the difference between the setpoints of their heater and chiller. As will be shown in more detail below, this is problematic because the nanofilm and air layers make up a minuscule portion of the total thickness and there can be significant temperature drops in other components of the system, even if those components have much larger thermal conductivities than those of air. Finally, both Chou *et al.* and Schäffer *et al.* identified the dominant instability wavelength by measuring the distance between peaks by hand which is suboptimal when trying to identify a global characteristic in something that doesn't have long range order. The experimental setup of McLeod *et al.* [1] improved upon each of these limitations and this was the experimental setup for the data shown in Ch. 3 and Ch. 4. First, they used *in situ* optical observations to measure the characteristic wavelength at early times to more accurately compare to linear stability predictions. Second, they used finite element simulations to calculate the temperature drop across each layer

of the system and extracted only the temperature drop across the nanofilm and air layers. Finally, they used Fourier analysis to extract the characteristic wavelength of the instability instead of measuring distances by hand which was a more robust measurement technique.

The experimental setup presented in this chapter improves further upon the work of McLeod *et al.* in each of these key areas. We have improved the *in situ* observations by using a larger viewing area to observe the growth of more peaks for improved statistics. Additionally, we switched from the white light illumination used by McLeod *et al.* to single wavelength illumination to more clearly highlight the instability growth at early stages. In terms of temperature control and measurement we have improved accuracy through the use of platinum resistance temperature detectors (RTDs) which have a higher resolution than the thermocouples used previously (0.1 °C vs. 1 °C, respectively [46, 47]). We also accessed a broader range of ΔT values by improving the thermal contact between layers in the new setup and using a higher power heating element. Finally, we have improved the wavelength extraction technique by using a new fitting function derived specifically for this physical system which allows us to measure the wavelength and growth rate simultaneously. This fitting function is a marked improvement over the Gaussian or Lorentzian fitting functions used previously. Overall, the improvements to all areas of the experimental setup have made us much more confident in the determination of the dominant instability mechanism.

The remainder of this chapter is divided into five major sections. First, we describe the details of the experimental setup in Sec. 5.2. Then the finite element simulations used to compute the temperature drop across the polymer/air bilayer are described in Sec. 5.3. Next, the analysis procedure used to extract the wavelength and growth rate for each experimental run is delineated in Sec. 5.4. Sec. 5.5 then details the comparison of the measured wavelengths and growth rates to the proposed models through the scaled quantities presented in Table 5.4. Finally, we discuss the experimental results and some of the biggest experimental challenges in Sec. 5.6. We conclude by emphasizing that the TC model is best supported by this experimental data.

5.2 Description of Experimental Setup

The redesigned experimental setup was inspired by the setup described in Ref. [1] and a diagram of the new experimental setup is exhibited in Fig. 5.1. The major

features of the setup are briefly described here and then a detailed account of the setup is presented below. The setup was divided into two halves to facilitate the loading and unloading of samples for different experimental runs. The bottom half ends at the nanofilm and the upper half starts with the SU-8 spacers attached to the sapphire window. The top half of the setup was stationary and consisted mainly of the large aluminum chiller and the camera attached to the microscope which was used to observe the instability *in situ*. The bottom half of the setup was mobile to allow loading of samples and was composed of several translation stages and the heater which provided the driving thermal flux through the system. Most of the instruments were digitally controlled and all the instruments that interfaced with the computer were controlled by a custom MATLAB GUI.

Starting from the bottom of the setup and moving upwards, a motorized XY translation stage (HT1111, Prior Scientific) supported the bottom half of the experimental setup and allowed for nanofilms to be inserted into the setup with its long travel range. Vertical displacement of the nanofilm was controlled by a manual z-axis dovetail translation stage (DS40-z, Thorlabs) attached to an adapter plate (MRP3-0.125, Newport) which was separated by 3.2 mm thick fiberglass insulation (9323K21, McMaster-Carr) and 127 micron thick polyimide film (500HN Kapton, DuPont). To help ensure parallelism between the sapphire window and the supporting silicon substrate, the adapter plate supported 4 springs (#235, Jones Spring Co.) around four 1/4-20 screws which attached to an identical adapter plate. The presence of the springs gave the heater holder and nanofilm extra degrees of freedom to tip and tilt so that it could more closely conform to the spacers on the sapphire window and achieve better parallelism. The upper adapter plate attached to the custom fabricated aluminum heater holder through four 6-32 screws. To prevent excessive thermal losses through the supporting structure, the adapter plate and heater holder were separated by 127 micron thick polyimide and 2 layers of 3.2 mm thick fiberglass insulation. Inside the heater holder was an alumina ceramic heater which provided the thermal flux in the system through Joule heating and is described in Sec. 5.2.1. Thermal paste (Heat-Away 638, Aremco Products, Inc.) was used to provide a strong thermal contact between the aluminum heater holder and the silicon wafer (50.8 mm diameter, <100> orientation, 10-20 Ω-cm, thickness 279 ± 25 microns, Silicon Materials, Inc.). The thermal paste completely filled a rectangular path inset into the heater holder and then created a layer above the top of the holder where the silicon wafer was positioned. The inset's outer boundary was a square 25.4 mm on a side and the inner boundary of the inset was a square 12.7 mm on a side.

The thickness of the inset was 0.508 mm and the entirety of the inset was filled with thermal paste for every experimental run. Prior to insertion into the setup, the silicon wafer was spin coated with a solid polymeric nanofilm and these preparation steps are detailed in Sec. 5.2.2. In direct physical contact with the nanofilm was the sapphire window with patterned spacers which was held to the custom aluminum chiller (305 mm x 101.6 mm x 25.4 mm) using a vacuum created below the micro cover glass coverslip (25 mm x 25 mm x 0.15 mm, VWR). The instability was observed through a hole in the aluminum chiller using a camera attached to a microscope. The details of the image capture process are detailed in Sec. 5.2.3. Additionally, the entire setup was encased in a cardboard box to isolate the system from any ambient air currents. The whole optical table on which the microscope sits was surrounded by optical curtains and within these curtains a horizontal laminar flow clean bench ran continuously (CAP303-33691, Clean Air Products). As a final precaution against introducing dust and external contamination onto the nanofilm, a surgical mask (59928, Kimberly-Clark) and hair net (5357T1, McMaster-Carr) were worn in addition to a lab coat (414004-368, VWR) and nitrile gloves (Microflex Xceed) during sample preparation and the experimental runs.

5.2.1 Experimental Temperature Control

The temperature drop across the nanofilm/air bilayer, ΔT, is a crucial parameter when comparing the three proposed instability models because it is a distinguishing parameter between the SC and AP/TC models. Additionally, it is the only parameter which can be digitally controlled in the experimental setup. As such, ΔT was controlled in several ways. First, the electrical power dissipated by the alumina ceramic heater through Joule heating provided the heat flux through the system and was controlled digitally. An alumina ceramic heater of dimensions 25 mm x 25 mm x 1.1 mm with a resistance of 5 to 6 Ω (Induceramic) was contained in the aluminum holder described above. The heater was driven by a 30 V, 5 A programmable DC power supply (2200-30-5, Keithley) controlled by a desktop computer (Precision T3500, Dell) through a GPIB to USB converter (488-USB2, ICS Electronics) in MATLAB 2013a [25]. The aluminum heater holder also contained a platinum resistance temperature detector (RTD) with outer diameter 2.5 mm (RTD-3-F3105-36-T, Omega) which was inserted concurrently with thermally conductive paste to ensure good thermal contact. The RTD was located in the center of the holder directly above the heater. The RTD was monitored in real time by a logger (PT-140A, Omega) which interfaced with the desktop computer. The current and voltage

Figure 5.1: Diagram of the redesigned experimental setup

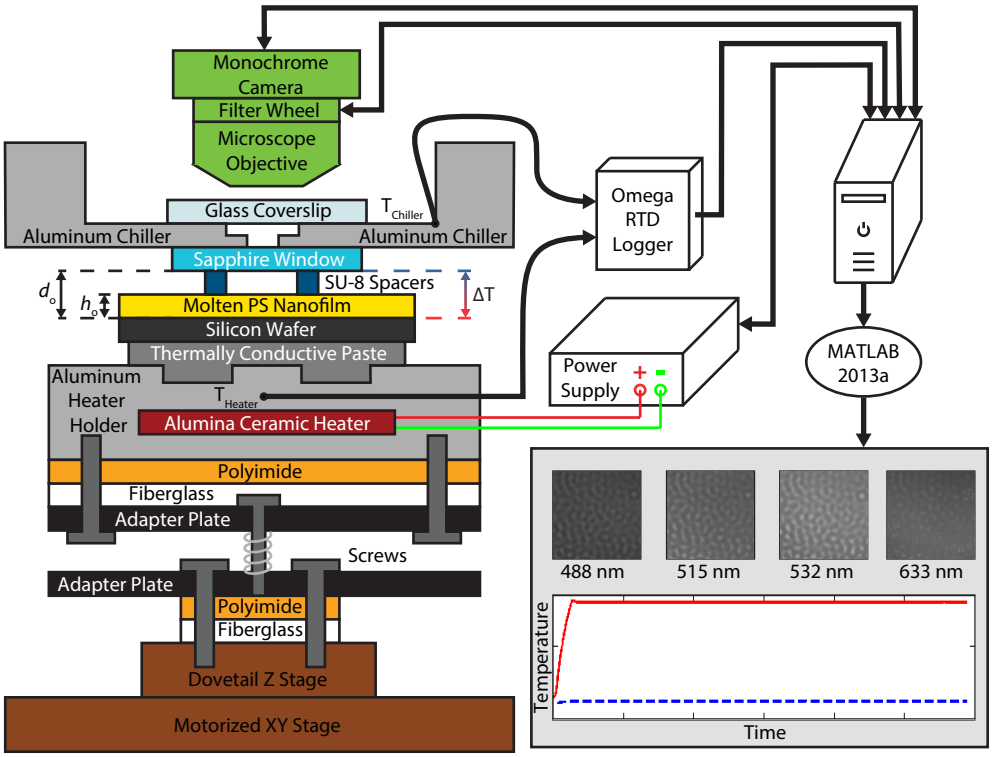

Diagram of the experimental setup (not drawn to scale) which was redesigned and improved from the one presented in Ch. 3 and Ch. 4. A full listing of the dimensions and materials can be found in the text.

of the power supply were controlled by the MATLAB GUI which implemented a PID loop evaluated approximately every half second with control parameters K_p = 0.1, K_i = 0, and K_d = 1 on the voltage. This PID loop was tuned by hand and we found that no integral gain was necessary to remove steady-state error, so K_i was set to zero. The feedback was implemented based on the temperature reported from the platinum RTD directly between the heater and the nanofilm and the temperature of this RTD was always found to be within 0.1 °C of the setpoint once the initial equilibration time (approximately 5 minutes) had elapsed. These parameters were chosen with an emphasis on minimizing overshoot of the temperature. The overshoot was less than 3 °C for any setpoint choice. The power supply imposed another restriction on the feedback loop because its maximum output voltage was 30 V and during initial heating this limit was often hit. For safety reasons, and to prevent large thermal shocks, we also restricted the maximum voltage increase to be less than 0.5 V in a single time step. Second, the external chiller which pumps water through the aluminum chiller had an active feedback loop which maintained

a fixed setpoint temperature of the external water bath. The aluminum chiller was attached to an external thermostat (RM6, Lauda Brinkmann) which pumped temperature controlled water through the chiller in a counterflow arrangement to expedite convective heat transfer. The temperature of the chiller was monitored with an RTD at the edge of the objective cutout and recorded by the same logger as the RTD in the aluminum heater holder. The advantage of using RTDs as compared to thermocouples in this system is that RTDs provide more precise measurements than thermocouples and the faster response time of a thermocouple was not needed. Finally, we enclosed the whole system in a cardboard box to prevent air currents from the laminar flow clean bench or the building ventilation system from interacting with our system. This prevented any external forced convection due to air currents and removed diurnal and seasonal variations in the steady state temperature profile.

5.2.2 Sample Preparation and Mask Fabrication

Prior to an experimental run, the polymeric nanofilm and mask patterns on the sapphire window were prepared. The polymeric nanofilms were created by spin coating a solution of the dissolved polymer onto a silicon wafer. During spin coating, the solvent evaporated, leaving a solid nanofilm ready for insertion into the experimental setup. The patterned spacers on the sapphire window were created photolithographically using standard techniques and these windows were reusable for many experimental runs.

The polystyrene (PS) (1.1k M_W, polydisperity 1.12, #771, CAS #9003-53-6, Scientific Polymer Products) was dissolved in reagent grade toluene (CAS #108-88-3) with weight percentages ranging from 1% to 8%. This solution was then filtered with an alumina matrix filter with 0.02 micron pore size (Anodisc 13, #6809-7003, unsupported filter, Whatman) in a stainless steel holder (#1980-001, GE Healthcare Life Sciences) attached to a 5 mL glass syringe with stainless steel Luer lock tip (5017, Cadence Science). Special care was taken to choose filtering components which did not dissolve in toluene, as previous attempts using polymeric filters and syringes showed unacceptable levels of defects due to contamination of the solution from dissolution of the filters and syringes. After initial filtration and storage in a glass jar with a PTFE lined cap (#12-100-276, Fisher Scientific), the solution was filtered again as it was dispensed for spin coating onto the silicon wafer. Spin speeds ranged from 1000 RPM to 3000 RPM with an acceleration of 1000 RPM/s (CEE-100, Brewer Science) for 30 seconds. The toluene evaporated during spin coating, so the PS nanofilm was ready for immediate thickness measurement with an ellip-

someter at a wavelength of 632.8 nm (Auto EL III, Rudolph). A single measurement was taken at the center of the wafer in the area which can be observed through the sapphire window to determine h_o. Previous ellipsometer measurements had shown that the thickness of a nanofilm spin coated with this instrument was consistent across the whole wafer to within the measurement uncertainty of the ellipsometer after the spin coater had been leveled. To level the spin coater, a spare 50.8 mm diameter silicon wafer was placed on the vacuum chuck. Isopropyl alcohol (IPA) was slowly dispensed in the center of the wafer and the direction of fastest spreading was noted. The wafer was spun until the IPA evaporated and the adjustable feet on the spin coater were adjusted to raise the direction of fastest spreading. This process continued until the IPA spread uniformly in all directions and reached the edge of the silicon wafer simultaneously. For more details on spin coating, please consult Appendix A.1.

When the nanofilm was inserted into the setup using the XY and Z translation stages, it was raised until it contacted the SU-8 spacers (SU-8 2000, Microchem) which were photolithographically patterned on the sapphire window (1 mm thick, 9.5 mm diameter, c-axis aligned, MSW037/040Z, Meller Optics). Using c-axis aligned windows minimized the birefringence of the sapphire window. Spacers were arranged in a hexagonal pattern at a radius of 3 mm and each individual spacer was circular with a 1 mm diameter. Before spinning the SU-8, the window was attached to a 25.4 mm square glass substrate (25.4 mm x 76.2 mm Gold Seal microscope slide scribed and broken to approximately 25 mm square, 3010-002, Thermo Scientific) with S1813 photoresist (Microposit S1813 G2 Photoresist, Dow). The sapphire/photoresist/substrate agglomerate was baked at 95 °C for 10 minutes on a hotplate (11301-016, VWR). By attaching the window to a substrate, the edge bead of the SU-8 was reduced and this allowed the spacers to be placed at a larger radius on the sapphire window while still preserving a uniform thickness. After baking the S1813, the SU-8 was spun onto the window using a spin coater (Model WS-400A-6NPP/Lite, Laurell) with speeds that varied between 1000 RPM and 3000 RPM and accelerations that varied between 1000 RPM/s and 3000 RPM/s for 60 seconds. After spinning, the SU-8 was pre-baked at 65 °C for 1 minute and 95 °C for 2 minutes. The window was then exposed to UV light through a custom patterned mask (UCLA Nanoelectronics Research Facility) for 60 seconds in a mask aligner (MJB3, Karl Suss). Then, the window was post-baked at 65 °C for 2 minute and 95 °C for 4 minutes. The SU-8 pattern was developed in SU-8 developer (MicroChem) for 30 seconds, followed by insertion into a bath of IPA

for 30 seconds. To detach the window from the substrate, the S1813 photoresist was dissolved with acetone and the window was rinsed with IPA to remove any residual acetone. The window was removed from the acetone as soon as it detached from the substrate (typically around 10 seconds) because long exposure of SU-8 to acetone before hard baking was found to crack the SU-8 and cause delamination from the sapphire. The developed window was then hard baked at 200 °C for 2 hours to complete the fabrication process. After the hard bake, the spacer heights were measured using a profilometer (XP-2, Ambios) and were ready for use in an experimental run. The spacer heights varied from 730 nm to 7 microns. After the experimental runs were completed, we observed that some PS remained underneath the spacers so the d_o values in Table 5.5 which represent the total gap thickness from the bottom of the nanofilm to the top of the air gap are equal to the initial film thickness plus the spacer height. For more details on mask fabrication, please consult Appendix A.3.

5.2.3 Optical Image Acquisition

Optical observation of the instability during deformation was accomplished through the use of a camera attached to a microscope. To accommodate the working distance (WD) of the microscope objective (10x EC Epiplan HD, WD = 14.3 mm, #422040-9960, Zeiss), a 50.8 mm x 50.8 mm x 19.1 mm section was removed from the center of the aluminum chiller. In the center of the cutout, a viewing hole (diameter 2.94 mm) allowed optical access to the film. This hole was designed to be as small as possible to maximize the possible temperature difference, but another hole (diameter 4.86 mm and depth 4.83 mm) was required for the light cone of the objective to be unimpeded. The microscope objective was attached to a Zeiss Axiotech 200 MAT microscope and the film was illuminated by a halogen white light bulb (HAL 100, Zeiss). The output of the microscope was filtered using narrow bandpass filters (FL 488-1, FL 514.5-1, FL 532-1, FL 632.8-1, Thorlabs) in a filter wheel (FW102C, Thorlabs) controlled by the desktop computer to aid with interferometric measurements of the film height. Since the light had been filtered to be effectively monochromatic, a grayscale camera (acA2500-14gm, Basler) was attached to the filter wheel to observe and record the film deformations dynamically on the computer. During the experimental runs, images were taken at time intervals of 15 seconds to allow time for the filter to rotate. This meant that a time series for each filter was taken with intervals between images of one minute.

5.3 Finite Element Simulations of Experimental Setup Temperature

With the set of thermal measurements and controls described above, the experimental ΔT was quite stable during the experimental runs. However, it was not possible to measure the temperature difference across the gap directly due to its small size (on the order of microns). Consequently, finite element simulations in COMSOL [28] were used to calculate the temperature of the experimental setup using the heat equation. Due to the vanishingly small product of the Prandtl and Reynolds number in nanofilm experiments [10], the temporal dependence of the heat equation can be ignored and we solved only Poisson's equation for the steady state temperature within each domain.

$$\boldsymbol{\nabla} \cdot (k_i \boldsymbol{\nabla} \mathrm{T}_i) = \dot{Q}_i, \tag{5.1}$$

where k_i is the thermal conductivity of the ith domain, T_i is the temperature, and $\dot{Q}_i$ is the contribution from any volumetric heat sources. Note that the symbol k has been used twice but it should be clear from the context whether thermal conductivity or wavevector is being indicated. In the absence of externally imposed boundary conditions both the temperature and thermal flux must be continuous at the interior interfaces between domains. If $\partial\Omega_{i,i+1}$ denotes the interface between the i and $i+1$ domains, then the simulations satisfy the following equations on $\partial\Omega_{i,i+1}$ for every i

$$\mathrm{T}_i = \mathrm{T}_{i+1}, \tag{5.2}$$

$$-k_i \boldsymbol{\nabla} \mathrm{T}_i = -k_{i+1} \boldsymbol{\nabla} \mathrm{T}_{i+1}. \tag{5.3}$$

Fig. 5.2(a) shows a diagram of the computational domain used for this study and the boundary conditions that were used. The layers are the same as Fig. 5.1, although we have not included layers below the alumina heater holder due to the large amount of thermal insulation nor the imaging components (the microscope objective, filter wheel, and camera) since they were not physically connected to any components which were actively heated or cooled. The thermal insulation beneath the aluminum heater holder was modeled by a thermally insulating boundary condition which is denoted by the black crosses in the figure. Note that the region between the glass coverslip and the sapphire window was continuously aspirated and so we assumed that there was no thermal conduction through this region. Therefore, the top of the sapphire, the inner portion of the aluminum chiller and the bottom of the glass coverslip were exterior boundaries which had a boundary condition of thermal insulation so that no flux passed normal to them. The simulation domain was chosen to be cylindrically symmetric. However, most of the experimental objects were

rectangular and so all rectangular objects were converted to cylinders with the same height. The radius of each cylinder was then chosen to preserve the total volume of the original experimental object. For a full listing of the simulation object sizes, see Table 5.1. The only domain which had volumetric heating (nonzero $\dot{Q}_i$) was the alumina ceramic heater and the value of the volumetric heating was set equal to the experimentally measured power supplied to the heater after the temperature setpoint was reached. The only other condition that was imposed on the interior of the domain was that the vertical wall of the chiller was set to be isothermal to the temperature measured experimentally by the RTD positioned there. In Fig. 5.2(a) this is denoted by the blue slanted lines. For the exterior boundaries, the vertical boundary at $r = 0$ had a no flux condition due to the cylindrical symmetry which is denoted by black crosses in Fig. 5.2(a). The bottom of the aluminum heater holder and the connected vertical edge directly beneath the edge of the holder also had a no flux condition. This was used because of the large amount of thermal insulation present beneath the holder. This insulation would be difficult to accurately model computationally and prevented most of the heat from traveling through the supporting materials, so it was assumed for this model that no thermal flux is lost to the plates supporting the heater holder. The remaining external boundaries represent the bounding cardboard box and were set equal to the ambient temperature of 23 °C.

At this point, we have a completely defined temperature simulation but have not incorporated the temperature measured by the RTD above the alumina ceramic heater which was used as the feedback setpoint. This additional value allowed us to calculate the thickness of the thermal paste layer which was not well characterized. The amount of thermal paste which provided thermal contact between the silicon wafer and the aluminum heater holder was not measured and varied somewhat between experimental runs. Additionally, the exact distribution could not be measured because the thermal paste shifted as the wafer and nanofilm were brought into contact with the SU-8 spacers on the sapphire window. The thermal paste also showed a change in viscosity as the temperature of the heater increased which led to further settling during the initial times before equilibrium. While we could not measure the thickness of this layer, we did quantify the lateral extent by measuring the residual thermal paste left on the silicon wafer after removal. Since there is only one unknown parameter left in the simulation (the thermal paste thickness) and we have one more experimentally measured value (T_{heater}), we varied the thickness until the temperature at the center of the aluminum holder directly above the ceramic heater agreed with the experimentally measured value there to within 0.01 °C.

Once the thickness of the thermal paste was determined, the simulated temperature profile in the experimental setup was calculated and the temperature difference across the nanofilm/air gap, ΔT, was computed. A sample temperature profile (to scale) from experiment run #18 is shown in Fig. 5.2(b). An important distinction between this chapter and the previous experimental comparisons to theory is the difference between the temperature drop across the nanofilm/air gap, ΔT, and the difference between the heater and chiller setpoints, $\Delta T_{out} = T_{Heater} - T_{Chiller}$. In particular, work by Schäffer [4–6, 15] used ΔT_{out} when comparing their experimentally measured wavelengths to the AP model. As Fig. 5.2(c) shows, ΔT_{out} is much larger than ΔT for these experimental runs. This crucial difference stems from the fact that the nanofilm and air layers are so much smaller than the rest of the components in the setup. This means that even though the thermal conductivities of the other components in the experimental setup are much higher than the polymer and air thermal conductivities (see Table 5.1 for a full listing of thermal conductivities), the vastly larger size of these components leads to sizable temperature drops. These external temperature drops are not incorporated into the theoretical models, so it is vitally important to use ΔT and not ΔT_{out} when comparing experimentally measured wavelengths to the predictions of linear stability analysis.

Figure 5.2: Diagram of the computational domain for the temperature simulations of the redesigned experimental setup

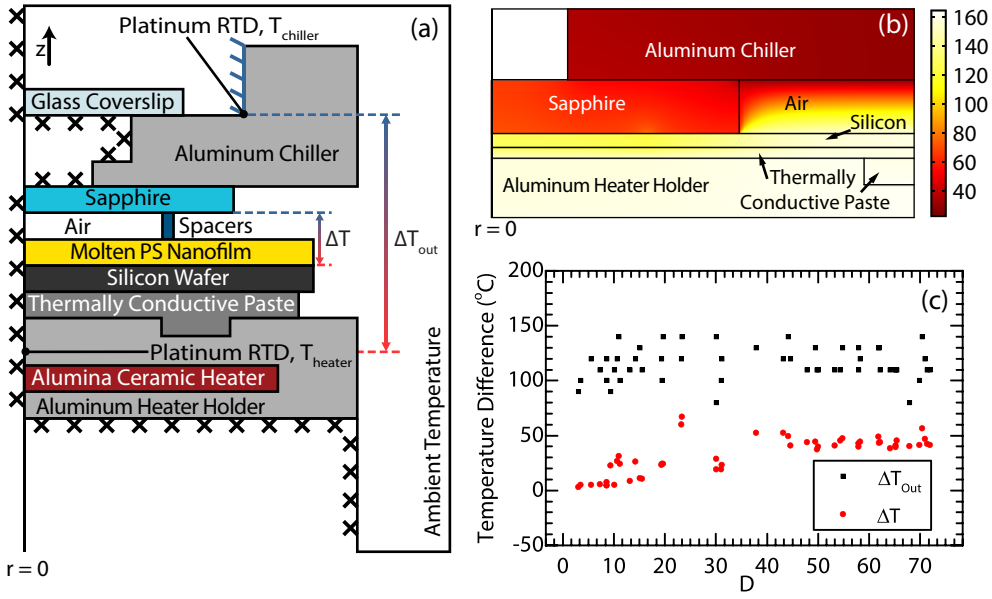

(a) Cylindrically symmetric simulation geometries for computation of the temperature profile within the experimental setup (not drawn to scale). For a complete listing of the sizes and positions of the the components, see Table 5.1. Due to cylindrical symmetry there is no radial thermal flux along the axis of symmetry at $r = 0$, and no thermal flux boundary conditions are denoted by black crosses. The inner vertical edge of the aluminum chiller is treated as an isothermal boundary condition and this is denoted by (blue) slanted lines. The heating is treated as a volumetric source in the alumina ceramic heater whose total power equals the measured electrical power dissipated by the heater. All the remaining exterior boundaries were isothermal boundary conditions set to the measured ambient temperature. (b) Numerical temperature profile of the experimental setup (to scale) as computed with COMSOL from experiment run #18. The nanofilm and spacers are too small to be seen in this figure so they are not labeled. (c) The temperature difference across the nanofilm/air bilayer, ΔT and the temperature difference between setpoints, ΔT_{out} as a function of the normalized separation distance, D, for all the experimental runs.

Table 5.1: Sizes and thermal conductivities for each domain in the numerical simulations of temperature within the experimental setup

Feature	**Inner Radius** (mm)	**Outer Radius** (mm)	**Thickness** (mm)	**Thermal Conductivity** (W/m-°C)
Aluminum chiller	0	57.3	25.4	200 (23.9 – 25 °C) [48]
Aluminum chiller cutout - Large	0	28.7	19.1	0.0257 – 0.0454 (20 – 300 °C) [28]
Aluminum chiller cutout - Medium	0	2.43	4.83	
Aluminum chiller cutout - Small	0	1.47	1.52	
Glass coverslip	0	14.3	0.150	1.09 (23 °C) [29]
Sapphire window	0	4.76	1.02	29.9 (69 °C) [31]
Air gap	0	2.88	d_o - h_o	0.0257 – 0.0454 (20 – 300 °C [28]
SU-8 spacers	2.88	3.13	d_o - h_o	0.300 [32]
PS film	0	25.4	h_o	0.130 (100 °C) [22]
Silicon wafer	0	25.4	0.279	93.9 (127 °C) [33]
Aremco Heataway 638 paste layer	0	r_{paste}	h_{paste}	2.23 [49]
Aremco Heataway 638 paste inset	7.16	14.3	0.508	
Aluminum heater holder	0	43.0	10.2	200 (23.9 – 25 °C) [48]
Alumina ceramic heater	0	14.3	1.10	20.0 (20 °C) [50]

The thermal conductivity of each domain is listed with the temperature found in the literature at which that value was measured. If no temperature is listed, then a temperature for the thermal conductivity measurement could not be found. All thermal conductivities were taken as constant, with the exception of the air domains where a COMSOL built-in material was used which had a temperature dependent thermal conductivity. The values of d_o, h_o, r_{paste}, and h_{paste} for each experimental run can be found in Table 5.5. The thermal paste domain comprises two parts. One part is paste which filled an inset into the aluminum heater holder. This inset was completely filled for every experimental run and was held constant for every simulation. On top of this inset thermal paste was added to form an additional layer which covered the center of the aluminum heater holder. Because the precise amount and distribution of the thermal paste layer was not known, this value was varied so that the temperature at the location of the RTD above the heater matched the value measured in the experimental run (T_{Heater}). The total size of the domain was 192 mm in radius and 254 mm in height. The domain was offset so that the top of the computational domain was 80 mm above the bottom of the aluminum chiller as this was the location of the bounding cardboard box. Note that the domain did not extend into the region directly beneath the aluminum heater holder nor into the region between the glass coverslip and the sapphire window as represented in Fig. 5.2(a). The point which represented the platinum RTD location was set to be on the axis of symmetry at $r = 0$ and 2.54 mm below the top of the aluminum heater holder.

During the finite element simulations, the nanofilm interface is treated as flat and static. Since the models are derived within the context of linear stability the perturbations to the film interface are infinitesimal and as long as measurements of the wavelength are made at early times the interface should be very close to flat. Furthermore, as was mentioned above, the interface can be treated as static in the heat equation due to the vanishingly small product of the Prandtl and Reynolds number. However, during instability growth the interface does deform in time and so the temperature drop across the system should decrease as the instability grows because the overall thermal conductivity of the air/nanofilm bilayer increases as protrusions grow. This increase in thermal conductivity leads to increased thermal flux through the system which is what causes the increased temperature drop. To confirm quantitatively that the temperature drop across the bilayer when the film is flat is very nearly equal to the temperature drop across the bilayer when the film is strongly perturbed, as it would be at late times, we performed additional numerical simulations. Fig. 5.3(a) shows a portion of the computational domain from Fig. 5.2(a) focusing solely on the air/nanofilm bilayer. Correspondingly, Fig. 5.3(b) shows the analogous bilayer interface with a sinusoidal perturbation which represents the film at late times after the protrusions have grown significantly. In the perturbed interface simulations, the rest of the geometry was identical to the simulations presented above. The value of the sinusoidal perturbation was equal to 0.9 h_o for each simulation and the wavelength was set to 50 microns. The sinusoid was chosen so that the maximum occurred at $r = 0$, as depicted in Fig. 5.3(b). The temperature drop in each of these two cases was computed by taking the difference between the value at the nanofilm/silicon interface and the value at the air/sapphire interface, evaluated at $r = 0$. With the perturbed interface, the temperature drop across the bilayer, ΔT_{sin}, is slightly smaller than the temperature drop across the flat interface, ΔT, as seen by the positive values in Fig. 5.3(c). In this figure, the differences in the temperature drops are plotted as a function of $h_o/d_o = D^{-1}$ which represents how much of the gap is filled by the nanofilm. When the nanofilm composes a larger portion of the gap, the perturbation has a stronger effect and so the difference in temperature drops is larger. However, even at the maximum value, the difference between the two techniques is less than 0.2 °C and so we were justified in using a flat interface for the temperature simulations to compute ΔT. Note that these simulations used the experimental parameters for each of the runs listed in Table 5.5. As such, there were multiple runs with the same value of h_o/d_o, but with different heater and chiller setpoints, which led to the observed scatter in Fig. 5.3(c).

Figure 5.3: Effect of a sinusoidal deformation to the molten nanofilm on the temperature simulations of the experimental setup

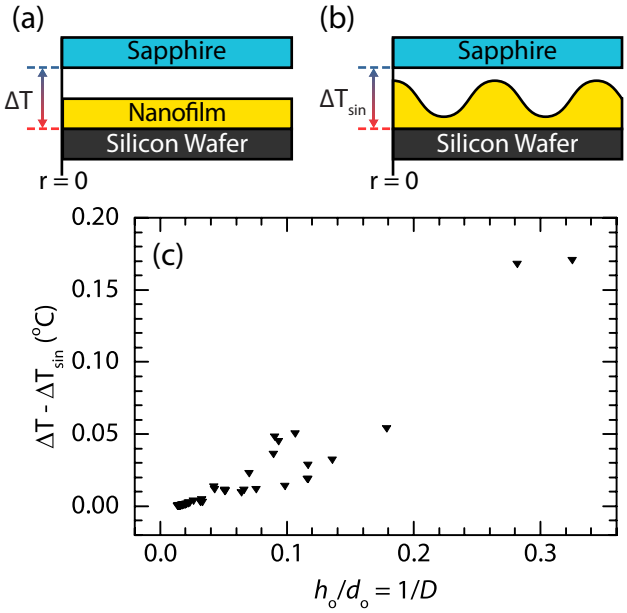

(a) Portion of the cylindrically symmetric simulation geometry from Fig. 5.2(a). (b) Analogous portion of the geometry showing a sinusoidal deformation to the nanofilm/air interface. The simulation geometry except for the deformation to the interface is identical to Fig. 5.2(a). (c) Difference between the computed temperature drop across the bilayer with a flat interface and the temperature drop across the bilayer with a sinusoidally deformed interface plotted as a function of h_o/d_o for each of the experimental runs listed in Table 5.5.

5.4 Image Analysis Process for the Extraction of the Wavelength and Growth Rate of the Fastest Growing Mode

The image analysis process was the defining feature of these experiments because this process yielded the characteristic wavelength, λ_o, and the growth rate, b_o, of the fastest growing mode of the instability. As mentioned above, the functional dependencies of these quantities differentiate the three proposed models and allow us to identify the dominant physical mechanism. As such, we have expanded upon the techniques used in previous instability studies of this system [1, 39] to measure λ_o and b_o. For the wavelength analysis we followed the general approach of previous studies. First, a defect free region was selected for analysis. Then, the 2D discrete Fourier transform of the image was computed. This was then converted to a power spectral density and averaged azimuthally to find the power spectral density as a function of wavevector, k. Then, the peak was determined to find the wavevector of the fastest growing mode which was then converted back to a real space wavelength. The key difference in this chapter was the choice of the fitting function to extract

the peak of the power spectral density. We derived a fitting function, presented below, that incorporated the physics of the hydrodynamic instability that allowed us to extract both the wavelength and the growth rate of the instability from the power spectral density simultaneously. Before detailing the fitting procedure, we will derive the new fitting function and highlight some of its features.

The fitting function used in this chapter to identify the peak of the power spectral density is markedly different than what was used in Ch. 3 or Ref. [1] . Traditionally, the fitting functions have been approximated as either Lorentzian or Gaussian peaks as is typically done in vibrational spectroscopy [51, 52]. However, in vibrational spectroscopy, the use of these peak functions is physically motivated and knowing the source of the signal is integral to the fitting process. For example, the Lorentzian lineshape function arises from the interaction of a driven oscillator with its environment while the Gaussian lineshape function occurs due to instrumental effects or Doppler broadening. To date, the use of these types of functions in the study of hydrodynamic instabilities has been an arbitrary ansatz and so we derived a fitting function based on the physical signal in this system. The details of this derivation will now be presented.

In this system, the intensity of the light reflected from the film was measured by the camera. By treating the polymer layer as an asymmetric Fabry-Pérot etalon, it can be shown that changes in the height of the polymer are linearly proportional to changes of the reflected intensity in the limit of small deformations. From Ref. [53], the reflected fraction of the incident intensity is

$$I_R = \frac{C_1 + C_2 \sin^2(C_4 l)}{C_3 + C_2 \sin^2(C_4 l)}, \tag{5.4}$$

where l is the length of the cavity, and C_1, C_2, C_3, and C_4 are constants which depend on the properties of the etalon, such as the refractive index, optical wavelength, and the reflectivities. Since we are only interested in the proportionality of a change in the cavity length from l to $l + \Delta l$, we can ignore the more complicated forms of these constants. We then take the difference

$$I_R(l + \Delta l) - I_R(l) = \frac{C_1 + C_2 \sin^2(C_4 l + C_4 \Delta l)}{C_3 + C_2 \sin^2(C_4 l + C_4 \Delta l)} - \frac{C_1 + C_2 \sin^2(C_4 l)}{C_3 + C_2 \sin^2(C_4 l)}. \tag{5.5}$$

After simplification, application of trigonometric identities, and a Taylor expansion in the cavity length change, Δl, we see that

$$I_R(l + \Delta l) - I_R(l) = \frac{(C_3 - C_1) \sin(2C_4 l) C_2 C_4 \Delta l}{C_3^2 + 2C_2 C_3 \sin^2(C_4 l) + C_2^2 \sin^4(C_4 l)} \propto \Delta l. \tag{5.6}$$

Thus our measured signal, I, can be expressed as the change of the film height from the initially undisturbed film height

$$I\left(\vec{x},t\right) \propto h\left(\vec{x},t\right) - h_o. \tag{5.7}$$

We used a Fourier series to express the position of the film interface as a function of both time and space so that

$$h(\vec{x},t) = h_o + \sum_{k'} \delta h_{k'} e^{i\vec{k'}\cdot\vec{x}} e^{b_{k'}t}. \tag{5.8}$$

In this expression, $\vec{k'}$ is a wavevector, $\delta h_{k'}$ are the Fourier coefficients that describe the configuration of the interface, and $b_{k'}$ is the (real) growth rate associated with the wavevector $\vec{k'}$. Substituting Eq. (5.8) into Eq. (5.7) yields

$$I\left(\vec{x},t\right) \propto \sum_{k'} \delta h_{k'} e^{i\vec{k'}\cdot\vec{x}} e^{b_{k'}t}. \tag{5.9}$$

We took the Fourier transform of the intensity

$$\tilde{I}\left(\vec{k},t\right) \propto \sum_{k'} \delta h_{k'} e^{b_{k'}t} \int_{-\infty}^{\infty} e^{i\vec{k'}\cdot\vec{x}} e^{-i\vec{k}\cdot\vec{x}} dx = \sum_{k} \delta h_k e^{b_k t}. \tag{5.10}$$

In the limit of a system which is infinite in lateral extent, the wavevectors will be infinitesimally close together and this sum becomes a continuous function of k

$$\tilde{I}\left(\vec{k},t\right) \propto e^{b(k)t}, \tag{5.11}$$

where $b\left(k\right)$ is the full dispersion relation derived from linear stability analysis. Then the power spectral density, $S\left(\vec{k},t\right)$, will be

$$S\left(\vec{k},t\right) \propto \left|\tilde{I}\left(\vec{k},t\right)\right|^2 = e^{2b(k)t}. \tag{5.12}$$

While the specific form of the dispersion relation varies depending on the model chosen to describe the instability, this sort of fitting function should fit the power spectral density of any hydrodynamic instability provided that the appropriate dispersion relation is inserted into Eq. (5.12). In the case of the present instability there is a common thread that unites all three proposed mechanisms and allows us

to define a generic fitting function that was used to find the wavelength and growth rate. Specifically, all the models have dispersion relations of the form

$$b(k) = C_1 k^2 - C_2 k^4, \tag{5.13}$$

where C_1 and C_2 are constants that depend on the specific model. However, the location of the maximum growth rate, k_o, is always

$$k_o = \sqrt{\frac{C_1}{2C_2}}. \tag{5.14}$$

Substituting k_o back into Eq. (5.13) yields the maximum growth rate, b_o,

$$b_o = b(k_o) = \frac{C_1^2}{4C_2}. \tag{5.15}$$

If we now factor this out of Eq. (5.13) then

$$b(k) = b_o \left(\frac{k}{k_o}\right)^2 \left[2 - \left(\frac{k}{k_o}\right)^2\right]. \tag{5.16}$$

Inspired by these results, we will fit the peak in the power spectral density with a function of the form

$$\mathcal{F}(k,t) = A \exp\left(2b_o t \left(\frac{k}{k_o}\right)^2 \left[2 - \left(\frac{k}{k_o}\right)^2\right]\right). \tag{5.17}$$

In this expression, there are three fitting parameters which were varied to achieve good fits to the peak of the power spectral density. k_o was a fitting parameter which describes the location of the peak and can be converted back to the real space characteristic wavelength using $\lambda_o = 2\pi/k_o$. b_o was a fitting parameter which describes the width of the peak and is equal to the growth rate at the time t. A was the fitting parameter which describes the amplitude of the peak.

There are several interesting things to note about this fitting function when comparing it to the traditional Gaussian or Lorentzian peaks. First, Eq. (5.17) is not symmetric about the peak ($k = k_o$). This follows from the fact that the dispersion relation is not symmetric about its maximum value. To illustrate this point, Fig. 5.4(a) shows the dispersion relation from Eq. (5.16). Returning to the full fitting function in Eq. (5.17), we denote the half maximum points of the peak by k_- and k_+ and they have the forms

$$k_- = k_o \sqrt{1 - \sqrt{\frac{\ln 2}{2b_o t}}}, \tag{5.18}$$

$$k_+ = k_o\sqrt{1+\sqrt{\frac{\ln 2}{2b_o t}}}. \tag{5.19}$$

Additionally, there is a temporal dependence to Eq. (5.17) and the peak gets taller and sharper in time, as Fig. 5.4(b) shows. In Fig. 5.4(b), we have set $A = 1$ for visualization purposes. Notice that there are two points where $b = 0$ (at $k/k_o = 0$ and $k_c/k_o = \sqrt{2}$) and those points do not move in time, regardless of the shape of the rest of the curve. We also compared this fitting function to the Gaussian and Lorentzian peak shapes in Fig. 5.4(c). The $t = 1.00/b_o$ curve from Fig. 5.4(b) was normalized by its maximum value and a nonlinear least squares fit was performed in OriginPro 2015[54] with Gaussian and Lorentzian functions of the forms

$$\mathcal{G}(k) = \frac{A_g}{w_g\sqrt{\pi/2}}\exp\left[-2\left(\frac{k-k_g}{w_g}\right)^2\right] + C_g, \tag{5.20}$$

$$\mathcal{L}(k) = \frac{2A_l}{\pi}\frac{w_l}{4(k-k_l)^2 + w_l^2} + C_l. \tag{5.21}$$

A full listing of the fitted parameters can be found in the caption of Fig. 5.4. The Gaussian and Lorentzian curves generally fit the peak moderately well, but the location of the peak is 5% smaller than the actual peak and this discrepancy highlights the need for a fitting function that accurately captures the physics of the underlying process.

With this new analysis tool opening a wider range of possibilities, we turned to the image analysis and fitting process. To begin, a region free of dust in the film or surface inhomogeneities was selected from the time series of experimental images. Previously, it had been shown that the presence of defects in the film can shift the location of the peak in the power spectrum, particularly at early times [39]. The size of the region selected for each experimental run can be found in Table 5.6. Next, the time series from a single filter wavelength was selected. Depending on the initial film thickness, h_o, and the total gap thickness, d_o, the features showed differing levels of contrast for different filters and in some cases showed a large degree of saturation. As such, the time series which showed the largest contrast was selected for further analysis and the choice for every experimental run is listed in Table 5.6.

Since the predictions for λ_o and b_o presented in Eqs. (5.23) to (5.28) were based upon the assumption of an infinitesimal perturbation, it is important that the images

Figure 5.4: Plots of the derived peak fitting function and comparison to Gaussian and Lorentzian peaks

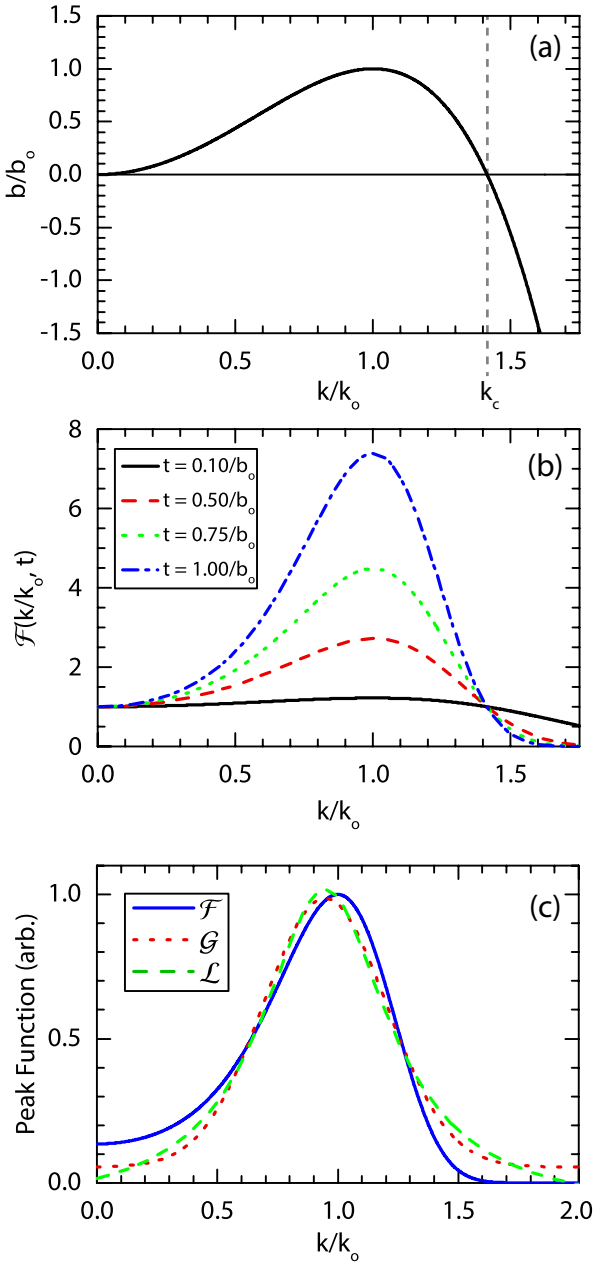

(a) Plot of the normalized dispersion relation, b/b_o, as a function of normalized wavevector, k/k_o. (b) Plot of Eq. (5.17) as a function of normalized wavevector at several different times. (c) Plot of Eq. (5.17) at $t = 1.00/b_o$ normalized to unity and fit by Gaussian, $\mathcal{G}$, and Lorentzian, $\mathcal{L}$, peaks. The Gaussian peak is the (red) dotted line and the Lorentzian peak is the (green) dashed line. The equations for these peaks are found in Eqs. (5.20) and (5.21), respectively. The parameters for the Gaussian fit were A_g = 0.596, w_g = 0.510, k_g = 0.947, and C_g = 0.0549. The parameters for the Lorentzian fit were A_l = 1.14, w_l = 0.646, k_l = 0.947, and C_l = -0.102.

are analyzed at the earliest possible times. A previous instability wavelength study [39] had used a background subtraction technique where an early time image which did not show any signs of instability was subtracted from all the later images in the time series to highlight the instability and remove any static background features. While the background subtraction technique worked well in that instance, it proved ineffectual for the present analysis for two reasons. The first reason was the presence of large scale interference fringes that slowly moved in the longer experimental runs. This study examined a larger area than had previously been accessible due to improved film preparation procedures and a better experimental setup. This meant that there were more fringes in the image for a given level of parallelism as compared to previous work. These fringes were much larger than the characteristic spacing of the instability, but still form an unwanted background signal in the power spectral density. Additionally, a much larger section of parameter space was examined and in certain regions the instability took a long time to develop, with some runs in excess of 8 hours. With these long evolution times the setup could settle and equilibrate over a long time, leading to slight shifts in the parallelism. Table 5.6 lists the total time elapsed in each experimental run, t_{final}. In most cases t_{final} coincided with the end of the experimental run, particularly for the longer runs. However, there were experimental runs where t_{final} occurred before the end of heating due to large amplitude peak growth which created interference fringes within the peaks themselves. These small scale interference fringes posed difficulties when computing the power spectral density because they added an extra peak at k values slightly larger than k_o. Moreover, if the peak growth was large enough to have interference fringes (> 100 nm) then we should have identified the instability wavelength earlier in the time series to more closely match the predictions of linear stability analysis and fulfill the assumption of an early time measurement. The second and more important issue is that the growth rate measurements are extracted from Eq. (5.17) based on the width of the peak. As a result, any image processing technique which changes the width of the peak will effect the measured growth rate. This caused us to eschew traditional techniques such as thresholding or the top-hat transform and perform computations directly on the raw image.

For each image in the time series of each experimental run, the mean of the image was subtracted to suppress the constant term in the Fourier spectrum. After subtraction of the mean, the two-dimensional discrete Fourier transform of the image was computed using MATLAB [25]. The absolute magnitude of this result was squared to find the power spectral density. We found that a major source of background came from

low frequency components in the vertical and horizontal directions which generally stemmed from nonuniform illumination or very large scale interference fringes. These manifested themselves as a large cross in the 2D power spectral density which caused extra background during the azimuthal average. To reduce this contribution, the values at both $k_x = 0$ and $k_y = 0$ were selected and these values were excluded from the azimuthal average. The remaining values were then averaged azimuthally to produce the power spectral density as a function of wavevector, $k = |\vec{k}|$. Because the images were not processed before the Fourier transform was computed, they showed a fair amount of noise with a large peak at small wavevectors. The peak was easily distinguishable near t_{final}, and so we defined a hard bandpass filter and only selected wavevectors between $k_{\max}$ and $k_{\min}$. The value of $k_{\max}$ was kept constant for every experimental run at $k_{\max} = 0.628\ 1/\mu\text{m}$ and simply served to remove any high frequency pixel noise from the camera. The value of $k_{\min}$ was chosen to be lower than the edge of the peak at t_{final} so that no part of the peak was removed. This was critical to the fitting process because the routines could not accurately fit parameters which were different by many orders of magnitude. To allow automation of the fitting process between all experimental runs, the power spectral densities derived from the time series of processed experimental images were normalized to the maximum value of the power spectral density at t_{final} for that experimental run. The image at t_{final} had the power spectral density with the largest magnitude for a given run because the instability was most well developed at that point. The end result of this step is a normalized plot of the power spectral density as a function of k for each image in the time series which were fit to find the peak wavevector. The fitting procedure fit the peak and the background simultaneously and the background was assumed to be Gaussian in nature and centered at $k = 0$. This assumption is that the very long wavelength interference fringes make up the majority of the background and that they were broadened by the pixelation and noise from the camera. As such, the complete fitting function had the form

$$W(k) \equiv \mathcal{G}(k)+\mathcal{F}(k) = A_g \exp\left[-C_g k^2\right]+A \exp\left(2b_o t\left(\frac{k}{k_o}\right)^2\left[2-\left(\frac{k}{k_o}\right)^2\right]\right). \quad (5.22)$$

In a manner similar to our previous work [39], the image analysis procedure started by fitting the power spectral density at t_{final} and then using those fitting parameters to fit the power spectral density of the image immediately proceeding t_{final}. This procedure continued iteratively for all images in the time series working backwards in time towards the first image in the time series. The initial fit at t_{final} was the

most difficult to converge and was quite sensitive to the initial values of the fitting parameters. Because the process was automated, we imposed a set of requirements to ensure that a converged fit was not spurious and that a valid peak truly existed. Specifically, we required that:

- The standard error on the fitted parameters k_o and b_o was not larger than the parameters themselves.
- The system had reached its steady state temperature: $t > 5$ min.
- Peak half maximum points must be within the bandpass filter bounds: $k_+ < k_{\max}$ and $k_- > k_{\min}$.
- Peak full width at half maximum $(k_+ - k_-)$ must be greater than the distance between consecutive wavevector points.
- At k_o, the peak must be greater than or equal to the background Gaussian: $\mathcal{F}(k_o) \geq \mathcal{G}(k_o)$
- At $k_\pm$, the peak must be greater than or equal to one half the background Gaussian: $\mathcal{F}(k_\pm) \geq \frac{1}{2}\mathcal{G}(k_\pm)$
- The whole fitting function must not be greater than 10 times the maximum of the peak anywhere: $\max[W(k)] < 10\mathcal{F}(k_o)$

These conditions serve to remove fits which numerically converged but were not physical, such as a very tall and narrow peak which was smaller than the distance between points. They also removed fits where the width of the peak is not well determined such as when the half maximum points are outside the fitted range of the bandpass filter. Once this process was completed for every image in a given experimental run, the reported values for k_o and b_o were taken as the earliest time at which a valid fit occurred.

To demonstrate this process on actual experimental data, Fig. 5.5 shows the application of this algorithm to experiment #18. For this experiment, the pictures taken with the 488 nm filter showed the largest contrast, so these were selected for the wavelength and growth rate extraction process and three pictures from the time series are shown in Fig. 5.5(a). Directly beneath each image from Fig. 5.5(a) the natural log of the 2D power spectral density is plotted. The natural log was taken to enhance the contrast of the dark ring, which is the signal of the instability. The

Table 5.2: Fitting constants for the curves shown in Fig. 5.5(c)

Time (min)	$A_g \times 10^{-2}$	$C_g(\mu\text{m}^2)$	$A \times 10^{-5}$	$b_o \times 10^{-3}$(1/min)	$k_o(\text{rad}/\mu\text{m})$
12	4.34	327	49.7	1.56	0.138
16	0.399	32.0	0.619	4.03	0.134
20	0.656	26.9	1.42	3.45	0.133
24	1.37	24.0	1.69	3.28	0.132
29	4.48	22.3	1.31	3.21	0.132

radius of the ring is related to the wavevector and the width of the ring is related to the growth rate. The vertical and horizontal white lines in each image of Fig. 5.5(b) are the regions which were removed to reduce the background due to nonuniform illumination effects. These clearly do not strongly effect the azimuthal average as the ring is visible in all three images and shows rotational symmetry. In contrast to Fig. 3.2(c) where incipient hexagonal order is evident, the images in Fig. 5.5(b) show an azimuthally symmetric ring. That fact that there is no superposed pattern on the ring suggests that these analysis images are from early times before the onset of nonlinear interaction between modes. Next, the 2D plots from Fig. 5.5(b) were azimuthally averaged to produce the curves in Fig. 5.5(c) where the power spectral density is plotted as a function of the magnitude of the wavevector, k. All the curves have been normalized by the maximum value of the power spectral density at t_{final}, which was 29 minutes for this experiment. As was expected, the amplitude of the peak increases as the instability grows in time. The parameters for the curve fits can be found in Table 5.2. Finally, the location of the peak was plotted as a function of time in Fig. 5.5(d). The vertical bars are not error bars, but instead denote the full width at half maximum of the peak as computed from k_- and k_+ in Eqs. (5.18) and (5.19), respectively.

One question that has persisted through earlier work [1, 39] is whether the wavevector (or equivalently, the wavelength) changes systematically as a function of time. At very late times, coarsening is expected to occur and will cause the characteristic wavelength to increase over time. However, within the confines of linear stability there is no expectation of time dependent behavior because the perturbation is assumed to be infinitesimal. Within the context of this chapter, we looked at the

Figure 5.5: Illustration of the image analysis process using the derived fitting function

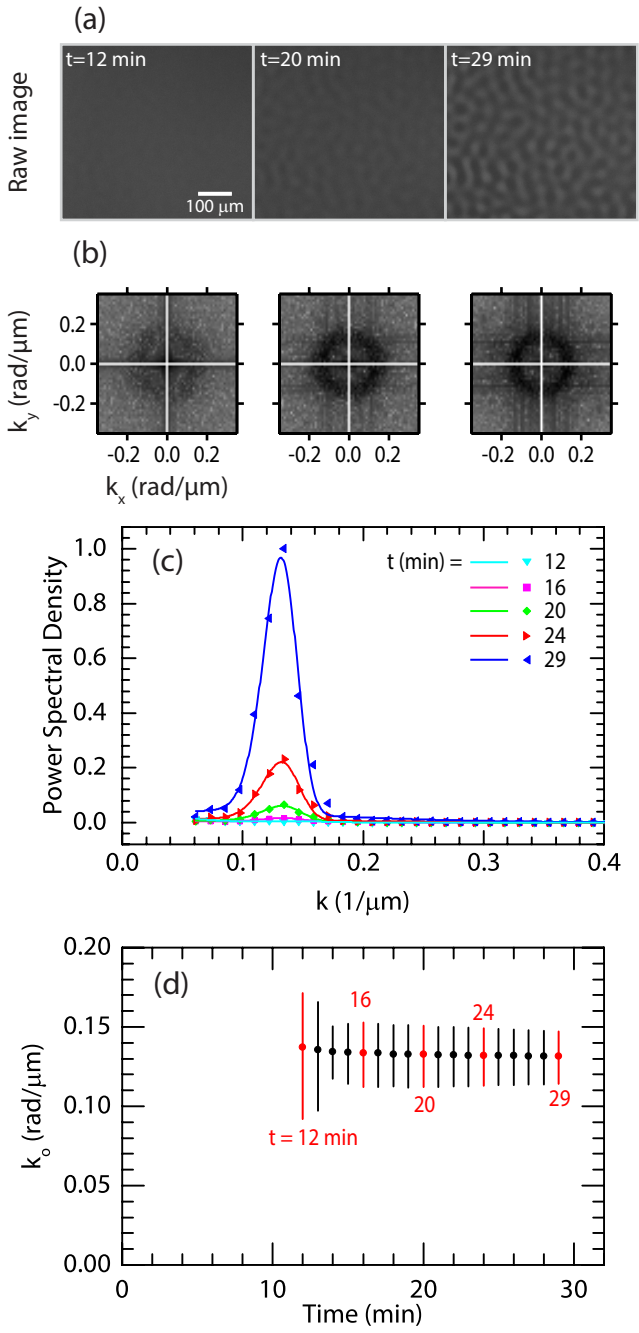

(a) Raw images from experiment #18 taken under 488 nm illumination. (b) Natural log of the 2D power spectral density of the corresponding raw images from (a). The white lines are the regions which were removed to reduce background. (c) Azimuthally averaged power spectral density as a function of wavevector, k (points) and the corresponding fits (solid lines). A full listing of the fit parameters can be found in Table 5.2. (d) Peak location, k_o, as a function of time for experiment #18. The vertical bars represent the full width at half maximum of the peak, as defined by k_- and k_+ in Eqs. (5.18) and (5.19), respectively.

Figure 5.6: Normalized wavevector plotted as a function of time for every experimental run

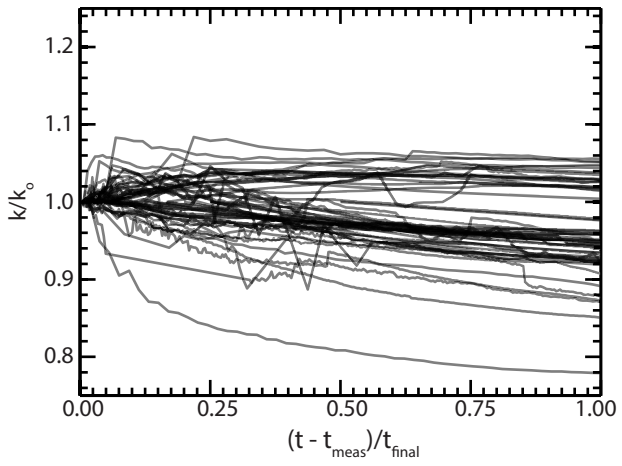

Normalized wavectors as a function of normalized time for every experimental run. The wavevectors were normalized by the first measured peak location, k_o. The times were shifted by subtracting the initial measurement time, t_{meas}, and then normalized by the final time, t_{final}. Each curve is semitransparent and so the darker regions are areas where multiple curves overlap.

temporal dependence of the wavevector for every experiment to see if there was a discernible trend. To do this, the wavector data as a function of time which was plotted in Fig. 5.5(d) was aggregated for all the experimental runs and then normalized. To promote comparison between experiments which could span very different length and time scales, the wavevectors were normalized by the initially measured value, k_o and the times were shifted by the time of the initial wavelength measurement, t_{meas}, so that they all started at the same point. Then each time series was scaled by the final time, t_{final}, so that the curves spanned the same range. The resulting curves were plotted in Fig. 5.6. Generally, there seems to be little systematic shift, as the mean of the normalized wavector at a t_{final} is 0.961, very close to the value of 1 which would be expected if the results were evenly distributed about the initial value. Furthermore, the curves do not show large slopes, particularly at late times. This suggests that the measured wavevectors are relatively constant to within an uncertainty of approximately ± 10%.

5.5 Comparison of Experimental Results to Proposed Mechanisms

With the wavelengths and growth rates computed for all the experimental runs, the experimental data was then compared to the theoretical predictions detailed in Ch. 2. Three models have been proposed to describe this instability [2–6, 8, 10, 15], and each model hypothesized a different destabilizing mechanism to overcome the

Figure 5.7: Diagram of the instability geometry

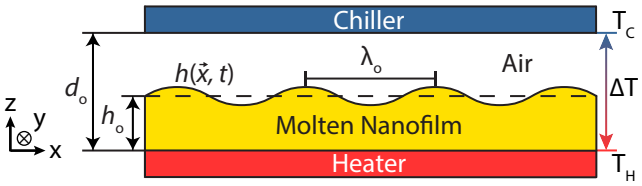

Diagram of the instability geometry (not to scale). In the literature [1–6, 15], the initial film thickness, h_o ranges from 50 to 390 nm; the total gap width, d_o ranges from 100 to 2360 nm; the measured characteristic wavelength, λ_o, ranges from 1.0 to 58 μm; and the temperature drop, ΔT, ranges from 11 to 46 °C.

stabilizing pressure due to surface tension. In each case, the models derive a thin film interface equation from the Navier-Stokes equations using the long-wavelength approximation. Most importantly for the present analysis, they each put forward a prediction for the experimentally measured wavelength, λ_o, and the corresponding growth rate of that wavelength, b_o, within linear stability analysis. While each of these models has been treated in detail previously, we will summarize them briefly in the following section and then scale them so that it is easier to differentiate them with the experimental data that is presented below. Note that in previous studies [1], the SC model had been effectively eliminated due to its lack of temperature dependence. We concur with this assessment, but still make comparisons to the SC model for completeness and to lend further support to the conclusion that it does not play a dominant role in this system.

5.5.1 Wavelength and Growth Rate from Three Proposed Instability Models

While each of these models has been treated in depth previously, we briefly summarize them and restate their expressions for the wavelength and growth rate. Each proposed model considered a simplified geometry which is shown in Fig. 5.7. The initial film thickness, h_o, is typically on the order of 100 nanometers and the distance from the heated substrate to the cooled plate, d_o, is typically on the order of microns. The temperature difference between the bottom of the nanofilm and the top of the air layer, ΔT, is typically on the order of a few degrees Celsius. The spontaneous deformations of the instability have a characteristic wavelength, λ_o, which is usually on the order of 10 microns and this relatively large value compared to the film thickness justifies the use of the long wavelength approximation.

Surface Charge (SC) Model

The SC model, developed by Chou and Zhuang [2, 3], is based upon a destabilizing electrostatic pressure. They hypothesized that charges at the nanofilm's free interface with the air, $h(\vec{x}, t)$ in Fig. 5.7), induce image charges in the heating and cooling plates. The combined effect of these charges is a destabilizing electrostatic pressure. The characteristic wavelength and growth rate in the SC model are

$$\frac{\lambda_o^{\mathrm{SC}}}{2\pi h_o} = \sqrt{\frac{2\varepsilon_o \varepsilon_p^2 \gamma}{\sigma^2 h_o D^2}} \left(D + \frac{1}{\varepsilon_p} - 1 \right)^{3/2}, \tag{5.23}$$

$$b_o^{\mathrm{SC}} = \frac{\sigma^4 h_o D^4}{12\mu\gamma\varepsilon_o^2\varepsilon_p^4 h_o^3} \left(D + \frac{1}{\varepsilon_p} - 1 \right)^{-6}. \tag{5.24}$$

In these expressions, h_o is the initial film thickness, ε_o is the permittivity of free space, ε_p is the permittivity of the nanofilm, γ is the surface tension of the molten nanofilm, σ is the interfacial charge density, μ is the viscosity of the nanofilm, and $D \equiv d_o/h_o$ is the normalized separation distance. A listing of the range of material and experimental parameters can be found in Table 5.3 for 1.1k M_W polystyrene (PS) which composes the nanofilms used in this study. Within all three of these models, the dependence of the material properties on temperature and electric field was treated as a higher order effect, with the notable exception of the surface tension in the thermocapillary model where it is explicitly included as the driving force. As such, all material properties were evaluated at the temperature of the nanofilm/air interface for each experiment. A full listing of the material properties for every experimental run can be found in Table 5.7.

Acoustic Phonon (AP) Model

Next, Schäffer *et al.* proposed the AP model [4–6, 15]. In this model, acoustic phonon reflections from every interface create a net acoustic pressure which destabilizes the interface and causes protrusions to grow. In the AP model, the characteristic wavelength and growth rate are

$$\frac{\lambda_o^{\mathrm{AP}}}{2\pi h_o} = \sqrt{\frac{\gamma u_p}{Q(1-\kappa)k_a \Delta \mathrm{T}}} \left(D + \kappa - 1 \right), \tag{5.25}$$

$$b_o^{\mathrm{AP}} = \frac{[Q(1-\kappa)k_a \Delta \mathrm{T}]^2}{3\mu\gamma u_p^2 h_o} \left(D + \kappa - 1 \right)^{-4}. \tag{5.26}$$

In addition to the parameters defined after Eqs. (5.23) and (5.24), Q is the acoustic phonon quality factor and is related to how much momentum is reflected by the interfaces, u_p is the speed of sound in the polymer, k_a is the thermal conductivity of air, and κ is the ratio of the thermal conductivities of the air and polymer layers. The values of these parameters and material properties can be found in Table 5.3 and Table 5.7.

Thermocapillary (TC) Model

Several years later, Dietzel and Troian proposed a model based on interfacial thermocapillary stresses [8, 10]. For a single component fluid, the surface tension must decrease as a function of temperature. Protrusions will be slightly cooler than valleys and they will have a correspondingly higher surface tension. The gradient in surface tension along the interface creates a destabilizing shear stress which causes growth. For the TC model, the characteristic wavelength and growth rate have the form

$$\frac{\lambda_o^{\mathrm{TC}}}{2\pi h_o} = \sqrt{\frac{4\gamma}{3\kappa\gamma_{\mathrm{T}}\Delta\mathrm{T}}}\left(\sqrt{D} + \frac{(\kappa-1)}{\sqrt{D}}\right), \tag{5.27}$$

$$b_o^{\mathrm{TC}} = \frac{3\left(\kappa\gamma_{\mathrm{T}}\Delta\mathrm{T}\right)^2}{16\mu\gamma h_o}\left(\sqrt{D} + \frac{(\kappa-1)}{\sqrt{D}}\right)^{-4}, \tag{5.28}$$

where γ_{T} is the thermocapillary coefficient, which is the absolute value of the derivative of the surface tension as a function of temperature. The values of these parameters and material properties can be found in Table 5.3 and Table 5.7.

5.5.2 Summary of Scaled Wavelength and Growth Rate Predictions from Proposed Models

Since each proposed model has a distinct mechanism, they each have different predictions for the functional forms of the wavelength and the growth rate. To investigate these differences systematically, each quantity can be scaled to isolate the dependence of the wavelength and growth rate on a single experimentally controlled parameter. In this chapter, we will focus on the normalized separation distance, $D \equiv d_o/h_o$, and the temperature drop, $\Delta\mathrm{T}$, as the two parameters which will be extensively varied. These parameters have the advantage that they are relatively easy to tune experimentally while keeping the same nanofilm material. This allows us to minimize uncertainties in the material properties while still probing the proposed models. In particular, we define the scaled quantities shown in Table 5.4. With these scaled quantities, the different functional dependencies provide a clean way

Table 5.3: Parameters for the experimental runs and material properties for 1.1k M_W polystyrene

h_o	Initial nanofilm thickness	96 – 352 nm
d_o	Gap width	826 – 7150 nm
D	Normalized separation distance	3.08 – 71.9
ΔT	Temperature drop across bilayer	3.6 – 67.2 °C
ε_o	Permittivity of free space	8.85×10^{-12} F/m
ε_p	Nanofilm relative permittivity	3.5
σ	Interfacial charge density	1 – 3 mC/m^2 [3]
μ	Viscosity	2 – 8030 Pa $\cdot$ s [24]
u_p	Speed of sound in nanofilm	1850 m/s [21]
Q	Acoustic phonon quality factor	6 [4–6, 15]
k_a	Air thermal conductivity	28.9 – 34.5 mW/m-°C [23]
k_p	Nanofilm thermal conductivity	120 – 129 mW/m-°C [22]
κ	Thermal conductivity ratio	0.23 – 0.27
γ	Surface tension	29.3 – 35.8 mN/m [22]
γ_{T}	Thermocapillary coefficient	79 μN/(°C-m) [22]

More details of the experimental parameters for each run can be found in Tables 5.5, 5.6, and 5.7. This table contains all the material parameters necessary to evaluate the wavelength and growth rate predictions for all three models.

to differentiate between the three models. For instance, note that the SC model has no temperature dependence, and so it can be readily distinguished from the other two models by investigating $\Lambda_{\Delta\mathrm{T}}^{\mathrm{SC}}$ and $\beta_{\Delta\mathrm{T}}^{\mathrm{SC}}$. The AP and TC models show a similar temperature dependence in $\Lambda_{\Delta\mathrm{T}}^{\mathrm{AP}}$ and $\Lambda_{\Delta\mathrm{T}}^{\mathrm{TC}}$, but they can be distinguished using the functional dependencies of Λ_D^{AP} and Λ_D^{TC} instead. Using all these expressions will allow us to provide a more complete and extensive comparison between experimental measurements and the predictions of linear stability than has been done previously.

Note that the way the normalization for the wavelengths and growth rates is different in Table 5.4 than the normalizations used in Ch. 3 and Ch. 4. In those chapters, the quantities, C^{AP} and C^{TC}, encapsulated all the material properties of the system and were treated as fitting parameters for each model. The groupings of the material

Table 5.4: Scaled wavelengths, Λ, and growth rates, β, for each of the proposed models

SC Model

$$\Lambda_D^{\mathrm{SC}} \equiv \frac{\lambda_o^{\mathrm{SC}}}{2\pi\sqrt{h_o}}\sqrt{\frac{\sigma^2}{2\varepsilon_o\varepsilon_p^2\gamma}} = \frac{\left(D+\varepsilon_p^{-1}-1\right)^{3/2}}{D} \qquad \beta_D^{\mathrm{SC}} \equiv \left(\frac{2\varepsilon_o\varepsilon_p^2\gamma}{\sigma^2}\right)^2 \frac{3b_o^{\mathrm{SC}}\mu}{h_o\gamma} = \frac{D^4}{\left(D+\varepsilon_p^{-1}-1\right)^6}$$

$$\Lambda_{\Delta\mathrm{T}}^{\mathrm{SC}} \equiv \frac{\lambda_o^{\mathrm{SC}} D}{2\pi\sqrt{h_o}\left(D+\varepsilon_p^{-1}-1\right)^{3/2}}\sqrt{\frac{\sigma^2}{2\varepsilon_o\varepsilon_p^2\gamma}} = 1 \qquad \beta_{\Delta\mathrm{T}}^{\mathrm{SC}} \equiv \left(\frac{2\varepsilon_o\varepsilon_p^2\gamma}{\sigma^2}\right)^2 \frac{3b_o^{\mathrm{SC}}\mu\left(D+\varepsilon_p^{-1}-1\right)^6}{h_o\gamma D^4} = 1$$

AP Model

$$\Lambda_D^{\mathrm{AP}} \equiv \frac{\lambda_o^{\mathrm{AP}}\sqrt{\Delta\mathrm{T}}}{2\pi h_o}\sqrt{\frac{Q(1-\kappa)k_a}{\gamma u_p}} = D+\kappa-1 \qquad \beta_D^{\mathrm{AP}} \equiv \frac{\left(\gamma u_p\right)^2 3b_o^{\mathrm{AP}}\mu h_o}{\left(Q(1-\kappa)k_a\right)^2\gamma(\Delta\mathrm{T})^2} = \frac{1}{(D+\kappa-1)^4}$$

$$\Lambda_{\Delta\mathrm{T}}^{\mathrm{AP}} \equiv \frac{\lambda_o^{\mathrm{AP}}}{2\pi h_o\left(D+\kappa-1\right)}\sqrt{\frac{Q(1-\kappa)k_a}{\gamma u_p}} = \frac{1}{\sqrt{\Delta\mathrm{T}}} \qquad \beta_{\Delta\mathrm{T}}^{\mathrm{AP}} \equiv \frac{\left(\gamma u_p\right)^2 3b_o^{\mathrm{AP}}\mu h_o\left(D+\kappa-1\right)^4}{\left(Q(1-\kappa)k_a\right)^2\gamma} = (\Delta\mathrm{T})^2$$

TC Model

$$\Lambda_D^{\mathrm{TC}} \equiv \frac{\lambda_o^{\mathrm{TC}}\sqrt{\Delta\mathrm{T}}}{2\pi h_o}\sqrt{\frac{3\kappa\gamma_{\mathrm{T}}}{4\gamma}} = \frac{D+\kappa-1}{\sqrt{D}} \qquad \beta_D^{\mathrm{TC}} \equiv \left(\frac{4\gamma}{3\kappa\gamma_{\mathrm{T}}}\right)^2 \frac{3b_o^{\mathrm{TC}}\mu h_o}{\gamma(\Delta\mathrm{T})^2} = \frac{D^2}{(D+\kappa-1)^4}$$

$$\Lambda_{\Delta\mathrm{T}}^{\mathrm{TC}} \equiv \frac{\lambda_o^{\mathrm{TC}}\sqrt{D}}{2\pi h_o\left(D+\kappa-1\right)}\sqrt{\frac{3\kappa\gamma_{\mathrm{T}}}{4\gamma}} = \frac{1}{\sqrt{\Delta\mathrm{T}}} \qquad \beta_{\Delta\mathrm{T}}^{\mathrm{TC}} \equiv \left(\frac{4\gamma}{3\kappa\gamma_{\mathrm{T}}}\right)^2 \frac{3b_o^{\mathrm{TC}}\mu h_o\left(D+\kappa-1\right)^4}{\gamma D^2} = (\Delta\mathrm{T})^2$$

properties for each model had the forms

$$C^{\mathrm{SC}} = 2\pi\sqrt{\frac{2\varepsilon_o\varepsilon_p^2\gamma}{\sigma^2}}, \tag{5.29}$$

$$C^{\mathrm{AP}} = 2\pi\sqrt{\frac{\gamma u_p}{Q(1-\kappa)k_a}}, \tag{5.30}$$

$$C^{\mathrm{TC}} = 2\pi\sqrt{\frac{4\gamma}{3\kappa\gamma_{\mathrm{T}}}}. \tag{5.31}$$

However, treating these quantities as a fitting parameter neglects the fact that each of the material properties has a temperature dependence that varies between experimental runs. This technique has the limitation that it requires the material parameters, such as γ or k_p, to be constant across every experimental run to be able to fit the functional form with the constants C^{AP} and C^{TC}, which depend on material properties, but not D or $\Delta\mathrm{T}$. However, we know empirically that these "constants"

show variation with temperature because their constituents do. A full listing of the material properties for each experimental run can be found in Table 5.7 to illustrate the ranges over which the parameters vary. Since we are scanning a much larger range of experimental parameters than in previous work, we wanted to do a more rigorous treatment of the variation in material properties between experimental runs. To remedy this issue, we chose to scale the expressions in Table 5.4 so that almost all of the material properties were absorbed into the scaled wavelength or scaled growth rate on the left hand side of the equation and then plot this quantity against the remaining experimentally tunable parameters on the right hand side. Plotted in this way, all the points for a given normalization should lie on a line with slope equal to one. We first turn to the wavelength scalings for each model and then transition to the growth rate scalings to examine the correspondence between the scaled experimental data and the predictions of the proposed models.

5.5.3 Nondimensional Wavelength Comparisons

For each of the three proposed models, we isolated the dependence of the wavelength on both the normalized gap separation distance, D, and the temperature drop, ΔT. Generally, the SC model is distinguished by the lack of dependence on ΔT while the AP and TC models can be most easily distinguished by the difference in the predicted dependence on D. A full listing of the scaled wavelengths can be found in the middle column of Table 5.4. Tables 5.5, 5.6, and 5.7 contain all the experimental parameters, material properties, and derived values for each run.

We first scaled the wavelength prediction of the SC model from Eq. (5.23) to yield Λ_D^{SC} and $\Lambda_{\Delta T}^{SC}$. The results of these scalings are shown in Fig. 5.8. For both Fig. 5.8(a) and Fig. 5.8(b), the solid line represents the expected relationship from the theoretical prediction with no adjustable fitting parameters. Neither scaling for the experimental data shows good agreement with the predictions of the SC model, as Λ_D^{SC} shows a generally constant behavior when it should be linear in Fig. 5.8(a) and $\Lambda_{\Delta T}^{SC}$ shows a decay with increasing ΔT when it should be constant in Fig. 5.8(b).

Next, we scaled the wavelength prediction of the AP model from Eq. (5.25) to yield Λ_D^{AP} and $\Lambda_{\Delta T}^{AP}$ and the results are shown in Fig. 5.9. As in Fig. 5.8, the solid line is the expected functional dependence for the theoretical prediction with no adjustable parameters. In Fig. 5.9(a), the behavior of Λ_D^{AP} shows a significant departure from linearity at larger values of $D + \kappa - 1$. The behavior of $\Lambda_{\Delta T}^{AP}$ in Fig. 5.9(b) is more linear and much closer to the predictions of the AP model, although there are some

Figure 5.8: Wavelengths normalized by the SC model

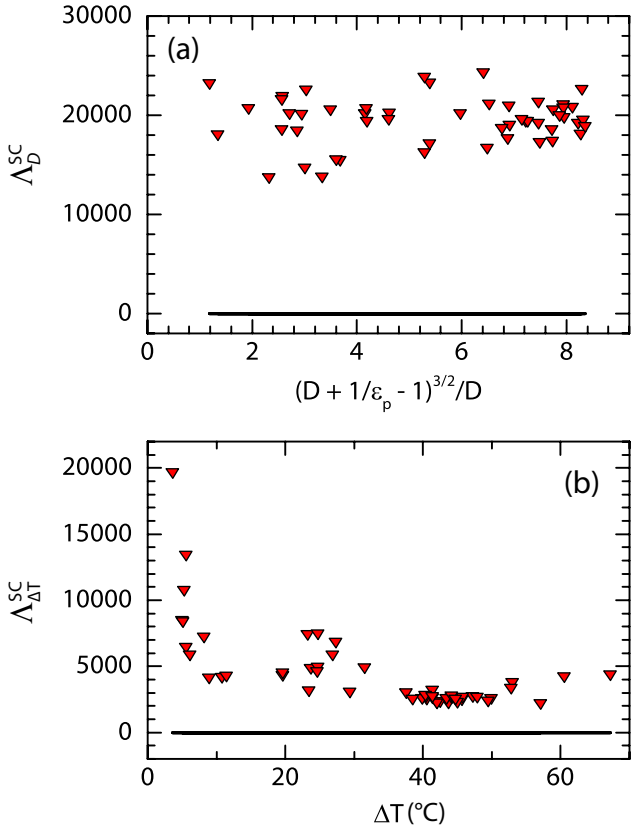

In each case, the (black) solid line is the theoretical prediction of the SC model with no adjustable parameters. (a) Wavelengths normalized to isolate the dependence of Λ_D^{SC} on D. (b) Wavelength normalized to isolate the dependence of $\Lambda_{\Delta T}^{SC}$ on ΔT.

large outliers at larger values of ΔT.

The last wavelength prediction comes from the TC model and was presented above in Eq. (5.27). The scaled results are shown in Fig. 5.10, with Λ_D^{TC} in Fig. 5.10(a) and $\Lambda_{\Delta T}^{TC}$ in Fig. 5.10(b). Both quantities show strongly linear behavior that is consistent with the theoretical prediction although they tend to overshoot the TC model somewhat.

Based on the wavelength scaling results, the experimental data supports the conclusion that the thermocapillary model is the dominant physical mechanism for this instability. There remains a disagreement between the theoretical prediction of the model and the experimental data, but this can reasonably be attributed to the uncertainty in the material properties, which will be discussed further below, after we examine the growth rate results.

Figure 5.9: Wavelengths normalized by the AP model

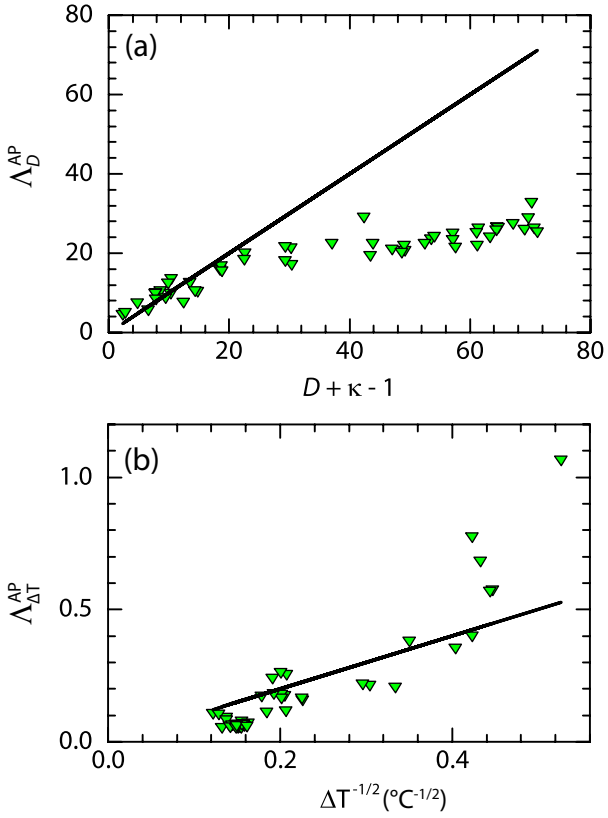

In each case, the (black) solid line is the theoretical prediction of the AP model with no adjustable parameters. (a) Wavelengths normalized to isolate the dependence of Λ_D^{AP} on D. (b) Wavelengths normalized to isolate the dependence of $\Lambda_{\Delta T}^{AP}$ on ΔT.

5.5.4 Nondimensional Growth Rate Comparisons

Beyond scaling the measured wavelengths, we also scaled the growth rates which were measured at the same time. Generally, this section will proceed similarly to the previous one, where we scale the predicted growth rates from each model separately to isolate their dependence on D and ΔT. However, before we treat each model individually, we can probe the consistency of the growth rate and wavelength measurements within the context of general linear stability. Looking at the growth rates for the three models derived in Ch. 2, there is a relationship between the growth rate, b_o, and the wavelength, λ_o, for thin film instabilities which stems from the dispersion relation. Specifically, the nondimensional relationship is

$$\beta_\Lambda \equiv b_o \frac{h_o \mu}{\gamma} = \frac{(2\pi)^4}{3} \Lambda^{-4}, \tag{5.32}$$

where β_Λ is a nondimensional growth rate and $\Lambda \equiv \lambda_o / h_o$ is a nondimensional wavelength. As such, if our growth rate and wavelength measurements exactly

Figure 5.10: Wavelengths normalized by the TC model

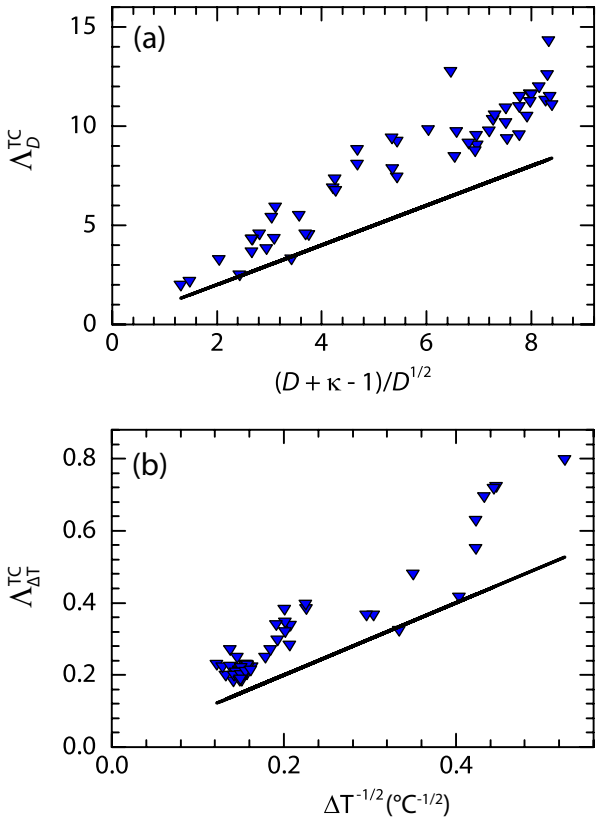

In each case, the (black) solid line is the theoretical prediction of the TC model with no adjustable parameters. (a) Wavelengths normalized to isolate the dependence of of Λ_D^{TC} on D. (b) Wavelengths normalized to isolate the dependence of of $\Lambda_{\Delta T}^{TC}$ on ΔT.

matched the predictions of linear stability analysis applied to thin film instabilities, independent of any specific model, we would expect this relationship to hold. In following our convention from the wavelength scaling, this relationship has been plotted in Fig. 5.11. The solid black line is the prediction from linear stability theory with no adjustable parameters. Generally, there are many points which lie close to the predicted line, but the scatter is large. Due to the large powers involved with making comparisons to the growth rate, even small discrepancies can be magnified quickly. We will discuss this discrepancy further after presenting the results for each individual model in turn. Note that all the scaled growth rates have been plotted on logarithmic axes whereas the scaled wavelengths presented above were plotted on linear axes. This is due to the much larger powers in the scaled growth rates which means that they span a much larger range.

The first growth rate scaling we investigated was for the SC model through Eq. (5.24).

Figure 5.11: Nondimensional growth rate plotted as a function of the nondimensional wavelength

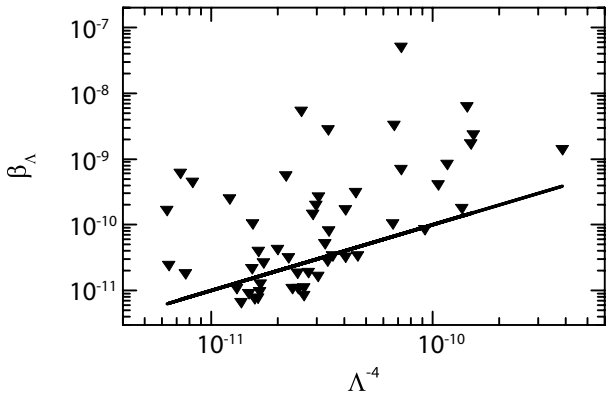

The (black) solid line is the theoretical prediction from linear stability with no adjustable parameters. The nondimensional growth rate is plotted as a function of the nondimensional wavelength.

As with the wavelength scaling, we isolated the functional dependence of the growth rate on D and ΔT. In both Fig. 5.12(a) and (b), the solid line is the theoretical prediction of the SC model with no adjustable parameters. Both of these plots show scatter up to three orders of magnitude.

Next, we isolated the dependencies of Eq. (5.26) to further probe the growth rate predictions of the AP model. Fig. 5.13(a) contains the scaled growth rate β_D^{AP} and Fig. 5.13(b) contains the scaled growth rate $\beta_{\Delta\mathrm{T}}^{\mathrm{AP}}$. The solid lines are the linear stability predictions of the AP model with no adjustable parameters. The data in Fig. 5.13(a) shows a linear relationship with a slight overestimation of the growth. On the other hand, the data in Fig. 5.13(b) is at least 10 orders of magnitude away from the theoretical prediction.

As compared to the AP model, the scaled growth rates of Eq. (5.28) derived from the TC model compare much more favorably. The values of β_D^{TC} plotted in Fig. 5.14(a) show modest agreement with the solid line. The values of $\beta_{\Delta\mathrm{T}}^{\mathrm{TC}}$ plotted in Fig. 5.14(b) show a great deal of scatter.

Due to the stronger dependencies of the growth rate on the key experimental parameters, the scaled growth rates provide a more stringent test of the physical models. Based solely on the scaled growth rate measurements it is more difficult to draw strong conclusions than with the corresponding scaled wavelength data due to the larger scatter. However, the AP model shows a massive disagreement of 10 orders of magnitude with the predictions for the scaled growth rate. Neither the SC nor the TC model predictions show strong agreement with the experimental data, but they

Figure 5.12: Growth rates normalized by the SC model

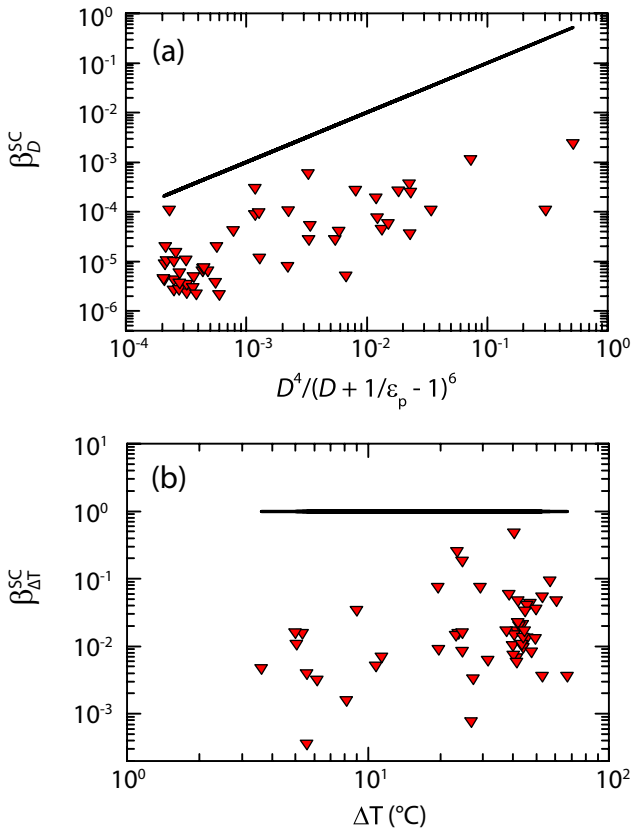

In each case, the (black) solid line is the theoretical prediction of the SC model with no adjustable parameters. (a) Growth rates normalized to isolate the dependence of β_D^{SC} on D. (b) Growth rates normalized to isolate the dependence of $\beta_{\Delta T}^{SC}$ on ΔT.

are significantly better than the AP model.

5.6 Discussion of Redesigned Experimental Setup Results

In this section, we first highlight and summarize the improvements that this chapter has made on previous experimental studies. Then, we comment on some of the remaining experimental challenges which hindered this analysis and could be improved in the future. Finally, we discuss the dominant physical mechanism driving this instability in light of the scaled wavelength and growth rate results presented above.

5.6.1 Comparison to Previous Experimental Studies

As compared to the work of McLeod *et al.* [1], the present study has focused on improving both the experimental setup and the analysis framework. Major

Figure 5.13: Growth rates normalized by the AP model

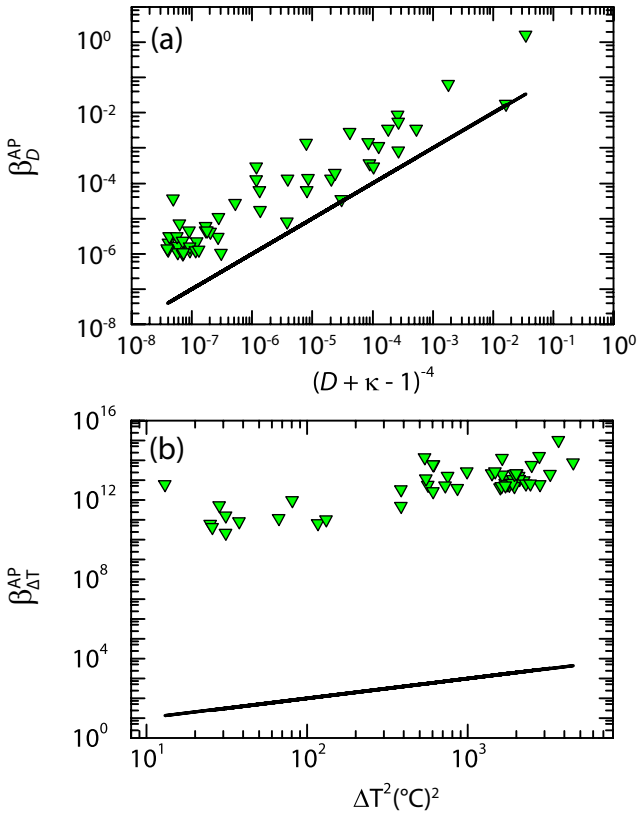

In each case, the (black) solid line is the theoretical prediction of the AP model with no adjustable parameters. (a) Growth rates normalized to isolate the dependence of β_D^{AP} on D. (b) Growth rates normalized to isolate the dependence of $\beta_{\Delta\mathrm{T}}^{\mathrm{AP}}$ on ΔT.

considerations when designing this setup centered around improvements to the thermal stability and improvements to the optical imaging. On the thermal stability front, we used a large integrated aluminum chiller unit for better thermal contact with both the sapphire window and the external circulator. We used an alumina ceramic heater which could access a larger range of temperatures and coupled this with platinum RTDs which were more accurate than thermocouples. This allowed for more precise control of the heater temperature as a function of time. Turning to the optical imaging process, we increased the viewing area so that there was more data for analysis and switched to single wavelength illumination to enhance the contrast of the instability growth. With this improved experimental setup we scanned a much larger range of parameters, both D and ΔT to highlight the differences in the proposed models. We also derived a fitting function for this particular physical system which allowed for the simultaneous extraction of both the wavelength and growth rate of the instability. Finally, we minimized the effects of the thermal

Figure 5.14: Growth rates normalized by the TC model

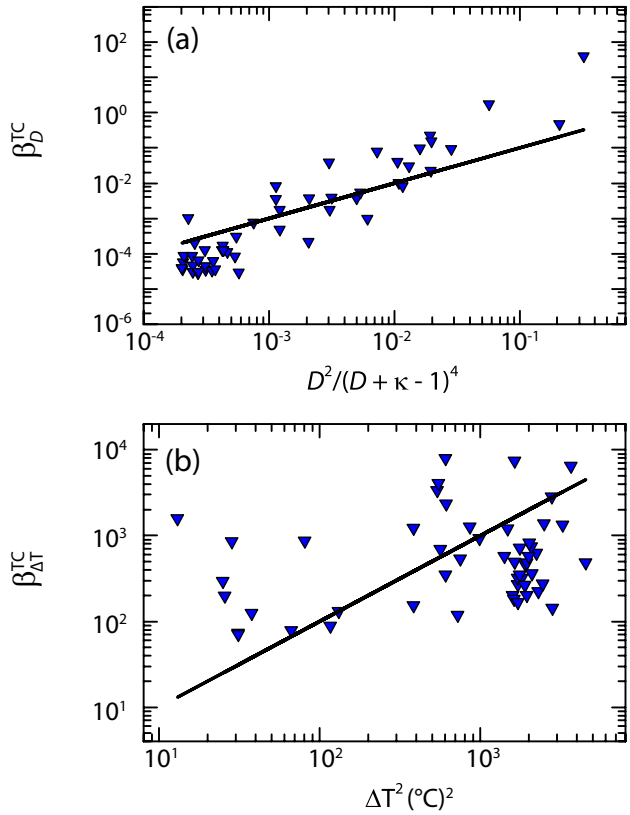

In each case, the (black) solid line is the theoretical prediction of the TC model with no adjustable parameters. (a) Growth rates normalized to isolate the dependence of β_D^{TC} on D. (b) Growth rates normalized to isolate the dependence of $\beta_{\Delta\mathrm{T}}^{\mathrm{TC}}$ on ΔT.

dependence of the material properties by introducing new scalings which account for the variation between experimental runs.

5.6.2 Remaining Experimental Challenges

Even with all the improvements to the experimental setup and the analysis procedure, there were still some areas which could be improved in future studies. First, the amount of thermal paste was not measured or strictly controlled during setup. In hindsight, this is a relatively easy thing to fix and would help reduce the scatter between similar experimental runs. In fact, it would probably be best to remove the thermal paste altogether and use a different heater holder which does not contain an inset. Instead, it could have a polished surface on which the silicon wafer is directly placed. This would eliminate several areas of uncertainty and hopefully improve reproducibility between experimental runs. Next, the larger viewing area can also pose technical difficulties. While it allows for more data collection during an ideal

run, it also imposes a stricter requirement on the cleanliness of the film and the substrates must be level over a larger area to not have interference fringes. Furthermore, the pressure on the spacers was not able to be measured with the experimental setup and could have varied between experimental runs. This uncertainty is further compounded by the fact that the thickness of the silicon wafers was only 279 μm and at this thickness can flex significantly under load. If the silicon was bent by the pressure of the spacers or the specific distribution of the thermal paste then this would have effected both the actual value of D and implicitly the numerically computed value of ΔT. The numerical temperature simulations also are assumed to be cylindrically symmetric, even though most of the components are rectangular. A more accurate, but much more computationally expensive, simulation would do a full 3D simulation of the geometry. At this point, we did not feel like this was the largest source of uncertainty as compared to the thermal paste and so it was not pursued. Additionally, we note that the material parameters of the low molecular weight PS that was used are not well measured, particularly in nanofilms. Whenever possible we have tried to use sources in the literature which specify the molecular weight, but the thermocapillary coefficient in particular is one of the parameters which we could not find as a function of molecular weight. Finally, there is a fundamental difficulty when comparing experimental data to the predictions from linear stability analysis. Since linear stability analysis is predicated upon infinitesimal perturbations, the ideal comparison would be a measurement on an infinitesimal experimental signal. This becomes impractical due to noise, but this analysis has tried to measure the wavelength and growth rate as early as possible. This means that the measured values are inherently noisy and show scatter. Furthermore, the growth rates in particular show large scatter and this is partly due to the way they were measured. The growth rates are computed from the width of a peak in the power spectral density and this value is much harder to estimate than the peak position when the peak is small. This is especially true in the presence of background noise which can obscure the lower edge of the peak at low values of the wavevector. We attribute most of the scatter in the growth rate comparisons to this experimental difficulty.

5.6.3 Dominant Instability Mechanism Indentification

At this point, we are in a position to further discuss which proposed model is best supported by the experimental evidence gathered in this study. Taken as a whole, both the wavelength and the growth rate measurements support the conclusion

that the TC model is consistent with the experimental data and best describes this experimental system. The SC and AP models are inconsistent with the experimental data. For the SC model, this is most clearly shown by the dependence of $\Lambda_{\Delta T}^{SC}$ on ΔT in Fig. 5.8(b). Not only is the data two to three orders of magnitude larger than the theoretical predictions, but it shows a clear dependence on temperature when the SC model would predict no thermal dependence at all. Turning to the AP model, it shows inconsistency in both the wavelength and growth rate data. In Fig. 5.9(a), the experimental wavelength data clearly diverges from the linear theoretical prediction at large values of $D + \kappa - 1$. The disagreement is even worse in Fig. 5.13(b), where the experimental data for $\beta_{\Delta T}^{AP}$ is 10 orders of magnitude larger than the predictions of the AP model.

In comparison to the SC and AP models, the TC model shows the best agreement with the experimental data. Both $\Lambda_{\Delta T}^{TC}$ and Λ_{D}^{TC} show linear behavior consistent with the TC model. The slopes are the same but suggest that there is a systematic discrepancy in one of the material parameters. In a similar manner, the growth rate measurements generally lie close to the model predictions which implies that the model is at least consistent, if not strongly supported, by the data.

Since the data supports the TC mechanism best, we have identified several areas where the SC and AP models do not accurately model the physical system. In the case of the SC model, the underlying physics is predicated upon the presence of surface charge at the interface of the nanofilm. However, there is no clear mechanism for this charge accumulation and it seems that the SC model, while not fundamentally incorrect, does not apply to this physical system. For the AP model, the issues appear to run deeper. Specifically, one of the key assumptions that is made in the derivation is that phonons can propagate coherently through a liquid, even when there is not a well-defined lattice in the molten nanofilm. While the initial experimental investigations of Schäffer *et al.* [4–6] were consistent with the AP model over a small range, the more rigorous investigation in this chapter shows that the AP model is inconsistent with this physical system.

5.7 Summary

In this chapter we have described our experimental investigations into the spontaneous instability which occurs in nanofilms with a free interface subject to a large transverse thermal gradient. Previously in the literature, three mechanisms had been proposed to describe this instability. The SC model is predicated upon the accumu-

lation of surface charge at the interface which destabilizes the free surface of the molten film. The AP model suggests that the instability arises from a destabilizing acoustic radiation pressure which builds up at the interface of the molten film. The TC model hypothesizes that the deformation occurs due to surface tension gradients which arise due to the temperature dependence of the surface tension along the film/air interface.

Using *in situ* optical observations of the instability during the growth process we have measured the characteristic wavelength and growth rate of the instability. We used a new fitting function derived above to fit the power spectral density which allowed for the simultaneous measurement of both of these quantities. When combined with numerical simulations of the temperature in the experimental setup, we compared the experimental data to the predictions of each model. The results of this comparison support the TC model as the dominant physical mechanism and show that the SC and AP models are inconsistent with the experimental data.

Table 5.5: Parameters and thermal conductivities for the thermal simulations

Exp. #	h_o (nm)	d_o (nm)	r_{paste} (mm)	T_{Chill} (°C)	T_{Heat} (°C)	Power (W)	ΔT_{Out} (°C)	ΔT_{sin} (°C)	h_{paste} (mm)	T_H (°C)	ΔT (°C)
1	154	6860	14.1	32.3	150	39.4	118	41.3	426	108	41.3
2	159	3060	20.3	32.9	150	49.0	117	23.7	341	103	23.7
3	159	6870	19.0	32.8	150	47.1	117	53.0	127	130	53.0
4	159	889	22.5	33.0	150	50.2	117	5.27	562	83.5	5.33
5	347	3250	18.0	32.8	120	41.1	87.2	23.2	149	98.0	23.2
6	352	1080	23.1	32.3	120	33.1	87.7	3.43	819	64.8	3.60
7	95.9	6810	18.1	32.9	150	43.7	117	47.3	239	120	47.3
8	96.3	3000	20.5	33.0	150	48.9	117	23.4	347	103	23.4
9	95.9	826	21.5	32.9	150	49.1	117	4.98	611	81.6	5.00
10	157	3060	21.4	42.9	140	47.0	97.1	24.7	149	115	24.7
11	97.5	6810	14.7	42.2	140	37.8	97.8	42.0	176	119	42.0
12	96.4	3000	25.0	42.4	140	40.9	97.6	19.6	344	101	19.6
13	96.7	827	25.0	42.8	140	45.9	97.2	5.05	400	90.9	5.07
14	285	3190	25.0	42.5	140	46.5	97.5	24.7	161	114	24.7
15	287	1020	18.1	42.7	140	46.3	97.3	5.41	375	92.3	5.58
16	155	6870	20.0	23.5	160	47.6	137	49.9	367	115	49.9
17	156	3060	25.0	23.7	160	53.2	136	24.6	472	97.1	24.7
18	96.6	6810	18.0	23.6	160	52.2	136	57.0	199	128	57.0
19	289	3190	22.0	24.2	160	61.3	136	31.4	227	116	31.5
20	300	7010	20.5	24.0	160	58.2	136	67.2	51.5	147	67.2
21	301	7010	22.6	33.2	150	52.2	117	60.5	10.1	144	60.5
22	300	3200	21.5	33.3	150	52.9	117	27.3	220	113	27.4
23	99.6	3000	22.6	24.1	160	59.7	136	29.3	273	111	29.3
24	100	6810	16.9	51.5	130	35.1	78.5	40.5	12.8	126	40.5
25	99.9	3000	19.7	51.8	130	37.6	78.2	19.6	157	109	19.6
26	182	6890	13.0	28.3	155	47.7	127	52.8	207	125	52.8
27	288	4100	18.6	32.7	150	43.5	117	26.8	470	99.1	26.9
28	109	7110	20.0	41.9	150	38.3	108	41.3	330	117	41.3
29	109	7110	19.0	42.2	150	40.8	108	45.6	210	125	45.6
30	143	7140	14.7	41.9	150	37.3	108	40.4	363	115	40.4
31	143	7140	13.0	41.7	150	35.2	108	37.5	479	110	37.5
32	109	7110	19.0	41.7	150	37.4	108	39.9	382	114	39.9
33	115	7120	15.2	32.5	160	41.5	128	43.7	498	112	43.7
34	117	1540	15.8	42.1	150	42.9	108	8.95	604	89.8	8.97
35	97.5	1520	15.2	41.5	150	48.2	108	10.8	398	98.0	10.8
36	158	1360	17.5	41.2	140	43.2	98.8	8.12	448	89.7	8.15
37	97.1	987	18.6	42.2	150	44.8	108	5.57	606	87.8	5.58
38	140	1030	14.1	42.4	150	46.3	108	6.11	510	91.2	6.14
39	101	1520	15.2	33.3	160	52.9	127	11.4	503	93.6	11.4
40	99.5	7100	18.6	41.8	150	39.0	108	42.5	294	119	42.5
41	98.7	7100	13.0	41.7	150	38.2	108	42.0	312	118	42.0
42	123	7120	14.1	41.6	150	37.2	108	40.3	369	115	40.3
43	131	7130	20.5	41.8	150	40.9	108	45.7	212	124	45.7
44	115	7120	14.7	41.8	150	39.7	108	44.2	250	122	44.2
45	123	7120	14.1	32.3	160	41.1	128	43.4	511	111	43.4
46	130	7130	19.0	32.6	160	44.5	127	47.8	356	119	47.8
47	115	7120	14.7	32.6	160	45.2	127	49.5	309	122	49.5
48	149	7150	20.0	41.9	150	39.9	108	44.1	251	122	44.1
49	134	7130	18.5	41.8	150	38.2	108	41.3	333	117	41.3
50	122	7120	18.0	32.4	150	41.1	118	45.0	338	114	45.0
51	145	7150	15.8	32.5	160	42.2	128	44.7	461	114	44.7
52	111	7110	18.6	41.7	150	36.5	108	38.5	436	112	38.5

This table contains the experimental run number, initial film thickness, h_o, and total gap distance, d_o. Next are the experimental values which were used in the simulations: the applied thermal paste radius, r_{paste}, the temperature of the aluminum chiller, T_{Chill}, the temperature of the ceramic heater, T_{Heat}, and the electrical power dissipated in the heater. Finally are the derived values: ΔT_{Out} is the difference between the measured heater and chiller temperatures, ΔT_{sin} is the temperature drop across the sinusoidally deformed bilayer, h_{paste} is the thickness of the thermal paste, T_H is the temperature at the bottom of the polymer film, and ΔT is the temperature drop across the undeformed bilayer.

Table 5.6: Image analysis parameters and measured wavelengths and growth rates

Exp. #	D	Filter (nm)	Image Size (μm×μm)	$k_{\min} \times 10^{-2}$ (1/μm)	t_{final} (min)	t_{meas} (min)	λ_o (μm)	$b_o \times 10^{-4}$ (1/s)
1	44.6	633	498 × 500	5.03	153.75	95.75	69.0	1.28
2	19.3	633	893 × 1190	5.03	66.75	26.75	67.4	10.4
3	43.2	633	397 × 377	3.14	174.75	34.75	78.6	2.93
4	5.59	633	558 × 686	5.03	36.75	14.75	70.7	27.1
5	9.36	488	891 × 1190	3.14	69.00	13.00	100.2	74.8
6	3.08	488	892 × 1190	2.51	480.00	71.00	120.6	3.38
7	71.0	488	696 × 901	5.03	110.00	34.00	57.6	4.21
8	31.1	488	432 × 598	5.03	108.00	16.00	44.5	35.1
9	8.61	515	516 × 870	5.03	135.25	36.25	58.4	3.93
10	19.5	633	886 × 1190	5.03	81.75	15.75	67.6	14.7
11	69.8	488	610 × 874	5.03	157.00	28.00	49.3	4.73
12	31.1	488	730 × 979	5.03	92.00	18.00	60.8	9.03
13	8.55	488	774 × 1200	5.03	61.00	14.00	57.0	9.52
14	11.2	515	884 × 644	3.14	48.25	13.25	99.7	166
15	3.55	532	895 × 691	5.03	104.50	20.50	82.0	14.0
16	44.2	633	898 × 911	5.03	98.75	19.75	54.4	10.6
17	19.6	532	888 × 1190	5.03	21.75	8.75	64.6	69.7
18	70.5	488	515 × 569	5.03	70.00	13.00	45.7	15.6
19	11.0	532	613 × 1200	5.03	15.75	8.75	65.3	76.9
20	23.4	532	569 × 1190	3.14	23.50	6.50	87.8	45.5
21	23.3	532	745 × 645	3.14	22.50	6.50	85.5	533
22	10.7	532	887 × 1190	3.14	43.50	6.50	91.2	36.6
23	30.1	515	826 × 1190	5.03	18.25	6.25	42.6	24.6
24	67.9	515	394 × 858	5.03	152.25	40.25	53.7	77.5
25	30.0	515	850 × 1120	5.03	152.25	57.25	62.7	2.69
26	37.9	488	815 × 1200	5.03	47.00	14.00	70.3	49.2
27	14.2	515	590 × 969	3.14	162.25	139.25	93.0	1.39
28	65.2	488	587 × 886	5.03	137.00	81.00	57.3	1.84
29	65.5	488	823 × 642	5.03	174.00	21.00	53.3	6.90
30	50.0	515	382 × 578	5.03	162.75	93.75	59.3	3.16
31	49.8	532	433 × 1020	5.03	400.75	163.75	65.8	2.53
32	65.2	488	765 × 519	5.03	434.00	137.00	56.7	0.907
33	61.9	488	474 × 1200	5.03	403.00	140.00	48.9	1.84
34	13.2	515	213 × 213	5.03	323.25	89.25	40.0	11.2
35	15.6	515	264 × 267	5.03	118.50	63.50	40.7	2.32
36	8.58	633	510 × 583	5.03	359.75	101.75	62.8	1.98
37	10.2	488	394 × 596	5.03	329.00	206.00	49.0	1.55
38	7.35	515	284 × 355	5.03	74.75	24.75	43.6	6.16
39	15.1	488	465 × 617	5.03	151.75	41.75	41.8	2.31
40	71.4	488	463 × 766	5.03	233.00	97.00	50.7	1.95
41	71.9	488	774 × 1190	5.03	279.00	71.00	48.9	1.96
42	57.9	532	885 × 1190	5.03	370.75	162.75	61.8	0.959
43	54.3	488	858 × 812	5.03	192.75	51.75	57.3	4.04
44	62.1	488	894 × 875	5.03	241.00	106.00	57.0	1.65
45	57.9	532	893 × 857	5.03	434.50	134.50	55.9	1.10
46	54.8	532	887 × 664	5.03	189.75	69.75	57.4	1.83
47	61.8	532	510 × 469	5.03	187.50	57.50	51.6	2.33
48	47.9	633	882 × 912	5.03	188.75	50.75	59.2	5.17
49	53.2	532	735 × 1200	5.03	425.75	97.75	59.2	1.15
50	58.3	633	712 × 1200	5.03	371.75	130.75	50.1	3.97
51	49.4	633	786 × 1100	5.03	442.75	93.75	55.5	3.34
52	64.1	532	694 × 945	5.03	495.75	228.75	55.2	4.61

This table contains the experimental run number and normalized gap separation distance, $D = d_o/h_o$. Next are the auxiliary experimental information which was used during the analysis process: the wavelength of the optical filter chosen, the size of the subimage which was selected for analysis (H×W), the lower bound of the bandpass filter, $k_{\min}$, and the point in the time series at which the analysis process was terminated, t_{final}. Finally are the results of the analysis procedure: the time of measurement, t_{meas}, the measured wavelength, λ_o, and the measured growth rate, b_o.

Table 5.7: Material properties at the temperature of each experimental run

Exp. #	D	k_a mW/m-°C	$\kappa \equiv k_a/k_p$	γ (mN/m)	μ (Pa*s)	$C^{\mathrm{SC}} \times 10^3$ $\left(\sqrt{\mu\mathrm{m}}\right)$	C^{AP} $\left(\sqrt{°\mathrm{C}}\right)$	C^{TC} $\left(\sqrt{°\mathrm{C}}\right)$
1	44.6	31.9	0.249	32.4	16.1	8.32	128	296
2	19.3	31.6	0.247	32.8	28.0	8.37	129	300
3	43.2	33.4	0.260	30.7	4.36	8.10	123	283
4	5.59	30.2	0.244	34.3	223	8.57	135	308
5	9.36	31.2	0.245	33.2	42.5	8.43	131	303
6	3.08	28.9	0.242	35.8	8030	8.75	141	316
7	71.0	32.7	0.255	31.5	7.52	8.20	125	289
8	31.1	31.6	0.246	32.8	28.6	8.38	130	300
9	8.61	30.1	0.244	34.4	295	8.58	136	309
10	19.5	32.4	0.252	31.8	10.6	8.25	126	292
11	69.8	32.7	0.254	31.5	7.74	8.21	125	289
12	31.1	31.4	0.245	32.9	33.0	8.40	130	301
13	8.55	30.8	0.244	33.7	85.8	8.49	133	305
14	11.2	32.3	0.252	31.9	11.8	8.27	127	293
15	3.55	30.8	0.245	33.6	76.1	8.48	133	305
16	44.2	32.4	0.253	31.8	10.5	8.25	126	292
17	19.6	31.2	0.245	33.2	45.3	8.43	131	303
18	70.5	33.3	0.259	30.8	4.59	8.12	123	283
19	11.0	32.4	0.253	31.8	10.4	8.25	126	292
20	23.4	34.5	0.267	29.3	2.03	7.92	119	272
21	23.3	34.3	0.266	29.5	2.29	7.95	120	274
22	10.7	32.2	0.251	32.0	12.9	8.28	127	294
23	30.1	32.1	0.251	32.1	13.9	8.29	127	294
24	67.9	33.1	0.258	30.9	5.28	8.14	124	285
25	30.0	32.0	0.250	32.3	15.3	8.31	128	295
26	37.9	33.1	0.257	31.1	5.74	8.15	124	286
27	14.2	31.3	0.245	33.1	37.1	8.42	131	302
28	65.2	32.5	0.253	31.7	9.10	8.23	126	291
29	65.5	33.0	0.257	31.1	5.82	8.15	124	286
30	50.0	32.4	0.253	31.8	10.5	8.25	126	292
31	49.9	32.0	0.250	32.2	14.8	8.30	128	295
32	65.2	32.3	0.252	31.9	11.3	8.26	127	292
33	61.9	32.2	0.251	32.1	13.1	8.28	127	294
34	13.2	30.7	0.244	33.8	95.9	8.50	133	306
35	15.6	31.2	0.245	33.2	40.2	8.42	131	302
36	8.58	30.7	0.244	33.8	97.5	8.51	133	306
37	10.2	30.5	0.244	34.0	124	8.52	134	306
38	7.35	30.8	0.244	33.7	83.5	8.49	133	305
39	15.1	30.9	0.245	33.5	61.3	8.47	132	304
40	71.4	32.7	0.254	31.5	7.82	8.21	126	289
41	71.9	32.6	0.254	31.6	8.38	8.22	126	290
42	57.9	32.4	0.252	31.8	10.9	8.26	127	292
43	54.3	33.0	0.257	31.1	5.91	8.16	124	286
44	62.1	32.8	0.256	31.3	6.85	8.18	125	288
45	57.9	32.1	0.251	32.1	13.7	8.29	127	294
46	54.9	32.7	0.255	31.5	7.66	8.21	125	289
47	61.8	32.9	0.256	31.3	6.65	8.18	125	287
48	47.9	32.8	0.256	31.3	6.87	8.19	125	288
49	53.2	32.5	0.253	31.7	9.25	8.24	126	291
50	58.9	32.3	0.252	31.9	11.8	8.27	127	293
51	49.4	32.3	0.252	31.9	11.7	8.27	127	293
52	64.1	32.2	0.251	32.1	13.3	8.29	127	294

This table contains the experimental run number and the normalized gap separation distance, $D = d_o/h_o$. Next are the material parameters evaluated at the temperature of the PS-air interface for each experimental run: the thermal conductivity of the air, k_a, the thermal conductivity ratio, κ, the surface tension, γ, and the viscosity, μ. Finally are the quantities which scale the nondimensional wavelengths and growth rates in Table 5.4: C^{SC}, C^{AP}, and C^{TC}.

Chapter 6

MICROANGELO SCULPTING: MICROLENS ARRAY FABRICATION

6.1 Background

In the following two chapters, thermocapillary forces are used to deform molten nanofilms into structures through the spatial modulation of surface tension. We call this technique MicroAngelo (μAngelo) in reference to how it sculpts interface on the microscale. At its most basic level, MicroAngelo operates by modulating thermocapillary forces through the application of a spatially inhomogeneous temperature distribution. As was described in Sec. 2.3.3, thermocapillary forces cause flow from warmer regions of the fluid interface to cooler regions and this induces spontaneous out of plane growth due to random fluctuations in the interface height. By using a patterned mask instead of a flat plate, we can bypass the random nature of instability growth to directly influence the temperature distribution and impose thermal inhomogeneities on the fluid interface which localize the deformation. Two examples of simple masks which create non-uniform temperature profiles are shown in Fig. 6.1. Due to the large disparity between the vertical and lateral length scales, lateral thermal conduction is negligible and so the regions underneath the mask patterns will be colder than the surrounding regions. This drives thermocapillary flow and consequently structure formation in a fabrication technique we call MicroAngelo. In effect, this technique harnesses the physical mechanism behind the instability investigated in the first portion of this thesis to localize and control film growth.

With the maturation of nanofabrication technology, complex optical devices have become increasingly dependent on micro-optical components to shape, filter, and steer light at the microscale. Traditional grinding and polishing techniques are incapable of achieving the fine resolution and optical quality demanded by such applications, thereby necessitating the use of complex multi-step fabrication processes. Conventional photolithography and scanning beam lithography are commonly used and well-established manufacturing processes, but typically require expensive advanced equipment, multiple post-processing steps, and are limited to producing two-dimensional surface structures. Numerous alternative methods of microfabri-

Figure 6.1: Basic MicroAngelo experimental setup for microlens array fabrication

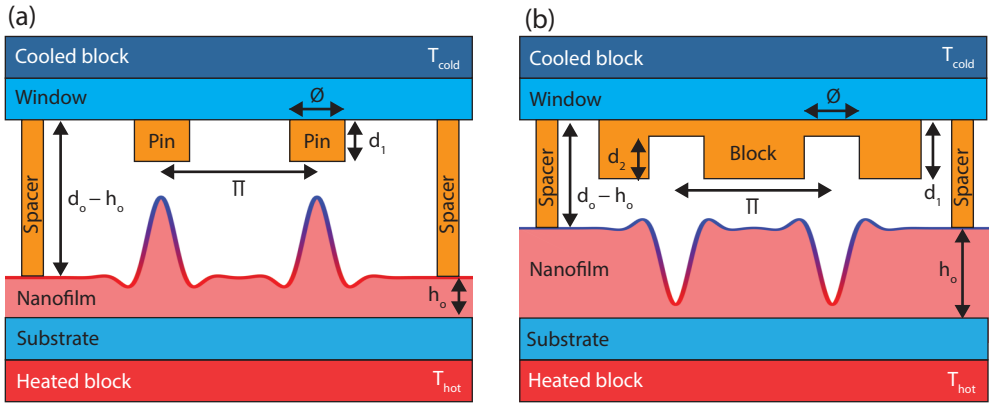

Diagrams of the MicroAngelo setup used to fabricate MLAs. For a full listing of the geometric parameters please consult Table 6.1. (a) Geometry to fabricate convex MLAs. In this configuration, the pins extend from the cooled sapphire window towards the film and growth is localized beneath the pins. (b) Geometry to fabricate concave MLAs. In this configuration, the depressions in the block on the cooled sapphire window localize depressions in the film. The film topographies shown in (a) and (b) are representative late-stage topographies after the film has deformed from its initially flat state. Figure courtesy of Daniel Lim.

cation exist to circumvent these challenges. Hou *et al.* detail twelve categories of fabrication procedures just to fabricate microlens arrays (MLAs) [55], the archetypal micro-optical device comprising periodically spaced micro-lenses arranged on a two-dimensional plane.

While the production of microlens arrays has a long history [56], the fabrication of microlens arrays with thermocapillary forces is quite minimal. Previously in the Troian group, Dr. Euan McLeod produced lens-like structures on silicon wafers using a mask design similar to Fig. 6.1(a) [16]. After Euan left the group, additional lens arrays on silicon wafers were fabricated, as seen in Fig. 6.2. While these arrays showed strong ordering, they were not functional as transmissive, refractive optical devices. When Daniel Lim started working in the lab, we wanted to do a comprehensive study of this fabrication process to explore the range of possible topographies, as well as transition from an opaque substrate (silicon) to a transparent one (fused quartz) so that the devices could be used in transmission like conventional microlens arrays.

The remainder of this chapter is organized as follows. First, we examine the experimental setup and detail the fabrication procedure with MicroAngelo in Sec. 6.2. Then, we describe the characterization of the microlens arrays in Sec. 6.3. After that, we discuss numerical simulations of the lens evolution process in Sec. 6.4. Next,

Figure 6.2: Optical images of MLAs produced on silicon wafers

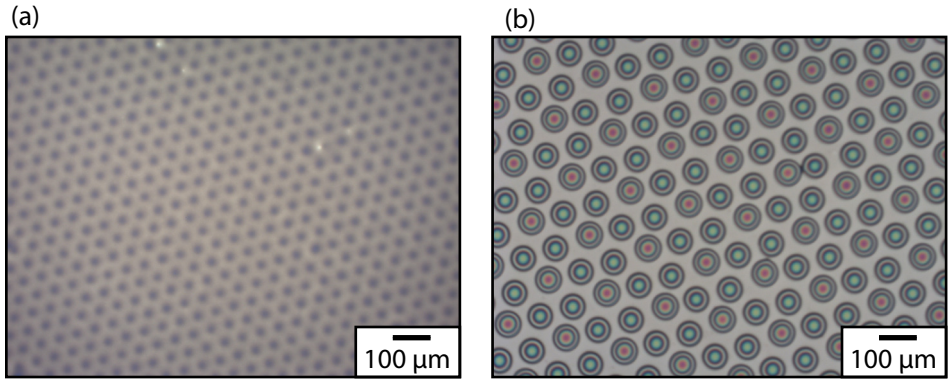

Optical microscope images of microlens arrays fabricated on silicon which show strong ordering. The colors are due to thin film interference fringes and reflect the film height similar to topographic maps. The lenses in (a) are small in height and do not show a full fringe and appear as dark spots. In (b), there are two different lens heights, as evidenced by the different colors of the lens apices.

we implemented a Shack-Hartmann wavefront sensor using an MLA fabricated with MicroAngelo in Sec. 6.5. Finally, we conclude with a discussion of the fabrication results in Sec. 6.6 and a brief summary in Sec. 6.7.

6.2 Experimental Setup and Fabrication Procedure

The experimental setup used for micro-optical device fabrication in this chapter and the next is conceptually very similar to the setups used for the flat plate experiments presented in Ch. 3, Ch. 4, and Ch. 5. However, there are several key differences and improvements which will be detailed below.

As shown in Fig. 6.3, a polymer nanofilm is heated from below and actively cooled from above in the presence of a photoresist pattern which localizes the temperature gradient and heat flux to produce the desired optical structures. Starting from the bottom of the setup and working upwards, the heating assembly and PS nanofilm were supported by a spring-mounted riser plate on a motorized z-translation stage (Oriel 16618). The springs allowed small deflections in tip and tilt of the heater so that the nanofilm and its supporting wafer would be parallel to the sapphire window. The heater was isolated thermally from the rest of the setup using fiberglass insulation. The ceramic heating element (Induceramic, 5.2 Ω, 25.4 mm square) was enclosed in a custom fabricated aluminum holder (50.8 mm diameter cylinder) and was powered by a DC power supply (Keithley 2200-30-5). Three holes were drilled into the aluminum holder for platinum RTDs (Omega RTD-3-F3105-36-T) which were monitored continuously by a data acquisition module attached to a computer

(Omega PT-104A). The RTD holes were located at the center of the holder, halfway to the edge, and at the edge of the holder. This holder was superior to the holder described in Sec. 5.2 because it was smaller and matched the size of the substrates better. Consequently, it localized heat flux more effectively through the nanofilm and its substrate. The measured temperature of the middle RTD (T_{Hot}) was controlled through active PID feedback in a custom MATLAB GUI controller. A small amount of thermal paste (Aremco Heat-Away 638, approximately 150 mg, 130 μm thick cylindrical layer) was used to ensure good thermal contact between the aluminum heater holder and the fused quartz windows (Ted Pella 16001-1, 25.4 mm diameter, 1.6 mm thickness) which served as the PS substrate.

To create the nanofilm, the PS (Scientific Polymer Products, M_w = 1100, M_n = 990) was dissolved in toluene, filtered, and then spun-coat onto the polished quartz substrates or silicon wafers (Silicon Materials, 50.8 mm diameter, <100> orientation, 279 ± 25 μm thickness). The film thickness of the PS on quartz was inferred from ellipsometry measurements of the same solution spun onto the silicon wafers which were measured using ellipsometry (Rudolph Auto EL III). We attempted to measure the PS thickness on the fused quartz directly but found that the index contrast between the two materials (n_{PS} = 1.58 vs. n_{Ox} = 1.457 at a wavelength of 632.8 nm) was too small to produce a reliable signal. There were also additional complications from back reflections off the back of the fused quartz substrate. Film thicknesses were averaged over nine measurements of a 3×3 grid near the center of the silicon wafer at 632.8 nm. The top of the PS nanofilm was contacted by the photoresist spacers (MicroChem SU-8 2010) which were photolithographically patterned on sapphire windows (Meller Optics MSW 037/040). The cylindrical spacers were arranged hexagonally at a radius of 3 mm and had heights ranging from 1.3 μm to 1.8 μm with a diameter of 1000 μm. An additional photoresist pattern was deposited in the center of the sapphire window which served to define the microlens array pattern and morphology. The patterns were generally on the order of 700 nm to 900 nm and a full listing of the geometric parameters can be found in Table 6.1. The photoresist spacers and patterns were cured using UV light (Karl Suss MJB3) through a custom chrome-on-glass patterned mask (UCLA Nanolab Mask Shop). After UV curing, the photoresist was hard baked at 200 °C for 2 hours to stabilize the structures. Then a self-assembled monolayer of perfluorooctyltrichlorosilane (PFOTS, Sigma Aldrich, CAS #78560-45-9) was deposited on the windows through molecular vapor deposition in an evacuated dessicator. The spacer and pattern heights were measured using stylus profilometry (Ambios XP2). Prior to use (either

spin coating or photolithrography), both the fused quartz and sapphire disks were cleaned using piranha (3:1 stock sulfuric acid to 30% hydrogen peroxide) to remove any organic contamination. The disks were placed in the solution for at least 15 minutes. After removal from the piranha solution, the windows were immediately rinsed in deionized water (Milli-Q Gradient A10). They were then rinsed in acetone and dried with nitrogen.

The silanized windows were placed directly on top of the solid polymer nanofilm before heating began and were brought into physical contact with the upper aluminum chiller. The custom machined chiller was water-cooled using an external thermal reservoir (Fisher Scientific Model 910). The other major improvement that this setup had as compared to the one presented in Ch. 5 is that there was no viewing hole in the aluminum chiller block for visualization making the convention of calling it a "window" inaccurate. However, to preserve consistency with previous chapters we will continue to refer to them as windows. The absence of this hole meant that while the growth could not be measured *in situ*, the driving thermal fields were much more uniform. The increased uniformity of the temperature field meant a corresponding increase in the uniformity of the fabricated structures. After insertion into the setup, the heater was engaged and temperature of the center RTD reached the desired setpoint to within ±1 °C in a time of approximately 5 minutes. After a predetermined length of time ranging from 5 minutes to 120 minutes, the ceramic heating element was automatically turned off and the setup allowed to cool. The setup cooled to within 10 °C of the cold reservoir temperature (measured with the center RTD) before the sample was removed.

6.3 Microlens Array Characterization

The characterization of the microlens arrays produced by thermocapillary replication began with inspection of the surface profile using coherence scanning interferometry (also called scanning white light interferometry). In this technique, white light incident on the sample surface is interfered with light which passed through a reference arm. The resulting interference pattern shows fringes modulated by an overall Gaussian envelope. The maximum of the envelope occurs when the length of the reference arm equals the length of the sample arm, so from this measurement the surface profile of the sample can be measured. Using a Zygo NewView 600 and a Zemetrics Zegage, we measured the surface profile of the fabricated microlens arrays and have presented four qualitatively distinct topologies in Fig. 6.4. The full list of fabrication parameters can be found in Table 6.1.

Figure 6.3: Diagram of the full MicroAngelo experimental setup

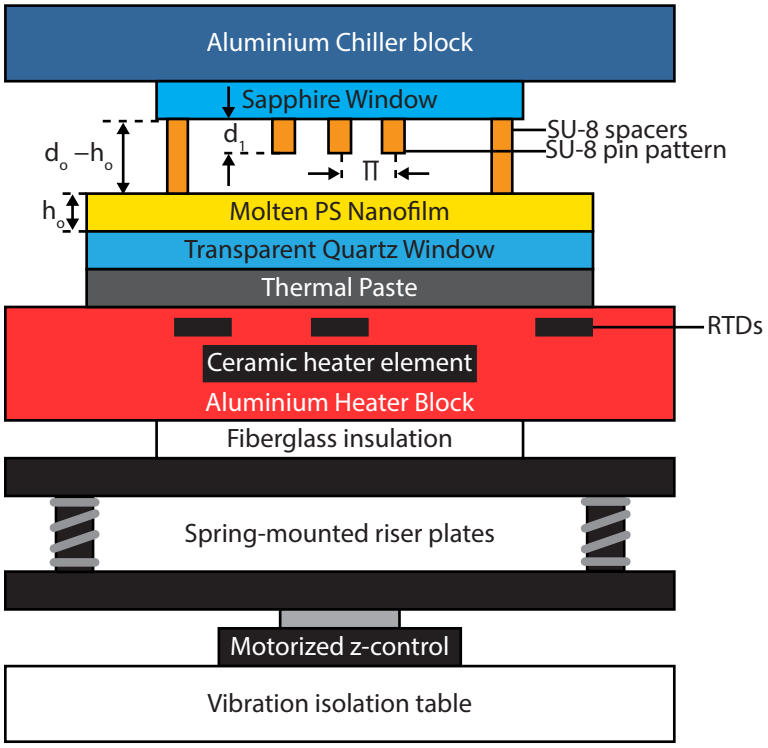

Diagram of the experimental setup used for MicroAngelo fabrication. Consistent with the geometries defined in previous chapters, the sample is heated from below and actively cooled from above. A full listing of the dimensions and parameters can be found in the text and in Table 6.1. Figure courtesy of Daniel Lim.

Fig. 6.4 exhibits four representative MLA topographies achieved through MicroAngelo fabrication, imaged using coherence scanning interferometry. The fabrication parameters and surface characteristics for each of the topographies are listed in Table 6.1. As seen in Fig. 6.4(a) and (b), we have successfully achieved both convex (converging) and concave (diverging) MLAs. Simple topologies are formed when the pin diameter, D_p, is much larger than the center-to-center pattern pitch, Π. When D_p is around the size of Π, the concave ridges around convex microlenses overlap to form smaller interstitial lens arrays. This achieves a hierarchical MLA structure where a smaller array of lenses is formed in the interstitial region of the larger lens array, as seen in Fig. 6.4(c). Hierarchical MLAs exhibit two distinct length scales, corresponding to the vertical size of the two lens arrays. We also report the fabrication of a lens structure with a central depression at the vertex of each microlens, seen in Fig. 6.4(d), which we call the caldera-like structure. During the course of this project, we discovered that the caldera-like microlens structure bears a strong resemblance to the microdonut topology fabricated by Vespini *et al.*

Figure 6.4: Topographies of fabricated microlens arrays

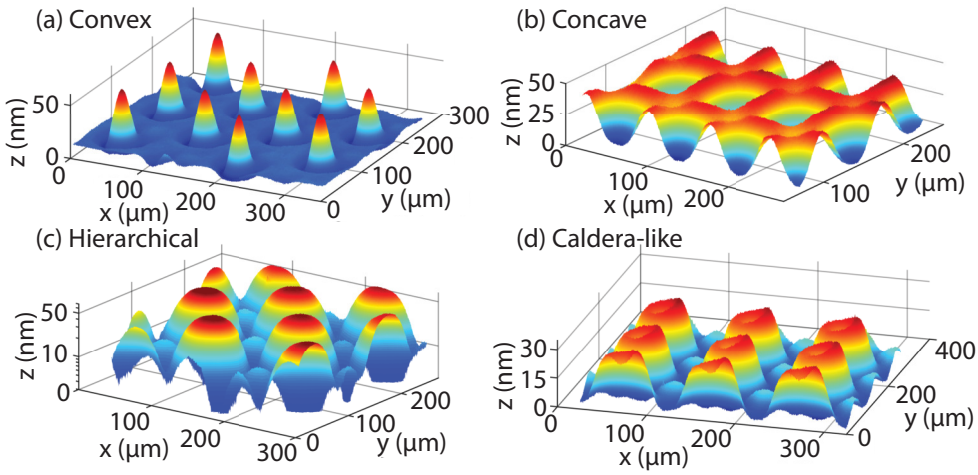

Surface topographies of fabricated microlens arrays imaged using coherence scanning interferometry. Note that the vertical axes have units of nanometers and the horizontal axes have units of microns; all microlenses shown here are actually wide and shallow. (a) Convex microlens array composed of converging lenses. (b) Concave microlens array composed of diverging lenses. (c) Hierarchical microlens array formed from two interdigitated arrays of different sizes. The vertical scale is logarithmically plotted to highlight the shorter secondary array between the main peaks. (d) Caldera-like microlens array with a central depression at the vertex of each lens. An additional array of smaller lenses is also visible in the interstitial region. Figure courtesy of Daniel Lim.

through spin-coating polymer onto a patterned pyroelectric substrate [57]. While Vespini *et al.* attributes the central depression formation to a slump of material away from the protrusion vertex during spin-coating, we will show through first-principles computational simulation in Sec. 6.4 that our caldera-like arrays evolve from the bottom-up and outside-in. The technique investigated by Vespini *et al.* has only achieved convex caldera-like ("microdonut") structures, whereas MicroAngelo has achieved concave caldera-like topologies as well and hence has access to a larger variety of curved topologies.

Beyond the qualitative observations gleaned from observation of microlens array surface profiles, we have also quantitatively characterized the microlens array properties using this surface profile data. In particular, we measured the lens diameter, fill factor, focal length, Fresnel number, asphericity, and surface roughness. Each of these measurements will be examined in the following sections.

6.3.1 Lens Diameter and Fill Factor

Since the lenses are formed with a continuous surface profile, there is no clear delineation between a lens and the neighboring interstitial regions. We defined a

Table 6.1: Parameter values for the fabricated microlens arrays

	Convex	Concave	Hierarchical	Caldera-like
t (min)	30	60	15	45
T_{cold} (°C)	60	60	60	60
T_{hot} (°C)	180	180	180	180
$d_o - h_o$ (nm)	1630 ± 40	1430 ± 50	1400 ± 30	1410 ± 20
d_1 (nm)	805 ± 7	880 ± 10	730 ± 10	730 ± 10
d_2 (nm)	-	320 ± 20	-	-
D_p (μm)	20	50	50	50
Π (μm)	100	75	100	100
h_o (nm)	228 ± 2	288 ± 4	288 ± 4	288 ± 4

Parameter values for the four microlens arrays imaged in Fig. 6.4. Uncertainties are one standard deviation unless otherwise stated. t is the fabrication time for which the heating elements were active. d_2 is the depth of the photoresist depression in a block and is only applicable to concave microlens array fabrication, as in the experimental setup shown in Fig. 6.1(b).

lens as the region of all contiguous pixels of the same curvature. Note that for the caldera-like lenses we included the center region of opposite curvature. We chose to use 8-connected pixels to determine neighboring pixels. The calculation of mean curvature is very noisy when performed on raw interferometric data, so first we smoothed the raw data using a cubic smoothing spline in MATLAB [25] (csaps routine with smoothing parameter set to 10^{-4}). From the fitted cubic spline, the mean curvature at all points was calculated and the points with the appropriate curvature were grouped together to form a lens. Note that the cubic spline was only used to find the points which were part of the lens. All calculations and derived values were performed on the raw and unsmoothed interferometric data. Since the resulting region was not strictly circular, we defined a characteristic diameter of the lens, D_{lens}, from the total area of the lens, A_{lens}, by the relation

$$D_{\text{lens}} = 2\sqrt{\frac{A_{\text{lens}}}{\pi}}. \tag{6.1}$$

The fill factor of the lens array was calculated by taking A_{lens} and dividing by the area of a unit cell. The computed lens diameters and fill factors can be found in Table 6.2.

6.3.2 Focal Length and Fresnel Number

With the lens domain determined by the sign of the curvature, the focal lengths of the fabricated microlenses were estimated by fitting the raw data within the lens domain to a paraboloid of the form

$$z(x, y) = z_{max} - \frac{(x')^2}{2R_1} - \frac{(y')^2}{2R_2}, \tag{6.2}$$

where z_{max} is the height of the lens at its vertex and R_1 and R_2 are the radii of curvature along the lateral principal axes, x' and y'. The principal axes of the lens are not guaranteed to coincide with the native coordinate system (x and y) of the interferometry data, so we used rotated coordinates

$$\begin{pmatrix} x' \\ y' \end{pmatrix} = \begin{pmatrix} \cos\theta & -\sin\theta \\ \sin\theta & \cos\theta \end{pmatrix} \begin{pmatrix} x - x_o \\ y - y_o \end{pmatrix}, \tag{6.3}$$

where θ is the angle of rotation of the principal axes (x', y') to the raw data axes (x, y) and (x_o, y_o) are the coordinates of the lens vertex in the raw data coordinates. The use of two independent radii of curvature allows us to account for any astigmatism in the lens. The corresponding focal lengths, f_1 and f_2, are then calculated from the lensmaker's equation using R_1 and R_2

$$\frac{1}{f_i} = \frac{n - 1}{R_i}, \tag{6.4}$$

where we have assumed that the lens is thin and that the back side of the lens is planar, corresponding to an infinite radius of curvature. The larger of the two calculated focal lengths was defined to be f_1 and the smaller was defined to be f_2. Since these lenses were used with HeNe lasers with an optical wavelength of 632.8 nm, a refractive index of 1.580 was used for the PS. This value was measured in our lab using an Abbe refractometer; for more details on this instrument please see Appendix A.6.

With the calculated lens diameters and focal lengths, we can evaluate whether the lenses are operating in the near-field or far-field regime at the focal plane of the MLA using the Fresnel number. The Fresnel number, evaluated at the focal plane of the lens, is defined by

$$F = \frac{a^2}{\lambda_{\text{opt}} f}, \tag{6.5}$$

where a is a characteristic size of the aperture and λ_{opt} is the wavelength of light at which the lens is being used. If F is less than 1, the beam is in the far-field while if F is greater than 1, the beam is in the near-field. In our case, we can evaluate the Fresnel numbers for both individual lenses, F_{lens}, and for the whole array F_{array}. These expressions are

$$F_{\text{lens}} = \frac{D_{\text{lens}}^2}{4\lambda_{\text{opt}} f}, \tag{6.6}$$

$$F_{\text{array}} = \frac{\Pi^2}{\lambda_{\text{opt}} f}, \tag{6.7}$$

where Π is the spatial period of the array. In all cases, the Fresnel numbers are small compared to unity, as can be seen in Table 6.2. This means that the lenses are operating in the Fraunhofer regime at the focal plane and diffraction is important.

6.3.3 Asphericity and Surface Roughness

To justify the selection of a paraboloidal geometry over a spherical geometry and quantify the degree of asphericity, we fit the lens cross section along its principal axes to an aspheric profile of the form

$$z(r) = z_{\text{max}} - \left[\frac{r^2}{(D_{\text{lens}}/2)\left(1 + \sqrt{1 - r^2/(D_{\text{lens}}/2)^2}\right)} + \alpha_4 r^4 \right], \tag{6.8}$$

where α_4 is the first aspheric coefficient and quantifies the degree of asphericity. The larger the value of α_4, the less spherical is the 1D lens profile. The lens profiles are displaced vertically so that the minimum (maximum) of the fitted convex (concave) lens lies at zero height and z_{max} corresponds to the height of the lens. To allow comparison of this asphericity over different lens sizes, we defined the asphericity ratio as the ratio of the α_4 contribution to the surface profile relative to the lens height, evaluated one characteristic radius away from the lens vertex

$$\text{AR} \equiv \left| \frac{\alpha_4 (D_{\text{lens}}/2)^4}{z_{\text{max}}} \right|. \tag{6.9}$$

The AR values calculated for the MLAs in Table 6.2 are less than one but still on the order of unity, indicating that the contribution due to the perturbing polynomial

is comparable to that of the spherical geometry. This result corroborates with the excellent fits obtained by the 2D paraboloidal surface in Eq. (6.2) over the lens surface. As a point of comparison for these reported values, a commercial spherical microlens array (Thorlabs MLA150-5C-M) evaluated using the same process yields an AR value of 0.04 ± 0.03 and a commercial parabolic microlens array (Thorlabs MLA300-14AR-M) yields a larger AR value of 0.13 ± 0.02.

The root mean square (RMS) residual of the 2D surface fit has two main contributions: the non-conformity of the microlens geometry to the paraboloid shape and the high spatial frequency surface roughness contribution. The RMS residual of this fit therefore provides an upper bound to the surface roughness of the fabricated surfaces. The majority of the microlens fits achieve an RMS residual of less than 2 nm, which also provides an upper bound to the low surface roughness of the ultrasmooth microlenses.

6.4 Numerical Simulations of Lens Evolution

To numerically simulate the growth and evolution of a microlens as a function of time, we have to return to the thin film equation for the thermocapillary model which was derived in Sec. 2.3.3. Specifically, we need a generalized form of Eq. (2.106) because that equation was derived under the assumption of perfectly flat, infinite bounding plates. Now that the top plate has nontrivial topography, we replace the constant D with a variable expression, $G(x, y)$, which describes the mask topography. The derivation proceeds identically to that presented in Ch. 2. The difference is that when we take the surface gradient of Γ the surface gradient acts on the variable G. G then replaces D in the denominator of the nondimensional temperature. As such, the thin film evolution equation for the TC model in the presence of bounding plates with topography is

$$\frac{\partial H}{\partial \tau} + \widetilde{\boldsymbol{\nabla}}_{||} \cdot \left[\frac{H^3}{3\overline{Ca}} \left(\widetilde{\boldsymbol{\nabla}}_{||}^3 H \right) + \frac{H^2 \kappa \overline{Ma}}{2} \widetilde{\boldsymbol{\nabla}}_{||} \left(\frac{H}{G + (\kappa - 1)H} \right) \right] = 0. \tag{6.10}$$

As before, H is the dimensionless film thickness, G is the dimensionless mask topography, τ is the dimensionless time, $\overline{Ca}$ is the modified capillary number, $\overline{Ma}$ is the modified Marangoni number, and κ is the thermal conductivity ratio. To proceed further with the finite element simulations this equation must be rewritten in terms of a coupled set of differential equations whose highest order derivatives are only

Table 6.2: Measured and derived values of the fabricated microlens arrays

	Convex	Concave	Hierarchical (interstitial array)	Caldera-like (depression)
D_{lens}	29.4 ± 0.5	51.3 ± 0.6	71 ± 2	71.0 ± 0.4
(μm)			(30 ± 2)	(21.6 ± 0.8)
Fill factor	7.9 ± 0.3	36.7 ± 0.8	39 ± 2	39.6 ± 0.4
(%)			(7.2 ± 0.7)	(3.7 ± 0.3)
f_1	6.2 ± 0.7	−23 ± 2	38 ± 9	
(mm)			(70 ± 10)	(−34 ± 6)
f_2	5.4 ± 0.3	−22 ± 2	29 ± 7	
(mm)			(47 ± 7)	(−23 ± 3)
$F_{\text{lens}} \times 10^{3\dagger}$	59 ± 5	46 ± 4	63 ± 14	
			(7 ± 2)	(7 ± 2)
$F_{\text{array}} \times 10^{3\dagger}$	687 ± 67	98 ± 8	127 ± 31	
			(72 ± 4)	(148 ± 36)
AR	0.5 ± 0.2	0.12 ± 0.03	0.5 ± 0.5	
			(0.5 ± 0.3)	(0.4 ± 0.2)
Roughness	1.3 ± 0.5	0.7 ± 0.1	1.4 ± 0.6	
(nm)			(0.49 ± 0.04)	(0.44 ± 0.02)

MLA parameters were measured for at least 10 lenses randomly selected over the array. Uncertainties are one standard deviation unless otherwise stated. For the hierarchical and caldera-like arrays, the values reported within parentheses correspond to the interstitial array and the central depression, respectively, while the main array values are immediately above them.
†Parameter was calculated at the HeNe laser wavelength λ_{opt} = 632.8 nm.

of second order. This yields

$$\frac{\partial}{\partial\tau}\begin{bmatrix} H \\ 0 \end{bmatrix} + \widetilde{\boldsymbol{\nabla}}_{||} \cdot \begin{bmatrix} \dfrac{1}{3\overline{Ca}} H^3 \widetilde{\boldsymbol{\nabla}}_{||} C + \dfrac{\kappa\overline{Ma}}{2} \dfrac{GH^2}{[G+(\kappa-1)H]^2} \widetilde{\boldsymbol{\nabla}}_{||} H \\ \widetilde{\boldsymbol{\nabla}}_{||} H \end{bmatrix} - \widetilde{\boldsymbol{\nabla}}_{||} \cdot \begin{bmatrix} \dfrac{\kappa\overline{Ma}}{2} \dfrac{H^3}{[G+(\kappa-1)H]^2} \widetilde{\boldsymbol{\nabla}}_{||} G \\ \widetilde{\boldsymbol{\nabla}}_{||} H \end{bmatrix} = \begin{bmatrix} 0 \\ C \end{bmatrix}, \quad (6.11)$$

where C is a dummy variable which equals the Laplacian of the film height, H. Within the context of these simulations, there is a well-defined lateral length scale,

the mask pin pitch, Π. As such, the same expressions from Ch. 2 still hold, but with L replaced by Π. This equation is now suitable for simulation in the commercial finite element simulation program, COMSOL [28]. The constituent elements are P2 Lagrange triangular elements.

The specific geometry chosen for the simulations is diagrammed in Fig. 6.5. A set of four pins arranged in a 2x2 grid were suspended over a nanofilm and the domain was modeled using periodic boundary conditions on all the lateral boundaries. Note that in the dimensionless units chosen for the simulations, the film thickness was 1 vertical unit and the mask pin pitch was also 1 lateral unit. The specific G that describes this geometry is

$$G = \frac{d_o}{h_o}(1 - \delta \times f_p), \tag{6.12}$$

where $\delta = d_1/d_o$ and f_p is the protrusion function which is a periodic extension of COMSOL's built-in rectangle function over the [0,2]×[0,2] computational domain.

$$f_p(x, y) = \text{rect}\left[\sqrt{(x - 0.5)^2 + (y - 0.5)^2}\right]. \tag{6.13}$$

The rectangle function was set to have an upper limit of 0.25 and a lower limit of -0.25 and a transition zone width of 0.1. The initial condition for the simulation was a dimensionless film height of unity plus small random noise

$$H(x, y, \tau = 0) = 1 + 0.1 \times rn(x, y), \tag{6.14}$$

where $rn(x, y)$ is the 2D random number generator native to COMSOL. Each argument of the random function is sampled from a normal distribution with $\mu = 0$ and $\sigma = 0.05$. Note that the model is not sensitive to the random initial height because the capillary term in the the thin film equation damps out high spatial frequency components and the time-dependent COMSOL computation is based on an implicit backward differentiation solver. These two facts guarantee the numerical stability of the solution and eliminate the high frequency components after the first timestep.

To further investigate the formation dynamics of the caldera-like MLA presented in Fig. 6.4(d), we chose the same parameters for the numerical system as were used in the experimental fabrication. A full listing of the parameters used in the simulation can be found in Table 6.3. We note that the temperature drop ΔT was computed from

Figure 6.5: Geometry of the mask used in MLA finite element simulations

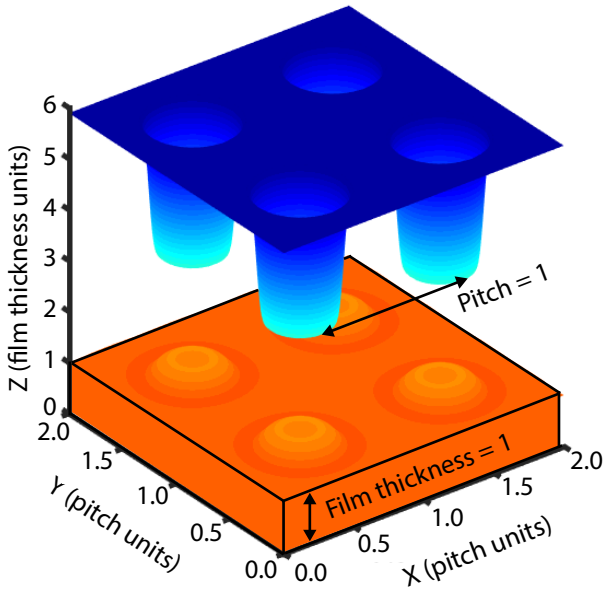

COMSOL simulation geometry of a 2x2 array of pins (blue) above a molten polymer surface (orange). Vertical heights are normalized to the initial film thickness and horizontal lengths are normalized to the pitch of the periodic array. Figure courtesy of Chengzhe Zhou.

a separate steady state finite element simulation of the temperature in the domain, consistent with the simulations described in Sec. 5.3.

The results of the finite element simulations described by Table 6.3 are shown in Fig. 6.6. Fig. 6.6(a) contains cross sections from the experimental surface profile measurements of Fig. 6.4 for comparison. Looking at the cross sections of the numerical simulations in Fig. 6.6(b) we see that polymer begins accumulating below the edges of the chilled pins to form a ring-like protrusion (0.6 minutes), then forms a caldera-like lens with a wide central depression (4.5 minutes). At late times, the central depression vanishes (5.7 minutes) and the microlenses form convex topographies (6.5 minutes). This transition from a caldera-like topography to a convex topography is also shown in Fig. 6.6(c) where the height of the central point in the microlens and the highest point of the microlens are simultaneously plotted. As we see, the caldera-like topographies are a transitory early stage in the film evolution and can only be accessed by halting fabrication during a specific regime.

6.5 Microlens Array Application: Shack-Hartmann Wavefront Sensor

To further characterize the MLAs fabricated with MicroAngelo, we wanted to investigate the focusing behavior of the caldera-like lenses as well as use them in a

Table 6.3: List of parameters for the simulation of microlens evolution

Parameter	Description	Value
h_o	Unperturbed film height	288 nm
$d_o - h_o$	Spacer height	1410 nm
d_1	Pin height	730 nm
Π	Pin pitch	100 μm
D_p	Pin diameter	50 μm
ΔT	Temperature jump across gap	6.27 K
γ	Film surface tension (extrapolated) [22]	3.5×10^{-2} N/m
$-d\gamma/d$T	Surface tension temperature coefficient [22]	7.2×10^{-5} N/(m-K)
k_{air}	Air thermal conductivity (interpolated) [21]	0.032 W/(m-K)
k_{film}	Film thermal conductivity [22]	0.128 W/(m-K)
η	Film viscosity (interpolated) [24]	32.5 Pa·s
ϵ	h_o/Π	0.00288
$\overline{CaMa}$	$\frac{\cancel{\eta\mu_c}}{\gamma\epsilon^3}\frac{\epsilon\gamma_{\text{T}}\Delta\text{T}}{\cancel{\eta\mu_c}}$	1490
D	$\frac{d_o}{h_o}$	5.90
δ	$\frac{d_1}{d_o}$	0.430
κ	$k_{\text{air}}/k_{\text{film}}$	0.247
t_{viscous}	$\eta\Pi/\gamma\epsilon^3$	3.89×10^6 s

Shack-Hartmann wavefront sensor. Shack-Hartmann wavefront sensors are devices which measure wavefront distortion and have applications in adaptive optics [58]. The general premise of this type of sensor is that each lens in the array will focus an incoming plane wave to a distinct spot on a camera. If the incoming plane wave has been perturbed, then the location of the focused spot will shift on the camera and this can be used to determine properties of the incident wave. A diagram of our implementation of a SHWS is shown in Fig. 6.7. In this setup we spatially filtered the output of a 632.8 nm HeNe laser, collimated the resulting beam and transmitted it through an MLA where it was then imaged. The air perturbations were then introduced between the collimating lens and the MLA.

Before we get to the results of the SHWS setup, we wanted to verify that our lenses adequately focused light and to probe the transmission pattern of the caldera-like

Figure 6.6: Comparison of experimental MLA cross sections to numerical simulation cross sections

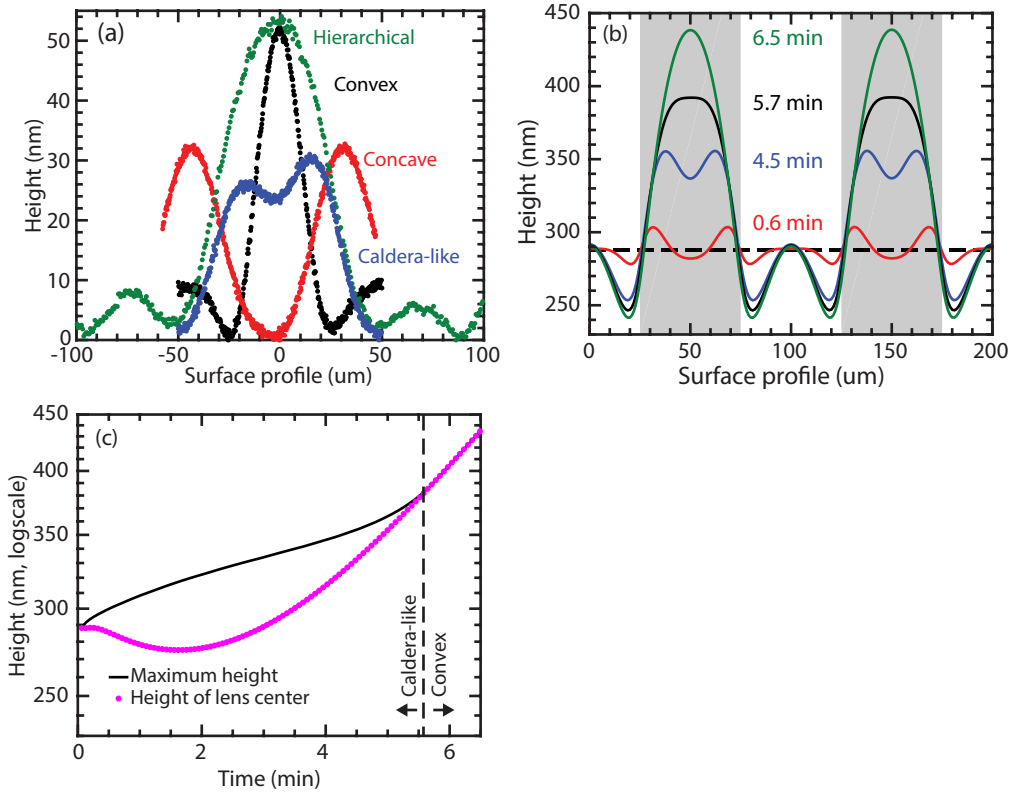

(a) Experimental cross sections from coherence scanning interferometry of microlenses from each of the four arrays in Fig. 6.4. (b) Cross sections from the simulation of convex microlens array evolution at four times. The gray shaded region represents the points directly under the photoresist pins. (c) Time dependence of the maximum height of a single microlens and central height of the microlens. The central region is initially lower than the maximum height, indicating that the microlens formed a caldera-like geometry with a concave top. At late times the central region becomes the highest point, indicating a transition from a caldera-like regime to a convex regime. Figure courtesy of Chengzhe Zhou and Daniel Lim.

lenses. The radial intensity of the transmitted light through a caldera-like MLA as a function of displacement from the lens surface is shown in Fig. 6.8(a). In this figure we see a clear annular focus at the left dashed line (green) and the corresponding camera image is shown in Fig. 6.8(b). Further away from the surface of the lens, at the right dashed line (red), we see that the light has been focused to an approximately Gaussian spot in Fig. 6.8(c). The central depression has opposite curvature and is responsible for the initial annular focusing. Further away, the MLA behaves as an ordinary converging lens array would. This data was recorded by placing the MLAs lens-side up on an optical microscope (Olympus BX60 with Olympus UMPlanFL 5x, 0.15 NA, 20.0 mm working distance objective) configured

Figure 6.7: Diagram of the Shack-Hartmann wavefront sensor setup

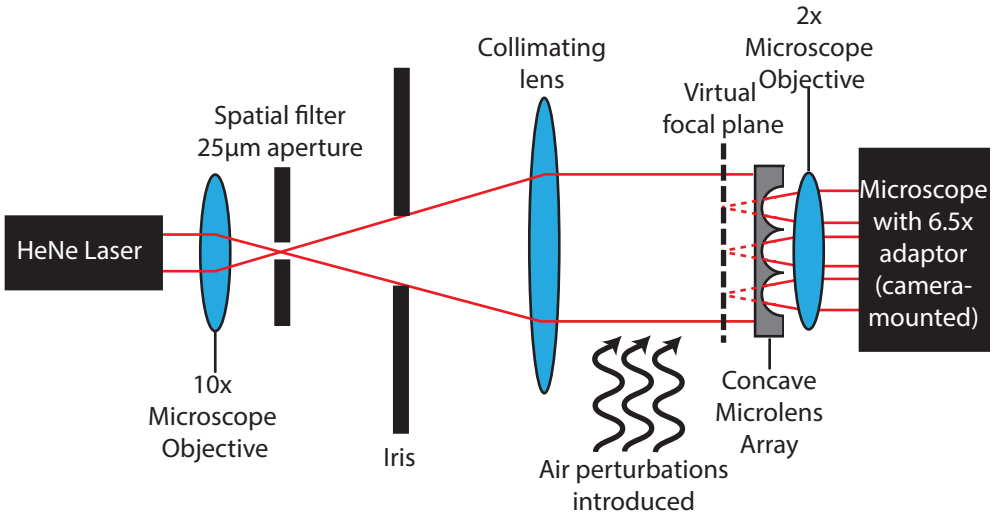

Shack-Hartmann wavefront sensor experimental setup for evaluating concave microlens arrays. Air perturbations will displace the incoming wavefront which is imaged by the MLA and the camera. Figure courtesy of Daniel Lim.

for transmitted light illumination from a halogen bulb. The vertical position of the MLAs was controlled to an accuracy of 1 μm using the microscope fine adjust knob and the resulting transmitted light images were captured at various vertical distances using a high resolution monochrome CMOS camera (Basler acA2500-14gm, 2592 $\times$ 1944 pixels, 2.2 μm $\times$ 2.2 μm pixel size) with a fixed exposure time set to avoid pixel saturation at any pixel in the stack. The zero of the vertical displacement was taken to be at the position where the surfaces of the lenses were in focus. The images were aligned in ImageJ (Template matching and Slice alignment plugin) [59–61] and were imported into MATLAB for radial averaging of the pixel intensities to be performed around each lens focus position. The radial averaged intensity distributions for each of 53 lens positions were averaged to obtain the radial intensity distribution for a single cross-sectional slice.

The remainder of Fig. 6.8 shows the results of a caldera-like MLA in a SHWS. This MLA had very large concave depressions that effectively behaved like a diverging MLA. This implementation of a SHWS is different than conventional approaches, which typically use converging lens arrays [58]. In our modified SHWS, a Helium-Neon laser (λ_{opt} = 632.8 nm, 05-LHP-991, Melles-Griot) was attenuated (ND 1.5, 30898, Edmund Optics), focused through a microscope objective (10x, 0.25 NA, Newport) onto a spatial filter (25 m diameter, 910PH-25, Newport) and collimated (KPX115AR.14 plano-convex lens, Newport). An iris was used to transmit only the

central Gaussian spot to be normally incident on the planar face of the fused quartz MLA substrate. A caldera-like MLA was used in conjunction with a 2x microscope objective (Mitutoyo M Plan Apo 2, NA 0.055, working distance 34 mm) to focus the incident wavefront onto a dot array. The microscope objective was coupled to a high resolution monochrome CMOS camera (Basler acA2500-14gm, 2592×1944 pixels, $2.2\ \mu\text{m} \times 2.2\ \mu\text{m}$ pixel size) by a Navitar 6.5x ultra-zoom lens. The microlens array was mounted onto a micrometer translation stage oriented along the direction of laser propagation and was positioned in front of the virtual focal plane so that the camera recorded an array of focused laser dots. The air in between the collimating lens and the microlens array was perturbed using short sprays of a canned air duster (Miller-Stephenson MS-222N containing 1,1,1,2- Tetrafluoroethane). The duster sprays were oriented perpendicular to the optical axis to avoid physical movement of the optical components. Since the shifts in dot array position were minuscule, the recorded video of the focused dots evolving under the air perturbation was processed using ImageJ in two steps. Firstly, an image of the dot array positions under stationary experimental conditions was subtracted from each frame in the video to accentuate the spatial displacement of each focused beam. Only focused dots that were displaced from their equilibrium positions were visible after this step. Secondly, the subtracted images were thresholded at the same level and converted into binary masks for improved contrast. Fig. 6.8(d) is an example of the perturbed dots after they have been processed, showing the location of the air perturbation. In Fig. 6.8(e) you can see the regular array of focused spots when there is no perturbation in the system which is subtracted from each video frame.

6.6 Discussion of Microlens Fabrication with MicroAngelo

As we presented the fabrication of microlenses in this chapter, there are several salient features of this process to highlight. First, since MicroAngelo is a noncontact technique, the fabricated microlens surfaces are very smooth, as was verified through the use of coherent scanning interferometry data. Surface roughness on the order of 2 nm corresponds to less than a 1% variation in total lens thickness. Beyond the quality of the fabricated lenses, MicroAngelo is a parallel fabrication technique able to make lens arrays over a large area. The MLAs presented above are approximately 2 mm square and this can easily be increased by using a large mask pattern. The only limit on the lateral extent of the fabricated arrays is a practical concern raised by the difficulty of keeping two flat plates parallel at a separation distance of a micron over large lateral distances. Additionally, we have demonstrated that MicroAngelo

Figure 6.8: Caldera-like MLA transmitted light profiles and SHWS image

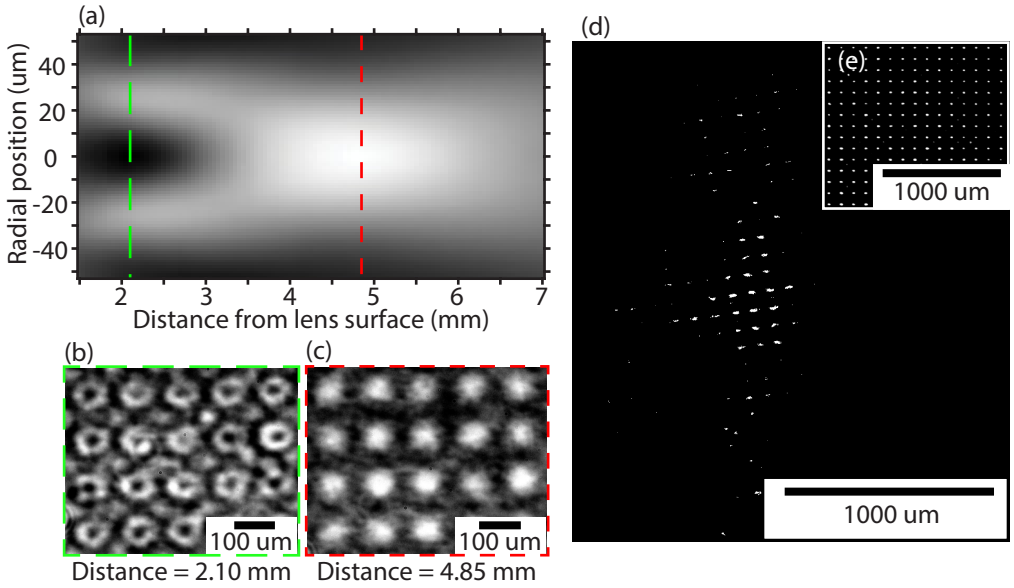

(a) Radial intensity of transmitted light through caldera-like array lens shown in Fig. 6.4(d) as a function of vertical displacement from the lens surface. The plot is azimuthally symmetric about the optical axis (radial position zero). (b) Transmitted light image captured 2.10 mm from the surface of the caldera-like MLA, corresponding to the green dotted line position in (a). Annular focusing with a central minima is observed due to the central caldera lens depression. (c) Transmitted light image captured 4.85 mm from the surface of the caldera-like MLA, corresponding to the red dashed line position in (a). Approximately Gaussian focusing is observed due to the convex portion of the lens. (d-e) Focused dot arrays from a collimated light source transmitted through a concave microlens array. Scale bars refer to distances along the camera sensor. The images have been despeckled once and the contrast has been enhanced. (d) Still frame of an air disturbance proceeding from left to right. The visible dots indicate positions where the focused dot was displaced from the still-air position. (e) The dot array in still air is well-defined and highly regular. Figure courtesy of Daniel Lim.

is capable of producing a variety of unique lens topographies from a single mask pattern by freezing the film at a transitory state in the film evolution process. This means that with suitable control of the process parameters exotic geometries can be achieved, such as the caldera-like lens arrays, which would not be accessible using a fabrication technique that always came to equilibrium.

While we believe that MicroAngelo has great potential for fabrication of micro-optical components, there are a couple areas where improvement is necessary. First, in the above work we were not able to achieve a fill factor approaching 100% due to the issue of overlap and interstitial feature creation, such as in the case of the hierarchical arrays. This means that less light will be focused than with a completely packed square or hexagonal lens array. Second, the lenses presented above show an astigmatism which is evident in the discrepancy between the two measured focal

lengths in Table 6.2. We believe that this is caused by unintended lateral flow of the lens material due to slight variations among the spacer heights. This would mean that there was a slight tilt between the cooled window and the supporting substrate which leads to macroscopic lateral flow. Regardless, both of these issues could be resolved through further experimental and numerical studies of the fabrication parameters.

6.7 Summary

Thermocapillary sculpting with MicroAngelo has been shown to be a viable, single-step method of fabricating microlens arrays by projecting a temperature field onto a polymer surface using thermal conduction from photoresist patterns. A wide range of microlens topographies are available, controlled by a number of tunable process parameters. Feature overlap can be used to create highly nontrivial features, including hierarchical arrays and caldera-like arrays, in a single process step. The functionality of the fabricated MLAs has also been proven in a wavefront sensing application.

Chapter 7

MICROANGELO SCULPTING: WAVEGUIDE FABRICATION

7.1 Background

Waveguides are one of the fundamental building blocks of photonic circuits because they form the connections between all other optical components. In this chapter, we report the use of a thermocapillary sculpting technique which possesses the advantages of both smooth surfaces and large area patterning in a single process step. This technique has been named MicroAngelo and was discussed in Ch. 6 in relation to the fabrication of microlens arrays. We investigated the use of MicroAngelo to fabricate linear polymeric waveguides and characterized their physical and optical properties.

The remainder of this chapter is organized in the following manner. First, in Sec. 7.2 we briefly describe MicroAngelo and the fabrication process. Next, we characterize the fabricated waveguides physically, optically, and numerically in Sec. 7.3. We then discuss the particular advantages and disadvantages of fabricating linear waveguides with MicroAngelo in Sec. 7.4 and conclude with Sec. 7.5.

7.2 Thermocapillary Sculpting of Optical Waveguides

Thermocapillary forces have been the subject of scientific interest since the dawn of the 20th century and have garnered continued interest since then [62–64]. Thermocapillary forces are surface forces which arise in free surface films due to variations in surface tension caused by thermal gradients. Since surface tension is a generally decreasing function of temperature, warmer regions have a lower surface tension while cooler regions have a higher surface tension. This gradient in surface tension creates a shear along the interface from low to high surface tension which deforms the interface and with it, the bulk. During the past decade, attention has focused on the application of thermocapillary forces to molten nanofilms across which a temperature gradient is applied [1, 8–10, 39]. A typical experimental geometry is depicted in Fig. 7.1. An initially flat nanofilm with height h_o is heated from below and held at a temperature T_{Hot}. Concurrently, a cooled plate held at a temperature T_{Cold} is brought a distance d_o away from the hot plate. On this cool plate is a periodic, linear pattern defined photolithographically with height L_{pin}. In this study, the periodicity of the pattern was set so that neighboring waveguides would not

Figure 7.1: Schematic of the experimental setup used to fabricate waveguides

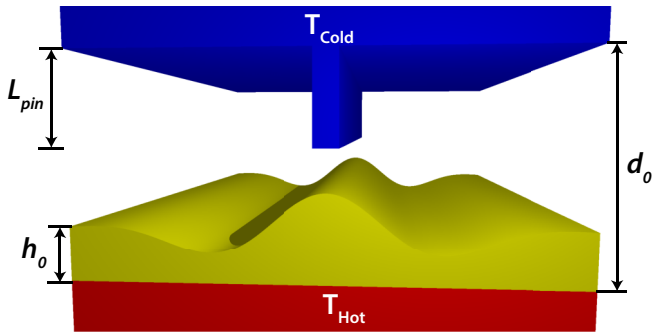

Schematic of the experimental setup (not to scale) which depicts the waveguide fabrication process. The molten nanofilm is bounded from below by a heated substrate and from above by a patterned linear mask which is actively cooled. The height of the pattern, L_{pin}, and the total plate separation, d_o, are typically on the order of microns, while the initial film thickness, h_o, is on the order of hundreds of nanometers. Note that only one line in the pattern is shown in this figure, but the patterns used in the study were periodic laterally on the order of 500 microns.

interact (periodicity of 500 μm or larger). The width of the protruding lines in the pattern was equal to 3 μm. The presence of the pattern localizes the thermocapillary stress beneath it and causes local deformation upwards which produces the desired waveguides. We note that the temperatures set for the heater, T_{Heater}, and the chiller, $T_{Chiller}$, are not equal to T_{Hot} and T_{Cold}, respectively, due to temperature drops within the setup itself.

The details of the heating and cooling in the experimental setup used in the this study have been described previously in Ch. 6. As such, we will only briefly outline the waveguide fabrication procedure here and highlight the differences in the patterned mask. The waveguide material was chosen to be polystyrene (PS) and the substrate was 5 micron thick thermal silicon dioxide on a silicon wafer (WRS Materials). PS is a commonly used polymer for optical devices because it has low optical absorption [65] and is readily available commercially [66]. The substrate material was chosen because the oxide has a lower refractive index than the PS which is a requirement for guided modes to exist in the PS layer. The wafer was also very flat, which allowed for precise fabrication and then for the underlying silicon wafer to be cleaved to produce coupling facets and to isolate the waveguides. To create the initially flat nanofilm, PS was dissolved in toluene at 3% to 6% weight and then spun coat on the oxide wafers at 2000 to 3000 RPM for 30 seconds with an acceleration of 1000 RPM/s. The toluene rapidly evaporated, which left a thin solid film of PS which was suitable for waveguide fabrication. The solid nanofilm was inserted into the experimental setup and brought into contact with patterned spacers on the top plate

Table 7.1: Experimental parameters for each of the four fabricated waveguides

Sample Number	1	2	3	4
h_o (nm)	164	147	138	223
d_o (μm)	10.7	10.7	10.7	10.3
L_{pin} (μm)	4.29	4.29	4.29	3.34
T_{Heater} (°C)	120	120	120	150
T_{Chiller} (°C)	30	30	30	40
t (min)	10	15	45	265

(not shown in Fig. 7.1) which set the total gap distance, d_o, to around 10 microns. The previously fabricated patterns had heights of L_{pin} ranging from 3.34 to 4.29 μm. A full listing of the experimental parameters for the waveguides presented in this study can be found in Table 7.1. As compared to the mask patterns in Ch. 6, these patterns are linear and show periodicity in only one direction whereas the patterns for MLA fabrication had 2D periodicity. The film was heated for times between 10 minutes and 4 hours at heater temperatures of 120 to 150 °C with an external chiller setpoint of 30 to 40 °C. After the fabrication period, the sample was allowed to cool back to the temperature of the chiller which occurred within 10 to 15 minutes. At this point, the waveguides had solidified and were removed from the experimental setup. After visual inspection to locate the waveguides, the silicon wafer was cleaved to isolate the fabricated waveguides and produce high quality end facets suitable for optical coupling.

7.3 Waveguide Characterization

We undertook an extensive study of the linear waveguides and their physical and optical properties. Physical characterization was accomplished using optical microscopy, coherence scanning interferometry, and profilometry to inspect the waveguide surface and extract the profile of its cross section. The optical characterization focused on measurement of the number of waveguide modes, the structure of those modes, a lower bound on the coupling efficiency, and the TM extinction ratio for those waveguides which supported only TE modes. Numerical simulations were also performed to compute the waveguide mode structure and compared with the experimental results.

Figure 7.2: Images of a fabricated waveguide

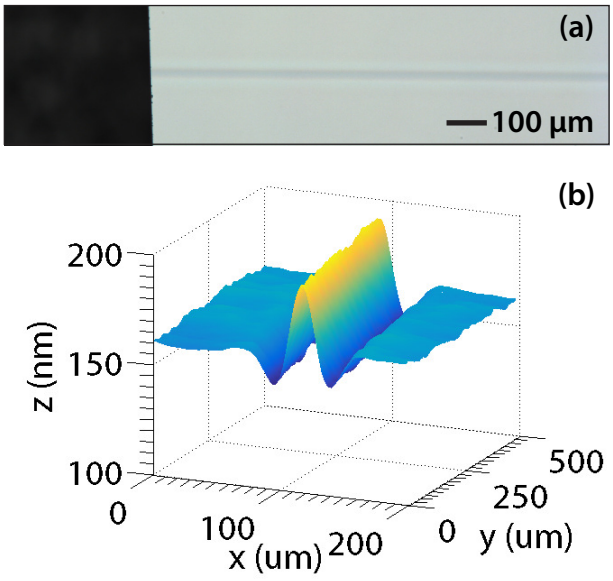

(a) Optical microscope image of a waveguide seen from above. The underlying substrate has been cleaved to produce the sharp facet seen on the left. (b) Coherence scanning interferometry data of the waveguide surface.

7.3.1 Physical Characterization of Waveguides

After cleaving, the waveguide structure was first visually inspected with an optical microscope for any large scale defects which interacted with the waveguide backbone. A representative image of the waveguide seen from above is shown in Fig. 7.2(a). The cleaved edge shows a sharp transition at the end facet with no rounding or deformation of the waveguide facet. The backbone of the waveguide is visible as a slightly darker horizontal stripe in this image due to thin film interference. The waveguide surface profile was then analyzed with a coherence scanning interferometer (Zemetrics ZeGage). One such surface profile scan is shown in Fig. 7.2(b).

Additionally, the waveguide cross section was measured with a profilometer (Dektak XT) in the direction perpendicular to the direction of light propagation within the waveguide. For the waveguide shown in Fig. 7.2(a), this corresponds to a scan in the vertical direction and four such scans are plotted in Fig. 7.3. The profile of the waveguide cross section was then fit by an analytic function so that it could be used in the numerical simulations described below. The fitting function for this structure was a sinusoid modulated by a Gaussian decay. All of the profilometer data was shifted so that the peak of the waveguide occurred at $x = 0$, which allowed us to use

Figure 7.3: Profilometer scans of waveguide cross sections

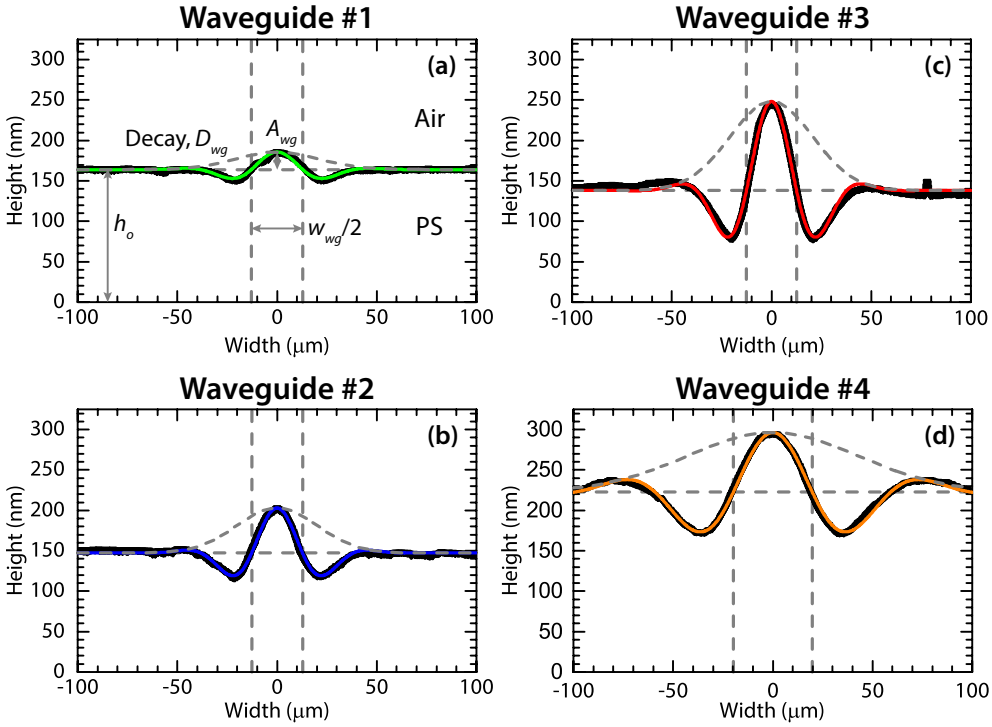

Profilometer cross sections of four waveguides perpendicular to the propagation direction. In the optical image from Fig. 7.2(a), this corresponds to a scan in the vertical direction. The solid curves are numerical fits parameterized by Eq. 7.1 and the numeric values of the constants can be be found in the third column of Table 7.2. The waveguide shown in Fig. 7.2 corresponds to the profilometer scan in (b).

a simple sinusoid without a lateral offset. The function had the form

$$F(x) = A_{wg} \cos\left(\frac{2\pi x}{w_{wg}}\right) e^{-(x/D_{wg})^2} + h_o, \tag{7.1}$$

where A_{wg} is the amplitude of the waveguide, w_{wg} is the waveguide width, D_{wg} is the decay of the Gaussian, and h_o is the background film height, which was equal to the initial film thickness of the solid nanofilm. A full listing of the fits for the waveguides considered in this study can be found in Table 7.2.

7.3.2 Optical Waveguide Modes

As seen in Fig. 7.3, the resulting waveguide cross section is very different from a traditional rectangular waveguide cross section produced from photolithographic techniques. As such, the structure of the waveguide modes is of interest here. To couple light into the MicroAngelo waveguides, we used a setup which is diagrammed

Table 7.2: Fitting constants for the measured waveguide cross sections for each of the waveguides

Sample Number	1	2	3	4
A_{wg} (nm)	22	56	110	73
w_{wg} (μm)	51	51	50	79
D_{wg} (μm)	29	29	29	61
h_o (nm)	164	147	138	223

Figure 7.4: Diagram of optical characterization setup

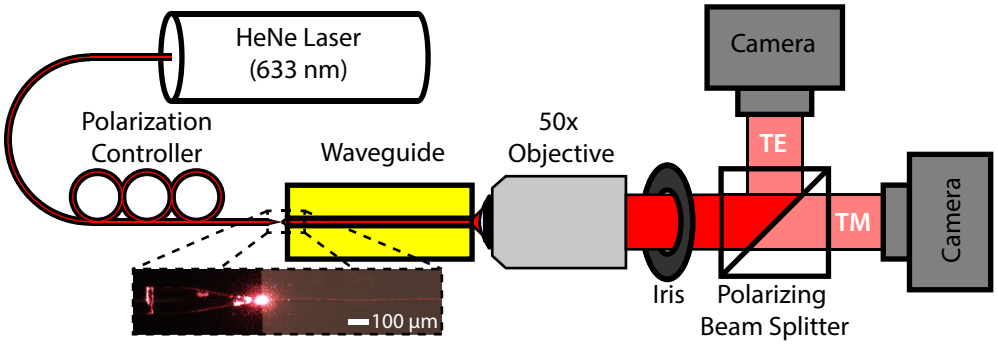

Diagram of the optical testing setup which allows for coupling of light into the waveguide modes and then visualization of the waveguide output. The waveguide modes are visualized simultaneously in both TE and TM polarizations through the use of a polarizing beam splitter (PBS).

in Fig. 7.4. Light from a HeNe laser (Meller Optics, 25-LHP-991-249, 633 nm) was coupled into a lensed single mode optical fiber (Lase Optics LF-SM-DW-07-630-HP-FC/APC, 500 nm x 10 μm spot size, 50°wedge angle) which was end coupled to the waveguide. This fiber was mounted on a stages which provided three translational degrees of motion as well as tip, tilt, and rotation control. After the sample was mounted on a separate stage with three translational degrees of freedom, the output facet of the waveguide was brought to the focal plane of a 50x microscope objective. The image of the microscope objective was focused concurrently on two cameras after passing through an iris and a polarizing beam splitter (Thorlabs PBS25-633). The iris was adjusted so that the only light which corresponded to the guided mode passed through. This reduced background scattered light from defects and cladding modes (when they exist). In addition to the polarization separation achieved by the beam splitter, the polarization of the input light was controlled through the use of a polarization controller (Thorlabs FPC030).

Generally, we have presented one waveguide from each of four different regimes in Table 7.2, starting from the smallest and proceeding to the largest waveguides. The smallest waveguide was single mode with only a single TE mode. The next smallest waveguide had several TE modes, but no TM modes. The third waveguide in the table had a few TM modes and many TE modes. The last, and largest, waveguide had many TE and many TM modes. The qualitative features of waveguide #1 and #2 are similar, as are #3 and #4. As such, we will only present coupling images for waveguides #2 and #3.

Waveguide #2 is the second smallest waveguide presented, (second column in Tables 7.1 and 7.2) and has several TE modes and these are shown in the left column of Fig. 7.5. Interestingly, no TM modes were observed for this waveguide. The different TE modes were selectively excited by moving the lensed optical fiber laterally along the input facet of the waveguide. The first order mode could be found in the middle of the waveguide and then small translations in either direction yielded successively higher order modes in sequential order. Looking closely at the higher order modes in Fig. 7.5(b) and (c) there is a slight asymmetry in the mode profile. We ascribe this to the fact that the coupling was dominated by the higher order mode but that there were still some lower order mode excitations which were localized on the side which the fiber was translated towards. For the higher order modes with multiple lobes, the image was normalized to the less intense lobe to highlight the structure. In general, we observed that the lateral extent of the mode increased as the mode order did. The vertical confinement was good at all mode orders although the exterior lobes of the higher order modes extended successively further into the silicon dioxide layer.

If we increase the dimensions of the waveguide, as in waveguide #3 (third column of Tables 7.1 and 7.2) the waveguide can then support TM modes. The images in Fig. 7.6 show the only two TM modes of waveguide #3. Generally, a modest number of modes of either polarization were easy to identify and selectively excite by moving the coupling fiber. Once there are many modes, as is the case for the TE modes of waveguide #3 and #4, it becomes difficult to definitively selectively excite and categorize them. This is especially true when simultaneously exciting TE and TM modes because the fiber position which excited a clean TM mode often excited multiple TE modes, and vice versa. As such, we have not presented TE modes for waveguide #3, although they do exist and are qualitatively similar to the TE modes presented in Fig. 7.5. No attempt was made to optimize and match the modes of the

Figure 7.5: Optical images of the TE modes from waveguide #2

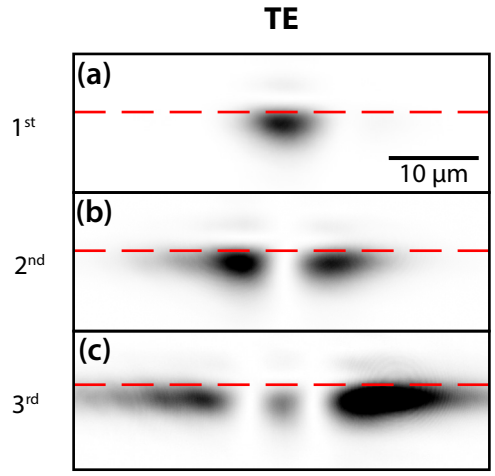

Optical images of the TE modes from a μAngelo waveguide. Each mode has been normalized to show the mode structure. The thickness of the PS film is approximately 100 nm to 200 nm and the dotted line is the presumed film location. Both the vertical and horizontal scales are equal.

Figure 7.6: Optical images of the TM modes from waveguide #3

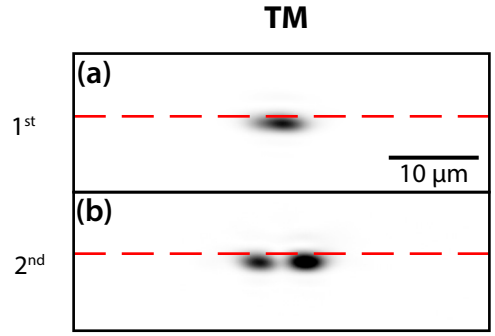

Optical images of the TM modes from a μAngelo waveguide. Each mode has been normalized to show the mode structure. The thickness of the PS film is approximately 100 nm to 200 nm and the dotted line is the presumed film location. Both the vertical and horizontal scales are equal.

fiber to the modes of the waveguides in this study.

Beyond the qualitative observations of the mode structure, this optical setup has the capability to quantitatively measure two aspects of the waveguides: a lower bound on the coupling efficiency and the TM extinction ratio. By replacing the cameras with photodiodes, the power of both the TE and TM polarizations was measured concurrently. In this configuration, the coupling efficiency was measured by normalizing the measured power in each photodiode when the waveguide was inserted by the measured power when the waveguide was not present and the optical fiber was at the focal point of the imaging objective. This measurement quantifies

Table 7.3: Coupling efficiency lower bounds and TM extinction ratio measurements

Sample Number	1	2
TE Coupling Efficiency Lower Bound (%)	2.4	16
TM Extinction Ratio (dB)	-36	-36

the amount of incident power which the waveguide transmitted, although it is only a lower bound because we did not optimize the mode matching between the coupling fiber and the waveguide. For the waveguides that only support TE modes, they can be used as polarizing waveguides in the same vein as in-line polarizers. It is therefore interesting to characterize the TM extinction ratio of the waveguides. Note that this measurement only applies to those waveguides which do not support TM modes. This measurement was completed by taking the ratio of the coupling efficiencies for the TM and TE modes for a given coupling position. In other contexts, this number is often computed by taking the ratio of the optical powers which pass through the waveguide or polarizer. This would be equivalent to the procedure described above if the amount of power in both the TE and TM modes was equal. However, MicroAngelo waveguides which only have TE modes are so efficient at damping optical power in the TM polarization that we must put significantly more TM power than TE power into the waveguide to have a measurable TM signal. As a result, the use of coupling efficiencies instead of raw optical powers compensates for the fact that the input power in each polarization was not equal. This technique relies on the assumption that the coupling for the TE and TM modes was equal, which will only strictly hold for the lowest order mode. As such, the coupling efficiency lower bounds and TM extinction ratio results for only the lowest order modes are listed in Table 7.3. We note that these extinction ratio measurements are pushing the limits of the experimental setup because the PBS is only listed to -35 dB. Additionally, this large extinction ratio was expected because this sample did not support TM modes.

7.3.3 Numerical Simulations of Waveguide Properties

Because of the special profile of the waveguides, it is important to understand the mode structure in the waveguide. Since the waveguide geometry described by Eq. (7.1) was too complicated to solve analytically for the waveguide modes we performed numerical simulations to investigate the number of modes, mode structure, and the effective refractive index of the modes. The finite element simulations

were performed using commercial software [28] to simulate the wave equation and the geometry of the simulations is diagrammed in Fig. 7.7(a). The overall domain measured 100 microns in width and 10 microns in height. The lower half of the domain was thermal oxide with refractive index 1.457 [67] (at λ_{opt} = 633 nm) and the waveguide surface was defined using Eq. (7.1) and the geometric parameters in Table 7.2. The PS was modeled with a refractive index of 1.58, which was measured by an Abbe refractometer (Vee Gee Instrubments C10); see Appendix A.6 for more details about this instrument. The remainder of the geometry was an air domain with a refractive index of 1.0001. The exterior boundaries of the domain were modeled as perfect electric conductors, although the exterior boundaries were positioned far enough away from the modes that the specific choice of boundary condition had virtually no effect on the calculated modes. The domain was meshed with mapped rectangular elements. Five elements composed the height of the waveguide and 32 elements were used in the vertical direction for the two domains above and below the waveguide. In the lateral direction, 2500 elements were used which kept the shape of the elements within the waveguide nearly square and smaller than $\lambda_{opt}/4$. In total, 170,000 elements were used with approximately 2×10^6 degrees of freedom. The geometry of the simulated waveguide is shown in Fig. 7.7(a) using the the waveguide geometries listed in Table 7.2. In Fig. 7.7, the numerical simulations of the modes corresponding to Figs. 7.5 and 7.6 are shown. Each mode is normalized to have unit intensity for presentation purposes and there is qualitative agreement between the simulated modes and the experimental modes presented previously.

Comparison of μAngelo Waveguides to Rectangular Waveguides

Waveguides fabricated lithographically typically have rectangular cross sections while MicroAngelo waveguides do not as Fig. 7.3 clearly demonstrates. As such, this difference in cross section is a natural comparison point for MicroAngelo waveguides. We have compared the mode structure of waveguides with a rectangular cross section to MicroAngelo waveguides in Fig. 7.8. The computational geometry for the rectangular waveguides is shown in Fig. 7.8(a). The geometric parameters of the rectangular waveguide were equivalent to those used in Fig. 7.7(a), although the decay parameter of the Gaussian, D, is not needed. For the purposes of this comparison, we chose to use the largest waveguide presented in the fourth column of Table 7.2. In Fig. 7.8(b) and 7.8(c) the intensity of the first 10 TE modes have been plotted as a function of lateral position. Each successive mode has been normalized to unity and offset vertically for visualization. These curves are produced

Figure 7.7: Computational domain and simulated waveguide modes

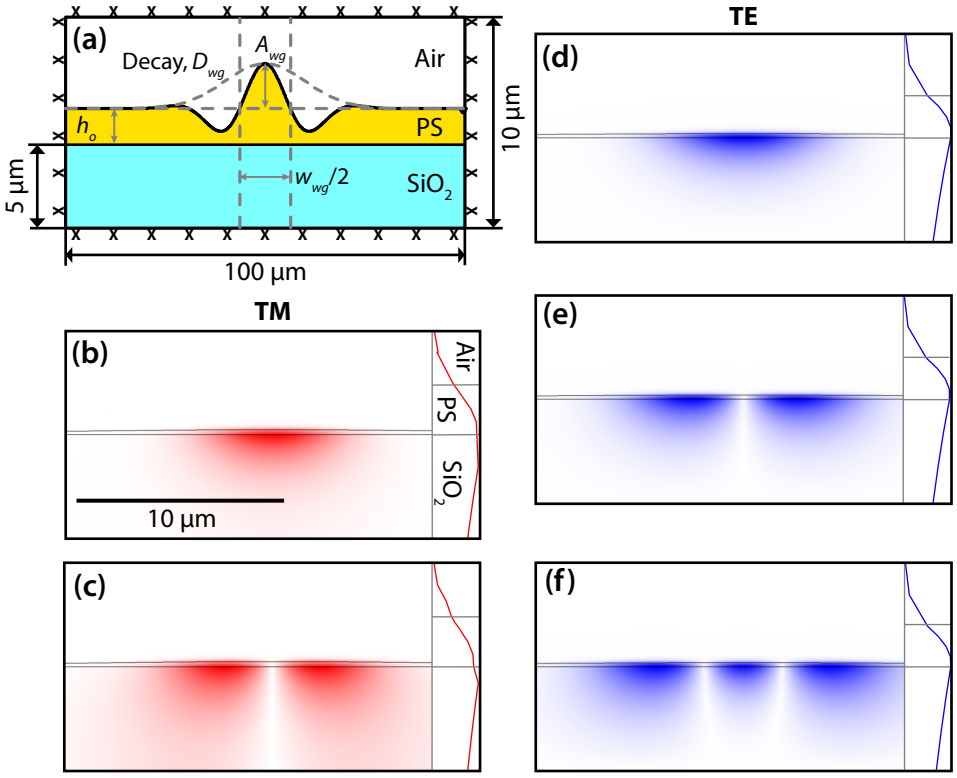

(a) Schematic of the domain (not to scale) used in the finite element simulations of the μAngelo waveguide modes. The overall domain is centered on the waveguide maximum whose analytic form was determined by fitting a profilometry scan of the waveguide cross section, as in Fig. 7.2(c). The boundary condition on all sides was a perfect electric conductor condition. (b), (c) Simulated TM modes for waveguide #3 which possessed two TM modes and whose experimentally measured modes were shown in Fig. 7.6. (d), (e), (f) Simulated TE modes for waveguide #2 whose experimentally measured modes were shown in Fig. 7.6. For all parts (b) through (f), the curves on the right show a magnified plot of the E-field magnitude through the three material layers at the lateral location of maximum intensity.

by integrating the mode structure, such as those shown in Fig. 7.7(b) and 7.7(c), in the vertical direction. In addition, the lateral extent of the rectangular waveguide has been added to Fig. 7.8(b) to highlight the fact that modes of every order extend over the entire cross section of the waveguide. In Fig. 7.8(c) the overlaid parabola does not correspond to the physical waveguide cross section, but is to help guide the eye and highlight the fact that higher order modes in MicroAngelo waveguides have larger lateral extent. Additionally, these two plots spur an analogy to quantum mechanics. The modes of the rectangular cross section waveguide in Fig. 7.8(b) bear a striking resemblance to the modes of the infinite square well. Similarly, the modes in Fig. 7.8(c) for a MicroAngelo waveguide bear a strong resemblance to the modes of the quantum harmonic oscillator. This implies that the mode structure of

the waveguides is analogous to the probability density of the wavefunction in the corresponding quantum system. Furthering this analogy we can also associate the eigenvalues of each problem so that the effective refractive index of the waveguide modes would be analogous to the energy of the corresponding quantum system. This analogy would imply that the same relationships hold between the energy differences of consecutive modes and the difference between the effective refractive index of consecutive modes. The energy difference between consecutive modes in the quantum harmonic oscillator is [68]

$$E_{\nu+1} - E_\nu = \hbar\omega \propto \text{Constant}, \tag{7.2}$$

where $\hbar$ is the reduced Planck's constant, ω is the frequency of the oscillator, and ν is the mode order. For the infinite square well, the energy difference between modes is

$$E_{\nu+1} - E_\nu = \frac{\hbar^2\pi^2\,(2\nu+1)}{2ma^2} \propto \text{Linear}. \tag{7.3}$$

In this expression, m is the mass, and a is the width of the well. Based on these results, we would expect that the difference between the effective refractive index of consecutive modes for the waveguide with a rectangular cross section should be linear in the mode number, while for MicroAngelo waveguides, the difference should be constant. As plotted in Fig. 7.8(d), the effective refractive index differences do indeed follow this trend for the first 10 modes. The trend continues until close to cutoff where the effective refractive index of the waveguide modes is very close to the refractive index of the cladding.

Single Mode μAngelo Waveguides

With a better understanding of how the waveguides studied in this work compare to traditional waveguides with rectangular cross sections, we investigated another major criteria for waveguide fabrication. The ability to create single mode waveguides is a crucial benchmark for future photonic circuits created with MicroAngelo because single mode waveguides are much easier to work with than multi-mode waveguides. All traditional lithographic techniques are able to make single mode waveguides and we have successfully fabricated a single mode waveguide with MicroAngelo. The dimensions of this waveguide are in the first column of Table 7.2 and we observed only a single TE mode which was quite similar to the first order mode shown in

Figure 7.8: Comparison between MicroAngelo and rectangular waveguides

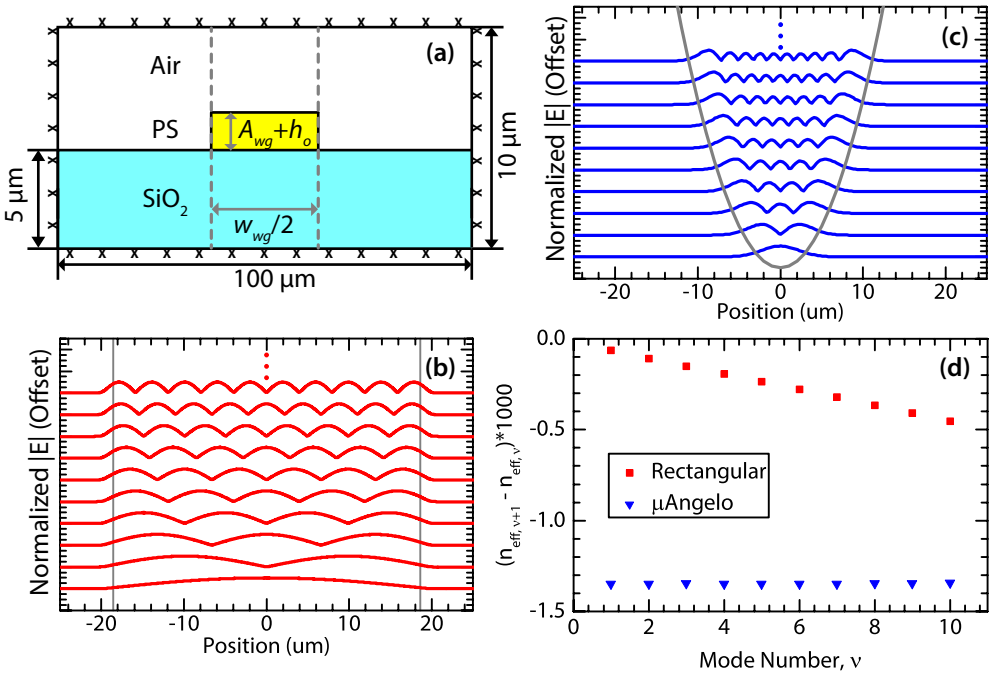

(a) Schematic of the domain (not to scale) used in the finite element simulations of the rectangular waveguide modes. The same waveguide dimensions are used to parameterize the rectangular geometry as in Fig. 7.7(a). The boundary conditions on the exterior edges of the domain are all perfect electric conductors. (b) Spatial distribution of waveguide mode intensity of a rectangular waveguide with the dimensions listed in the fourth column of Table 7.2. The vertical lines in this plot denote the edges of the rectangular waveguide. (c) Spatial distribution of waveguide mode intensity for a μAngelo waveguide with the dimensions listed in the fourth column of Table 7.2. The overlaid parabola in this plot does not correspond to the waveguide surface profile, it is solely to guide the eye. (d) Effective refractive index difference between successive modes plotted as a function of mode number for both rectangular and μAngelo waveguides.

Fig. 7.5(a). Generally, there are two ways to achieve single mode operation. The first is to tune the geometry to only support a single mode at a specified wavelength. The second is to tune the wavelength for a given geometry. We considered both of these scenarios in turn using numerical simulations to vary the relevant parameters.

To investigate the effect of geometry on the number of waveguide modes, we performed a numerical parameter sweep in which three parameters of the fitting function defined by Eq. 7.1 were varied. In particular, we varied the waveguide width, w_{wg}, the background film height, h_o, and the waveguide amplitude, A_{wg}. In a separate scan (not shown here), we also varied the Gaussian decay, D_{wg}, but found that it did not have an appreciable effect on the number of guided modes in the parameter regime where we have fabricated waveguides. The wavelength for this computational study was held fixed at 633 nm to match the experimental setup. The results of

the parameter sweep are plotted in Fig. 7.9(a) where we varied the waveguide width from 45 to 80 microns in steps of 5 microns. Simultaneously, the amplitude was varied from 5 to 160 nanometers in steps of 5 nanometers while the background film height was varied from 100 to 170 nanometers also in steps of 5 nanometers. Each point on this graph represents a set of geometric parameters which only supports a single TE mode. After completing this scan, we noted that the amplitude and the background film height are strongly correlated and so we have plotted this same data set in Fig. 7.9(b) where the waveguide width is plotted against the total waveguide height which was defined as $A_{wg} + h_o$. Based on these results, there is a clear region of parameter space where single mode waveguides can be fabricated, but that the tolerances on each of the geometric parameters, besides D_{wg}, are relatively strict.

Instead of varying the geometry as was done in Fig. 7.9, the geometry can be held fixed and the wavelength of the guiding light varied. In this way, a waveguide with a fixed geometry should be single mode for some range of wavelengths. For these simulations, the geometry of waveguide #2 was used while the wavelength was varied. The wavelength was varied from 550 nm to 750 nm in steps of 5 nm and over this range the refractive indices of the PS and the thermal oxide have significant variation. For this study, we used the refractive index values as a function of wavelength for silicon dioxide from literature [67], while for PS we used the Cauchy equation whose coefficients were determined from a set of three independent measurements made at different wavelengths using an Abbe refractometer (see Appendix A.6 for more details). The results of this wavelength scan are plotted in Fig. 7.10. There is a large range spanning over 100 nm in wavelength for which this waveguide geometry will support TE modes, but will not support TM modes. This is called the polarization window and MicroAngelo waveguides have polarization windows greater than 100 nm which is competitive with commercial polarizing optical fibers [69]. Furthermore, there is a 30 nm window in wavelength near 750 nm where this geometry will be single mode.

7.4 Discussion of MicroAngelo Waveguides

There are several unique features related to fabricating waveguides with MicroAngelo. First, the surfaces are solidified directly from a melt. As such, they have minimal surface roughness which means that there are minimal scattering losses from the waveguide surface. Second, the most unique property of the technique is that it can fabricate curved optical structures which would be difficult or time consuming with traditional techniques. Due to conservation of mass, the waveguide

Figure 7.9: Single mode MicroAngelo waveguide geometries

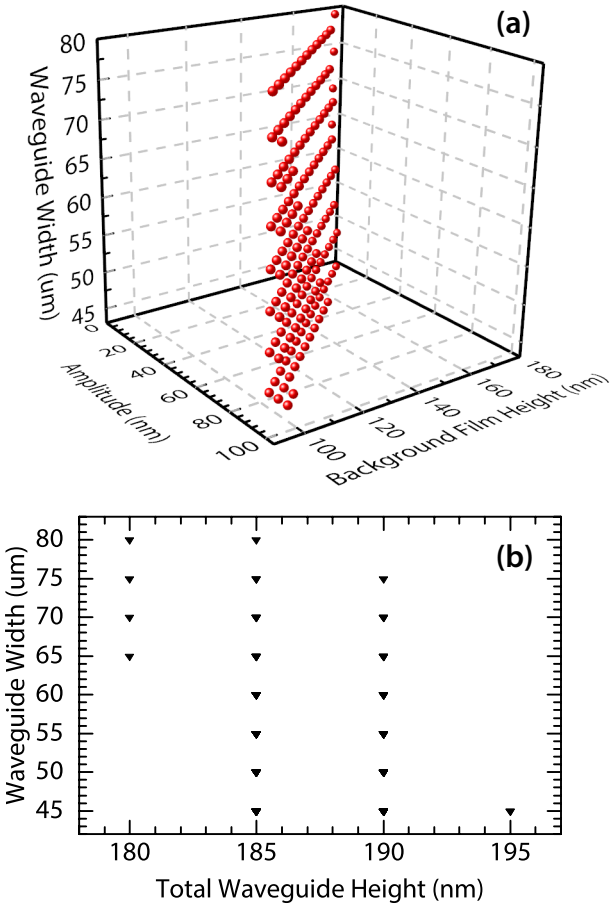

(a) Numerical parameter sweep of the waveguide dimensions to determine the geometries which would support only a single guided mode. These parameter ranges incorporate the full range of waveguides which have been fabricated to date. The value of the decay was fixed at 29 μm and variation of it was found to have negligible impact on the number of guided modes. (b) Single mode geometries as a function of waveguide width, w, and total waveguide height, $A_{wg} + h_o$.

formation process depletes the immediately adjacent regions which leads to a self-localizing effect. Third, MicroAngelo is a parallel fabrication technique which can pattern large areas simultaneously. This means that it is fast, efficient, and scalable.

On the other hand, MicroAngelo is restricted to the long wavelength regime. This means that the fabricated structures will always have relatively flat profiles, with small aspect ratios (height:width), which leads to strong geometric birefringence. Due to the vastly different length scales in the lateral and vertical directions, the TE polarization is strongly preferred over the TM polarization. This causes the polarizing behavior of waveguides 1 and 2 in Table 7.2 and the polarization window in Fig. 7.10. It is also interesting to note that single mode waveguide operation

Figure 7.10: Polarization window of waveguide #2

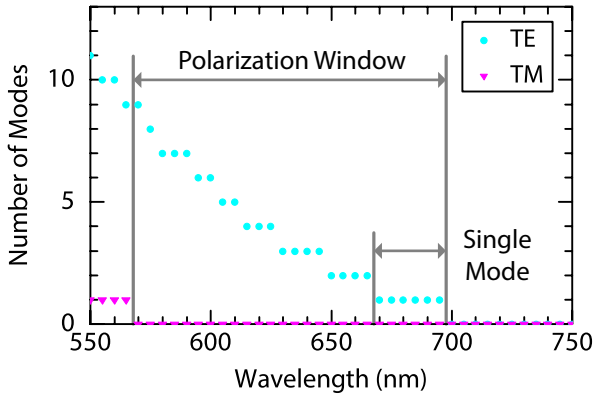

Number of guided modes as a function of the wavelength of light which is being guided. There is a significant region where the waveguide functions as a polarizing waveguide since it supports TE modes but not TM modes. Additionally, a subset of this region supports only a single TE mode.

in this case is truly single mode in the sense that there is only one mode with TE polarization. Most single mode waveguides support one mode in each of the two orthogonal polarizations, TE and TM.

The strong geometric birefringence in waveguides created by the small aspect ratio is not solely restricted to waveguides fabricated with MicroAngelo. For instance, a rectangular waveguide which has a small height and a large width would show similar effects [70]. What is unique about the nonrectangular cross sections of these waveguides is that they localize the modes near the center of the waveguide. This mitigates the difficulties associated with coupling from an optical fiber into the waveguide modes. From a practical perspective, this means that you can get the unique polarization characteristics in a MicroAngelo waveguide with far less of a decrease in coupling efficiency as compared to an equivalent rectangular waveguide.

The ability of these waveguides to act as polarizing elements means that they can be integrated natively onto a chip and function as useful optical elements without the need for a polarization splitter or rotator. Additionally, we have shown that they possess characteristics comparable to commercial alternatives but with a much smaller footprint. This work on linear waveguides has also laid the foundation for the fabrication of more complex optical components which could be fabricated with MicroAngelo. In the future, these optical components could be integrated into optical photonic circuits which can be fabricated in a single process step.

7.5 Summary

In this chapter, we have demonstrated the capability of thermocapillary sculpting to fabricate linear optical waveguides out of polymeric nanofilms. We extensively characterized their physical characteristics and optical properties. We identified the unique properties of these waveguides. In particular, the very small aspect ratio of the waveguides induced geometric birefringence which preferentially suppressed the TM modes in favor of TE modes. Due to the nonrectangular cross section of the waveguide, the modes were localized near the center of the waveguide which allowed us to couple to them more effectively than would have been otherwise possible. The waveguide mode structure observed experimentally showed qualitative agreement with the numerical simulations. Furthermore, we performed numerical parameter sweeps to investigate geometries and wavelengths where these waveguides would support only a single guided TE mode. The fabrication process and unique waveguide properties open new possibilities in integrated photonic circuits and sensor applications.

Chapter 8

CONCLUSIONS AND SUGGESTED EXPERIMENTAL IMPROVEMENTS

My thesis has been broadly presented in two parts. The first part contained Ch. 2, Ch. 3, Ch. 4, and Ch. 5 and dealt primarily with basic scientific investigations of nanofilm instabilities. Specifically, we investigated the dominant physical mechanism behind a thin film instability driven by large transverse thermal gradients. We determined that the dominant mechanism was thermocapillary forces which act along the nanofilm interface from warmer regions to cooler regions due to the variation of surface tension with temperature. After determination that thermocapillary forces played a key role in the dynamics of this system, the second part of the thesis, Ch. 6 and Ch. 7, focused on the fabrication of mirco-optical devices. In particular, we fabricated and characterized mircolens arrays and optical waveguides.

Looking back at the complete body of work, there are several overarching themes and observations about this system which will be examined. In particular, we will discuss some of the lessons learned during determination of the instability mechanism in Sec. 8.1. Then, Sec. 8.2 contains a discussion of MicroAngelo as a thermocapillary sculpting fabrication technique and finally, in Sec. 8.3, we conclude with areas of improvement and future study.

8.1 Dominant Instability Mechanism: Thermocapillary Forces

As has been extensively detailed in Ch. 3, Ch. 4, and Ch. 5, the thermocapillary (TC) model best describes this experimental system. However, it is interesting to look at what this means for the other two proposed models. The surface charge (SC) model is a completely valid thin film instability that just doesn't apply to this experimental system. It seems there is no clear mechanism for interfacial charge accumulation in our experimental setup. However, intentional placement of charge at the interface could be achieved with an additional processing step under an electron beam or ion gun which would make the SC model very relevant. On the other hand, the acoustic phonon (AP) model is more problematic as there is no clear system which would correspond to this model. The assumption of phonon propagation and then coherent reflection off the interface of a molten film is a stringent one and it is not satisfied by this material system.

Conductive heat transfer through the nanofilm/air bilayer is what makes these experiments possible. We have found that these experiments required large, sustained thermal gradients which can be difficult to achieve due to thermal diffusion. As compared to other fields, such as electric fields, it is much more difficult to localize heat flux because the spread in conductivities between thermal conductors and insulators is much smaller than the corresponding spread between electrical conductors and insulators. In surmounting this difficulty, we found that even small absolute temperature drops can lead to enormous gradients, provided that the gap for the temperature drop is small enough. We also learned that in nanofilm experiments the incredibly large difference in scales between the largest and smallest component can lead to counter intuitive behavior. In this system, the small size of the low thermal conductivity layers means that even though the thick layers have much higher thermal conductivity, the total temperature drop across the macroscopically large, high thermal conductivity layers can be greater than the drop across the nanoscale, low thermal conductivity layers. This is very counter intuitive when transitioning from macroscopic systems where all the components are of approximately the same size. In these macroscopic systems, the temperature drop is usually strongly localized in the low thermal conductivity layers and the high thermal conductivity layers can typically be ignored when considering the heat transfer through the system. This lesson is highlighted by our finite element simulations of the temperature within the experimental setup presented in Fig. 5.2(c). If you were to use the nominal difference between the heater and chiller setpoints as the temperature drop across the nanofilm/air bilayer, then you would vastly overestimate the actual temperature drop.

The last major theme for my experimental instability investigations is that when comparing experimental data to the predictions of linear stability theory, it is crucial to extract the experimental data at the earliest possible times because linear stability is a perturbative technique. This will typically make the experiments much more difficult. In our case, we needed to do *in situ* observation of the instability with height deflections on the order of nanometers. However, it represents a significant improvement over previous experimental investigations in this system which were allowed to grow far outside the linear range where other effects like contact with the bounding plate and film depletion became important.

8.2 Thermocapillary Sculpting of Nanofilms: MicroAngelo

The use of thermocapillary forces to sculpt nanofilms through the MicroAngelo technique shows a great deal of promise for future study. While we focused specifically on polymer nanofilms in this thesis, this was for experimental convenience and not a restriction of the technique. Indeed, MicroAngelo is generalizable to basically any thin film due to the universality of surface tension. The only requirement is that the film be molten, but this is an engineering challenge, not a physical limitation. Especially now that we know the dominant physical mechanism driving the deformation, the design and fabrication of structures is an area ripe for joint exploration by experimental and numerical studies of the deformation process. We spent most of our time in the long wavelength regime where the vertical length scales were significantly smaller than the lateral ones because it allowed the easiest connection between theoretical predictions and experimental measurements. However, this assumption can be relaxed during fabrication and might also lead to the creation of novel features. Due to its reliance on surface tension, MicroAngelo creates smooth and rounded structures, which means that it can act as a complimentary technique to traditional lithographic techniques which typically produce flat, 2.5 D structures. Empirically, it appears that patterns with in-plane curvature, such as rings, are easier to fabricate than long, straight patterns.

8.3 Areas for Further Study and Improvement

There are a few immediate improvements that could be made to the fabricated microlens arrays and waveguides. For the microlenses, fabrication would have been somewhat easier with a lower chiller temperature. In the regime chosen for fabrication, the chiller setpoint was approximately equal to the glass transition temperature of the polymer. This could have potentially influenced the resulting lens topography during removal from the setup. With a lower chiller temperature, the lenses would have solidified faster and been less sensitive to the conditions during removal. For the waveguides, it would have been useful to introduce a slight bend in the waveguide to offset the input and output ports. This did not end up being extremely problematic, but it would have helped to reduce the effect of cladding modes and background scattered light.

In terms of general fabrication improvements with the current setup, removing the thermal paste between the silicon wafer and the aluminum heater holder from the setup is highly recommended. The thermal paste was originally designed to provide good thermal contact between the aluminum heater holder and the nanofilm

substrate. Unfortunately, the thermal paste was highly non-Newtonian and was not amenable to precision dispensation. Even when we filled a mold in an attempt to control the amount of thermal paste, variable amounts of thermal paste were left on the mold depending on the speed, direction, and technique of removal. As the thermal conductivity of the paste is not very large, it could be beneficial to remove it completely and rely on the contact between the back surface of the substrate and the polished top surface of the aluminum holder. This would remove a major source of uncertainty in the fabrication process and hopefully improve the reproducibility of the fabrication.

The last major issue with this iteration of the experimental setup is that achieving parallelism to within nanometers over centimeters is very challenging. We tackled this issue by taking great care to use a level spin coater when making the spacers on the sapphire window. We made them photolithographically, but it would be interesting to fabricate them out of metal instead because they would probably have better structural properties. A more radical solution would be to remove the top plate to sidestep the issue completely. This would require a different heat transfer mechanism than pure conduction to create the necessary gradients, but would offer significant advantages during sample preparation.

BIBLIOGRAPHY

[1]E. McLeod, Y. Liu, and S. M. Troian, "Experimental verification of formation mechanism for pillar arrays in nanofilms subject to large thermal gradients", Phys. Rev. Lett. **106**, 175501 (2011).

[2]S. Y. Chou, and L. Zhuang, "Lithographically induced self-assembly of periodic polymer micropillar arrays", J. Vac. Sci. Technol. B **17**, 3197–3202 (1999).

[3]L. Zhuang, "Controlled self-assembly in homopolymer and diblock copolymer", PhD thesis (Princeton Univ., Princeton, NJ, 2002).

[4]E. Schäffer, "Instabilities in thin polymer films: structure formation and pattern transfer", PhD thesis (Konstanz Univ., 2001).

[5]E. Schäffer, S. Harkema, R. Blossey, and U. Steiner, "Temperature-gradient-induced instability in polymer films", Europhys. Lett. **60**, 255–261 (2002).

[6]E. Schäffer, S. Harkema, M. Roerdink, R. Blossey, and U. Steiner, "Morphological instability of a confined polymer film in a thermal gradient", Macromol. **36**, 1645–1655 (2003).

[7]J. Peng, H. Wang, B. Li, and Y. Han, "Pattern formation in a confined polymer film induced by a temperature gradient", Polymer **45**, 8013–8017 (2004).

[8]M. Dietzel, and S. M. Troian, "Formation of nanopillar arrays in ultrathin viscous films: the critical role of thermocapillary stresses", Phys. Rev. Lett. **103**, 074501 (2009).

[9]M. Dietzel, and S. M. Troian, "Thermocapillary Patterning of Nanoscale Polymer Films", in *Materials Systems and Processes for Three Dimensional Micro- and Nanoscale Fabrication and Lithography*, Vol. 1179E, edited by S. M. Kuebler, and V. T. Milam, (Materials Research Society, 2009).

[10]M. Dietzel, and S. M. Troian, "Mechanism for spontaneous growth of nanopillar arrays in ultrathin films subject to a thermal gradient", J. Appl. Phys. **108**, 074308 (2010).

[11]F. Ay, A. Kocabas, C. Kocabas, A. Aydinli, and S. Agan, "Prism coupling technique investigation of elasto-optical properties of thin polymer films", J. Appl. Phys. **96**, 7147–7153 (2004).

[12]K. Kurabayashi, M. Asheghi, M. Touzelbaev, and K. E. Goodson, "Measurement of the thermal conductivity anisotropy in polyimide films", J. Microelectromech. Syst. **8**, 180–191 (1999).

[13]P. Deshpande, X. Sun, and S. Y. Chou, "Observation of dynamic behavior of lithographically induced self-assembly of supramolecular periodic pillar arrays in a homopolymer film", Appl. Phys. Lett. **79**, 1688–1690 (2001).

[14]S. Y. Chou, L. Zhuang, and L. Guo, "Lithographically induced self-construction of polymer microstructures for resistless patterning", Appl. Phys. Lett. **75**, 1004–1006 (1999).

[15]E. Schäffer, S. Harkema, M. Roerdink, R. Blossey, and U. Steiner, "Thermomechanical lithography: pattern replication using a temperature gradient driven instability", Adv. Mater. **15**, 514–517 (2003).

[16]E. McLeod, and S. M. Troian, "One step non-contact fabrication of polymer microlens arrays by thermocapillary lithography", CLEO:2011 - Laser Applications to Photonic Applications, CML3 (2011).

[17]S. J. VanHook, M. F. Schatz, J. B. Swift, W. D. McCormick, and H. L. Swinney, "Long-wavelength surface-tension-driven Benard convection: experiment and theory", J. Fluid Mech. **345**, 45–78 (1997).

[18]S. J. VanHook, M. F. Schatz, W. D. McCormick, J. B. Swift, and H. L. Swinney, "Long-wavelength instability in surface tension driven Benard convection", Phys. Rev. Lett. **75**, 4397–4400 (1995).

[19]L. G. Leal, *Advanced Transport Phenomena: Fluid Mechanics and Convective Transport Processes* (Cambridge University Press, 32 Avenue of the Americas, NY 10013-2473, USA, 2007).

[20]D. J. Griffiths, *Introduction to electrodynamics*, 3rd ed. (Prentice-Hall, Inc., Upper Saddle River, New Jersey 07458, 1999).

[21]D. R. Lide, ed., *CRC Handbook of Chemistry and Physics*, 81st (CRC Press, Boca Raton, 2000).

[22]Z. Pu, "Polystyrene", in *Polymer Data Handbook*, edited by J. E. Mark, (Oxford University Press, New York, 1999).

[23]J. R. Welty, C. E. Wicks, and R. E. Wilson, *Fundamentals of Momentum, Heat, and Mass Transfer*, 3rd ed. (John Wiley & Sons, 1984).

[24]O. Urakawa, S. F. Swallen, M. D. Ediger, and E. D. von Meerwall, "Self-diffusion and viscosity of low molecular weight polystyrene over a wide temperature range", Macromol. **37**, 1558–1564 (2004).

[25] MATLAB, *Version 8.1.0 (r2013a)* (The MathWorks Inc., Natick, Massachusetts, 2013).

[26]F. J. Harris, "On the use of windows for harmonic analysis with the discrete Fourier transform", Proc. of the IEEE **66**, 51–83 (1978).

[27]A. Naranjo, M. del Pilar Noriega, T. Osswald, A. Roldan-Alzate, and J. D. Sierra, *Plastics Testing and Characterization: Industrial Applications* (Carl Hanser Verlag, Munich, 2008).

[28] COMSOL, Inc., *COMSOL Mutliphysics®* (Los Angeles, CA).

[29] Corning, Inc., *Corning® 1737* (Corning, NY).

[30] McMaster-Carr Supply Co., *Multipurpose 110 Copper* (Santa Fe Springs, CA).

[31] Y. S. Touloukian, R. W. Powell, C. Y. Ho, and P. G. Klemens, *Thermal Conductivity - Nonmetallic Solids*, Vol. 2, Thermophysical Properties of Matter (IFI/Plenum, NY, 1970).

[32] MicroChem Corp., *SU-8 2000 Epoxy Photoresist* (Westborough, MA).

[33] W. Fulkerson, J. P. Moore, R. K. Williams, R. S. Graves, and D. L. McElroy, "Thermal conductivity, electrical resistivity, and Seebeck coefficient of silicon from 100 to 1300 K", Phys. Rev. **167**, 765–782 (1968).

[34] OMEGA Engineering, Inc., *OMEGATHERM® 201* (Norwalk, CT).

[35] Delta Technologies, Ltd., *Part No. CB-50IN-S205* (Loveland, CO).

[36] T. Ashida, A. Miyamura, N. Oka, Y. Sato, T. Yagi, N. Taketoshi, T. Baba, and Y. Shigesato, "Thermal transport properties of polycrystalline tin-doped indium oxide films", J. Appl. Phys. **105**, 073709 (2009).

[37] K. A. Leach, Z. Lin, and T. P. Russell, "Early stages in the growth of electric field-induced surface fluctuations", Macromol. **38**, 4868–4873 (2005).

[38] M. Hartl, I. Krupka, and M. Liska, "Differential colorimetry: tool for evaluation of chromatic interference patterns", **36**, 2384–2391 (1997).

[39] K. R. Fiedler, and S. M. Troian, "Early time instability in nanofilms exposed to a large transverse thermal gradient: improved image and thermal analysis", J. Appl. Phys. **120**, 205303 (2016),

[40] F. A. Jenkins, and H. E. White, *Fundamentals of optics*, 4th ed. (McGraw-Hill Inc., 1976).

[41] I. D. Nikolov, and C. D. Ivanov, "Optical plastic refractive measurements in the visible and the near-infrared regions", **39**, 2067–2070 (2000).

[42] Tydex, J. S. Co., *Tydex® Sapphire* (St. Petersburg, Russia).

[43] M. A. Green, and M. J. Keevers, "Optical properties of intrinsic silicon at 300 K", Prog. Photov. **3**, 189–192 (1995).

[44] P. Yeh, *Optical waves in layered media* (John Wiley and Sons, Inc., Hoboken, New Jersey, 2005).

[45] M. Born, and E. Wolf, *Principles of optics: electromagnetic theory of propagation, interference and diffraction of light* (Cambridge University Press, 1999).

[46] OMEGA Engineering, Inc., *RTD Reference Sheet* (Norwalk, CT).

[47] OMEGA Engineering, Inc., *Thermocouple Tolerances* (Norwalk, CT).

[48] McMaster-Carr Supply Co., *Multipurpose 6061 Aluminum* (Santa Fe Springs, CA).

[49] Aremco Products Inc., *Aremco Heat-Away™ 638* (Valley Cottage, NY).

[50] Induceramic, *Alumina Metallic Ceramic Heating Element* (Waterloo, Ontario, Canada).

[51] A. G. Marshall, and F. R. Verdun, *Fourier Transforms in NMR, optical and mass spectrometry: a user's handbook* (Elsevier, New York, NY, 1990).

[52] R. J. Meier, "On art and science in curve-fitting vibrational spectra", Vib. Spectrosc. **39**, 266–269 (2005).

[53] A. Yariv, and P. Yeh, *Photonics: optical electronics in modern communications* (Oxford University Press, Inc., New York, New York, 2007).

[54] OriginLab, *Origin* (Northampton, MA).

[55] T. Hou, C. Zheng, S. Bai, Q. Ma, D. Bridges, A. Hu, and W. W. Duley, "Fabrication, characterization, and applications of microlenses", Appl. Opt. **54**, 7366–7376 (2015).

[56] H. Zappe, *Fundamentals of micro-optics* (Cambridge University Press, 2010).

[57] V. Vespini, O. Gennari, S. Coppola, G. Nasti, L. Mecozzi, V. Pagliarulo, S. Grilli, C. Carfagna, and P. Ferraro, "Electrohydrodynamic assembly of multiscale PDMS microlens arrays", IEEE J. Quantum Elec. **21**, 1–8 (2015).

[58] B. Platt, and R. Shack, "History and principles of Shack-Hartmann wavefront sensing", J. Refract. Surg. **17**, S573–S577 (2001).

[59] C. A. Schneider, W. S. Rasband, and K. W. Eliceiri, "NIH Image to ImageJ: 25 years of image analysis", Nature Methods **9**, 671–675 (2012).

[60] J. Schindelin, I. Arganda-Carreras, E. Frise, V. Kaynig, M. Longair, T. Pietzsch, S. Preibisch, C. Rueden, S. Saalfeld, B. Schmid, J. Tinevez, D. J. White, V. Hartenstein, K. Eliceiri, P. Tomancak, and A. Cardona, "Fiji: an open-source platform for biological-image analysis", Nature Methods **9**, 676–682 (2012).

[61] Q. Tseng, "Study of multicellular architecture with controlled microenvironment", Thesis (Université de Grenoble, 2011).

[62] V. G. Levich, and V. S. Krylov, "Surface-tension-driven phenomena", Annu. Rev. Fluid Mech. **1**, 293–316 (1969).

[63] S. H. Davis, "Thermocapillary instabilities", Annu. Rev. Fluid Mech. **19**, 403–435 (1987).

[64] M. F. Schatz, and G. P. Neitzel, "Experiments on thermocapillary instabilities", Annu. Rev. Fluid Mech. **33**, 93–127 (2001).

[65] J. P. Harmon, and G. K. Noren, eds., *Optical polymers: fibers and waveguides* (Oxford University Press, New York, New York 10016, 2001).

[66] Scientific Polymer Products Inc., *Polystyrene Standard, Cat #771* (Ontario, New York).

[67]I. H. Malitson, "Interspecimen comparison of the refractive index of fused silica", J. Opt. Soc. Am. **55**, 1205–1209 (1965).

[68]D. J. Griffiths, *Introduction to quantum mechanics*, 2nd ed. (Prentice-Hall, Inc., Upper Saddle River, New Jersey 07458, 2005).

[69] Thorlabs Inc., *Zing™ Fiber* (Newton, New Jersey).

[70]J. F. Bauters, M. J. R. Heck, D. John, D. Dai, M.-C. Tien, J. S. Barton, A. Leinse, R. G. Heideman, D. J. Blumenthal, and J. E. Bowers, "Ultra-low-loss high-aspect-ratio Si_3N_4 waveguides", Opt. Exp. **19**, 3163–3174 (2011).

[71]R. N. O'Brien, F. P. Dieken, and A. Glasel, "Use of He-Ne laser with Abbe refractometer to obtain some electrolyte refractive indices", J. Chem. and Eng. Data **18**, 142–144 (1973).

[72]J. Rheims, J. Köser, and T. Wriedt, "Refractive-index measurements in the near-IR using an Abbe refractometer", Meas. Sci. and Tech. **8**, 601–605 (1997).

[73]I. Z. Kozma, P. Krok, and E. Riedle, "Direct measurement of the group-velocity mismatch and derivation of the refractive-index dispersion for a variety of solvents in the ultraviolet", J. Opt. Soc. Am. B **22**, 1479–1485 (2005).

[74]M. Daimon, and A. Masumura, "Measurement of the refractive index of distilled water from the near-infrared region to the ultraviolet region", Appl. Opt. **46**, 3811–3820 (2007).

[75]E. Schäffer, T. Thurn-Albrecht, T. P. Russell, and U. Steiner, "Electrically induced structure formation and pattern transfer", Nature **403**, 874–877 (2000).

[76]L. F. Pease, and W. B. Russel, "Linear stability analysis of thin leaky dielectric films subjected to electric fields", J. Non-Newton. Fluid Mech. **102**, 233–250 (2002).

[77]L. F. Pease, and W. B. Russel, "Electrostatically induced submicron patterning of thin perfect and leaky dielectric films: a generalized linear stability analysis", J. Chem. Phys. **118**, 3790–3803 (2003).

[78]D. A. Saville, "Electrohydrodynamics: the Taylor-Melcher leaky dielectric model", Annu. Rev. Fluid Mech. **29**, 27–64 (1997).

[79]V. Shankar, and A. Sharma, "Instability of the interface between thin fluid films subjected to electric fields", J. Colloid Interface Sci. **274**, 294–308 (2004).

Appendix A

EXPERIMENTAL PROTOCOLS

A.1 Polystyrene Nanofilm Preparation

The quality of the solid nanofilms which were then liquefied at the start of the molten nanofilm experiments detailed above is of critical importance. In the case of the flat plate experiments described in Ch. 3, Ch. 4, and Ch. 5, the presence of defects can lead to nonlinear growth or dewetting, which obscures the desired instability and corrupts the measured wavelengths and growth rates. Defects will also destroy the optical properties of the micro-optical devices described in Ch. 6 and Ch. 7 because they are scattering centers which induce optical loss. The preparation of high quality nanofilms starts with pure solvents to make sure that additional contaminants are not introduced. Specifically, the polystyrene (PS) solvent was toluene and it dissolves both standard washbottles and plastic filters. This causes contamination in the final films, so any materials used during nanofilm preparation were either glass or metal. To reduce all sources of contamination precise filtering was performed during preparation and while dispensing the solution for spin coating. The nanofilm preparation procedure has been divided into two sections: one devoted to the initial creation of the solution and the other devoted to the spin coating process. Note that all of these steps were accomplished in labs which were not a cleanroom, although this would have been helpful. Instead, polyester filters were placed in the air registers of the room and changed annually. To further reduce the level of airborne contaminants a HEPA filter (Alen BreatheSmart) was run continuously on its highest setting near the fume hoods.

A.1.1 Dissolving and Filtering Polystyrene in Toluene

1. Begin preparations by donning a lab coat, nitrile gloves, safety glasses, a hair net, and a surgical mask. The use of a hair net and surgical mask are to reduce the amount of contamination that is introduced from external sources into the solution.

2. Rinse a glass bottle and a glass beaker with toluene and dry with nitrogen. **DO NOT USE TOLUENE FROM A WASHBOTTLE.** Toluene dissolves the bottle and leads to contaminants in the resulting nanofilms. Instead, pour

the toluene from the large 4 L glass bottle into a smaller beaker and use it directly from the beaker. Refill this secondary beaker as needed throughout the process. The cleansed beaker will be the initial mixing vessel and the bottle will house the final solution. The toluene in the washbottle is only for cleaning the spin coater.

3. Rinse a small metal scoopula with toluene and dry with nitrogen. Tear off a small section (approximately 2" x 2") of weighing paper and put it onto the balance. Tare the balance.

4. Weigh out the appropriate amount of polymer onto the weighing paper for your desired solution concentration. Several different weight percent solutions and typically make at least 10 mL of solution at a time. In 10 mL of toluene, the amount of PS that is needed for the corresponding weight percent is listed: 1% = 87.9 mg; 2% = 177.6 mg; 4% = 362.5 mg; 8% = 756.5 mg.

5. Fill the initial mixing beaker with 10 mL of toluene and carefully pour the polymer on the weighing paper into this solution. Cover and leave solution to dissolve while performing the next three steps.

6. Clean the glass syringe with stainless steel Leur lock tip and glass plunger (Cadence Science) by rinsing in pure toluene from a glass beaker. Separate the two pieces and clean them individually. Then dry them using nitrogen gas.

7. Disassemble and clean each part of the stainless steel filter holder (Whatman) with toluene individually. Dry each component with nitrogen and then re-assemble in the same order (large donut gasket beneath the steel mesh, flat spacer above steel mesh) with the Anodisc filter (0.02 micron pore size) inserted directly above the steel mesh and below the flat spacer. Attach the filter holder assembly to the end of the 5 mL glass syringe. The holder will screw into the metal end of the syringe. Both of these seals should be at least finger tight and should not leak during normal filtering operations.

8. Clean the metal scoopula with toluene, dry it with nitrogen and put it away. If the polymer solution is not completely mixed at this point, it can be swirled by hand to promote mixing. In cases of high PS weight percentage, the solution can also be sonicated for one to two minutes. The solution can also be heated

on a hotplate to promote mixing, but care must be taken so that toluene does not evaporate during this process and so generally sonication is preferred.

9. Once the solution has mixed completely, remove the plunger from the 5 mL glass syringe and pour about half the 10 mL solution into the syringe. Replace the plunger and apply just enough pressure so that the solution passes through the filter at a rate of approximately 1 drop per second. Do not exert too much pressure to prevent the Anodisc filter from cracking which will cause solution to leak out of the connection between the filter holder and the syringe. Refill the syringe and repeat this process until the entire solution has been filtered. After filtering approximately two full syringes, the filter will tend to be saturated with material and the pressure required to filter the solution will increase markedly. This is more of a problem at high weight percentages (e.g. at 8% this typically occurs after one full syringe) and can be remedied by cleaning the filter holder and inserting a new Anodisc filter, as in Step 7.

10. Label the solution with the date, the preparation parameters such as the type of polymer and weight percentage, and any other relevant information.

11. Clean up the rest of the materials by disassembling the filter holder, disposing of the Anodisc filter in the glass disposal container, and rinsing each piece of the filter holder with toluene. Dry the pieces and then reassemble the holder. Wrap the filter holder in aluminum foil to prevent contamination from dust and store in the cabinet. Rinse the plunger and glass syringe separately with toluene and then dry with toluene. Store in the box and return it to the cabinet. Dispose of any remaining toluene that is not in the large 4L bottle by cleaning the initial mixing beaker and then disposing of any other toluene in the waste container.

A.1.2 Spin Coating Nanofilms

1. Begin preparations by donning a lab coat, nitrile gloves, safety glasses, a hair net, and a surgical mask. Clean the glass syringe and the filter holder as in Steps 6 and 7 in Sec. A.1.1.

2. Rinse a glass bottle and a glass beaker with toluene and dry with nitrogen. **DO NOT USE TOLUENE FROM A WASHBOTTLE.** Toluene dissolves the bottle and leads to contaminants in the resulting nanofilms. Instead, pour

the toluene from the large 4 L glass bottle into a smaller beaker and use it directly from the beaker. Refill this secondary beaker as needed throughout the process. The cleansed beaker will be the initial mixing vessel and the bottle will house the final solution. The toluene in the washbottle is only for cleaning the spin coater.

3. Grab a clean 2" silicon wafer from the pack by grasping the flat edge and place it onto the spin coater. Try to stay as close to the edge as possible while maintaining mechanical stability because anywhere the tweezers touch becomes contaminated with defects in the resulting nanofilm. Silicon wafers are generally cleanest as they come from the manufacturer and that more defects are introduced by attempting to clean them (with solvents, piranha, HF, etc.).

4. Turn on the spin coater (Cee-100, Brewer Science) and select the program by pressing 'Run' and then the program number. There is an initial centering step that should be completed before the solution is applied to the wafer. This step can be completed by pressing 'Start' once. If the wafer is not centered, it can be adjusted and tested again by pressing '0'. All of the programs for the spin coater should be listed on the blackboard next to the fume hoods. They can all be modified and the interested user should consult the manual for a full listing of the possible options. If a program is changed, then the list on the blackboard should be updated.

5. Once the wafer is centered, draw solution slowly into the 5 mL glass syringe without the filter holder attached. Take care to have a constant pull speed to avoid introducing extraneous bubbles into the solution. Dispense three to five drops of solution back into the container to fill the dead space in the filter holder. Dispense the solution slowly onto the wafer opposite the flat edge to avoid spreading defects. Dispense close to the wafer so that a meniscus forms and the solution can be dispensed continuously without the formation of drops. To improve reproducibility, dispense solution until the point when the entire wafer is covered by solution. An alternative technique to this is to always draw the same amount of solution into the syringe (1 mL, for example) and then dispense the entire syringe. When utilizing this approach, care must be taken to fill the dead space of the filter holder before measuring the correct amount of solution in the syringe.

6. Close the spin coater and start the spin coating process which is typically a 30 second spin at 3000 RPM with an acceleration of 1000 RPM/s. Once the chuck has stopped rotating, visually inspect the quality of the film, looking for dust and comets in the film. After inspection, immediately place the wafer into a 2" wafer carrier. Label the carrier with the date, your initials, the type of solution, and any other information relevant to this wafer. The sample is now ready for film height measurement with the ellipsometer or deformation in the experimental setup.

A.2 Film Thickness Measurements through Ellipsometry

The thickness of transparent thin films can be measured through ellipsometry and this technique was used extensively above to measure the thickness of our PS nanofilms. However, there are several important limitations of the instrument, a Rudolph Auto EL III Ellipsometer. First, it cannot measure the thickness of thicker films (greater than about a micron). Second, the film thickness measurements are periodic in the film height and if the initial guess is not sufficiently close to the true value, it can report the wrong thickness. This effect can be mitigated by measuring at another wavelength (this ellipsometer can measure at 405 nm, 546.1 nm, and 632.8 nm), since the periodicity is wavelength dependent. If the same thickness is measured at two different wavelengths then it is probably the correct value for your film. The third limitation of this instrument is that it has difficulty with multiple transparent layers. When the refractive index difference between two layers is small, there is relatively little reflection from that interface which means that the observed signal is small. Even with these limitations, the ellipsometer was quite effective at measuring the thickness of PS nanofilms on silicon substrates. The steps in a typical thickness measurement are detailed below.

1. Begin preparations by donning a lab coat, nitrile gloves, safety glasses, a hair net, and a surgical mask.

2. Turn on the ellipsometer using the key on the lower left part of the ellipsometer, flip the switch on the upper left part of the ellipsometer which controls the illumination source, and flip the rocker switch on the upper right part of the front panel which controls the alignment light. Load the sample on to the stage. Adjust the position of the sample so that the ellipsometer spot hits a section that is flat and free from defects.

3. Adjust the sample height. Start by pulling the magnifier at the bottom of the periscope outwards. If the sample is at the correct height the circle should have crisp edges and be in focus. If it is not, then turn the large wheel underneath the stage until the bright spot is focused.

4. Adjust the sample tilt. Push the magnifier at the bottom of the periscope towards the ellipsometer as far as it will go. The bright spot should be centered on the reticle, completely within the black circle. If it is not, then adjust the three smaller screws beneath the stage until it is. After adjustment, all screws should be snug so that tilt is not affected by small vibrations.

5. After hitting enter to confirm that the sample was inserted and aligned, press the RUN button and select the appropriate program from the white board opposite the ellipsometer. Each of these programs can be modified and for a full list of details and options consult the ellipsometer manual. There are two main types of programs that we use. Programs 00 through 02 calculate both the film thickness and the refractive index while programs 03 through 05 only calculate the film thickness and assume the refractive index is fixed. When possible use 03 through 05 because they are slightly more accurate and repeatable, but the refractive index of the film material must be known from a different measurement to use these. When running a program it will typically prompt the user to provide a guess for the film thickness and the film refractive index. Provide a reasonable guess for the film thickness, otherwise an incorrect value could be reported due to the periodicity of the technique. Typically, the approximate thickness can be estimated by eye using the film color. There are several tables around the lab which show color as a function of film thickness for PS films on silicon wafers. They can also be derived using the equations of thin film interference.

6. Pay attention to the ellipsometer display as the printer does not work effectively, for the ellipsometer in the lab. The film thickness (and refractive index if the chosen program calculates it) value will flash briefly on this screen and should be written down. Generally, these measurements are quite repeatable so if the value was not written down, then the program can be run again. The ellipsometer will also provide the raw values which can be used if something more complex than a thickness measurement is desired.

A.3 SU-8 UV Photolithography on Sapphire

This set of instructions will detail how to make the photoresist spacers which determine the size of the air gap above the molten nanofilm. When making the spacers, great care was taken to make sure that they were all the same height and free from defects which would disturb the parallelism. This is in contrast to most photolithographic applications where the surface of the photoresist is unimportant since it is typically used as a binary mask. For the flat plate experiments described in Ch. 3, Ch. 4, and Ch. 5 only a set of spacers was deposited onto the sapphire. For the micro-optical device fabrication described in Ch. 6 and Ch. 7, another set of deposition steps was required which defined the pattern on the superstrate that influenced the film growth. This second pattern was of a different height than the spacers, which is why two distinct photolithography exposures were necessary. These fabrication steps were performed in a class 1000 cleanroom to reduce contamination.

1. Start with a clean sapphire window. This could be a new window directly from the manufacturer (Meller Optics) or one that has been cleaned with piranha (see Sec. A.4). Typically, if a window has a damaged or unwanted pattern it can be removed with piranha and then rinsed with acetone followed by a rinse with isopropyl alcohol (IPA). This should be visually inspected to ensure that it is free from dust and other contamination. Small amounts of dust can usually be removed with a quick blast from the nitrogen guns in the hood.

2. Prepare for future baking steps by setting two hotplates in the cleanroom to 65 °C and 95 °C.

3. Attach the sapphire window to a larger glass slide using Shipley S1813 photoresist to reduce the presence of the edge bead. The reduction of edge bead makes the spacers more uniform. To do this, place a drop of S1813 underneath a window and bake at 95 °C for 10 minutes for 3/8" diameter windows (15 minutes or longer for the 1” diameter windows). Remove from the hot plate and let cool to approximately room temperature. At this point, there is no danger of overbaking the resist as the longer it bakes, the better the adhesion of sapphire to the glass. Note that the use of specifically S1813 is not required. This resist was used because it would not dissolve in SU-8 developer or the IPA rinse which immediately followed. As such, multiple spinning and exposure steps could be achieved sequentially without reapplying the adhesion photoresist.

4. OPTIONAL: Level the spin coater to improve the uniformity of the spacer heights. If this has been done recently and the spin coater has not been disturbed, then this should only need to be done infrequently (perhaps annually for the spin coater in Watson 153 and much more frequently for the spin coater in the cleanroom). Take a silicon wafer and put it onto the desired chuck. Dispense IPA using a plastic syringe held vertically in the middle of the wafer and watch which direction it spreads fastest. Then, adjust the feet of the spin coater to raise that direction. Alternatively, that direction can be shimmed with a piece of Technicloth. Spin the wafer briefly to remove the IPA. Repeat this procedure of dispensing IPA and then leveling until the IPA spreads evenly in all directions. At this point, the spin coater is level and spinning should produce films uniform to within a few percent of the total film thickness over the whole wafer.

5. Load the sapphire window on the glass slide into the spin coater. Dispense the SU-8 solution steadily and evenly to cover the entire window. With the higher viscosity solutions, areas which were not covered initially tend not to be covered after spinning, so it is important to have complete coverage initially. Spin the window at 3000 RPM for 60 seconds with a 3000 RPM/s acceleration. This can be varied and will depend on both the SU-8 solution viscosity and the desired film thickness, but it is a good place to start. The standard SU-8 2010 solution can be diluted using cyclopentanone according to the table in the MicroChem datasheet [32] to produce different viscosities. NOTE: when using 2" square glass slides as substrates, do not use the PTFE holder as the vacuum is not strong enough to keep the glass slide from breaking at 3000 RPM. Instead, place it directly on the chuck with no holder in place.

6. Pre-bake the window for 1 minute at 65 °C; then transfer it immediately to the 95 °C hotplate for 2 minutes. Remove from the hotplate and let the sample cool to approximately room temperature. These baking times have been fairly resilient for films of any thickness up to 10 microns, but for more precise times recommended by MicroChem for different thickness regimes consult the datasheet [32].

7. Load the sample into the mask aligner and align the middle of the sample beneath the desired pattern. Expose the sample for 60 seconds for thin films (<2 microns) and 90 seconds for thick films (>2 microns). Alignment of the pattern can be achieved by using the large enclosing ring which can be seen

around each pattern in Fig. A.1. After coarse alignment of the sample under the pattern, precise alignment can be achieved by translating the sample in the vertical direction until it is barely visible through the top of the outer ring. Then, the top of the window should be aligned with the top of the pattern. Move the sample so that it is just hidden under the pattern and shift your focus to the bottom of the pattern. Count the number of turns on the translation micrometer that it takes for the sample to just become visible at the bottom of the pattern. Go backwards half the number of turns it took to reach the bottom and the sample should be aligned with the center of the pattern as long as the micrometers do not have too much slop when changing directions.

8. After exposure, remove the sample from the mask aligner and post-bake the window for 2 minute at 65 °C; then transfer it immediately to the 95 °C hotplate for 4 minutes. Remove from the hotplate and allow the sample to cool to approximately room temperature.

9. Develop the sample by complete immersion and agitation for 30 seconds in SU-8 developer. Immediately dip the sample in IPA for approximately 15 seconds and then rinse with fresh IPA. The sample can then be dried with nitrogen. If the features are not completely developed, put it back into developer for approximately 15 seconds and repeat the process. Thicker films will typically require longer development times, but it is better to err on the side of less development because the sample can always be developed more. The features are not fully developed if there is a milky residue on the sample when you initially put it in the IPA. The residue will also be visible under the microscope as a set of small dots. Once development is complete the features should be crisp and well-defined. With thin, high-aspect ratio features, the development and drying process can destroy the desired pattern. If this becomes a problem, do not agitate the sample during the SU-8 developer or IPA immersion steps. Additionally, do not use the nitrogen gun to dry the sample; let it air dry instead.

10. OPTIONAL: Perform another set of spinning and photolithography exposure steps to define a pattern. When making windows with both spacers and a pattern, Step 5 can be repeated with a different viscosity solution to create a pattern with a smaller height. This is more efficient than proceeding to Step 12 and hard baking both the spacers and pattern separately because the sapphire window only needs to be attached to the glass substrate once and only needs

Figure A.1: SU-8 photomask example

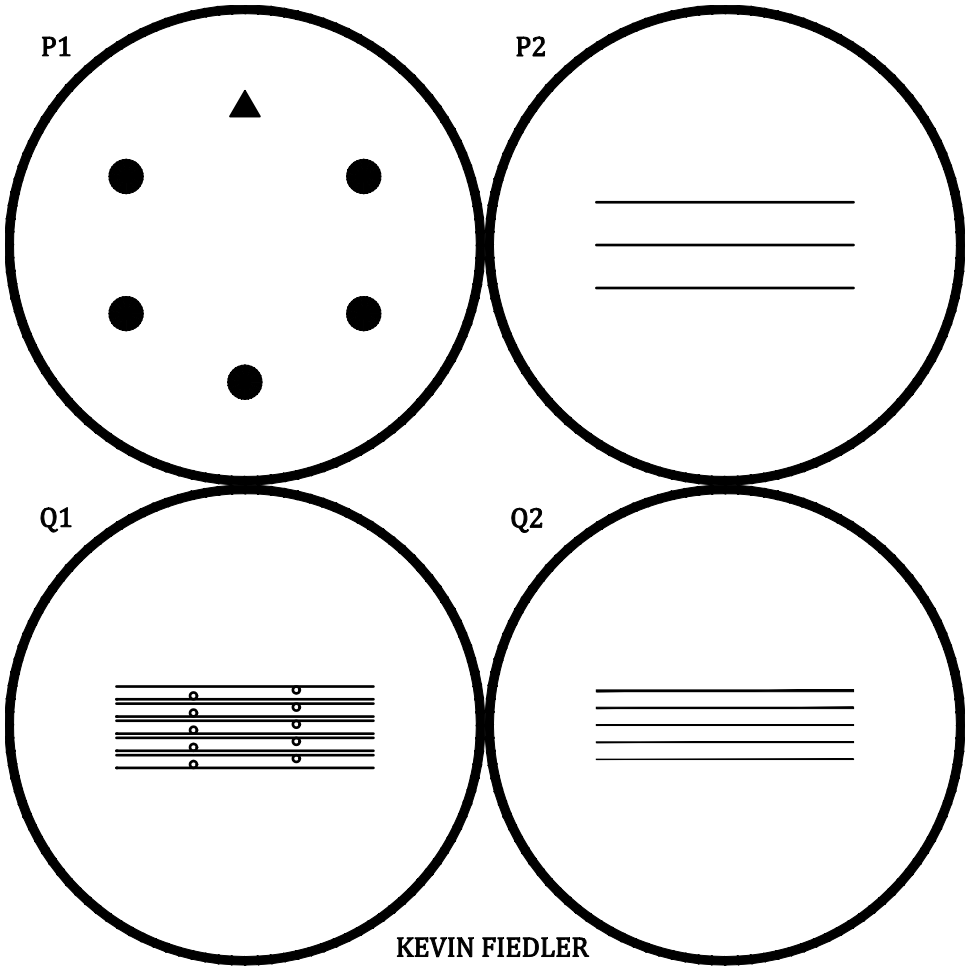

Example of an SU-8 photomask used to make the features on the sapphire windows. The dark regions are areas which would be transparent in the chrome on glass pattern. All these patterns are designed for 1" diameter sapphire windows and are not drawn to scale. Pattern P1 is the hexagonally arranged spacers. The triangle allows for easier orientation of subsequent pattern steps. The remaining patterns are examples of waveguides.

to be hard baked once. The spacers should be patterned first because they are large and will not be affected by the subsequent spinning step. If very fine patterns were made in the first step, then the high viscosity solution for the spacers could remove the features when it is applied.

11. Once the spacers and the pattern are developed completely, remove the window from the glass substrate using acetone. When dissolving the S1813 with acetone, try not to submerge the SU-8 pattern in acetone and remove the window as quickly as possible once it comes off the glass substrate. A moderate amount of pressure is required to remove the window from the glass substrate. If the window sits with the pattern submerged, the acetone will destroy the SU-8 pattern. This sensitivity of SU-8 to acetone will persist until the window has been hard baked. One technique to avoid this issue is to put down a thin layer of acetone so that it barely covers the glass substrate. Then it will not come over the top of the sapphire window into contact with the spacers or pattern. This thin layer can then diffuse under the window to remove the photoresist and allows for a little more flexibility in the time required to remove the window.

12. Hard bake the windows at 200 °C for 2 hours to cure them. This step does not necessarily have to be done in a cleanroom. If it is not done in a cleanroom, then cover the hotplate but do not form a seal. This will allow the SU-8 to degas and cure without being contaminated with dust from the environment.

13. Measure the height of the spacers and the pattern, if it exists, with a profilometer (Ambios XP2). Do this after the window has been hard baked, otherwise the force from the profilometer tip can scratch the SU-8 and leave behind a pattern which will influence the growth of the features in the molten films.

A.4 Cleaning with Piranha Solution

To clean off the SU-8 patterns from sapphire windows or remove PS from a quartz window we typically use piranha solution. This is a mixture of sulfuric acid and hydrogen peroxide, typically in an approximately 3:1 ratio. It will dissolve most organic material, including elemental carbon. Additionally, it will dissolve metals, so it is important that you use PTFE (Teflon) tweezers instead of metal ones. The mixing process is highly exothermic, so it is very important that this procedure is performed in a fume hood on a hot plate and that the mixing container is not held

by hand while pouring. It is also crucial to have another person in the lab for safety purposes.

1. Begin preparations by donning a lab coat, nitrile gloves, safety glasses, a hair net, and a surgical mask. Additionally, an acid apron must be donned when working with acids.

2. Measure approximately 75 mL of sulfuric acid (H_2SO_4) into a beaker. Note that the viscosity of sulfuric acid is significantly different than the viscosity of water and it will not pour in the same way.

3. Pour the sulfuric acid into the glass container where the samples will be cleaned. This container should be located on top of a hot plate during the mixing process because it is quite exothermic.

4. Measure approximately 25 mL of 30% concentrated hydrogen peroxide (H_2O_2) into a different beaker than the one which contained the sulfuric acid.

5. Add the hydrogen peroxide to the sulfuric acid in the mixing container and allow the solution to cool. It will typically steam slightly.

6. Rinse the hydrogen peroxide beaker with deionized water and pour the mixture into the sulfuric acid beaker. Rinse the sulfuric acid beaker with more water and dispose of the resulting solution into the hazardous waste bottle.

7. Insert the samples to be cleaned into the piranha solution and let them sit for approximately 20 minutes. It will be clear that the solution is working if the organic matter turns brown/black and bubbles slowly. Then, the sample is clean once the brown/black material has disappeared. The solution will lose its effectiveness over time because the hydrogen peroxide is light sensitive, so use it soon after it has been prepared. Additionally, the solution can saturate if there is a lot of organic material to be removed. In this case, not all the of the brown/black material will disappear and the samples should be cleaned again.

8. Remove the clean samples from the piranha solution and transfer them to a beaker filled with deionized water using the PTFE tweezers. After all the samples have been removed put them in the rinse bath and put it under a steady stream of deionized water. While the water is overflowing the container,

remove the samples through the stream of deionized water. This process will prevent any residual organic matter which accumulates on the top of the rinse bath from redepositing on the sample as it is removed from the rinse beaker.

9. After removal from the rinse bath, dry the sample with either Technicloth or nitrogen from the fume hoods. The samples are now clean and ready for use.

10. To dispose of the piranha solution after cleaning, pour it into the waste bottle. Then, rinse the mixing container with deionized water and pour this into the waste container as well. Flush all the beakers and mixing containers that have been used with excess water and dry them using paper towels. Leave them in the fume hood to finish drying.

A.5 Wafer Cleaving for Waveguide Isolation

As detailed in Ch. 7, polymeric waveguides were fabricated on substrates which were composed of a 5 micron wet thermal oxide layer grown on a <100> silicon wafer. To produce optical quality end facets which would allow light to be coupled in and out of the waveguide, the waveguide substrate was cracked. Due to the nanoscale heights of the waveguide, they cracked cleanly and simultaneously with the silicon wafer. The cleaving of silicon is a common process in semiconductor processing where a wafer is typically scratched by hand on the unpolished side with a diamond scribe, then flipped over and cracked from the polished side. This technique posed two difficulties for the specific application of cracking waveguides. First, the waveguides were fabricated on the polished side of the wafer and putting the wafer with the polished side down could scratch or otherwise damage the waveguides. Second, the scratches defining the cleave axis must be aligned with the location of the waveguide and this is difficult to do without being able to see the position of the waveguide as the scratches were made. As such, a few modifications to the traditional process were made and are detailed below.

1. Begin preparations by donning a lab coat, nitrile gloves, safety glasses, a hair net, and a surgical mask. Lay out a fresh piece of Technicloth on which the wafer will be cracked. Place the room temperature wafer on the Technicloth with the fabricated waveguides facing up.

2. Scratch the top side of the wafer along the crystal axes near the wafer flat. Align one scratch near the left end of the waveguide, as close to the end as possible while avoiding defects. Align another scratch near the right end of

Figure A.2: Wafer cleaving diagram

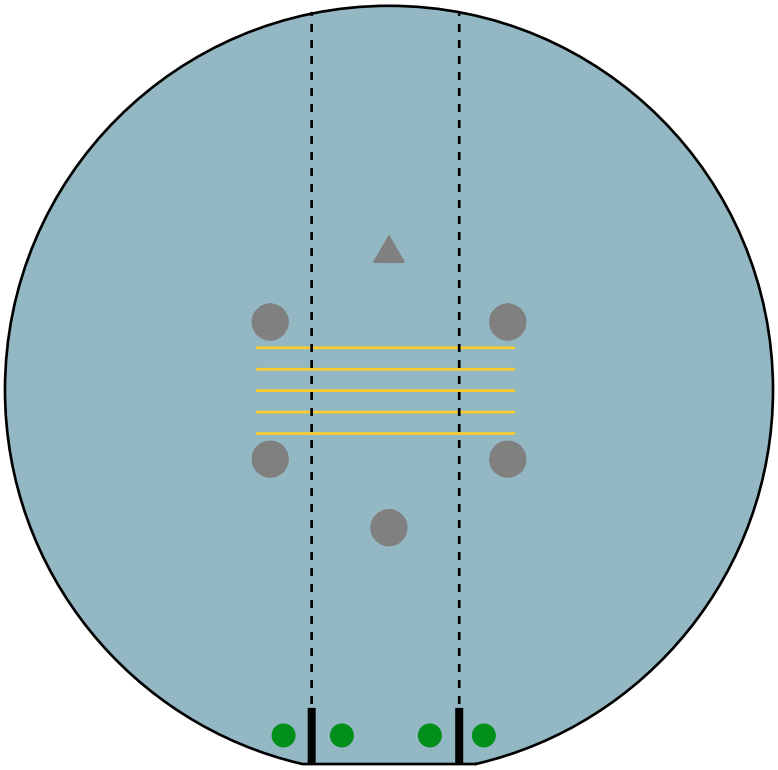

Diagram of the approximate geometry used for cleaving a wafer. The scratches in the wafer are denoted by the thick solid black lines perpendicular to the wafer flat. The dotted lines represent the propagation direction of the cleave which is perpendicular to the waveguides (denoted by the yellow lines). The hexagonally arranged gray objects are the spacers and the green dots are locations where pressure should be applied to propagate the crack through the wafer.

the waveguide, as close to the other end as possible. The scratches only need to be a couple millimeters long and should not produce large amounts of silicon dust. Ideally, the scratches would be aligned to the crystal axes of the wafer (perpendicular to the flat for <100> wafers) and would only require one motion. The approximate location of good scratch locations are shown by the solid black lines near the bottom of Fig. A.2.

3. Insert a straightened paper clip or staple underneath the scratch so that it is aligned parallel to the desired cleave direction. Press on either side of the scratch until the wafer cracks. Press relatively close to the position of the scratch and can use the end of tweezers or toothpicks to push down on the wafer. The approximate location to apply pressure is shown by the green dots in Fig. A.2. Too much pressure will cause the wafer to shatter and if the wafer feels difficult to crack, make the scratches deeper. Typically only two

cleaves are needed to create input and output facets on the waveguide. The undeformed regions near the top and bottom of the wafer make convenient handles to maneuver and mount the sample.

A.6 Abbe Refractometer Refractive Index Measurements

The dispersion of an optical material is a critical parameter when designing structures because the refractive index will determine the required dimensions and other properties. To this end, an Abbe refractometer was used to measure the refractive index of PS at several discrete wavelengths. An Abbe refractometer uses total internal reflection to measure the refractive index of a sample which is sandwiched between two prisms. However, this particular Abbe refractometer (Vee Gee Instruments C10) was originally intended solely for measurement at a wavelength of 589 nm. This instrument was designed using two double Amici prisms to compensate for the dispersion of a broadband illumination source. To allow measurement at discrete wavelengths, this compensating prism was removed and three single wavelength illumination sources were chosen. The measurement wavelengths were 405 nm, 532 nm, and 633 nm. Using three distinct wavelengths allowed the refractive index of materials to be fit as a function of wavelength through the Cauchy equation

$$n(\lambda_{\text{opt}}) = B + \frac{C}{\lambda_{\text{opt}}^2} + \frac{D}{\lambda_{\text{opt}}^4}. \tag{A.1}$$

In this equation, $n(\lambda_{\text{opt}})$ is the refractive index, λ_{opt} is the optical wavelength and B, C, and D are fitting constants. For the PS used above, these coefficients were $B_{\text{PS}} = 1.574$, $C_{\text{PS}} = -0.002248\ \mu\text{m}^2$, and $D_{\text{PS}} = 0.001813\ \mu\text{m}^4$.

In addition to the modifications which were performed on the measurement instrument, the choice of low molecular weight PS also posed challenges. Typically, solid samples must be large and optically polished to provide a smooth interface which can be placed on the refractometer prism. Attempts to fabricate a macroscopic polished sample of PS were unsuccessful because the PS stuck to the molds, such as aluminum foil or glass. It was also too brittle to withstand the mechanical stress of polishing. As a result, molten PS was poured directly on to the prism and allowed to cool within the setup, as will be detailed in the steps below.

For each of the measurement wavelengths the refractometer was calibrated using solutions with known refractive indices. The calibration samples were common liquid samples of acetone, ethylene glycol, toluene, and water. The measurement steps enumerated below were performed for each calibration liquid at each measurement

wavelength. Then the measured refractive index values were compared to literature values and the deviation of the measured refractive index value from the literature value was computed. These deviations were averaged over all the calibration samples independently at each wavelength to provide offsets to use when measuring unknown samples. A full listing of the calibration liquids, their measured refractive indices, and the literature values can be found in Table A.1.

1. Begin preparations by donning a lab coat, nitrile gloves, safety glasses, a hair net, and a surgical mask. Measurements are easier when performed with the room lights turned off, but the lights can be left on during sample preparation in Step 2.

2. Place the sample on the lower refractometer prism and close the refractometer to bring the upper prism into contact with the sample. For liquid samples the solution will be dispensed directly on the prism and should cover the entire prism face. In the case of solid samples, an index matching fluid is typically required to provide good optical contact between the prism and the sample. For the prisms used in this refractometer, 1-bromonapthalene was the index matching fluid. Certain solid samples, such as the calibration sample, will be too large for the upper prism to close, but this should not cause measurement difficulties as long as some illumination passes through the sample. As mentioned above, the PS sample was melted on an external hotplate at approximately 100 °C. The molten PS was removed from the hotplate and immediately poured onto the lower prism and the upper prism was quickly brought into contact with the PS, exerting mild pressure on the still molten sample. Since this sample was initially molten, an index matching fluid was not required to achieve optical contact.

3. Turn off the room lights if this has not already been done. Select the desired illumination wavelength and turn the source on. The source should already be aligned to illuminate the aperture of the upper prism which will transmit through the sample. If it is not, then the steering mirrors can be adjusted. Also note that the aperture should be covered with a Kimwipe which functions as a diffuser. The presence of the diffuser more evenly illuminates the sample and reduces speckle in the transmitted light [71]. This allows for a more precise measurement of the refractive index.

Table A.1: Abbe refractometer calibration data and PS refractive index

Calibration Samples - Measured			
	405 nm	532 nm	632.8 nm
Acetone	1.3325	1.3619	1.3718
Ethylene Glycol	1.4044	1.4335	1.4423
Toluene	1.4865	1.5014	1.5056
Water	1.3038	1.3363	1.3464
Calibration Samples - Literature			
	405 nm	532 nm	632.8 nm
Acetone [72]	N/A	1.3615	1.3578
Ethylene Glycol [73]	1.4412	1.4335	1.4308
Toluene [73]	1.5211	1.5006	1.4940
Water [74]	1.3427	1.3350	1.3317
Mean Offset	0.0368	-0.0007	-0.0130
Measured PS Values	1.5886	1.5894	1.5930
Final PS Refractive Indices	1.6254	1.5887	1.5800

4. Looking through the eyepiece, adjust the knob on the side of the refractometer so that the middle of the "X" is aligned with the line of demarcation between the light and dark regions. The light region should be the same color as the illuminating beam; if it is not, then there is light contamination from an external source (or a different source is still on). The line should be very distinct in proportion to the wavelength spread of the source.

5. Read the refractive index of the sample off the scale at the bottom of the field of view when looking through the eyepiece. With the room lights turned off, the scale is very dim, so it is usually necessary to turn on the small lamp to the left of the refractometer which illuminates the measurement scale. After measuring this value, compensate the measurement using the calibration values in Table A.1. Typically it is easiest to load a sample, measure all three wavelengths and then load another sample for measurements as opposed to keeping the illumination source constant and cycling through samples.

A.7 Optical Coupling to Polymeric Waveguides

To couple light into the optical waveguides whose fabrication and characterization were detailed in Ch 7, a coupling setup located at the Jet Propulsion Laboratory was used. The basic setup is diagrammed in Fig. 7.4 and this section will detail how to effectively image the output of the waveguide modes.

1. Mount the waveguide sample which has already been cleaved on to a holder. This was typically done using SEM tabs (Ted Pella #16084-1, 12 mm outer diameter) on a long aluminum cantilever. The SEM tabs can be reused between samples although the back of the sample must be free of thermal paste for it to adhere. The back of the sample should be cleaned with IPA and a Kimwipe. Then the sample should be attached to a piece of Scotch tape several times to remove any remaining residue. Cleaning the back of the sample will prolong the life of the SEM tabs.

2. Align the optical fiber to the focal point of the microscope objective so that the smallest spot size is imaged by the Basler cameras. If the sample is currently configured to use a PBS and two cameras, then this step can also ensure the spot is centered simultaneously in both cameras and that they are in the same focal plane. Mark the location of the front of the microscope objective and the fiber tip on the TV/screen which is used to visualize the setup. This gives a good estimate for the focal distance and focal plane of the microscope objective in the present configuration.

3. OPTIONAL: Adjust the polarization controller to change the relative amount of light in the TE and TM polarizations. For certain measurements, it can be desirable for the amount of light to be equal in both the TE and TM polarizations while for other measurements it can be better for more power to be in one of the two polarizations. This is the most convenient point to adjust the polarization because the sample has not yet been inserted. Move the PBS mounted on the optical rail away from the cameras and directly beneath the reflection photodiode (Thorlabs PDA55) and swing the transmission photodiode into place. Cover the setup with the cardboard box cover to reduce environmental effects and adjust the gain of the photodiodes so that they are not saturated. Turn on the multimeters connected to the photodiodes and adjust the polarization controller to the desired polarization settings. When

the polarization has been adjusted, move the PBS back into position between the cameras.

4. Move the optical fiber from the focal plane of the microscope objective and leave plenty of room for the sample to be inserted. Attach the holder to the three axis translational stage. At this point, do a coarse alignment of the optical fiber to one of the waveguides on the chip, both laterally and vertically. This can mostly be done by eye, but will save time during the precision alignment later. Bring the waveguide sample into the focal plane of the microscope objective and align the waveguide to the mark which was made before. Depending on the lighting and camera the waveguide might not be visible. If the waveguide isn't visible this is not concerning as the position will be adjusted later when an image is formed.

5. Bring the optical fiber into coupling position at the input facet of the waveguide sample. This should be done carefully so as to not crash the optical fiber into the sample. Align the sample under 5x optical magnification. For this step, it is necessary to be able to see the interference fringes in the waveguide. If the waveguide is not visible, change the lighting until it is. This is best done with illumination through a dedicated microscope, but can be done with a lamp or the fluorescent room lights. When aligning the fiber, start by moving it to the center of the waveguide. Put a screen after the microscope objective but well before the PBS to get a rough idea of the light passing through the setup in the current configuration. Bing the fiber to the plane of the waveguide from above. There will be many closely spaced fringes on the screen which get further apart as the correct plane is approached. There will also probably be pieces of dust on the waveguide surface that are visible through the observation microscope in the correct plane for alignment. If light is coupled into the waveguide, then it should light up and this will be easiest to see with the room lights turned off. There should also be a faint horizontal line and a bright spot on the screen after the microscope objective. Once coupling to the waveguide has occurred, remove the screen.

6. Adjust the lateral position of the microscope objective so that the bright spot on the screen is aligned to the active part of the camera. Do not adjust the focal distance until the spot is on the camera. Otherwise, finding the correct focal plane will be very difficult. The position or opening of the iris might need to be adjusted, but after this has been done once it should be pretty close for

subsequent testing. If nothing is visible on the camera, then it typically helps to turn up the camera gain significantly so that scattered light is visible. Once the spot is on the camera, adjust the gain and the separation of the microscope objective and the waveguide sample until the image is in focus. Turn down the camera gain so that the image is not saturated and then adjust the separation distance until a clear image is formed.

7. Move the optical fiber to find the desired mode. Typically different modes can be accessed by small lateral translations of the fiber. The vertical position of the fiber can also be adjusted until the maximum coupling to the mode. At this point, images of the modes can be recorded or the transmitted power through the waveguide can be measured using the photodiodes.

Appendix B

EVALUATION OF DRIVING FIELDS AT PERTURBED INTERFACES

B.1 Background

One interesting aspect of the derivation presented in Ch. 2 is that the driving mechanisms, the electric field for the SC model and the temperature field for the AP and TC models, are evaluated at the perturbed film interface $h(x, y, t)$, not the unperturbed film interface h_o. Intuitively, this is reasonable because the force due to surface tension is based on the perturbed surface since there is no curvature in the unperturbed state. To balance a driving force against surface tension, it should be calculated in the same configuration where the surface tension was calculated. One method for calculating the driving force is to use perturbation theory where the perturbed fields are typically evaluated at the base state, not the perturbed state. Evaluating some elements at the perturbed interface while evaluating others at the unperturbed interface leads to a subtle dissonance in the derivation which results in errors. This appendix will detail an example to show the error that can occur if the driving forces are not consistently evaluated at the perturbed interface.

The derivation of the SC model that was presented in Sec. 2.3.1 is actually a subset of the full derivation presented in the Ph.D. thesis of Zhuang [3]. In his original derivation, he considered a more general system in which an overall potential difference was applied across the nanofilm/air bilayer in addition to the surface charge present at the interface. This applied potential difference was not applicable to the experimental setup presented above, so the applied potential difference was not included in Ch. 2. However, the case where there is no interfacial charge density and only an applied potential difference has been investigated as a separate instability, called the electrohydrodynamic (EHD) instability. The EHD instability has garnered considerable interest both experimentally [4, 5, 75] and theoretically [76, 77]. As shown in Fig. B.1, the geometry is the same as in Ch. 2 except instead of an applied temperature gradient, there is an applied electric field. This appendix will focus on the theoretical work of Pease and Russel [76, 77] and demonstrate that their electric fields yield a tangential stress which is incompatible with Maxwell's equations.

Figure B.1: Instability geometry in EHD model

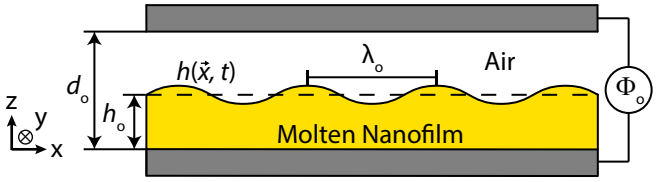

The driving force in the EHD model is the applied potential difference across the bilayer, Φ_o.

The rest of this appendix is organized as follows. In Sec. B.2, it is shown that there are no tangential stresses at a perfect dielectric interface with no free charge which arises directly from Maxwell's equation. Then, electric fields in the bilayer are derived from the nondimensional governing equations within the lubrication approximation when evaluated at the perturbed interface in Sec. B.3. Next, the tangential stresses due to these electric fields are computed in Sec. B.4 to show that the tangential stresses at the perturbed interface are zero. Then, a dimensional perturbation calculation follows to evaluate the perturbed electric field at the unperturbed interface in Sec. B.5. In Sec. B.6, it is demonstrated that these electric fields do not consistently satisfy Maxwell's equations and in Sec. B.7 the results are briefly discussed.

B.2 Tangential Stresses at a Perfect Dielectric Interface

The Maxwell stress tensor in the absence of magnetic fields, originally defined in Eq. (2.49), has the form

$$\mathbf{T}^{\text{em}} = \vec{E}\vec{D} - \frac{1}{2}\mathbf{I}\left(\vec{E}\cdot\vec{D}\right). \tag{B.1}$$

To compute the tangential stresses at the interface, this equation is dotted by the tangential unit vector, $\hat{t}$, on the left, dotted by the normal unit vector, $\hat{n}$, on the right, and the difference between the stress tensors in the air and film layers is taken. Note that all of these terms are evaluated at the film/air interface.

$$\hat{t}\cdot\mathbf{T}^{\text{em}}_{\text{air}}\cdot\hat{n} - \hat{t}\cdot\mathbf{T}^{\text{em}}_{\text{film}}\cdot\hat{n} = \hat{t}\cdot\vec{E}_{\text{air}}\vec{D}_{\text{air}}\cdot\hat{n} - \hat{t}\cdot\vec{E}_{\text{film}}\vec{D}_{\text{film}}\cdot\hat{n}.$$

The normal and tangential unit vectors are orthogonal so that $\hat{t}\cdot\mathbf{I}\cdot\hat{n} = 0$ which was used to simplify the preceding equation. The tangential components of the electric field must be equal across the interface because $\boldsymbol{\nabla}\times\vec{E} = 0$. Therefore, the subscripts on the electric field terms are dropped and the common terms factored out front

$$\hat{t}\cdot\mathbf{T}^{\text{em}}_{\text{air}}\cdot\hat{n} - \hat{t}\cdot\mathbf{T}^{\text{em}}_{\text{film}}\cdot\hat{n} = \left(\hat{t}\cdot\vec{E}\right)\left(\vec{D}_{\text{air}}\cdot\hat{n} - \vec{D}_{\text{film}}\cdot\hat{n}\right).$$

The difference in the normal components of the electric displacement field across the interface is simply the free charge at the interface, σ_{free}. In this system, there is no free charge, so the tangential stresses at the interface must be

$$\hat{t} \cdot \mathbf{T}^{\text{em}}_{\text{air}} \cdot \hat{n} - \hat{t} \cdot \mathbf{T}^{\text{em}}_{\text{film}} \cdot \hat{n} = \left(\hat{t} \cdot \vec{E}\right) \sigma_{\text{free}} = 0. \tag{B.2}$$

The fact that there can be no tangential stresses at a perfect dielectric interface if there is no free charge was well known to the leaky dielectric community [78]. As such, Pease and Russel did not calculate the tangential stresses at the perturbed interface in their derivation. However, as shown below in Sec. B.5 and Sec. B.6, their electric field expressions did cause tangential stresses anytime the interface was perturbed from the initially flat state. Before this is done, an electric field solution which is self-consistent with Maxwell's equations at the perturbed film interface will be demonstrated.

B.3 Electric Field Evaluated at a Perturbed Interface

The basics of the governing equations for the electric field within the lubrication approximation have been presented in Sec. 2.3.1, although in this section the potential scaling and the boundary conditions will be slightly different. All scaled quantities in this appendix will be denoted with a prime to signify the change in scaling. The characteristic potential scale is now

$$\Phi'_c = \Phi_o. \tag{B.3}$$

The electrostatic boundary conditions are changed to

$$\widetilde{\phi}'_{\text{film}}(Z = 0) = 0, \tag{B.4}$$

$$\widetilde{\phi}'_{\text{air}}(Z = D) = 1, \tag{B.5}$$

$$\widetilde{\phi}'_{\text{film}}(Z = H) = \widetilde{\phi}'_{\text{air}}(Z = H), \tag{B.6}$$

$$\varepsilon_{\text{film}} \frac{\partial \widetilde{\phi}'_{\text{film}}(Z = H)}{\partial Z} = \frac{\partial \widetilde{\phi}'_{\text{air}}(Z = H)}{\partial Z}. \tag{B.7}$$

The solutions for the electric potential have the same general solution

$$\widetilde{\phi}'_{\text{film}} = A^{\text{EHD}}_{\text{film}} Z + B^{\text{EHD}}_{\text{film}},$$
$$\widetilde{\phi}'_{\text{air}} = A^{\text{EHD}}_{\text{air}} Z + B^{\text{EHD}}_{\text{air}},$$

where $A^{\text{EHD}}_{\text{film}}$, $B^{\text{EHD}}_{\text{film}}$, $A^{\text{EHD}}_{\text{air}}$, and $B^{\text{EHD}}_{\text{air}}$ are integration constants. Applying the Dirichlet boundary conditions from Eq. (B.4) and (B.5) yields

$$\begin{aligned}\widetilde{\phi}'_{\text{film}} &= A^{\text{EHD}}_{\text{film}} Z,\\ \widetilde{\phi}'_{\text{air}} &= A^{\text{EHD}}_{\text{air}}(Z-D)+1.\end{aligned}$$

Applying Eq. (B.7) gives

$$\varepsilon_{\text{film}} A^{\text{EHD}}_{\text{film}} = A^{\text{EHD}}_{\text{air}}.$$

This implies that the electric potentials become

$$\begin{aligned}\widetilde{\phi}'_{\text{film}} &= A^{\text{EHD}}_{\text{film}} Z,\\ \widetilde{\phi}'_{\text{air}} &= \varepsilon_{\text{film}} A^{\text{EHD}}_{\text{film}}(Z-D)+1.\end{aligned}$$

The final boundary condition is continuity of the potentials at the interface from Eq. (B.6). This allows $A^{\text{EHD}}_{\text{film}}$ to be determined

$$A^{\text{EHD}}_{\text{film}} = \frac{1}{\varepsilon_{\text{film}} D - (\varepsilon_{\text{film}}-1)H}.$$

The electric potentials are therefore

$$\widetilde{\phi}'_{\text{film}} = \frac{Z}{\varepsilon_{\text{film}} D - (\varepsilon_{\text{film}}-1)H}, \tag{B.8}$$

$$\widetilde{\phi}'_{\text{air}} = \frac{\varepsilon_{\text{film}}(Z-D)}{\varepsilon_{\text{film}} D - (\varepsilon_{\text{film}}-1)H} + 1. \tag{B.9}$$

From this the electric fields are computed and then broken into components

$$\widetilde{E}'_{\text{film,z}} = \frac{-1}{\varepsilon_{\text{film}} D - (\varepsilon_{\text{film}}-1)H}, \tag{B.10}$$

$$\widetilde{E}'_{\text{film},\parallel} = \frac{-Z(\varepsilon_{\text{film}}-1)\epsilon\widetilde{\boldsymbol{\nabla}_{\parallel}}H}{\left[\varepsilon_{\text{film}} D - (\varepsilon_{\text{film}}-1)H\right]^2}, \tag{B.11}$$

$$\widetilde{E}'_{\text{air,z}} = \frac{-\varepsilon_{\text{film}}}{\varepsilon_{\text{film}} D - (\varepsilon_{\text{film}}-1)H}, \tag{B.12}$$

$$\widetilde{E}'_{\text{air},\parallel} = \frac{-\varepsilon_{\text{film}}(Z-D)(\varepsilon_{\text{film}}-1)\epsilon\widetilde{\boldsymbol{\nabla}_{\parallel}}H}{\left[\varepsilon_{\text{film}} D - (\varepsilon_{\text{film}}-1)H\right]^2}. \tag{B.13}$$

B.4 Tangential Stresses from Electric Field Evaluated at Perturbed Interface

In Sec. 2.3.1, an expression for the normal component of the stress tensor dotted into the normal vector was computed. Recall that this expression is

$$\hat{n}\cdot\mathbf{T}^{\text{em}}\cdot\hat{n} = \frac{\varepsilon_o \varepsilon}{2} E_z^2. \tag{B.14}$$

To find the tangential stresses this quantity must be subtracted from the stress tensor dotted into the normal vector. This quantity is

$$\mathbf{T}^{\text{em}}\cdot\hat{n} = \varepsilon_o\varepsilon\begin{bmatrix} -\frac{1}{2}E_z^2 & 0 & E_xE_z \\ 0 & -\frac{1}{2}E_z^2 & E_yE_z \\ E_xE_z & E_yE_z & \frac{1}{2}E_z^2 \end{bmatrix}\begin{bmatrix} -\epsilon\frac{\partial H}{\partial X} \\ -\epsilon\frac{\partial H}{\partial Y} \\ 1 \end{bmatrix} = \varepsilon_o\varepsilon\left(\frac{\epsilon}{2}E_z^2\widetilde{\boldsymbol{\nabla}}_{\|}H + E_z\vec{E}_{\|} + \frac{1}{2}E_z^2\hat{z}\right).$$

The tangential components of the stress tensor are

$$\begin{aligned}(\mathbf{T}^{\text{em}}\cdot\hat{n})_{\|} &= \mathbf{T}^{\text{em}}\cdot\hat{n} - (\hat{n}\cdot\mathbf{T}^{\text{em}}\cdot\hat{n})\,\hat{n} \\ &= \varepsilon_o\varepsilon E_z\left(E_z\epsilon\widetilde{\boldsymbol{\nabla}}_{\|}H + \vec{E}_{\|}\right). \end{aligned} \tag{B.15}$$

The difference in the tangential stress tensors in the air and the film is now verified to be zero. This implies that there are no tangential stresses.

$$\begin{aligned}\left(\mathbf{T}^{\text{em}}_{\text{air}}\cdot\hat{n}\right)_{\|} - \left(\mathbf{T}^{\text{em}}_{\text{film}}\cdot\hat{n}\right)_{\|} =& \varepsilon_o E'_{\text{air,z}}\left(E'_{\text{air,z}}\epsilon\widetilde{\boldsymbol{\nabla}}_{\|}H + \vec{E}'_{\text{air,}\|}\right) \\ &- \varepsilon_o\varepsilon_{\text{film}}E'_{\text{film,z}}\left(\epsilon E'_{\text{film,z}}\widetilde{\boldsymbol{\nabla}}_{\|}H + \vec{E}'_{\text{film,}\|}\right) \\ =& \frac{\varepsilon_o\varepsilon_{\text{film}}\Phi'^2_c}{h_o^2}\widetilde{E}'_{\text{film,z}}\left(\epsilon\widetilde{\boldsymbol{\nabla}}_{\|}H\left(\widetilde{E}'_{\text{air,z}} - \widetilde{E}'_{\text{film,z}}\right) + \widetilde{E}'_{\text{air,}\|} - \widetilde{E}'_{\text{film,}\|}\right).\end{aligned}$$

In this expression the fact that $E'_{\text{air,z}} = \varepsilon_{\text{film}}E'_{\text{film,z}}$ has been used. Substitution of the electric field expressions into this equation yields

$$\begin{aligned}\left(\mathbf{T}^{\text{em}}_{\text{air}}\cdot\hat{n}\right)_{\|} - \left(\mathbf{T}^{\text{em}}_{\text{film}}\cdot\hat{n}\right)_{\|} =& \frac{\varepsilon_o\varepsilon_{\text{film}}\Phi'^2_c}{h_o^2}\widetilde{E}'_{\text{film,z}}\epsilon\widetilde{\boldsymbol{\nabla}}_{\|}H\Bigg(\frac{1-\varepsilon_{\text{film}}}{\varepsilon_{\text{film}}D - (\varepsilon_{\text{film}}-1)H} \\ &+ \frac{H(\varepsilon_{\text{film}}-1) - \varepsilon_{\text{film}}(H-D)(\varepsilon_{\text{film}}-1)}{\left[\varepsilon_{\text{film}}D - (\varepsilon_{\text{film}}-1)H\right]^2}\Bigg) \\ =& 0.\end{aligned}$$

This demonstrates that the electric fields derived from the perturbed interface consistently satisfy Maxwell's equations and do not have any tangential stresses when there is no free charge at the interface.

B.5 Electric Field Perturbations Evaluated at an Unperturbed Interface

The derivation of Pease and Pussel computed the electric fields in the bilayer in two steps. First, a base state electric field was computed for the unperturbed

film interface, within the geometry shown in Fig. B.1. Then, a perturbation to the film height was introduced which created perturbations in the electric fields. Their derivation proceeded in dimensional quantities and was then scaled after computation of the perturbed electric field.

B.5.1 Base State Electric Field

Base state quantities are denoted with the superscript ^{o}. The boundary conditions for this system are

$$\phi^o_{\text{film}}(z = 0) = 0, \tag{B.16}$$

$$\phi^o_{\text{air}}(z = d_o) = \Phi_o, \tag{B.17}$$

$$\varepsilon_{\text{film}} E^o_{\text{film}}(z = h_o) = E^o_{\text{air}}(z = h_o), \tag{B.18}$$

$$\phi^o_{\text{air}}(z = d_o) - \phi^o_{\text{film}}(z = 0) = -\int_0^{h_o} E^o_{\text{film}} dz - \int_{h_o}^{d_o} E^o_{\text{air}} dz. \tag{B.19}$$

The last condition is an equivalent statement to the continuity of electric potential at an interface which arises from the tangential electrostatic boundary conditions. Combining the four equations presented above into one simplifies to

$$\Phi_o = -h_o E^o_{\text{film}} - \varepsilon_{\text{film}}(d_o - h_o) E^o_{\text{film}},$$

from which the electric field in the film at $z = h_o$ was found

$$\vec{E}^o_{\text{film}}(z = h_o) = \frac{-\Phi_o \hat{z}}{\varepsilon_{\text{film}} d_o - (\varepsilon_{\text{film}} - 1) h_o}. \tag{B.20}$$

From this expression the electric field in the air layer at $z = h_o$ was computed to be

$$\vec{E}^o_{\text{air}}(z = h_o) = \frac{-\varepsilon_{\text{film}} \Phi_o \hat{z}}{\varepsilon_{\text{film}} d_o - (\varepsilon_{\text{film}} - 1) h_o}. \tag{B.21}$$

These are the base state electric fields which can now be perturbed.

B.5.2 Perturbed Electric Field

With the base state electric fields computed, the position of the film/air interface was perturbed

$$h = h_o + \delta h e^{i\vec{k}_\parallel \cdot \vec{x}_\parallel}. \tag{B.22}$$

The perturbed electric quantities, $\delta\phi$, $\delta\vec{E}$, and $\delta\vec{D}$ are added to the their respective base state quantities. For each layer, the total potential, electric field, and electric displacement field must satisfy Maxwell's equations. Due to the linearity of Maxwell's equations the perturbed electric fields must satisfy

$$\boldsymbol{\nabla} \times \delta\vec{E} = 0, \tag{B.23}$$

$$\boldsymbol{\nabla} \cdot \delta\vec{E} = 0. \tag{B.24}$$

These two equations imply that the perturbed electric field can be written as the negative gradient of the perturbed potential and that this perturbed potential will satisfy Laplace's equation

$$\boldsymbol{\nabla}^2 \delta\phi = 0. \tag{B.25}$$

The perturbed potential was expanded in terms of normal modes as was the film height perturbation. The specific form is

$$\delta\phi = \widetilde{\phi}(z) e^{i\vec{k}_{\parallel}\cdot\vec{x}_{\parallel}}. \tag{B.26}$$

Laplace's equation of the perturbed potential then becomes

$$\frac{d^2\widetilde{\phi}}{dz^2} - k^2\widetilde{\phi} = 0. \tag{B.27}$$

Two linearly independent solutions to this equation in the two layers are

$$\widetilde{\phi}_{\text{film}} = A^{\text{EHD}}_{\text{film}} \sinh kz + B^{\text{EHD}}_{\text{film}} \cosh kz, \tag{B.28}$$

$$\widetilde{\phi}_{\text{air}} = A^{\text{EHD}}_{\text{air}} \sinh kz + B^{\text{EHD}}_{\text{air}} \cosh kz. \tag{B.29}$$

Because the base state solution already satisfies the boundary conditions at $z = 0$ and $z = d_o$, the perturbed potential must satisfy the following Dirichlet boundary conditions

$$\delta\phi_{\text{film}}(z = 0) = 0, \tag{B.30}$$

$$\delta\phi_{\text{air}}(z = d_o) = 0. \tag{B.31}$$

Upon simplification the perturbed potentials become

$$\widetilde{\phi}_{\text{film}} = A^{\text{EHD}}_{\text{film}} \sinh kz,$$

$$\widetilde{\phi}_{\text{air}} = A^{\text{EHD}}_{\text{air}} \sinh k(z - d_o),$$

where in the last expression a constant factor has been absorbed into the definition of $A_{\text{air}}^{\text{EHD}}$ since it would have canceled later. The two remaining boundary conditions are more complicated to apply and in the work of Pease and Russel were evaluated at the unperturbed film position $z = h_o$, even though it should have been $z = h$. Denoting the difference across the interface (air minus film) of a quantity by enclosing it in brackets, the usual electrostatic boundary conditions are

$$\hat{n} \times [\vec{E}] = 0, \tag{B.32}$$

$$\hat{n} \cdot [\vec{D}] = 0. \tag{B.33}$$

The vector quantities are now broken into components to more effectively take the dot and cross product in the above equations. The base state electric field has no $\hat{x}$ and $\hat{y}$ components, and the normal component of the base state electric displacement field is continuous across the interface because there is no free charge. Consequently the differences across the interface have the form

$$\begin{aligned}
[E_x] &= [\delta E_x], \\
[E_y] &= [\delta E_y], \\
[E_z] &= [E^o] + [\delta E_z], \\
[D_x] &= [\delta D_x], \\
[D_y] &= [\delta D_y], \\
[D_z] &= [\delta D_z].
\end{aligned}$$

The boundary condition in the normal direction is

$$\hat{n} \cdot [\vec{D}] = -\frac{\partial \delta h}{\partial x}[\delta D_x] - \frac{\partial \delta h}{\partial y}[\delta D_y] + [\delta D_z] = 0.$$

The first two terms in this expression are second order and have been dropped to first order. Consequently, this equation implies

$$\delta E_{\text{air},z} = \varepsilon_{\text{film}} \delta E_{\text{film},z}.$$

Or, in terms of the potential,

$$\frac{\partial \widetilde{\phi}_{\text{air}}}{\partial z} = \varepsilon_{\text{film}} \frac{\partial \widetilde{\phi}_{\text{film}}}{\partial z}.$$

This equation was evaluated at $z = h_o$ and yields one constant in terms of the other

$$A_{\text{film}}^{\text{EHD}} = \frac{A_{\text{air}}^{\text{EHD}}}{\varepsilon_{\text{film}}} \frac{\cosh k(h_o - d_o)}{\cosh k h_o}, \tag{B.34}$$

which means that the perturbed potentials are now

$$\widetilde{\phi}_{\text{film}} = \frac{A_{\text{air}}^{\text{EHD}} \cosh k(h_o - d_o)}{\varepsilon_{\text{film}}} \frac{\sinh kz}{\cosh k h_o},$$
$$\widetilde{\phi}_{\text{air}} = A_{\text{air}}^{\text{EHD}} \sinh k(z - d_o).$$

The tangential electrostatic boundary conditions requires the evaluation of the cross product

$$\hat{n} \times [\vec{E}] = \begin{bmatrix} \hat{x} & \hat{y} & \hat{z} \\ -\dfrac{\partial h}{\partial x} & -\dfrac{\partial h}{\partial y} & -1 \\ [\delta E_x] & [\delta E_y] & [E^o] + [\delta E_z] \end{bmatrix} = 0.$$

The $\hat{z}$ component of this cross product is second order and the $\hat{x}$ and $\hat{y}$ expressions have the same form. As such, the $\hat{x}$ component was chosen without loss of generality. In terms of the potential it is

$$\left[-\frac{\partial \delta\phi}{\partial y} + E^o \frac{\partial h}{\partial y} \right] = 0.$$

Because both the potential perturbation and the height perturbation were expanded in the same set of normal modes, the partial derivative brings down the same term from the exponential which then cancels, leaving

$$\left[-\widetilde{\phi} + E^o \delta h \right] = 0.$$

The difference in perturbed potentials is then

$$\widetilde{\phi}_{\text{film}} - \widetilde{\phi}_{\text{air}} = \delta h \left(E_{\text{film}}^o - E_{\text{air}}^o \right). \tag{B.35}$$

From this equation the last remaining constant in the perturbed potentials is determined

$$A_{\text{air}}^{\text{EHD}} = \frac{\varepsilon_{\text{film}}}{\cosh k(h_o - d_o)} \frac{\delta h \left(E_{\text{film}}^o - E_{\text{air}}^o \right)}{\tanh k h_o - \varepsilon_{\text{film}} \tanh k(h_o - d_o)}. \tag{B.36}$$

Substituting this back into the expressions for the perturbed potentials yields

$$\widetilde{\phi}_{\text{film}} = \frac{\delta h(\varepsilon_{\text{film}} - 1)E^o_{\text{film}}}{\varepsilon_{\text{film}} \tanh k(h_o - d_o) - \tanh kh_o} \frac{\sinh kz}{\cosh kh_o}, \tag{B.37}$$

$$\widetilde{\phi}_{\text{air}} = \frac{\varepsilon_{\text{film}}\delta h(\varepsilon_{\text{film}} - 1)E^o_{\text{film}}}{\varepsilon_{\text{film}} \tanh k(h_o - d_o) - \tanh kh_o} \frac{\sinh k(z - d_o)}{\cosh k(h_o - d_o)}. \tag{B.38}$$

The components of the electric field at the perturbed interface ($z = h$) are needed for the evaluation of the tangential stresses. As before, the electric field is broken into components normal and tangential to the interface

$$\delta E_{\text{film,z}} = \frac{-\delta h(\varepsilon_{\text{film}} - 1)E^o_{\text{film}}}{\varepsilon_{\text{film}} \tanh k(h_o - d_o) - \tanh kh_o} \frac{k \cosh kh}{\cosh kh_o}, \tag{B.39}$$

$$\delta E_{\text{film},\parallel} = \frac{-(\varepsilon_{\text{film}} - 1)E^o_{\text{film}} \boldsymbol{\nabla}_\parallel \delta h}{\varepsilon_{\text{film}} \tanh k(h_o - d_o) - \tanh kh_o} \frac{\sinh kh}{\cosh kh_o}, \tag{B.40}$$

$$\delta E_{\text{air,z}} = \frac{\varepsilon_{\text{film}}\delta h(\varepsilon_{\text{film}} - 1)E^o_{\text{film}}}{\varepsilon_{\text{film}} \tanh k(h_o - d_o) - \tanh kh_o} \frac{k \cosh k(h - d_o)}{\cosh k(h_o - d_o)}, \tag{B.41}$$

$$\delta E_{\text{air},\parallel} = \frac{-\varepsilon_{\text{film}}(\varepsilon_{\text{film}} - 1)E^o_{\text{film}} \boldsymbol{\nabla}_\parallel \delta h}{\varepsilon_{\text{film}} \tanh k(h_o - d_o) - \tanh kh_o} \frac{\sinh k(h - d_o)}{\cosh k(h_o - d_o)}. \tag{B.42}$$

Since these electric fields are in dimensional units, they are nondimensionalized and then the lubrication approximation is applied to them in the following equations. During the application of the lubrication approximation the hyperbolic functions are Taylor expanded. Note that all dependence on the wavevector, K, cancels after the Taylor expansion.

$$\widetilde{\delta E}'_{\text{film,z}} = \frac{-(H-1)(\varepsilon_{\text{film}}-1)\widetilde{E}^o_{\text{film}}}{\varepsilon_{\text{film}}\tanh\epsilon K(1-D)-\tanh\epsilon K}\frac{\epsilon K\cosh\epsilon KH}{\cosh\epsilon K}$$
$$\approx (H-1)\frac{(\varepsilon_{\text{film}}-1)\widetilde{E}^o_{\text{film}}}{\varepsilon_{\text{film}}D-(\varepsilon_{\text{film}}-1)}, \tag{B.43}$$
$$\widetilde{\delta E}'_{\text{film},\parallel} = \frac{-(\varepsilon_{\text{film}}-1)\widetilde{E}^o_{\text{film}}\epsilon\widetilde{\boldsymbol{\nabla}}_\parallel H}{\varepsilon_{\text{film}}\tanh\epsilon K(1-D)-\tanh\epsilon K}\frac{\sinh\epsilon KH}{\cosh\epsilon K}$$
$$\approx \epsilon H\widetilde{\boldsymbol{\nabla}}_\parallel H\frac{(\varepsilon_{\text{film}}-1)\widetilde{E}^o_{\text{film}}}{\varepsilon_{\text{film}}D-(\varepsilon_{\text{film}}-1)}, \tag{B.44}$$
$$\widetilde{\delta E}'_{\text{air,z}} = \frac{-(H-1)\varepsilon_{\text{film}}(\varepsilon_{\text{film}}-1)\widetilde{E}^o_{\text{film}}}{\varepsilon_{\text{film}}\tanh\epsilon K(1-D)-\tanh\epsilon K}\frac{\epsilon K\cosh\epsilon KH}{\cosh\epsilon K}$$
$$\approx (H-1)\frac{\varepsilon_{\text{film}}(\varepsilon_{\text{film}}-1)\widetilde{E}^o_{\text{film}}}{\varepsilon_{\text{film}}D-(\varepsilon_{\text{film}}-1)}, \tag{B.45}$$
$$\widetilde{\delta E}'_{\text{air},\parallel} = \frac{-\varepsilon_{\text{film}}(\varepsilon_{\text{film}}-1)\widetilde{E}^o_{\text{film}}\epsilon\widetilde{\boldsymbol{\nabla}}_\parallel H}{\varepsilon_{\text{film}}\tanh\epsilon K(1-D)-\tanh\epsilon K}\frac{\sinh\epsilon K(H-D)}{\cosh\epsilon K}$$
$$\approx \epsilon(H-D)\widetilde{\boldsymbol{\nabla}}_\parallel H\frac{\varepsilon_{\text{film}}(\varepsilon_{\text{film}}-1)\widetilde{E}^o_{\text{film}}}{\varepsilon_{\text{film}}D-(\varepsilon_{\text{film}}-1)}. \tag{B.46}$$

Additionally, the scaled base state electric fields at the unperturbed interface are

$$\widetilde{E}^o_{\text{film}} = \frac{-1}{\varepsilon_{\text{film}}D-(\varepsilon_{\text{film}}-1)}, \tag{B.47}$$
$$\widetilde{E}^o_{\text{air}} = \frac{-\varepsilon_{\text{film}}}{\varepsilon_{\text{film}}D-(\varepsilon_{\text{film}}-1)}. \tag{B.48}$$

B.6 Tangential Stresses from Electric Field Evaluated at Unperturbed Interface

From Sec. B.4 the tangential components of the stress tensor have the form

$$\left(\mathbf{T}^{\text{em}}\cdot\hat{n}\right)_\parallel = \varepsilon_o\varepsilon\left(\epsilon E_z^2\widetilde{\boldsymbol{\nabla}}_\parallel H + \vec{E}_\parallel E_z\right). \tag{B.49}$$

The $\hat{z}$ component of the electric field is composed of a base state and a perturbation. Substituting and only keeping terms to first order in ϵ, this expression becomes

$$\left(\mathbf{T}^{\text{em}}\cdot\hat{n}\right)_\parallel = \varepsilon_o\varepsilon\left(\epsilon\widetilde{\boldsymbol{\nabla}}_\parallel H(E^o)^2 + \vec{E}_\parallel E^o\right).$$

This implies that the tangential stress difference between the air and film layers is

$$\left(\mathbf{T}^{\text{em}}_{\text{air}}\cdot\hat{n}\right)_\parallel - \left(\mathbf{T}^{\text{em}}_{\text{film}}\cdot\hat{n}\right)_\parallel = \frac{\varepsilon_o\Phi_c'^2}{h_o^2}\varepsilon_{\text{film}}\widetilde{E}^o_{\text{film}}\Bigg(\epsilon\widetilde{\boldsymbol{\nabla}}_\parallel H\widetilde{E}^o_{\text{film}}(\varepsilon_{\text{film}}-1) + \widetilde{\delta E}'_{\text{air},\parallel} - \widetilde{\delta E}'_{\text{film},\parallel}\Bigg).$$

Focusing on the right hand side of the equation, substitution of the scaled electric fields from above gives

$$\begin{aligned}\left(\mathbf{T}^{\text{em}}_{\text{air}}\cdot\hat{n}\right)_{\parallel}-\left(\mathbf{T}^{\text{em}}_{\text{film}}\cdot\hat{n}\right)_{\parallel}=&\frac{\varepsilon_o\varepsilon_{\text{film}}\Phi_c'^2}{h_o^2}\left(\widetilde{E}^o_{\text{film}}\right)^2\epsilon\widetilde{\boldsymbol{\nabla}}_{\parallel}H(\varepsilon_{\text{film}}-1)\times\\&\left(1-\frac{\varepsilon_{\text{film}}D-(\varepsilon_{\text{film}}-1)H}{\varepsilon_{\text{film}}D-(\varepsilon_{\text{film}}-1)}\right)\\\neq&0.\end{aligned}\tag{B.50}$$

This result demonstrates that this technique for calculating the electric field is not consistent with Maxwell's equations any time that the interface is not flat ($H = 1$).

B.7 Summary

In the first case when the electric field was evaluated at the perturbed interface, the governing equations were scaled and the lubrication approximation was invoked very early in the derivation. This use of the lubrication approximation simplified Laplace's equation, which allowed for an easy solution of the electric field in the bilayer since the $\hat{z}$ equations decouple from the other directions. In the second case, the electric field was computed in dimensional quantities, scaled, and then the lubrication approximation was applied afterwards. This leads to a more complicated solution process which can obscure the fact the electric fields are not consistent with Maxwell's equations any time the interface is not flat. From an intuitive perspective, the choice to evaluate the perturbed electric field at the unperturbed interface is problematic because it attempts to find a consistent electric field at a flat interface when the interface will be deformed during growth. The computation of the electric fields in the perturbed case could have been fixed by applying the final two electrostatic boundary conditions at $z = h$ instead of $z = h_o$.

As an interesting historical note, this issue with the inconsistent tangential stresses was corrected in later work (e.g. [79]) without comment, so it is not clear if this issue was ever noticed. It also bears mentioning that even with this error Pease and Russel still derived the correct expression for λ_o^{EHD} in linear stability (not presented here). They found the correct answer because in linear stability the stresses are evaluated at the unperturbed interface where the tangential stresses don't contribute. This means that the only place where this issue would cause significant problems is in numerical simulations of the EHD thin film evolution equation at late times when using the evolution equation derived by Pease and Russel.